November 12, 2021

JOHANNES GUTENBERG
UNIVERSITY

Radiative corrections to Compton processes on the proton and to the Drell-Yan process

Dissertation zur Erlangung des Grades
"Doktor der Naturwissenschaften"
am Fachbereich Physik, Mathematik und Informatik

vorgelegt von: **Matthias Heller**

1st Supervisor: Marc VANDERHAEGHEN
2nd Supervisor: Andreas VON MANTEUFFEL

Abstract

For a solid interpretation of experimental data and comparison with predictions from the Standard Model of Particle Physics, one needs a precise theoretical understanding of the underlying scattering processes and incorporate higher-order corrections into theoretical predictions. However, the calculation of these corrections is in general very cumbersome and time-consuming and new techniques need to be developed that facilitate the computation. In this thesis, we study radiative corrections to two different processes at very different energy scales. Despite the fact that the underlying theories are quite different, the techniques and tools to calculate higher-order effects in both situations are the same.

In the first project, we calculate the leading-order corrections in quantum electrodynamics to the Compton process on the proton in different experimental setups. The Compton process is one of the most important processes to study the internal structure of nucleons using scattering data at different energies and from different experiments to access the Compton amplitude phenomenologically. To extract structure functions from the data, it is important to know the size of radiative corrections on the level of the theoretically predicted cross section when comparing with experimental data. We study these corrections in various experimental situations and for different models, describing the Compton amplitude in two different energy regimes.

In the second project, we study the mixed electroweak-strong radiative corrections to the Drell-Yan process. Although this type of correction received a significant amount of attention in the particle physics community during the last decades, the calculation of the full set of contributions without any approximation remained a challenge for a long time. The main technical issue was the calculation of the master integrals with two masses using differential equations. They fall into a class of integrals whose differential equations contain non-rationalizable algebraic functions such that the standard algorithm to integrate the differential equation does not work. We develop new techniques to tackle this class of differential equations and successfully calculate all master integrals for the mixed electroweak-strong two-loop corrections to the Drell-Yan process. Using these integrals, we furthermore calculate the virtual two-loop mixed electroweak-strong helicity amplitudes for the first time.

Zusammenfassung

Um neue, immer präziser-werdende Streuexperimente zu analysieren und mit Vorhersagen des Standardmodells der Teilchenphysik zu vergleichen, braucht man ein gutes theoretisches Verständnis der zugrunde liegenden Streuprozesse und muss daher Korrekturen höherer Ordnung in die Rechnung mit einbeziehen. Die Berechnung dieser Korrekturen ist im Allgemeinen jedoch sehr zeitaufwendig und komplex und neue Algorithmen und Methoden müssen entwickelt werden, um solche Rechnungen zu ermöglichen. In der vorliegenden Arbeit werden Strahlungskorrekturen zu zwei verschiedenen Prozessen bei sehr unterschiedlichen Energien berechnet. Obwohl die zugrundeliegende Theorie zu beiden Prozessen sehr unterschiedlich ist, sind die Methoden und Werkzeuge zur Berechnung in beiden Fällen die selben.

Im ersten Projekt werden Strahlungskorrekturen erster Ordnung in der Quantenelektrodynamik zum Compton-Prozess am Proton berechnet. Dieser ist einer der wichtigsten Prozess um die interne Struktur des Nukleons bei unterschiedlichen Energien zu untersuchen, indem man die Compton-Amplitude phänomenologisch aus verschiedenen Experimenten extrahiert. Dafür ist es aber erforderlich die Größenordnung der Strahlungskorrekturen auf den theoretisch vorhergesagten Wirkungsquerschnitten zu kennen, wenn man sie mit den experimentellen Daten vergleicht. In dieser Arbeit werden die Korrekturen für verschiedene experimentelle Situationen und für verschiedene Modelle der Compton-Amplitude untersucht.

Im zweiten Projekt werden die gemischt-elektroschwach-starken Zwei-Schleifen-Korrekturen zum Drell-Yan Prozess berechnet. Obwohl sie eine große Aufmerksamkeit seitens der Teilchenphysik-Community im Laufe der letzten Jahrzehnte erhielten, ist die Berechnung dieser Korrekturen, ohne dabei Näherungen zu machen, technisch sehr herausfordernd. Der konzeptionell schwierigste Teil ist dabei die Berechnung der zwei-massigen Masterintegrale mittels Differentialgleichungen. Diese fallen in eine Klasse von Integralen, deren Differentialgleichungen nicht-rationalisierbare, algebraische Funktionen enthalten, so dass die Standardalgorithmen um sie zu integrieren nicht funktionieren. Wir entwickeln eine neue Methode, die es erlaubt solche Differentialgleichungen zu vereinfachen und anschließend zu lösen, und berechnen so alle Masterintegrale, die zu den gemischten elektroschwach-starken Zwei-Schleifen-Korrekturen zum Drell-Yan Prozess beitragen. Diese Integrale nutzen wir, um auch die gemischt-elektroschwach-starken virtuellen Zwei-Schleifen-Korrekturen der Helizitätsamplituden zum ersten Mal zu berechnen.

List of publications

[1] M. Heller, O. Tomalak, and M. Vanderhaeghen. "Soft-photon corrections to the Bethe-Heitler process in the $\gamma p \to l^+ l^- p$ reaction". In: *Phys. Rev. D* 97.7 (2018), p. 076012. DOI: 10.1103/PhysRevD.97.076012. arXiv: 1802.07174 [hep-ph].

[2] M. Heller et al. "Leading Order Corrections to the Bethe-Heitler Process in the $\gamma p \to l^+ l^- p$ Reaction". In: *Phys. Rev. D* 100.7 (2019), p. 076013. DOI: 10.1103/PhysRevD.100.076013. arXiv: 1906.02706 [hep-ph].

[3] M. Heller, A. von Manteuffel, and R. M. Schabinger. "Multiple polylogarithms with algebraic arguments and the two-loop EW-QCD Drell-Yan master integrals". In: *Phys. Rev. D* 102.1 (2020), p. 016025. DOI: 10.1103/PhysRevD.102.016025. arXiv: 1907.00491 [hep-th].

[4] M. Heller et al. "Mixed QCD-EW two-loop corrections to Drell-Yan production". In: *PoS* RADCOR2019 (2019), p. 042. DOI: 10.22323/1.375.0042. arXiv: 1912.09110 [hep-ph].

[5] M. Heller, N. Keil, and M. Vanderhaeghen. "Leading-order QED radiative corrections to timelike Compton scattering on the proton". In: *Phys. Rev. D* 103.3 (2021), p. 036009. DOI: 10.1103/PhysRevD.103.036009. arXiv: 2012.09565 [hep-ph].

[6] M. Heller et al. "Mixed EW-QCD two-loop amplitudes for $q\bar{q} \to \ell^+ \ell^-$ and γ_5 scheme independence of multi-loop corrections". In: *JHEP* 05 (2021), p. 213. DOI: 10.1007/JHEP05(2021)213. arXiv: 2012.05918 [hep-ph].

[7] M. Heller and A. von Manteuffel. "MultivariateApart: Generalized partial fractions". In: *Comput. Phys. Commun.* 271 (2022), p. 108174. DOI: 10.1016/j.cpc.2021.108174. arXiv: 2101.08283 [cs.SC].

[8] M. Heller. "Planar two-loop integrals for μ**e** scattering in QED with finite lepton masses". In: *unpublished* (). arXiv: 2105.08046 [hep-ph].

[9] M. Heller, N. Keil, and M. Vanderhaeghen. "Soft-photon radiative corrections to the $e^- p \to e^- p l^- l^+$ process". In: *Phys. Rev. D* 104.7 (2021), p. 073007. DOI: 10.1103/PhysRevD.104.073007. arXiv: 2108.02088 [hep-ph].

Contents

1 Introduction

1.1 The Standard Model and Precision Physics

The Standard Model of particle physics is beyond any doubt one of the most successful theories in physics. Being developed throughout the second half of the 20th century, it establishes a uniform way to describe three out of the four fundamental forces in nature. The Standard Model is based on quantum field theory (QFT), the relativistic generalization of quantum mechanics. It is able to describe phenomena over a broad range of energy scales. On the one hand, for low energies, it is capable to describe electromagnetic interactions of electrons with nucleons or atoms in scattering experiments and spectroscopy, as well as the weak interactions of nucleons, which are responsible for the radiative decay of atomic nuclei. These interactions are incorporated in the electroweak (EW) sector of the Standard Model, which includes the theory of electromagnetic interactions, called quantum electrodynamics (QED). On the other hand, for high energetic proton-proton collisions at the Large-Hadron-Collider (LHC) at CERN, the Standard Model is also capable of predicting cross sections based on quantum chromodynamics (QCD), the theory of strong nuclear interactions.

In order to describe interactions of particles in QFT, one defines so called Feynman (or scattering) amplitudes which give the probability of a quantum transition of an initial state $|i\rangle$ to a final state $\langle f|$ as:

$$\mathcal{M}_{fi} = \langle f| \mathcal{S} |i\rangle \,, \tag{1.1}$$

where the $\mathcal{S}$-matrix encodes the time evolution of the system and can be calculated by means of the Dyson expansion

$$\mathcal{S} = 1 + \sum_{n=1}^{\infty} \frac{(-i)^n}{n!} \int d^4x_1 \dots d^4x_n \mathcal{T}[\mathcal{H}_{int}(x_1) \dots \mathcal{H}_{int}(x_n)]. \tag{1.2}$$

In Eq. (1.2), $\mathcal{H}_{int}$ denotes the interaction Hamiltonian that can be deduced from the Lagrangian of the theory and $\mathcal{T}$ denotes the time-ordered product. Eq. (1.2) gives a perturbative solution to a Feynman amplitude. Since $\mathcal{H}_{int}$ is proportional to the coupling constants of the interacting quantum fields, one effectively expands the amplitude in these couplings. Each term in the sum of Eq. (1.2) corresponds to a set of Feynman diagrams, which one has to take into account at a given order. Terms beyond the leading order in the expansion are also called radiative corrections and the Feynman diagrams corresponding to them are called loop diagrams.

Feynman amplitudes as defined in Eq. (1.1) are not physical observables by themselves since they can not be measured directly in an experiment. For instance, considering a scattering process of particles, one could measure the total cross section of that process in an experiment. This cross section is proportional to the squared amplitude summed over all final states. If the amplitude is a sum of several terms, this shows that in an experiment one is sensitive to the interference of these terms.

In order to compare experimental data with predictions of the Standard Model, it is important to have a precise theoretical understanding on these predictions. In

the perturbative solution of QFT, this means one has to include radiative corrections to a given observable. As a famous example let us mention the discrepancy between the measured and the theoretical value of the anomalous magnetic moment of the muon [1], the latter being now calculated up to the tenth order in the electron coupling in QED, corresponding with up to five-loop diagrams [2]. Although the theoretical value of the anomalous magnetic moment of the muon only differs after the eighth digit from the experimental value, that difference still amounts to roughly four standard deviations and thus might be a signal for physics beyond the Standard Model. What becomes clear from this example is that precision matters: a tiny deviation from the Standard Model prediction in an experiment can only be identified if radiative corrections are under control to the precision reached by experiments.

However, the calculation of radiative corrections is in general very complicated and time-consuming. This has several reasons. Firstly, as mentioned above, including higher-order terms in the expansion means one has to calculate more and more Feynman diagrams. Secondly, the calculation of these diagrams becomes more difficult. This is, in general, due to a more complex algebraic structure of the amplitudes, as well as due to Feynman integrals appearing in higher-order calculations, which become more complicated with an increasing number of loops. Thirdly, Feynman diagrams involving loops are in general divergent. Thus, in order to get a physically meaningful and finite result, one has to perform a so-called renormalization which becomes more involved if one includes higher-order corrections.

With the increasing amount of data collected at colliders all over the world, precision physics is becoming more and more important for both high- and low-energy experiments. It is thus crucial to develop new tools and automate calculations, such that precise predictions from the theory side can be performed with less effort.

In this thesis, we study the radiative corrections to two different processes at very different energy scales. Namely, in one project, we study radiative corrections from QED in electromagnetic interactions with the proton. Those are important if one wants to study the internal structure of the proton, which typically is accessed through various scattering experiments. For the interpretation of the data of such experiments, radiative corrections need to be known. In another project, we study radiative corrections to the Drell-Yan process, a very prominent process measured in proton-proton collisions at the LHC. In this case, the underlying theory is not only QED (together with the EW sector) but also QCD in the perturbative domain. Here, higher-order corrections are again crucial for a robust interpretation of the data. Although the two processes are very different with respect to the energy scale and the involved particles that are responsible for the interactions, in both cases the setup used for the calculation is quite similar and relies heavily on modern tools and computer algebra. In the remainder of this chapter, we give a brief introduction to both projects and a motivation why the studied subjects are important.

1.2 Electromagnetic interactions of the nucleon

1.2.1 Compton scattering on the proton

For several decades, Compton scattering, corresponding to the process

$$\gamma + N \to \gamma + N, \tag{1.3}$$

has been a prime tool to study electromagnetic interactions of the proton and its internal structure. The Feynman diagram of the Compton process in the most general case with arbitrary photon virtualities is shown in Fig. 1.1. In general, one can

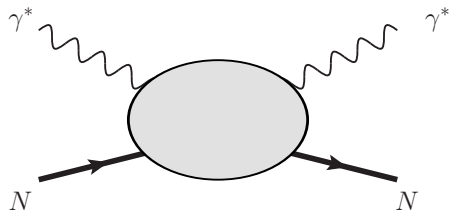

FIGURE 1.1: Diagram representing the most general Compton process, in which both photons are off-shell.

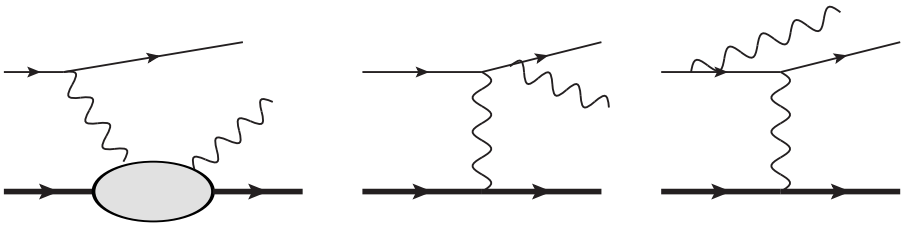

FIGURE 1.2: Diagrams contributing to the $e^- p \to e^- p\gamma$ reaction. One distinguishes between the VCS process (left diagram) and the BH process (central and right diagrams)

describe this process in terms of 18 independent helicity amplitudes or structure functions [3]. Depending on the photon virtualities, one distinguishes between different cases.

The real Compton scattering (RCS) process on the proton, with both photons being real, has already been studied in the 1950s [4] and has been used extensively since then to extract the electric, magnetic and spin polarizabilities of the nucleon experimentally. These fundamental constants describe how the proton or nucleon response to an external electromagnetic field. RCS is the cleanest way to extract nucleon structure functions, as it is not diluted by background processes. However, one is only able to access six out of the 18 structure functions for on-shell kinematics.

To extract more general information of the proton structure, virtual Compton scattering (VCS) has become more and more important during the past three decades. VCS refers to a Compton scattering process with an incoming photon with spacelike virtuality and an outgoing real photon and can be accessed experimentally through the $e^- p \to e^- p\gamma$ reaction. The VCS process is always accompanied by the Bethe-Heitler (BH) process, referring to the photo-production on a nucleon target. The Feynman diagrams for these processes are shown in Fig. 1.2. Since only the elastic proton form factors enter the BH amplitude, it does not contain any new information on the proton structure beyond these. Although the BH process typically dominates the cross section, VCS has been considered in various kinematic domains to study the proton structure. In order to be able to extract the relevant information on the proton structure from experimental data, it is thus important to have a solid theoretical understanding of the interference term between BH and VCS amplitude. This of course also includes the knowledge of radiative corrections, which become increasingly more important with more and better data available.

In recent years also timelike Compton scattering (TCS) has been widely discussed in the literature as a complementary tool to VCS to extract information of the proton

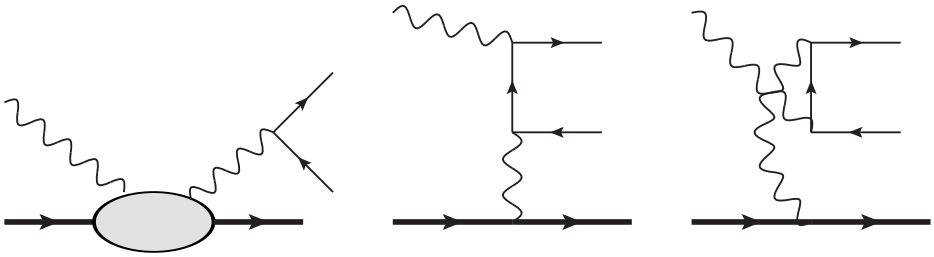

FIGURE 1.3: Diagrams contributing to the $\gamma p \to e^- e^+ p$ reaction. One distinguishes between the TCS process (left diagram) and the BH process (central and right diagrams)

structure in the timelike region. The TCS amplitude is experimentally accessible through the reaction $\gamma p \to e^- e^+ p$, which is related to the VCS reaction by a crossing symmetry. Like for the VCS case, this reaction is accompanied by a BH process. The Feynman diagrams are shown in Fig. 1.3. Also for TCS, it is important to note that the BH amplitude is typically the dominant contribution. Therefore, also in this case it is crucial to have a precise theoretical understanding of radiative corrections to be able to interpret experimental data accordingly.

In the most general case, in which both photons have finite virtuality, we speak of the double virtual Compton scattering (dVCS). The dVCS amplitude is accessible via the $e^- p \to e^- l^+ l^- p$ reaction, in which the produced dilepton ($l^- l^+$) can be either an $e^- e^+$ or a $\mu^- \mu^+$ pair. From all cases considered here, it is the most challenging to measure experimentally, as it has the largest background due to the BH process at the cross section level and is suppressed by an additional power in the QED coupling constant α_{em} compared to VCS or TCS.

Compton scattering at low energies

As mentioned above, RCS allows to experimentally access electric and magnetic polarizabilities of the proton. In the low-energy regime, one can think of the proton as being composed of a quark core that is surrounded by a pion cloud, which gets deformed after applying an external electromagnetic field. The strength of this deformation is characterized by the polarizabilities.

Using the VCS process instead of RCS, one can access more information and extract the so-called generalized polarizabilities [5], which encode not only the strength of the deformation of the charge density but also its spatial dependency [6]. At low energies, one can interpret the final state real photon as an almost constant external electromagnetic source. In that picture, one can think of the VCS process as an electron-proton scattering experiment with an external electromagnetic background field applying a charge deformation on the proton. Over the past two decades, generalized polarizabilities have been extracted at different facilities and various experiments at MIT-Bates, MAMI and Jefferson Lab (JLab) through a measurement of the VCS process. For a review of VCS and generalized polarizabilities see Ref. [7].

Another important application for low-energy Compton scattering is related to the forward double-virtual Compton scattering (VVCS) amplitude, which corresponds to a special limit of dVCS, in which the initial and final photons have the same non-zero space-like virtuality. In contrast to the VCS process discussed above, the forward VVCS process is not directly measurable. It enters however in the leading hadronic corrections to the muonic hydrogen Lamb shift and hyperfine splitting through the two-photon exchange [8, 9]. The interest in the improvement of these corrections is

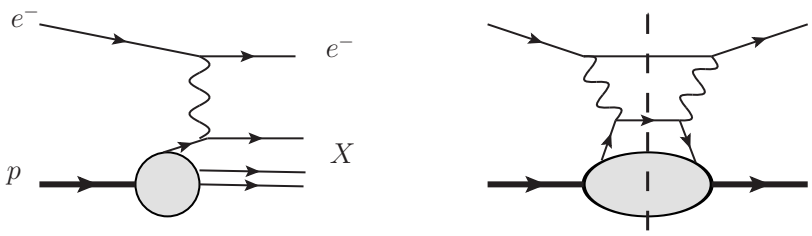

FIGURE 1.4: Left panel: Feynman diagram contributing to DIS in the $e^-p \to e^-X$ process. Squaring the amplitude corresponds to taking a cut through the diagram shown on the right. One can identify the forward Compton amplitude (shown as a blob) in that diagram.

motivated by the so-called proton radius puzzle, which stands for the discrepancy of the extraction of the proton charge radius in different experiments using muonic spectroscopy vs electron data. We will give more details on the proton radius puzzle in a subsequent section. Here, it is important to note that the dominant theoretical error in the radius extraction from spectroscopy up to date stems from the dispersive subtraction function entering the VVCS process [9–11]. Thus, to get a better theoretical understanding of the spectroscopy experiments one needs more constraints on this function. At second order in the photon virtuality, it can be constrained by the proton magnetic polarizability. However, to fourth order, one low-energy constant in the subtraction function is at present empirically unconstrained [12], and one relies on chiral effective field theory calculations [10, 13] or phenomenological estimates [14]. In Ref. [15] it was proposed to access this low-energy nucleon structure constant experimentally through the dVCS amplitude in the $e^-p \to l^-l^+e^-p$ reaction, where $l^- = e^-$ or $l^- = \mu^-$. As a part of this thesis, we study the impact of one-loop QED corrections in the soft-photon approximation to this process and its sensitivity to this low-energy constant using a low-energy model for the Compton amplitude. The results have been published in Ref. [16].

Compton scattering at high energies

At high energies one can use the factorization theorem to calculate the Compton scattering amplitude. The interaction of the photon with the proton factorizes into a hard partonic subprocess, which is calculated in perturbative QCD, and a parton distribution of the proton which encodes the non-perturbative physics. This formalism of QCD factorization was firstly applied in inclusive deep inelastic scattering (DIS) in the reaction $e^-p \to e^-X$, where X indicates the unobserved, inclusive final state. First experiments of DIS were performed in the 1960s at SLAC and were able to proof the existence of quarks for the first time [17].

QCD factorization works for high scattering energies, i.e. for large center-of-mass energy and large photon virtuality $Q \gg 1/\text{fm}$. Using the optical theorem, the cross section of DIS can be related to the imaginary part of the forward Compton amplitude, in which the initial and final photon and proton momenta are equal. This is depicted in Fig. 1.4. On the left panel, we show the Feynman diagram contributing to $e^-p \to e^-X$. Taking the squared amplitude corresponds to a cut through the diagram shown on the right, in which we can identify the forward Compton amplitude. The cut is understood as an on-shell sum over all possible states in the Compton blob. Thus, using DIS, we can only test the forward dynamics of the Compton amplitude, meaning the case in which the initial state momenta equals the final state momenta.

This corresponds to the Parton Distribution Functions (PDFs) in forward direction, encoding the longitudinal momentum fraction of the partons.

To complement the information on the proton structure from the forward amplitude, one can access the Compton amplitude in the more general case in which both photons have different virtuality. The factorization still works as long as at least one virtuality is large enough. In this case, the interaction is described by so-called Generalized Parton Distributions (GPDs), which were first introduced in Refs. [18–21]. In contrast to the regular PDFs, GPDs encode in addition to the longitudinal also the transverse structure of the proton, thus providing a fully three-dimensional picture.

One of the cleanest ways to extract GPDs is through the measurement of the deeply-virtual Compton scattering (DVCS) process in which the virtuality of the final state photon is zero. Measurements of this process have been carried out over the last two decades at HERA and JLab [22–25]. Information accessed through the VCS process can be further complemented by a measurement of the TCS process such that GPDs can be extracted also in the timelike region. A first measurement of the TCS amplitude through the $\gamma \to e^- e^+ p$ process in the high-energy region has very recently been performed at JLab [26], in which the cross section, as well as the beam-spin and forward-backward asymmetries, have been measured. It was found that both asymmetries are non-zero, thus providing strong evidence of the GPD mechanism for timelike kinematics for the first time. One main objective of this thesis is the calculation of the first-order radiative corrections to these observables and to study their impact as well as the sensitivity on the GPDs. The results have been published in Ref. [27].

A further extension of either the DVCS or TCS process in the high-energy near-forward region has been proposed through the $e^- p \to e^- p l^- l^+$ reaction (with l^- either an e^- or μ^-), which accesses the double deeply virtual Compton scattering (DDVCS) process with incoming space-like photon and outgoing time-like photon. The DDVCS process is of particular interest as it allows to extend the DVCS beam spin asymmetry measurements, which directly access GPDs, into the so-called Efremov-Radyushkin-Brodsky-Lepage (ERBL) domain [28, 29]. A feasibility study of the DDVCS experiment has shown that the SoLID@JLab project with its high luminosity and large acceptance is very promising to perform such measurements [30]. In this thesis, we study the impact of first-order soft-photon corrections in such an experimental setup, studying the cross section as well as forward-backward and beam spin asymmetry to the process $e^- p \to e^- p l^- l^+$. The results have been published in Ref. [16].

1.2.2 The proton radius puzzle and lepton universality

As mentioned above, the proton radius puzzle refers to the discrepancy between the extracted values of the proton charge radius from electron data vs muon data. Originally, this discrepancy amounted to around 5.6 σ when comparing the value of $R_E = 0.879(8)$ fm obtained from electron-proton scattering experiments from the A1@MAMI Collaboration in 2001 [31, 32] with the value of $R_E = 0.84087(39)$ fm from muonic spectroscopy data from the year 2010 [33, 34]. The puzzle spurred a lot of research activity and although recent electron spectroscopy measurements [35, 36] as well as an electron-proton scattering experiment at JLab [37] are now in favor of the smaller value obtained from the muonic spectroscopy, there are still new experiments planned to further clarify the situation. The most prominent experiments to mention are probably the first ones to study muon-proton scattering: the MUSE experiment at the Paul-Scherer-Institute [38, 39], which is still ongoing and aims to extract the proton radius with low-energy muon scattering data, and the COMPASS experiment

at CERN [40], which plans to measure elastic muon scattering off a proton using a 100 GeV muon beam.

Of course the proton radius puzzle also led to a lot of speculation on new physics scenarios to explain the discrepancy, see for example Refs. [41–50]. In any such scenario it is clear that lepton universality has to be violated. In the Standard Model all leptons have the same tree-level couplings, therefore predicting identical couplings for electrons and muons to the proton. In this context another experiment has been proposed in Ref. [51], which aims to test lepton universality by exploiting the ratio of cross sections of the reaction $\gamma p \to e^- e^+ p$ vs. $\gamma p \to \mu^- \mu^+ p$. In order to extract this ratio, the cross section measurement can be performed below and slightly above the di-muon threshold (but below the two-pion threshold). By calculating the ratio of two cross sections one does not rely on the precision which can be achieved for an absolute cross section measurement. It was found that the difference between both original values for the extracted proton charge radius mentioned above amounts to an effect of 0.2 % on this ratio. One result of this thesis is the calculation of the radiative corrections to this ratio, c.f. Refs. [52, 53]. We found that the inclusion of these corrections is imperative, as they shift the ratio by more than the 0.2 % effect from changing the coupling of the proton to the muon. The experiment is currently planned at MAMI.[1]

1.3 The Drell-Yan process

1.3.1 The basic process

The Drell-Yan (DY) process is one of the most important and basic processes measured at the LHC. The process, described by the reaction

$$pp \to l^+ l^- + X, \quad \text{with } l^- = e^- \text{ or } l^- = \mu^-, \tag{1.4}$$

was firstly measured in 1970 in the case of di-muon production, which showed a rapidly falling cross section with increasing di-muon mass. The theoretical mechanism for the production of dilepton pairs in proton-proton collisions was introduced in the same year by Drell and Yan using Feynman's parton model [54]. In this model, the quarks q are treated as free particles during the collision, neglecting the binding energy in the proton. Both quarks carry a momentum fraction x_1 and x_2 of the colliding proton momenta P_1 and P_2. Like in the high-energy case of Compton scattering, the interaction of the two protons factorizes in terms of a hard scattering sub-process and parton distributions. The hard scattering sub-process can be calculated using perturbative QFT and is described at leading order by the reaction

$$q\bar{q} \to l^+ l^-, \tag{1.5}$$

where q denotes a constituent quark of the proton. The basic Feynman diagram is shown in Fig. 1.5. Thus, provided the PDFs are known, the cross section of Drell-Yan scattering can be calculated without any further free parameters within this model. At the time, the parton distributions were already extracted from DIS, and a first comparison between the theoretical predicted cross section with the experimentally determined one resulted in a cross section that was too small by roughly a factor of two. Later it was realized that the inclusion of QCD subprocesses, like gluon-gluon or quark-gluon annihilation, was able to explain this deviation. Thus, the

[1] https://www.blogs.uni-mainz.de/fb08-mami-experiments/files/2016/09/LOI-A2-01-2016.pdf

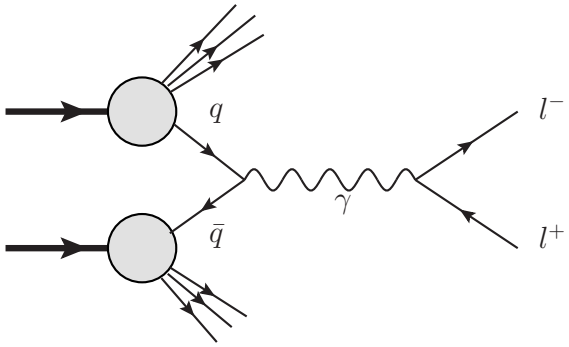

FIGURE 1.5: Feynman diagram of the neutral Drell-Yan process.

Drell-Yan process provided one of the first experimental tests of the universality of parton distributions, the QCD factorization theorem, as well as a powerful test of perturbative QCD.

With increasingly large scattering energies at the LHC, the Drell-Yan process was later used for the production of the heavy EW gauge bosons. Indeed, by replacing the virtual photon in Fig. 1.5 with a Z boson, the Drell-Yan process was the leading contribution in the UA1 and UA2 experiments at CERN that led to the discovery of Z and $W^{\pm}$ bosons in 1983 and was awarded the Nobel prize in 1988 [55, 56]. Nowadays the Drell-Yan process is used for precision measurements of Standard Model parameters, like the $W^{\pm}$ or Z mass, and the weak mixing angle, but as well for searches of physics beyond the Standard Model. For a review on the Drell-Yan process see Ref. [57].

1.3.2 Higher order corrections

As mentioned above, the difference between the theoretical predicted cross section and the experimental one in the early days of Drell-Yan production was an effect of radiative corrections. For searches of deviations from the Standard Model in experimental data we thus again see how important the incorporation of radiative corrections is. It therefore comes as no surprise that a lot of effort has been put in the theoretical calculation of higher order corrections to the Drell-Yan process during the last four decades. The corrections to the cross section from pure QCD have already been calculated up to two-loop order in the 1990s [58–64]. Regarding the EW corrections, up to now only the pure QED corrections are known at the two-loop level [65, 66], but the full set of EW corrections is only available at one-loop order [67–75]. Due to their large size, it has long been of interest in the particle physics community to calculate also the mixed EW-QCD corrections of relative order $\alpha_{\text{em}}\alpha_s$. Those are at present the main uncertainty on the Drell-Yan cross section. Many partial results have been obtained over the last decade: a calculation of the subset of QED-QCD corrections in Ref. [76] as well as approximations that are valid in the resonance region of the Z or $W^{\pm}$ gauge boson [77–83].

One objective of this thesis is the calculation of the mixed EW-QCD virtual corrections to the Drell-Yan process, which have been published in Refs. [84, 85]. Recently, also the full set of mixed corrections of order $\alpha_{\text{em}}\alpha_{\text{s}}$, including real radiation, have been calculated [86].

1.4 Outline of the thesis

This thesis is organized into three parts.

Part I gives a brief overview on different steps that are necessary to calculate Feynman amplitudes. In Chapter 2, we give a brief review on Feynman integrals, whose calculation is often the most difficult step in the calculation of the amplitude. Parts of that chapter are based on Refs. [84, 87] in which we introduce a novel method, that helps to calculate a special class of Feynman integrals involving non-rationalizable square roots in their differential equations. In Chapter 3, we introduce briefly the automated setup that we use to calculate Feynman amplitudes. Chapter 4 is based on Ref. [88], in which we discuss a novel algorithm to simplify rational functions based on partial functioning. Since this algorithm was used extensively for the calculation of different Feynman amplitudes studied in this thesis, we briefly present it here.

Part II is based on four publications [16, 27, 52, 53], which all deal with radiative QED corrections to Compton scattering and the Bethe-Heitler process in different experimental setups. In Chapter 5, based on Refs. [27, 52, 53], we study the process $\gamma p \to l^- l^+ p$ and discuss how it can be used to test lepton universality and access the TCS amplitude via forward-backward and beam spin asymmetries. Accessing the TCS amplitude allows one to test the underlying non-perturbative nucleon structure model, and in Ref. [27] we studied the sensitivity on two different nucleon models in a low and a high-energy regime. However, the main objective of this chapter is to study the leading-order QED corrections and check how they affect the cross sections and asymmetries. Chapter 6 is based on Ref. [16], in which we generalized the calculation from the TCS case to the double virtual case, the dVCS amplitude. We show how the dVCS amplitude can be accessed through the $e^- p \to e^- l^- l^+ p$ reaction, again studying two different models for different energy scales. Regarding radiative corrections, in this case, we restrict ourselves to the approximation of soft-photon corrections and again study their size on cross sections as well as asymmetries.

In Part III we present the calculation of the mixed EW-QCD two-loop corrections to the Drell-Yan process. The work on these corrections has led to two publications [84, 85]. In Ref. [84] we calculated the two-loop master integrals with two internal masses that are needed to calculate all terms contributing to the amplitude without any approximations. The calculation of these integrals is computational challenging since it involves a square root in the differential equation which is non-rationalizable. The results of this work are presented in Chapter 7. In Chapter 8 we present parts of Ref. [85], in which we report on the calculation of the two-loop corrected helicity amplitudes. The main contribution of this thesis to these results was an independent calculation of the unpolarized amplitude. This calculation served as an important cross-check for the calculation of the helicity amplitudes in Ref. [85] and we will discuss how the comparison was performed.

Part I

The Art of Multi-Loop Calculations

2 Review of Feynman integrals

2.1 Introduction

Feynman integrals appear in multi-loop calculations in QFT due to the exchange of virtual particles in Feynman diagrams. As an example how Feynman integrals emerge in QFT and how they look, let us consider the vacuum polarization diagram shown in Fig. 2.1. Using Feynman rules, the amplitude corresponding to this diagram is given by

$$\Pi^{\mu\nu}(q) = ie^2 \int \frac{d^4l}{(2\pi)^4} \frac{\mathrm{Tr}\left[\gamma^\mu(\not{l} - \not{k} + m)\gamma^\nu(\not{l} + m)\right]}{[(l-k)^2 - m^2 + i\delta][l^2 - m^2 + i\delta]}, \tag{2.1}$$

where m denotes the mass of the lepton in the loop and the integration has to be performed over all four-momentum configurations of the loop momentum l, corresponding to the momentum of the virtual particle in the loop of Fig. 2.1. The infinitesimal imaginary part $i\delta$ (which we will supress in the following) is introduced due to the Feynman prescription to invoke the choice of physical branch cuts.

In general, Feynman integrals can be divergent. This is also true for the integral in Eq. 2.1, which diverges (after performing the Wick rotation) for Euclidean $l \to \infty$. Using spherical coordinates, in the limit $l \to \infty$, the integral scales as

$$\Pi^{\mu\nu}(q) \propto \int dl\, l^3 \frac{l^2}{l^4} = \int dl\, l \to \infty. \tag{2.2}$$

A Feynman integral which diverges for $l \to \infty$ is called ultraviolet (UV) divergent. To make sense of an UV divergent amplitude one needs to perform a renormalization and introduce counterterms, which render the amplitude finite.

There is a second type of divergences, that can occur in the calculation of Feynman integrals called infrared (IR) divergence. Those can be further distinguished between soft and collinear divergences. A soft divergence emerges from a massless propagator $1/l^2$ in the limit $l \to 0$, while a collinear divergence results from a point where the loop momenta l is collinear to an external momentum k. IR divergences can not be removed by renormalization. Instead, to get a finite and physical meaningful result, one has to include so-called bremsstrahlung diagrams to the cross section, which correspond to diagrams with additional photons or gluons in the final state.

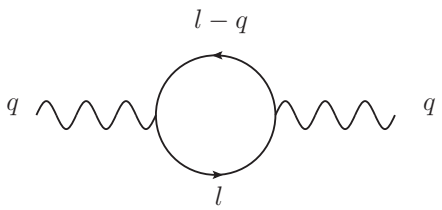

FIGURE 2.1: Vacuum polarization diagram. The wavy line denotes a photon, the solid lines a (virtual) fermion.

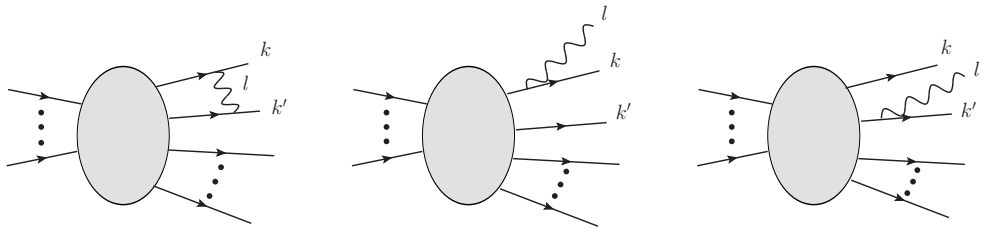

FIGURE 2.2: The virtual IR divergent one-loop correction (left diagram) and real-radiation diagrams (center and right diagrams) that need to be included to cancel the IR divergence.

Those diagrams possess the same infrared structure as their virtual counterparts and thus cancel the infrared divergences of the virtual corrections. As an example, let us consider the diagrams shown in Fig. 2.2. The dots in these diagrams indicate that more particles can be incoming or outgoing. The amplitude corresponding to the virtual correction, shown in the left diagram, has an IR divergence. However, taking into account real radiation (corresponding to the center and right diagrams), this divergence cancels out in the sum on the level of the cross section. Note that for the real-radiation diagrams an integration over the final-state photon has to be performed,

$$d\sigma_r = \int \mathrm{d}\Phi \, |\mathcal{M}_r|^2 \,, \tag{2.3}$$

where the matrix element of the real radiation diagrams is proportional to

$$\mathcal{M}_r \propto ie\bar{u}(k') \left[\not{\epsilon}_{\lambda_l}(l) \frac{\not{k}' + \not{l} + m}{2k' \cdot l} \Gamma_{\text{tree}} - \Gamma_{\text{tree}} \frac{\not{k} - \not{l} + m}{2k \cdot l} \not{\epsilon}_{\lambda_l}(l) \right] u(k), \tag{2.4}$$

where Γ_{tree} denotes the Dirac structure of the diagram without the additional photon, and where $\int d\Phi$ denotes the integral over the phase-space which includes the integration over the photon momenta and helicities λ_l, i.e. $\mathrm{d}\Phi \propto \int \frac{d^3 l}{2l^0} \sum_{\lambda_l}$. Here we see explicitly that $\mathcal{M}_r$, and thus also $d\sigma_r$, diverge if

$$k \cdot l = 0 \quad \text{or} \quad k' \cdot l = 0, \tag{2.5}$$

which is either true for $l \to 0$ (soft divergence) or $l \propto k^{(\prime)}$ (collinear divergence). Note that collinear divergences only appear if $k^2 = k'^2 = 0$, since only in that case l can become collinear to one of these momenta.

2.2 Dimensional regularization

To make sense of divergent Feynman amplitudes, one needs to introduce some regularization technique to split the divergent part of an integral from its finite remainder. Throughout this thesis, we use dimensional regularization, which was first introduced by 't Hooft and Veltman in Ref. [89]. In dimensional regularization the loop integral is not performed in $d = 4$, but in $d = 4 - 2\epsilon$ dimensions:

$$\int \frac{d^4 l}{(2\pi)^4} \to \left(\mu^2\right)^{\epsilon} \int \frac{d^{4-2\epsilon} l}{(2\pi)^{4-2\epsilon}}, \tag{2.6}$$

where ϵ is a complex number and μ the 't Hoost scale, that is introduced to maintain a dimensionless action. In that way, divergences of the integral manifest themselves as poles of the form $1/\epsilon^n$, where n is a natural number.

Dimensional regularization can be used to treat UV as well as IR divergences. Assuming that an integral is IR finite but UV divergent we have to choose the dimension of the integral as $d < 4$, thus $\mathrm{Re}(\epsilon_{\mathrm{UV}}) = 2 - d/2 > 0$. Similarly, assuming that an integral is only IR divergent, we have to choose $d > 4$ and thus we have $\mathrm{Re}(\epsilon_{\mathrm{IR}}) = 2 - d/2 < 0$. However, integrals, and thus of course also amplitudes, can be both, UV and IR divergent. We can still use dimensional regularisation for both types of divergences at the same time, by splitting the domain of integration into a part where the integral is UV divergent and a part where it is IR divergent. Then, by performing an analytic continuation from $d < 4$ for the UV divergent part to $d > 4$ and vice versa for the IR divergent part, we get a result that is valid for the whole complex d plane.

As we will see, in our setup it is very complicated to distinguish between UV and IR divergences on the level of the bare (i.e. unrenormalized) amplitude. This is not a problem in practice. Once we renormalize the amplitude by introducing counterterms, we know that all remaining divergences have to be IR divergences.

As a consequence of dimensional regularization, we also have to pay attention how to treat the Lorentz and Dirac algebra in d dimensions. There are different schemes how to do that. In conventional dimensional regularization all particle momenta and polarization vectors, including also the external states, are extended to d dimensions, such that interference terms between tree and loop diagrams can be treated consistently in d dimensions [90]. In this scheme one therefore always has

$$g^{\mu\nu} g_{\mu\nu} = 4 - 2\epsilon\,, \tag{2.7}$$

$$\{\gamma_\mu, \gamma_\nu\} = 2 g_{\mu\nu}\, \mathbf{1}\,, \tag{2.8}$$

$$\text{and} \quad \gamma^\mu \gamma_\mu = \frac{1}{2} g^{\mu\nu} \{\gamma_\mu, \gamma_\nu\} = g^{\mu\nu} g_{\mu\nu} = 4 - 2\epsilon. \tag{2.9}$$

In the 't Hooft-Veltman scheme [89], one only extends the momenta and polarization states of unobserved particles to d dimensions, while external polarisation states and four-momenta remain four-dimensional. Finally, in the four-dimensional helicity scheme [91], only the loop momenta are d dimensional and all polarization vectors of all particles remain four-dimensional.

In what follows, we will introduce concepts and algorithms that facilitate the calculation of Feynman integrals in dimensional regularization.

2.3 Integral families and IBP identities

A scalar l-loop Feynman integral can, in general, be written in terms of propagators as

$$I_{a_1 \ldots a_n} = \int \left(\prod_{i=1}^{L} d^d l_i \right) \frac{1}{\prod_{i=1}^{n} D_i^{a_i}}, \tag{2.10}$$

where $D_i = q_i^2 - m_i^2$ are called propagators and where q_i are linear combinations of the external momenta p_i and internal momenta l_i,

$$q_i = \sum_j \lambda_{ij} l_j + \sum_j \sigma_{ij} p_j, \quad \lambda_{ij}, \sigma_{ij} \in \{-1, 0, 1\}. \tag{2.11}$$

The exponents a_i in Eq. (2.10) are integers, which can also be negative such that non-trivial numerators are possible. The set of all Feynman integrals that can be built from Eq. (2.10), is called integral family.

In dimensional regularization, the integral over a total derivative yields zero. Let $I'_{a_1\ldots a_n}$ be the integrand of Eq. (2.10). Then, the integral over a total derivative can be written as:

$$\int d^d l_i \frac{\partial}{\partial l_i^\mu} q^\mu I'_{a_1\ldots a_n} = 0. \tag{2.12}$$

where q^μ can be either a loop or an external four-momentum. Working out the differentiation explicitly, one can rewrite the left-hand side (lhs) of this equation as a sum of integrals with new indices $a'_1 \ldots a'_n$. This leads to linear relations between integrals of one family with shifted indices, which are called integration-by-part (IBP) identities. As an example of an IBP relation let us consider the integral family corresponding to a massless three-point function,

$$I'_{a,b,c} = \left(\frac{1}{l^2}\right)^a \left(\frac{1}{(l-p_1)^2}\right)^b \left(\frac{1}{(l-p_1-p_2)^2}\right)^c. \tag{2.13}$$

IBP identities can be generated by empolying the differentiation with respect to l^μ:

$$\frac{\partial}{\partial l^\mu} I'_{a,b,c,0} = -2aI_{a+1,b,c,0} l_\mu - 2bI_{a,b+1,c,0}\left(l_\mu - p_{1\mu}\right) - 2cI_{a,b,c+1,0}\left(l_\mu - p_{1\mu} - p_{2\mu}\right). \tag{2.14}$$

Contracting this equation with l^μ, p_1^μ and p_2^μ leads to three different equations generating IBP identities:

$$\begin{aligned}
0 =& - c\, I_{a-1,b,c+1} - b\, I_{a-1,b+1,c} - 2\, a\, I_{a,b,c} \\
& - b\, I_{a,b,c} - c\, I_{a,b,c} + c\, s\, I_{a,b,c+1} + d\, I_{a,b,c}, \\
0 =& - c\, I_{a-1,b,c+1} - b\, I_{a-1,b+1,c} + c\, I_{a,b-1,c+1} \\
& - a\, I_{a,b,c} + b\, I_{a,b,c} + c\, s\, I_{a,b,c+1} + a\, I_{a+1,b-1,c}, \\
0 =& - c\, I_{a,b-1,c+1} - b\, I_{a,b,c} + c\, I_{a,b,c} + b\, I_{a,b+1,c-1} \\
& - a\, I_{a+1,b-1,c} + a\, I_{a+1,b,c-1} - a\, s\, I_{a+1,b,c},
\end{aligned} \tag{2.15}$$

where $s \equiv (p_1+p_2)^2$ and where $d\ I_{a,b,c}$ in the first equation is coming from the derivative

$$g_{\mu\nu} \frac{\partial l_i^\mu}{\partial l_j^\nu} = d\delta_{ij}, \tag{2.16}$$

after commuting the derivative for $q^\mu = l^\mu$ in Eq. (2.12). In principle, one could now try to solve such a system analytically for generic values of a, b and c. In practice this is too complicated (or unknown how to do in general), so instead one plugs in specific values for a, b and c. This procedure is known as *Laporta's algorithm* [92] in the literature. For instance, if one wants to reduce the integral

$$I_{1,1,1} = \int d^d l \frac{1}{l^2 (l-p_1-p_2)^2 (l-p_1)^2}, \tag{2.17}$$

one can plug in 0, 1 and -1 as values for a, b and c and write down a system of linear equations. Using Gaussian elimination one finds

$$I_{1,1,1} = \frac{1-2\epsilon}{\epsilon s}\, I_{1,0,1}, \tag{2.18}$$

which shows that the massless three-point function is reducible to the massless two-point function. This example also shows two additional interesting aspects in IBP reductions. Firstly, the coefficients in front of master integrals can be divergent (i.e.

contain poles in ϵ). If that happens, we have to evaluate the corresponding integral up to higher orders in ϵ. Secondly, IBP relations mix IR and UV divergences: the massless three-point function is IR divergent, while the massless two-point function is UV divergent. Nonetheless Eq. (2.18) relates them both. It is therefore in general impossible to distinguish between both types of divergences once the bare amplitude is reduced to master integrals. As already mentioned before, this is not a problem in practice. We first perform the UV renormalization of the amplitude and then know that all remaining divergences have to be IR divergences.

2.4 Passarino-Veltman tensor reduction

The Passarino-Veltman (PV) tensor reduction allows one to express any tensor integral in terms of scalar integrals. This is achieved by considering all external momenta of the integrand and constructing a tensor basis using them as building blocks. As an example consider the two-point function of tensor rank two,

$$B_2^{\mu\nu}(s, m_1^2, m_2^2) = \int d^d l \frac{l^\mu l^\nu}{[(l-p)^2 - m_1^2][l^2 - m_2^2]}, \tag{2.19}$$

where $s \equiv p^2$. The integrand only depends on one external momentum p^μ. The two building blocks to construct a tensor basis are therefore $p^\mu p^\nu$ and $g^{\mu\nu}$. We have

$$B_2^{\mu\nu}(s, m_1^2, m_2^2) = g^{\mu\nu} B_{2,00}(s, m_1^2, m_2^2) + p^\mu p^\nu B_{2,11}(s, m_1^2, m_2^2). \tag{2.20}$$

By contracting both sides of the equation with $g^{\mu\nu}$ and $p^\mu p^\nu$, one gets a system of equations relating $B_{2,00}$ and $B_{2,11}$ with scalar integrals:

$$\begin{aligned}
\int d^d l \frac{l^2}{[(l-p)^2 - m_1^2][l^2 - m_2^2]} &= d\, B_{2,00}(s, m_1^2, m_2^2) + s\, B_{2,11}(s, m_1^2, m_2^2) \\
\int d^d l \frac{(lp)^2}{[(l-p)^2 - m_1^2][l^2 - m_2^2]} &= s\, B_{2,00}(s, m_1^2, m_2^2) + s^2 B_{2,11}(s, m_1^2, m_2^2).
\end{aligned} \tag{2.21}$$

The lhs of Eq. (2.21) can be reduced with the help of IBP reductions in terms of simpler integrals. One can easily verify that

$$\begin{aligned}
\int d^d l \frac{l^2}{[(l-p)^2 - m_1^2][l^2 - m_2^2]} &= A_0(m_1^2) + m_2^2\, B_0(s, m_1^2, m_2^2), \\
\int d^d l \frac{(lp)^2}{[(l-p)^2 - m_1^2][l^2 - m_2^2]} &= \frac{m_2^2 - m_1^2 + 3s}{4} A_0(m_1^2) + \frac{m_1^2 - m_2^2 - s}{4} A_0(m_2^2) \\
&\quad + \frac{(m_1^2 - m_2^2 - s)^2}{4} B_0(s, m_1^2, m_2^2).
\end{aligned} \tag{2.22}$$

Therefore, one can express the two tensor integrals in terms of the master integrals B_0 and A_0:

$$\begin{aligned}
B_{2,00}(s, m_1^2, m_2^2) =& \frac{m_2^2 - m_1^2 + s}{4(-1+d)s} A_0(m_2^2) + \frac{m_1^2 - m_2^2 + s}{4(-1+d)s} A_0(m_1^2) \\
&- \frac{m_1^2 + (m_2^2 - s)^2 - 2m_1^2(m_2^2 + s)}{4(-1+d)s} B_0(s, m_1^2, m_2^2)
\end{aligned} \tag{2.23}$$

$$\begin{aligned}
B_{2,11}(s, m_1^2, m_2^2) =& \frac{d(m_1^2 - m_2^2 - s)}{4(-1+d)s^2} A_0(m_2^2) + \frac{d(m_2^2 - m_1^2 + 3s) - 4s}{4(-1+d)s^2} A_0(m_1^2) \\
&+ \frac{d(m_2^2 - m_1^2 + s)^2 - 4m_2^2 s}{4(-1+d)s^2} B_0(s, m_1^2, m_2^2),
\end{aligned} \tag{2.24}$$

where A_0 and B_0 are defined as

$$A_0(m^2) = \int \frac{d^d l}{l^2 - m^2}, \tag{2.25}$$

$$B_0(s, m_1^2, m_2^2) = \int d^d l \frac{1}{[(l-p)^2 - m_1^2][l^2 - m_2^2]}. \tag{2.26}$$

In general, the system of equations can become very cumbersome to solve for more complicated functions with more external scales or higher loop orders. In these cases it can be useful to use finite field techniques to solve the system of equation, cf. Refs. [93, 94]

2.5 Feynman parametrization

In order to evaluate Feynman integrals analytically or numerically, it is often useful to use the so-called Feynman parametrization, which makes use of the identity

$$\frac{1}{D_1 \cdots D_n} = (n-1)! \int_0^1 dx_1 \cdots \int_0^1 dx_n \frac{\delta(x_1 + \ldots + x_n - 1)}{[x_1 D_1 + \ldots + x_n D_n]^n}, \tag{2.27}$$

where the D_i are the propagators of a given Feynman integral. Given a scalar integral, it allows one to rewrite the denominator in terms of just one propagator $x_1 D_1 + \cdots x_n D_n$, raised to power n such that it becomes spherically symmetric. Using this identity for a generic L-loop Feynman integral without numerator (as given in Eq. (2.10) with all $a_i > 0$), after performing the integration over the loop momenta, one arrives at:

$$I_{a_1,\ldots a_n} = (-1)^a \left(i\pi^{\frac{d}{2}}\right)^L \Gamma\left(a - \frac{Ld}{2}\right) \prod_{j=1}^n \int_0^1 dx_j x_j^{a_j - 1} \delta(x_1 + \ldots + x_n - 1) \frac{\mathcal{U}^{a - d/2(L+1)}}{\mathcal{F}^{a - Ld/2}}, \tag{2.28}$$

where $a = a_1 + \ldots + a_n$. The polynomials $\mathcal{U}$ and $\mathcal{F}$ in Eq. (2.28) are called first and second Symanzik polynomial and depend on the Feynman parameters x_i, the external momenta and internal masses. Both polynomials can be constructed algorithmically from the topology of the Feynman graph corresponding to the Feynman integral [95]. As an example let us consider again the two-point function defined in Eq. (2.26). Its Feynman parameter representation is given by

$$B_0(s, m_1^2, m_2^2) = i\pi^{\frac{d}{2}} \Gamma\left(2 - \frac{d}{2}\right) \int dx\, dy\, \delta(1 - x - y) \left[x m_1^2 + y m_2^2 - xys - i\delta\right]^{-2 + d/2}, \tag{2.29}$$

where the $i\delta$ is due to the Feynman prescription.

Note that from Eq. (2.28) it is clear, that any Feynman integral can be written as an iterated integral over the Feynman parameter with a rational function as integrand. Thus, Feynman integrals admit at most singularities of the form $\ln(s - s_0)^n/(s - s_0)^m$ for a given limit in some scale $s \to s_0$.

2.6 The method of differential equations

In this section, we will introduce the method of differential equations to calculate Feynman integrals analytically. Let us consider a family of scalar integrals with n master integrals, $\vec{m} = (m_1, ..., m_n)$, and perform all derivatives with respect to all external scales and internal masses, which we call $\vec{x} = (x_1, ..., x_n)$. Performing

these derivatives, it is clear that on the right-hand side (rhs) only integrals of the same family appear, which we can again reduce to the n master integrals using IBP identities. We therefore arrive at a system of differential equations, that can be written as follows:

$$\partial_{x_i} \vec{m} = A_i(\epsilon, \vec{x})\ \vec{m}, \tag{2.30}$$

where the A_i are matrices with rational functions of the variables $\vec{x}$ and the dimensional regulator ϵ as entries.

As we saw in Section 2.5, Feynman integrals have at most logarithmic singularities. Therefore, the system of differential equation (2.30) is of *Fuchsian type*. Differential equations of Fuchsian type can always be cast into a form, in which the matrices A_i have only first-order poles in all scales x_i. Such a transformation can be interpreted as a basis change of master integrals. Defining the matrix T that transforms the vector $\vec{m}$ of master integrals to a new vector $\vec{m}' = T\ \vec{m}$ (a new basis of master integrals), the new master integrals $\vec{m}'$ fulfill the differential equation

$$\partial_{x_i} \vec{m}' = \partial_{x_i} T \vec{m} = \partial_{x_i} T \vec{m} + T A_i \vec{m} = \left(\partial_{x_i} T T^{-1} + T A_i T^{-1}\right) \vec{m}' \equiv A_i' \vec{m}'. \tag{2.31}$$

If one finds a transformation matrix T, such that all A_i' as defined above have only first order poles, the differential equation is in *Fuchsian form*.

Let us clarify these steps with an example. We consider the one-loop two-point function with two identical masses m, given by

$$B_0(s, m^2) = \int \frac{d^d l}{[(l-p)^2 - m^2][l^2 - m^2]}, \tag{2.32}$$

where $s \equiv p^2$. The function depends on the two scales s and m^2. We perform the differentiation with respect to m and s and find after using IBP reductions:

$$\begin{aligned}
\partial_m B_0(s, m^2) &= \frac{2(\epsilon-1)}{(s-4m^2)m} A_0(m^2) + \frac{2(-1+2\epsilon)}{s-4m^2} B_0(s, m^2), \\
\partial_s B_0(s, m^2) &= \frac{2(-1+\epsilon)}{s(s-4m^2)} A_0(m^2) + \frac{2m^2 - \epsilon s}{s(s-4m^2)} B_0(s, m^2), \\
\partial_m A_0(m^2) &= \frac{2(\epsilon-1)}{m} A_0(m^2), \quad \partial_s A_0(m^2) = 0.
\end{aligned} \tag{2.33}$$

Without loss of generality, we can write the differential equation in terms of one dimensionless variable $x = \frac{s}{m^2}$. Defining the vector

$$\vec{m} = \begin{pmatrix} A_0(m^2)/m^2 \\ B_0(s, m^2) \end{pmatrix}, \tag{2.34}$$

we find

$$\partial_x \vec{m} = \begin{pmatrix} 0 & 0 \\ \frac{2(\epsilon-1)}{(x-4)x} & \frac{2-\epsilon x}{(x-4)x} \end{pmatrix} \vec{m}. \tag{2.35}$$

We have now derived a differential equation for the Feynman integrals, which we can in principle solve using standard tools from mathematics. In the next section, we show how to simplify the differential equation further and how to solve it analytically in terms of a certain class of functions, called multiple polylogarithms. As an alternative, it is also possible to solve the differential equation numerically using a power series as ansatz.

2.7 The canonical basis

In many physical applications further simplifications of the differential equation can be achieved by transforming to another basis of master integrals. If, in addition to the single-pole criterion, one can also achieve a decoupling of the dimensional regulator ϵ, one arrives at a so-called *canonical basis* [96]. In this case the differential equation takes the form

$$\mathrm{d}\mathbf{m}_i = \epsilon \sum_{j,k} \mathrm{d}\ln(l_k)(A^{(k)})_{ij}\,\mathbf{m}_j\,, \tag{2.36}$$

where l_k are called letters, $A^{(k)}$ are matrices with rational coefficients and d stands for the total derivative, $\mathrm{d}\mathbf{m}_i \equiv \sum_j \partial_{x_j}\mathbf{m}_i \mathrm{d}x_j$. Written in this way, one effectively reduces the multi-scale differential equation to a single-scale problem, since the rhs of Eq. (2.36) only depends on logarithmic forms of the letters.

Coming back to the example of Eq. (2.35), we find the canonical basis by transforming

$$\vec{\mathbf{m}} = T\vec{m}, \tag{2.37}$$

where the matrix T is given by

$$T = \begin{pmatrix} (1-\epsilon)\epsilon & 0 \\ (\epsilon-1)\epsilon\sqrt{\frac{-x}{4-x}} & -\epsilon(2\epsilon-1)\sqrt{\frac{-x}{4-x}} \end{pmatrix}. \tag{2.38}$$

In general, finding the T-matrix that transforms a given differential equation into canonical form can be quite difficult and a lot of effort has been put into algorithms to automate its determination, see e.g. Refs. [97–99]. In our example, in the new basis the differential equation now reads

$$\begin{aligned} \mathrm{d}\mathbf{m}_1 &= 0, \\ \mathrm{d}\mathbf{m}_2 &= \epsilon\left[\mathrm{d}\ln\left(2-x-\sqrt{x(x-4)}\right)\mathbf{m}_1 - \mathrm{d}\ln(4-x)\,\mathbf{m}_2\right]. \end{aligned} \tag{2.39}$$

In order to solve the canonical differential equation as given in Eq. (2.36) in general, one can define a formal solution in terms of Chen iterated integrals. By introducing a single-scale parametric path $\gamma(t)$ connecting two points $\vec{x}_0$ and $\vec{x}$ in phase space, one can define the solution as:

$$\vec{\mathbf{m}}(\epsilon,\vec{x}) = \mathcal{P}\exp\left[\epsilon\int_\gamma \mathrm{d}\mathbb{A}\right]\vec{\mathbf{m}}(\epsilon,\vec{x}_0), \tag{2.40}$$

where

$$\mathrm{d}\mathbb{A} = \sum_k \mathrm{d}\ln(l_k)A^{(k)}\,, \tag{2.41}$$

and where $\vec{\mathbf{m}}(\epsilon,\vec{x}_0)$ are the boundary constants of the master integrals at the point $\vec{x}=\vec{x}_0$. The path-ordered exponential in Eq. (2.40) is defined as an infinite series of integral operators acting to the right,

$$\mathcal{P}\exp\left[\epsilon\int_\gamma \mathrm{d}\mathbb{A}\right] \equiv \mathbf{1} + \epsilon\int_\gamma \mathrm{d}\mathbb{A} + \epsilon^2\int_\gamma \mathrm{d}\mathbb{A}\otimes\mathrm{d}\mathbb{A} + \cdots\,. \tag{2.42}$$

The product of several differential forms in Eq. (2.42) have to be performed iteratively. For instance, the integral over a straight line connecting 0 and x of the product of two d ln forms can be evaluated as follows:

$$\int_\tau \mathrm{d}\ln(x)\otimes\mathrm{d}\ln(x+1) = \int_0^x \frac{\mathrm{d}x_2}{x_2+1}\left[\int_0^{x_2}\frac{\mathrm{d}x_1}{x_1}\right]. \tag{2.43}$$

In order to calculate these iterated integrals in terms of analytic functions, we use Goncharov polylogartithms. Those are defined recursively:

$$G(a_1,\ldots,a_1;x) = \int_0^x \frac{dt}{t-a_1} G(a_2,\ldots,a_1;x), \tag{2.44}$$

with the recursion start $G(;x) = 1$. Thus, in the example above, we have

$$\int_\tau \mathrm{d}\ln(x) \otimes \mathrm{d}\ln(x+1) = G(-1,0;x). \tag{2.45}$$

We define the transcendental weight of a G function as the number of integrations in Eq. (2.44) that have to be performed.

Now, as a concrete example, let us come back again to Eq. (2.39) and solve it in the Euclidean region, in which $x < 0$. Up to order ϵ, the solution is straight-forwardly given by

$$\mathbf{m}_1 = c_{1,0} + \epsilon\, c_{1,1} + \epsilon^2\, c_{1,2} + \ldots \tag{2.46}$$

$$\mathbf{m}_2 = c_{2,0} + \epsilon \left(c_{2,1} + \ln\left(2 - x - \sqrt{x(x-4)}\right) c_{1,0} - \ln(4-x) c_{2,0} \right) + \epsilon^2 \mathbf{m}_2^{(2)} + \ldots, \tag{2.47}$$

where the $c_{i,j}$ are boundary constants from the integration. At order ϵ^2, the second integral is formally given by

$$\begin{aligned}\mathbf{m}_2^{(2)} = \int_{\tau_x} & c_{2,0}\, \mathrm{d}\ln(4-x) \otimes \mathrm{d}\ln(4-x) - c_{1,0}\, \mathrm{d}\ln\left(2 - x - \sqrt{x(x-4)}\right) \otimes \mathrm{d}\ln(4-x) \\ & + c_{1,1}\, \mathrm{d}\ln\left(2 - x - \sqrt{x(x-4)}\right) - c_{2,1}\, \mathrm{d}\ln(x-4).\end{aligned} \tag{2.48}$$

The result of this integration is most easily obtained by performing a change of variable that rationalizes the square roots. This can be achieved by $x \to -(1-y)^2/y$, resulting in the substitution of the square root $\sqrt{x(x-4)} \to (-1+y^2)/y$. Using this reparametrization, it is straight forward to evaluate each term (2.48) separately. For instance

$$\int_{\tau_x} \mathrm{d}\ln\left(2 - x - \sqrt{x(x-4)}\right) \otimes \mathrm{d}\ln(x-4) = \int_{\tau_y} \mathrm{d}\ln\left(\frac{2}{y}\right) \otimes \mathrm{d}\ln\left(\frac{(1+y)^2}{y}\right). \tag{2.49}$$

The rhs of this equation can be integrated in terms of Goncharov polylogarithms considering a straight line path connecting 0 and y:

$$\begin{aligned}\int_{\tau_y} \mathrm{d}\ln\left(\frac{2}{y}\right) \otimes \mathrm{d}\ln\left(\frac{(1+y)^2}{y}\right) &= -\int_{\tau_y} \mathrm{d}\ln(y) \otimes \left(2\mathrm{d}\ln(1+y) - \mathrm{d}\ln(y)\right) \\ &= G(0,0;y) - 2G(-1,0;y).\end{aligned} \tag{2.50}$$

The full result is thus given by

$$\begin{aligned}\mathbf{m}_2^{(2)} =& c_{2,0} \frac{1}{2} \ln\left(\frac{(1+y)^2}{y}\right)^2 + c_{1,0} \left(G(0,0;y) - 2G(-1,0;y)\right) \\ & - c_{1,1} \ln\left(\frac{1}{y}\right) - c_{2,1} \ln\left(\frac{(1+y)^2}{y}\right) + c_{2,2}.\end{aligned} \tag{2.51}$$

In order to determine the integration constants $c_{i,j}$, we will use the analytic expression for A_0, given by

$$\left(\frac{\mu}{m}\right)^{-2\epsilon} \frac{A_0(m^2)}{i\pi^{d/2} r_\Gamma} = -\frac{\Gamma(-1+\epsilon)}{m^2 r_\Gamma}, \tag{2.52}$$

where

$$r_\Gamma = \frac{\Gamma^2(1-\epsilon)\Gamma(1+\epsilon)}{\Gamma(1-2\epsilon)}. \tag{2.53}$$

We therefore find

$$\left(\frac{\mu}{m}\right)^{-2\epsilon} \frac{\mathbf{m}_1}{i\pi^{d/2} r_\Gamma} = 1 + \epsilon^2 \frac{\pi^2}{6} + \mathcal{O}(\epsilon^3), \tag{2.54}$$

from which we can read off the integration constants for $\mathbf{m}_1$. In order to fix the integration constants of the second integral, we will make use of the Feynman parameterization of B_0 given in Eq. (2.29). Factoring out the same prefactor as before, we find

$$\begin{aligned}\left(\frac{\mu}{m}\right)^{-2\epsilon} \frac{B_0(s,m^2)}{i\pi^{d/2} r_\Gamma} &= \frac{\Gamma(\epsilon)}{r_\Gamma} \int_0^1 da \left[-a(1-a)x + 1 + i\delta\right]^{-\epsilon} \\ &= \frac{\Gamma(\epsilon)}{r_\Gamma} \int_0^1 da \left[1 - \epsilon \ln(1-(1-a)ax) + \frac{\epsilon^2}{2} \ln^2(1-(1-a)ax) + \dots\right]\end{aligned} \tag{2.55}$$

From this expression we easily see, that the rhs yields zero for $x = 0$ (starting at zeroth order in ϵ), which corresponds to $y = 1$. Thus, we know the boundary constants at $y = 1$ and we can write down the complete expression for $\mathbf{m}_2$:

$$\begin{aligned}\left(\frac{\mu}{m}\right)^{-2\epsilon} \frac{\mathbf{m}_2}{i\pi^{d/2} r_\Gamma} &= -G(0;y)\epsilon \\ &\quad + \left(G(0,0;y) - 2G(-1,0;y) + 2G(-1,0;1)\right)\epsilon^2 + \mathcal{O}(\epsilon^3).\end{aligned} \tag{2.56}$$

In the solution from Eq. (2.56), we see an interesting feature: the functions that appear at the n-th order in ϵ have transcendental weight n. This is a general feature of the canonical differential equation, and the canonical integrals are said to be of uniform transcendental weight.

In general, if all letters of the differential equation are linear, it is always possible to integrate Chen iterated integrals as in Eq. (2.40) in closed form using G functions, as in the example above. This is no longer true, however, if one encounters non-linear or non-rational letters. In the former case, it is often possible to choose an appropriate integration order, for which the non-linear letters appear only in the final integration kernel, such that the integration can be performed. If one encounters non-rational symbol letters, the standard integration algorithms for G functions cannot be applied. In many cases, a transformation can be found which simultaneously rationalizes all letters of the alphabet [100]. This is indeed exactly what we did above to get rid of $\sqrt{x(4-x)}$ in the example. In the next section, we will discuss what can be done in the case of non-linear letters, or even worse, in the case of algebraic letters if no rationalization of some square root is possible.

2.8 Integrating non-linear and algebraic letter

This section is partly taken from Ref. [84] and discusses an alternative method to integrate Eq. (2.36) in terms of generalized polylogarithms, so-called Li functions. These functions can be defined as nested sums as:

$$\mathrm{Li}_{m_1,\dots,m_k}(x_1,\dots,x_k) = \sum_{n_1<n_2<\dots<n_k} \frac{x_1^{n_1} x_2^{n_2} \cdots x_k^{n_k}}{n_1^{m_1} n_2^{m_2} \cdots n_k^{m_k}}, \quad \text{for} \quad |x_i| < 1. \tag{2.57}$$

The Li functions are related to the Goncharov polylogarithms defined in Eq. (2.44) by the following identity:

$$\mathrm{Li}_{m_1,\ldots,m_k}(x_1,\ldots,x_k) = (-1)^k G_{m_k,\cdots,m_1}\left(\frac{1}{x_k},\ldots,\frac{1}{x_1\cdots x_k}\right), \tag{2.58}$$

where

$$G_{m_k,\cdots,m_1}(t_1,\cdots t_k) = G(\underbrace{0,\ldots,0}_{m_1-1},t_1,\ldots,\underbrace{0,\ldots,0}_{m_k-1)},t_k;1). \tag{2.59}$$

Therefore, both define the same class of functions. In analogy to the transcendental weight defined for the G functions, the transcendental weight of a $\mathrm{Li}_{m_1,\ldots,m_k}$ function is given by $m_1+\cdots+m_k$.

2.8.1 Matching the symbol

The methods discussed in the following, are based on the algorithms from Ref. [101] for the case of rational (linear or non-linear) letters. In order to solve the differential equation (2.36), the idea is to construct a suitable ansatz which can be matched against it. This is done with the help of the so-called symbol calculus. The symbol of a function is defined in terms of its total derivative. Given a function f, it is defined recursively as follows: if the total derivative of f is given by

$$\mathrm{d}f = \sum f_i \,\mathrm{d}\ln r_i, \tag{2.60}$$

then the symbol $\mathcal{S}$ of f takes the form

$$\mathcal{S}(f) = \sum_i \mathcal{S}(f_i)\otimes r_i. \tag{2.61}$$

As an example, let us consider the symbol of Li_n functions:

$$\mathcal{S}(\mathrm{Li}_n(f)) = -(1-f)\otimes\underbrace{f\otimes\ldots\otimes f}_{(n-1)\text{ times}}. \tag{2.62}$$

Terms inside the symbol can be treated in the same way as one would treat arguments of $\mathrm{d}\ln$. In that way one can expand the symbol into irreducible components. For rational arguments, this means one can factorize them and then expand according to the rule $\ln(ab)=\ln(a)+\ln(b)$. For example one has:

$$\mathcal{S}\left(\mathrm{Li}_2\left(\frac{1}{x}\right)\right) = -\left(1-\frac{1}{x}\right)\otimes\frac{1}{x} = \frac{-1+x}{x}\otimes x = (-1+x)\otimes x - x\otimes x. \tag{2.63}$$

From its definition, we see that the symbol of a constant is zero since $\mathrm{d}\ln(c)=0$ if c is constant. Therefore, in order to integrate a total derivative it is not enough to just match its symbol. To make our point, let us look at an example and let us assume someone gives us the task to find a function, whose total derivative is given by

$$\mathrm{d}f = \mathrm{Li}_2(1/x)\mathrm{d}\ln(x) + \pi\ln(-x)\mathrm{d}\ln(x). \tag{2.64}$$

Considering the symbol, we have

$$\mathcal{S}(f) = \mathcal{S}\left(\mathrm{Li}_2\left(\frac{1}{x}\right)\right)\otimes x + \mathcal{S}(\pi)\otimes x\otimes x = (-1+x)\otimes x\otimes x - x\otimes x\otimes x + 0, \tag{2.65}$$

where we used the fact that $\mathcal{S}(\pi) = 0$. One can immediately verify that the symbol is matched, for example, by the function

$$F = -\mathrm{Li}_3(x) - \frac{1}{6}\ln(-x)^3, \tag{2.66}$$

and use it as an ansatz. However, this function does not match the total derivative, since the symbol is not sensitive to terms of type constant times function (because the symbol of the constant yields zero). Therefore, we have to make sure our ansatz matches the total derivative in an addtitional step. Taking the difference of both total derivatives, we have

$$\mathrm{d}F - \mathrm{d}f = \left(-\mathrm{Li}_2(x) - \frac{1}{2}\ln(-x)^2 - \mathrm{Li}_2\left(\frac{1}{x}\right) - \pi\ln(-x)\right)\mathrm{d}\ln(x). \tag{2.67}$$

The next step depends on what values for x we consider. We will assume that $x < 0$, such that all functions are real-valued and we do not need to consider any analytic continuation. Then we have

$$-\mathrm{Li}_2(x) - \frac{1}{2}\ln(-x)^2 - \mathrm{Li}_2\left(\frac{1}{x}\right) = \frac{\pi^2}{6} \quad \text{for } x < 0, \tag{2.68}$$

and using this identity, we find

$$\mathrm{d}F - \mathrm{d}f = \left(\frac{\pi^2}{6} - \pi\ln(-x)\right)\mathrm{d}\ln(x), \tag{2.69}$$

and all we have to do is to match the symbols x and $x \otimes x$ corresponding to these two terms. Finally we obtain

$$f = -\mathrm{Li}_3(x) - \frac{1}{6}\ln(-x)^3 + \frac{1}{2}\pi\ln(-x)^2 - \frac{1}{6}\pi^2\log(-x) + c, \tag{2.70}$$

where c is a constant.

To conclude, let us rephrase the main message of this section. If we want to find a function f that matches a given total derivative

$$\mathrm{d}f = \sum_i f_i\,\mathrm{d}\ln r_i \tag{2.71}$$

using the symbol calculus, we have to make sure that our ansatz F

1. matches the full symbol, i.e. $\mathcal{S}(F) = \sum_i \mathcal{S}(f_i) \otimes r_i$, and
2. that the difference of the total derivatives $\mathrm{d}f - \mathrm{d}F$ yields zero. If it doesn't, we have to add terms of type constant times function to F, to which the symbol is not sensitive.

2.8.2 Matching the differential equation

Coming back to differential equations, note that the differential equation in the form of (2.36) fully defines the symbol at a given order in ϵ of the master integrals. The first task is then to find a solution, that matches this symbol. To do that, one constructs an ansatz of polylogarithmic functions and chooses the arguments of these functions such, that their symbol does not contain spurious letters. Note, that there is no proof that this always works. There might be cases in which additional, spurious letters need to be introduced.

At weight one, it is clear that logarithms of the letters are admissible functions. For higher weights we consider the symbol of Li_n functions as given in Eq. (2.62). We see that we have to choose their arguments f such, that both f and $1-f$ may also be written as a power product of other symbol letters, which already appear in the differential equation. In practice, one therefore forms power products f out of the letters from the differential equation and tests if $1-f$ factorizes over the alphabet. If it does, f is a valid argument.

As mentioned above, in Ref. [101] this method was introduced for rational functions. In the presence of square roots, one needs a generalized concept of factorization. In Refs. [84, 87] we use a heuristic factorization algorithm to search for admissible function arguments. For a given expression g and a list of symbol letters $l_1 \dots l_n$ we are interested in factorizations of the form

$$g = c^{a_0} l_1^{a_1} l_2^{a_2} \cdots l_n^{a_n}, \tag{2.72}$$

with a rational number c and $a_i \in \mathbb{Q}$. It is non-trivial to find such factorizations using standard computer algebra systems, if square roots are present in the l_i. However, note that the factorization (2.72) implies

$$\ln(g) - a_0 \ln(c) - a_1 \ln(l_1) - a_2 \ln(l_2) - \ldots - a_n \ln(l_n) = 0\,. \tag{2.73}$$

Replacing the variables by numerical samples and using *heuristic integer relation* finders [102] allows us to find $a_0, a_1 \dots a_n$, such that (2.72) is fulfilled.

Let us come back to our example considered before, the two-point function considered in Eq. (2.39). From Eq. (2.47) we know the solution up to first order in ϵ, and we now have to solve for $\mathbf{m}_2^{(2)}$. From the differential equation we can deduce the symbol of $\mathbf{m}_2^{(2)}$:

$$\mathcal{S}\left(\mathbf{m}_2^{(2)}\right) = -c_{1,0}\; l_1 \otimes l_2 + c_{2,0}\; l_2 \otimes l_2, \tag{2.74}$$

where $l_1 = 2 - x - \sqrt{x(x-4)}$ and $l_2 = 4 - x$. Next, we form power products from the set $\{2, l_1, l_2\}$ and use our heuristic factorization algorithm to find admissible function arguments. In total we find six admissible arguments for the Li_2 functions:

$$\left\{ \frac{\sqrt{2}\sqrt{l_2}}{\sqrt{l_1}}, \frac{2}{l_1}, \frac{l_1}{2}, \frac{\sqrt{l_1}}{\sqrt{2}\sqrt{l_1}}, -\frac{\sqrt{l_1}\sqrt{l_2}}{\sqrt{2}}, \frac{-\sqrt{2}}{\sqrt{l_1}\sqrt{l_2}} \right\}. \tag{2.75}$$

Note that we introduced 2 as an additional function argument and that square roots of letters appear in our ansatz. We observed that including 2 as an additional letter is often necessary in the presence of square roots, thus we always add it as an additional letter to our alphabet. We proceed by trying to match Eq. (2.74). The matching of the second term is trivial, since

$$\mathcal{S}(\ln^2(l_2)) = 2\; l_2 \otimes l_2. \tag{2.76}$$

In order to match the first term in Eq. (2.74) we have several candidates. For instance note that

$$\mathcal{S}\left(\frac{1}{2}\ln^2(l_1) + 2\,\mathrm{Li}_2\left(\frac{\sqrt{2}\sqrt{l_2}}{\sqrt{l_1}}\right)\right) = l_1 \otimes l_2, \tag{2.77}$$

but also

$$\mathcal{S}\left(\ln(l_1)\ln(l_2) - \frac{1}{2}\ln^2(l_1) - 2\,\mathrm{Li}_2\left(1 - \frac{\sqrt{2}\sqrt{l_2}}{\sqrt{l_1}}\right)\right) = l_1 \otimes l_2. \tag{2.78}$$

We will prefer the second choice, since $\mathrm{Li}_2\left(1-\frac{\sqrt{2}\sqrt{l_2}}{\sqrt{l_1}}\right)$ is real-valued for all $x<0$ in the Euclidean region. We can proceed by writing down a function, that matches the first term of the symbol of $\mathbf{m}_2^{(2)}$:

$$F=-c_{1,0}\left(\ln(l_1)\ln(l_2)-\frac{1}{2}\ln^2(l_1)-2\,\mathrm{Li}_2\left(1-\frac{\sqrt{2}\sqrt{l_2}}{\sqrt{l_1}}\right)\right). \tag{2.79}$$

However, as explained above, this is not enough since we need a function that matches the total derivative of $\mathbf{m}_2^{(2)}$, not just the symbol. The total derivative proportional to the constant $c_{1,0}$ of $\mathbf{m}_2^{(2)}$ is given by

$$\mathrm{d}\mathbf{m}_2^{(2)}=-c_{1,0}\,\ln(l_1)\,\mathrm{d}\ln(l_2). \tag{2.80}$$

Comparing this with the total derivative of our ansatz we find

$$\begin{aligned}\mathrm{d}F=-c_{1,0}\Big[&\ln(l_1)\mathrm{d}\ln(l_2)+(\ln(l_2)-\ln(l_1))\mathrm{d}\ln(l_1)\\&+2\ln\left(\frac{\sqrt{2}\sqrt{l_2}}{\sqrt{l_1}}\right)\mathrm{d}\ln\left(1-\frac{\sqrt{2}\sqrt{l_2}}{\sqrt{l_1}}\right)\Big].\end{aligned} \tag{2.81}$$

Next, we will use the following identity, which can be detected using the heuristic factorisation approach:

$$\ln(l_1)+\ln\left(-1+\frac{\sqrt{2}\sqrt{l_2}}{\sqrt{l_1}}\right)=\ln(2)\;\Rightarrow\;\mathrm{d}\ln\left(1-\frac{\sqrt{2}\sqrt{l_2}}{\sqrt{l_1}}\right)=-\mathrm{d}\ln(l_1), \tag{2.82}$$

to rewrite $\mathrm{d}F$ as

$$\mathrm{d}F=-c_{1,0}\big[\ln(l_1)\mathrm{d}\ln(l_2)-\ln(2)\,\mathrm{d}\ln(l_1)\big]. \tag{2.83}$$

Thus, to get the function which matches the total derivative, we have to correct for the terms comparing Eq. (2.83) with Eq. (2.80), i.e. we have to add $\ln(2)\ln(l_1)$ to F. We therefore get

$$\begin{aligned}\mathbf{m}_2^{(2)}=-c_{1,0}&\left[\ln(l_1)\ln(l_2)-\frac{1}{2}\ln^2(l_1)-2\,\mathrm{Li}_2\left(1-\frac{\sqrt{2}\sqrt{l_2}}{\sqrt{l_1}}\right)+\ln(2)\ln(l_1)\right]\\&+c_{2,0}\,\frac{1}{2}\ln^2(l_2)-c_{1,1}\ln(l_1)+c_{2,1}\ln(l_2)+c_{2,2}.\end{aligned} \tag{2.84}$$

One can determine all integration constants in the same way as before. One finds:

$$c_{2,0}=0,\quad c_{2,1}=\ln(2),\quad c_{2,2}=\frac{\pi^2}{6}+\frac{\ln(2)^2}{2}. \tag{2.85}$$

We have now discussed how to match the differential equation up to second order in ϵ using Li_2 functions. For higher orders, we need functions with higher weight and higher depth than two. The symbols of these functions are more complicated and lead to additional constraints. For instance, to treat $\mathrm{Li}_{2,1}$, $\mathrm{Li}_{3,1}$, and $\mathrm{Li}_{2,2}$, let $\mathcal{F}$ be the union of the set of admissible Li_n function arguments and the set $\{1\}$. Then, the symbol demands, using the same argument as above that no new letters appear in the symbol of our ansatz, that a possible pair of arguments (f_i,f_j) for these functions has to be chosen such that $1-f_if_j$ factorizes over the alphabet.

2.8.3 Simplifying the alphabet

The above algorithm has been applied for several processes in practice, see e.g. Refs. [97, 103–107]. However, in all these cases the symbol alphabet was either rational or could be rationalized. In Ref. [108] it was applied for the first time to a non-trivial alphabet involving a square root, that was not rationalized for the integration, i.e. using the heuristic factorization approach discussed above. However, it turned out later, that there actually *was* a reparametrization to fully rationalize the alphabet, that the authors were not aware of.

The first time the algorithm was successfully applied to a case involving one provably non-rationalizable square root [109] in the letters, was in Ref. [84], in which we calculated the two-mass two-loop integrals contributing to the mixed EW-QCD corrections to the Drell-Yan process. However, before being successful in this case, we had to overcome two main problems specific to differential equations with non-rational symbol letters compared to the case with rational symbol letters:

(i) In general, one needs to allow for non-integer powers, e.g. 1/2, 1/4, etc. when forming power products f (we also saw this in the example above). Consequently, one may have to test many more expressions than in the rational case in order to construct enough function arguments to successfully "integrate the symbol." In fact, without additional constraints, the inherent combinatorial complexity makes the extension of the Duhr-Gangl-Rhodes method to algebraic letters too costly for many applications

(ii) Factorization over algebraic functions is not unambiguously defined; in principle, it is not clear where to "stop" factorizing. Consider, for instance, the set of letters $\{\sqrt{x}, \sqrt{y}, x-y\}$ and note that it is *a priori* unclear whether one ought to factor the third letter further, *i.e.* $x - y = (\sqrt{x} + \sqrt{y})(\sqrt{x} - \sqrt{y})$.

In the cases we considered so far, cf. Refs. [84, 87], both of these problems could be tackled by the following observations: given an alphabet, we introduce the subset of rational letters, $\mathcal{L}_R$, and the subset of intrinsically non-rational letters, $\mathcal{L}_A$. Let us assume that in $\mathcal{L}_A$ we encounter a square root, r. We find it natural to take r itself to be an element of $\mathcal{L}_A$. For a given algebraic letter with a non-trivial rational part, l_a, we define the conjugated letter, $\bar{l}_a$, by making the replacement $r \to -r$ in l_a. For each $l_a \in \mathcal{L}_A$ we observe that $\bar{l}_a$ can be written as a power product of other symbol letters; that is to say, one could exchange any letter for its conjugate without affecting the singularity structure of the alphabet. As a consequence, the product $l_a \bar{l}_a$ always factorizes over the rational part of the alphabet, $\mathcal{L}_R$.

This observation implies that one can in fact predict all algebraic symbol letters which can appear, once the square root r and the rational part of the alphabet, $\mathcal{L}_R$ are known. In other words, it is possible to *construct* the algebraic part of the alphabet, $\mathcal{L}_A$, unambiguously. We will use this feature to construct a simplified alphabet in the following. Knowing only r and $\mathcal{L}_R$, we make an ansatz of the form

$$l_a = q_a + r, \tag{2.86}$$

where q_a is a rational function depending on kinematic variables x_i and then requiring that $l_a \bar{l}_a$ factorize over $\mathcal{L}_R$. In practice, it is more convenient to directly make an ansatz of the form

$$(q_a + r)(q_a - r) = q_a^2 - r^2 = \sum_{i_1 i_2 \ldots i_n} a_{i_1 i_2 \ldots i_n} x_1^{i_1} x_2^{i_2} \cdots x_n^{i_n} - r^2, \tag{2.87}$$

and then solve for the unknowns a_{ij}. We can perform this search degree by degree. An algorithm for the construction of simple letters, given the rational part of the alphabet and a square root r thus reads:

Input: rational part of alphabet and square root r depending on x_i
Result: simplified letters
initialization: monlist=monomials of rational alphabet up to degree n;
for f *in monlist* **do**
  $d_i = deg(f, x_i)$;
  polynomial ansatz: $p = \sum_i \sum_{n_i}^{d_i} a_{n_i} x_i^{n_i}$;
  solve $f = p - r^2$ for unknown coefficients a_{n_i};
  if p *is perfect square* **then**
    set polynomial $q \equiv \sqrt{p}$;
    add $l = q + r$ to new alphabet;
  end
end

As mentioned above, we applied this simplification algorithm to two different processes: in Ref. [84] we applied it to the calculation of the master integrals of the mixed EW-QCD two-loop corrections to Drell-Yan production, while in Ref. [87] it was applied to a family of planar master integrals that contribute to $e^-\mu^-$ scattering at two-loop. In both cases it was crucial to first simplify the alphabet before beeing able to match the differential equation against an ansatz and solve it. The calculation of the EW-QCD integrals will be presented in more detail in Chapter 8. Therefore, in the present section, we will briefly showcase the simplification of the alphabet in the second application [87]. In that reference we derived a canonical differential equation for one planar integral family of two-loop master integrals contributing to $e^-\mu^-$ scattering,

$$\mu^-(p_1) + e^-(p_2) \to \mu^-(p_3) + e^-(p_4), \tag{2.88}$$

where $p_1^2 = p_3^2 = m_1^2$ and $p_2^2 = p_4^2 = m_2^2$. The integral family is defined by nine propagators,

$$\begin{aligned}
&D_1 = k_1^2 - m_1^2, && D_2 = k_2^2 - m_1^2, && D_3 = (k_1 - k_2)^2, \\
&D_4 = (k_1 - p_1)^2, && D_5 = (k_2 - p_1)^2, && D_6 = (k_1 - p_1 - p_2)^2 - m_2^2, \\
&D_7 = (k_2 - p_1 - p_2)^2 - m_2^2, && D_8 = (k_1 - p_3)^2, && D_9 = (k_2 - p_3)^2.
\end{aligned} \tag{2.89}$$

In total we find 37 master integrals, and without going into too much details, we were able to express the differential equation in the form

$$\vec{\mathrm{m}} = \epsilon \sum_{i=1}^{30} A_i \mathrm{d} \ln\left(\tilde{l}_i\right) \vec{\mathrm{m}}. \tag{2.90}$$

At first sight, we found in this differential equation in total 30 different, independent letters, which we list here:

$$\begin{aligned}
\tilde{\mathcal{L}} = \Big\{ & x - y, x + y, y, 2y + 1, 2y + z + 1, 2y - 1, 2y - z - 1, z, 2y + \sqrt{4y^2 - 4x + 1} - 1, \\
& 2y + \sqrt{4y^2 - 4x + 1} + 1, \sqrt{4y^2 - 4x + 1}, \sqrt{4x + 4y - z} + \sqrt{-z}, \sqrt{4x + 4y - z}, \\
& \sqrt{4x - 4y - z} + \sqrt{-z}, \sqrt{4x - 4y - z}, 2y - z + \sqrt{4y^2 + z^2 - 4x - 4xz + 2z + 1} - 1, \\
& 2y + z + \sqrt{4y^2 + z^2 - 4x - 4xz + 2z + 1} + 1, -4y^2 + 4x - z - 1, 4y^2 - z - 1,
\end{aligned}$$

$$
\begin{aligned}
&-4y^2+2zy+4x-z+\sqrt{4y^2-4x+1}\sqrt{4y^2+z^2-4x-4xz+2z+1}-1,\\
&-4y^2-2zy+4x-z+\sqrt{4y^2-4x+1}\sqrt{4y^2+z^2-4x-4xz+2z+1}-1,\\
&-4\sqrt{-z}x+\sqrt{-z}z-2y\sqrt{-z}+\sqrt{-z}+\sqrt{4x+4y-z}\sqrt{4y^2+z^2-4x-4xz+2z+1},\\
&-4\sqrt{-z}x+\sqrt{-z}z+2y\sqrt{-z}+\sqrt{-z}+\sqrt{4x-4y-z}\sqrt{4y^2+z^2-4x-4xz+2z+1},\\
&2\sqrt{-z}y+\sqrt{4y^2-4x+1}\sqrt{4x+4y-z}+\sqrt{-z},4y^2+4y-z+1,\\
&-8y^3+8xy^2-4zy^2+8y^2-8xy+2zy-2\sqrt{4y^2-4x+1}\sqrt{z}\sqrt{-4x+4y+z}y\\
&-2y+2x+2xz-z+\sqrt{4y^2-4x+1}\sqrt{z}\sqrt{-4x+4y+z},\\
&-16y^4+16y^3+16xy^2-8y^2-16xy-4zy+4\sqrt{4y^2-4x+1}\sqrt{z}\sqrt{-4x+4y+z}y\\
&+4y-z^2+4x+4xz-2\sqrt{4y^2-4x+1}\sqrt{z}\sqrt{-4x+4y+z}-1,\\
&4x-z+\sqrt{-4x-4y+z}\sqrt{-4x+4y+z}-2,\sqrt{4y^2+z^2-4x-4xz+2z+1},\\
&2\sqrt{-z}y+\sqrt{4y^2-4x+1}\sqrt{4x-4y-z}-\sqrt{-z}\Big\},
\end{aligned}
\tag{2.91}
$$

where

$$
x=\frac{m_1^2+m_2^2}{2s},\qquad y=\frac{m_1^2-m_2^2}{2s},\qquad z=\frac{t}{s},
\tag{2.92}
$$

where s, t and u are the usual Mandelstam variables.

Clearly, the structure of the letters is very complicated and it was crucial to simplify them as much as possible before trying to match the symbol. We will do this along the lines as discussed above. First, we identify the rational part of the alphabet and note that there are four roots, which are given by

$$
\begin{aligned}
&r_1=\sqrt{1-4x+4y^2},\quad r_2=\sqrt{-4xz+4yz+z^2},\quad r_3=\sqrt{-4xz-4yz+z^2},\\
&r_4=\sqrt{1-4x+4y^2+2z-4xz+z^2}.
\end{aligned}
\tag{2.93}
$$

Our starting point for the construction of new and simpler letters is now to consider the rational part of the alphabet, given by

$$
\begin{aligned}
\tilde{\mathcal{L}}_R=\Big\{&x-y,x+y,y,2y-1,2y+1,z+1,4x-4y^2-z-1,z,4y^2-z-1,\\
&2y+z+1,2y-z-1,4y^2+4y-z+1,4y^2-4y-z+1\Big\}.
\end{aligned}
\tag{2.94}
$$

We proceed by making an ansatz to find simple algebraic letters, which factorize over the rational alphabet, i.e. for all four roots we try to find letters of the form

$$
l=q(x,y,z)+r_i,\qquad \bar{l}=q(x,y,z)-r_i,
\tag{2.95}
$$

such that $\bar{l}l$ factorizes over the set of functions in Eq. (2.94), and where q is a polynomial in x, y and z. In this way, we find the following candidates:

$$
\begin{aligned}
\Big\{&\frac{r_1}{2}+\frac{1}{2}(-1+2x),\frac{r_1}{2}+\frac{1}{2}(-1+2y),\frac{r_1}{2}+\frac{1}{2}(1+2y),\frac{r_2}{2}+\frac{1}{2}(2x-2y-z),\\
&\frac{r_2}{2}+\frac{z}{2},\frac{r_3}{2}+\frac{1}{2}(2x+2y-z),\frac{r_3}{2}+\frac{z}{2},\frac{1}{2}(-1+2x-z)+\frac{r_4}{2}\Big\}.
\end{aligned}
$$

However, it turns out that using only these candidates we do not find enough new simpler letters to re-express all old letters from Eq. (2.91) in terms of the new ones. Therefore, we need to include more terms in our search. To do this, we proceed by making another ansatz with two roots,

$$
l=q(x,y,z)+r_ir_j,\qquad \bar{l}=q(x,y,z)-r_ir_j,
\tag{2.96}
$$

such that again $\bar{l}l$ factorizes over the set of functions in Eq. (2.94).

In the present calculation, we discovered that some of the candidates we find with this extended ansatz can be reduced even further. For example, we find that

$$l = \frac{1}{2}\left(-z + 2yz + r_1 r_2\right) \tag{2.97}$$

is a valid candidate, since

$$\frac{1}{2}\left(-z + 2yz + r_1 r_2\right)\frac{1}{2}\left(-z + 2yz - r_1 r_2\right) = -(x-y)(-1+4x-4y^2-z)z. \tag{2.98}$$

However, it is possible to factorize that candidate further taking into account another root, r_4. In particular, we have

$$\frac{1}{2}\left(-z + 2yz + r_1 r_2\right) = \frac{1}{2}(r_1+r_2+r_4)\frac{1}{2}(r_1+r_2-r_4), \tag{2.99}$$

which gives us two simpler candidates with lower degree in x, y and z, i.e. $(r_1+r_2+r_4)/2$ and $(r_1+r_2-r_4)/2$. We therefore always try to simplify a given candidate with two roots further along the same lines as above as a sum of three roots.

Using these ideas, we are able to simplify the initial alphabet drastically. Our final alphabet is given by the rational part

$$\mathcal{L}_R = \left\{x-y, x+y, -1+4x-4y^2-z, z\right\} \tag{2.100}$$

and the algebraic part

$$\begin{aligned}\mathcal{L}_A = \Big\{&r_1, r_2, r_3, r_4, \frac{1}{2}(-1+2y+r_1), \frac{1}{2}(1+2y+r_1), \frac{1}{2}(r_2+z), \frac{1}{2}(r_3+z),\\ &\frac{1}{2}(-1+2x-z+r_4), \frac{1}{2}(r_2+r_1+r_4), \frac{1}{2}(r_3+r_1+r_4), \frac{1}{2}(r_2-r_1-r_4),\\ &\frac{1}{2}(r_3-r_1-r_4), \frac{1}{2}(r_1-r_3-r_4), \frac{1}{2}(r_1-r_2-r_4), \frac{1}{2}(z(-2+4x-z)+r_2 r_3)\Big\}.\end{aligned} \tag{2.101}$$

Note, that the new alphabet has a remarkably simple structure. Especially the structure of the letters which are sums of three roots seems much more natural compared to the initial alphabet in Eq. (2.91). Note also, that the number of letters was reduced from 30 in the starting alphabet to only 20 in the final one. This shows not only the power of our method, but also how difficult it is to see if a given differential equation in $\mathrm{d}\ln$ form with algebraic functions has a minimal number of letters. For more details on the computation of the master integrals, we refer the reader to Ref. [87].

Finally, it should be noted that there are examples of canonical differential equations involving non-rationalizable square roots, that *can not* be integrated in terms of multiple polylogarithms [110]. It would be interesting to know, under which conditions it is possible to integrate a given canonical differential equation in terms of polylogarithms and when not.

3 Automated computation of Feynman amplitudes

Particle physics has always been an important and active field for the development of new computer algebra tools and programs. To name a few, `Reduce`, `Schoonship` and also `Mathematica` all have their roots in the particle physics community. In this chapter, we will give a short overview of the typical workflow of calculating Feynman amplitudes starting with Feynman diagrams using computer algebra. Such a workflow of a multi-loop calculation is shown in Fig. 3.1. It typically consists of the following three steps:

- generate all diagrams contributing to an amplitude at a given loop order
- use Feynman rules to derive the amplitudes and simplify the resulting expressions (Dirac algebra, IBP relations etc.)
- implement the amplitudes in a numerical routine to evaluate them

In our setup, we use for the generation of Feynman diagrams the program `QGRAF` [111] written in `FORTRAN`. The program is quite versatile as it allows to define so-called model files, in which all particles and interactions between them can be defined. In that way, it is easy to restrict to parts of the full Standard Model, e.g. it allows to consider QED interactions only. After setting it up, `QGRAF` generates all possible Feynman graphs using the vertices and propagators from the model file at a given loop order. These graphs are represented by field indices with propagators and vertices connecting them. `QGRAF` allows defining the output format in a general way by providing a so-called style file, making it compatible with other computer algebra systems for further processing of the diagrams.

For the second step in the calculation, we use `Form` [112] for the implementation of Feynman rules and the Dirac algebra. `Form` has built-in routines to take traces of Dirac matrices in four and d dimensions. In `Form` we implement Feynman rules to process the symbolic input from `QGRAF`. Furthermore, we implement Passarino-Veltman reductions such that any Feynman amplitude is expressed in terms of scalar Feynman integrals. These integrals can be reduced further using IBP relations. For the generation of these relations we use the `C++` program `Reduze 2` [113], which generates replacement rules, that can be used in `Form` directly. In this way, the amplitude is expressed as a sum over master integrals, with rational functions depending on the space-time dimension d and all external kinematic invariants and masses as coefficients.

As an additional step, we need to simplify those coefficients. To cast them into a unique form, we employ a novel multivariate partial functioning algorithm, which we first introduced in Ref. [88] and present in the next chapter.

The last step is to implement the analytic expression in a numeric `C++` code. For the numerical evaluation of generalized polylogarithms which appear in the calculation of Feynman integrals, we use the `C++` library `GiNaC` [114, 115].

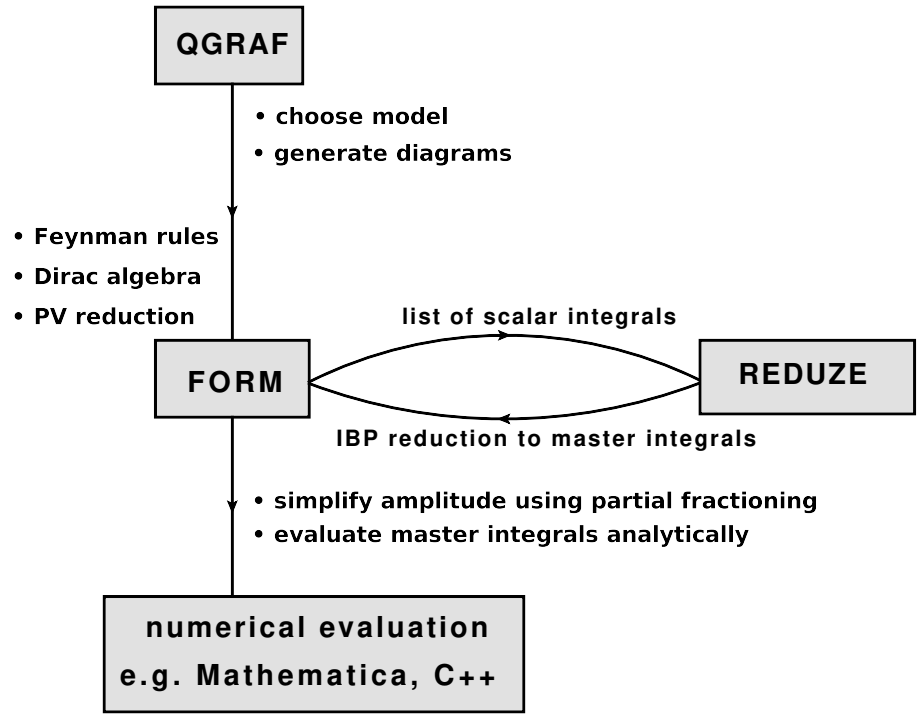

FIGURE 3.1: Overview of the typical workflow of a multi-loop calculation in our setup

4 MultivariateApart: Generalized Partial Fractions

This chapter is based on Ref. [88] in which we introduced a novel algorithm for multivariate partial fractioning. As mentioned in the previous chapter, we use partial fractioning to bring rational functions into a unique form when calculating Feynman amplitudes. Our algorithm has been used in several applications, including also by other researchers, see e.g. Refs. [27, 116–119]. It has been published in Computer Physics Communications.

An implementation of naive partial fractioning in one variable was already available in `Schoonschip` [120], one of the first computer algebra systems that were developed for the calculation of Feynman amplitudes. `Schoonship` had the capability to partial fraction two or three rational functions [121]. With `Schoonship`'s successor `Form` [112, 122], partial fraction decomposition of rational functions became widely established in the particle physics community. While the standard partial fraction decomposition is a method for rational functions of a single variable, it is often applied iteratively to treat multivariate functions. However, this generalization has two drawbacks: first, this method generally introduces new denominator factors, i.e. spurious singularities, and second, it is often slower than reduction schemes in which spurious singularities are avoided from the beginning. A method to separate linearly dependent denominators without introducing spurious poles was presented in Ref. [123] for the special case of multivariate but linear denominator factors. A representation for the general multivariate case which avoids spurious denominators is known as Leĭnartas' decomposition [99, 124–126]. It separates denominators that don't share common zeros or are algebraically dependent.

Here, we discuss a method to compute a partial fraction decomposition via polynomial reductions. Our general approach coincides with that of Refs. [127, 128], but we present new insights concerning the choice of a good monomial ordering and the resulting output forms. In particular, we propose a new monomial ordering, which still guarantees the separation of denominator zeros but allows for deviations from Leĭnartas' form to allow for lower denominator degrees. We also discuss performance optimizations and other practical issues, such as the local elimination of specific denominators, if they are known to be spurious globally. We implement our algorithms in a `Mathematica` package which is publicly available. It can be used to partial fraction rational functions directly in `Mathematica` but also allows to generate local replacement rules that can be incorporated in `Form`.

This chapter is organized as follows. In Section 4.1, we motivate our method. We demonstrate the problem with iterated univariate partial fractions and discuss ambiguities when applying the "classical" Leĭnartas decomposition to individual terms of a sum. We spell out an explicit wish-list for an ideal partial fraction algorithm and discuss which items are addressed by available implementations and the one described in this chapter, respectively. In Section 4.2, we introduce our algorithm in detail, give examples and show how it can be used efficiently in complicated cases. Furthermore, we present some considerations concerning the reconstruction of rational functions

from finite field samples, which can be useful to speed-up tasks like linear system solving. In Section 4.3, we conclude and provide an outlook. Appendix 4.A, gives a brief introduction to polynomial reductions. Appendix 4.B discusses the relation between Leĭnartas' decomposition and our polynomial reduction method.

4.1 Motivation

4.1.1 Spurious poles in iterated partial fractions

We consider a univariate rational function $r(x) = n(x)/d(x)$, where n and d are polynomials in x and the coefficient field K could be e.g. the set of rational numbers. The denominator $d(x)$ can be factored into irreducible factors $d_i(x)$ such that $d(x) = \prod_i d_i^{\alpha_i}(x)$, where the polynomials d_i can not be written as a product of two non-constant polynomials and $\alpha_i \in \mathbb{N}$. The *univariate partial fraction decomposition* of $r(x)$ is given by

$$r(x) = \sum_i \sum_{j \leq \alpha_i} \frac{n_i(x)}{d_i^j(x)}, \tag{4.1}$$

where in each term the degree of the numerator is smaller than the degree of the denominator. As an example, consider the partial fraction decomposition

$$\frac{x}{(x-1)(x+1)^2} = -\frac{1}{4(x+1)} + \frac{1}{2(x+1)^2} + \frac{1}{4(x-1)}. \tag{4.2}$$

In the case of multivariate rational functions $r(x, y, \ldots)$ the partial fractioning can be performed iteratively in each variable. One performs a partial fraction decomposition with respect to the first variable x, treating the other variables as constants during this step. The resulting coefficients p_i are now rational functions of the remaining variables, and one can perform a partial fraction decomposition of the $p_i(y, \ldots)$ with respect to the next variable y. One iterates until the coefficients are actual numbers. As an example, consider the function $r(x, y) = 1/((x - f(y))(x - g(y)))$, where $f(y)$ and $g(y)$ are two different polynomials of y. A partial fractioning with respect to x gives

$$\frac{1}{(x-f(y))(x-g(y))} = \frac{1}{(f(y)-g(y))}\frac{1}{(x-f(y))} - \frac{1}{(f(y)-g(y))}\frac{1}{(x-g(y))}. \tag{4.3}$$

The partial fractioning in x thus introduces a denominator $f(y) - g(y)$, which may have zeros at regular points of the original rational function $r(x, y)$. For example, consider the special case

$$\frac{1}{(x+y)(x-y)} = \frac{1}{2y}\frac{1}{(x-y)} - \frac{1}{2y}\frac{1}{(x+y)}, \tag{4.4}$$

where the subsequent partial fractioning of the x-independent coefficients in y is trivial. Although the original expression is manifestly regular at $y = 0$, the individual terms of the partial fractioned form are not—they introduce spurious poles $1/y$. This obscures the interpretation of the singularity structure of the expression and can lead to loss of precision in its numerical evaluation close to $y = 0$. Note, that a different spurious pole would have appeared in this example, if we had chosen to partial fraction in y first and then in x.

We conclude that iterated partial fractioning will in general introduce spurious poles and is therefore not an ideal approach to the multivariate case.

4.1.2 Features of Leĭnartas' decomposition

Leĭnartas' decomposition is an approach to multivariate partial fractioning, which avoids the introduction of spurious singularities. In this section, we review this decomposition and comment on possible ambiguities arising in practical calculations. Polynomial reductions and the usage of Gröbner bases will play an important role here and in the following; in case the reader is not familiar with these concepts we recommend reading Appendix 4.A first.

Definition 1 Leĭnartas' decomposition *[124, 125] of a rational function r of the variables $x_1, \ldots, x_n$ with coefficients in the field K is a decomposition of the form*

$$r(x_1, \ldots) = \sum_{\mathcal{S}} \frac{n_{\mathcal{S}}(x_1, \ldots)}{\prod_{i \in \mathcal{S}} d_i^{\alpha_i}(x_1, \ldots)}, \tag{4.5}$$

where, for each term of the decomposition, $\mathcal{S}$ is an index set, such that all denominators d_i with $i \in \mathcal{S}$

(i) have common zeros in $\overline{K}^n$, and

(ii) are algebraically independent.

Here, $\overline{K}$ denotes the algebraic closure of K, e.g. the algebraic numbers for $K = \mathbb{Q}$ or $\mathbb{C}$ for $K = \mathbb{R}$.

A set of polynomials $\{d_1, \ldots, d_m\}$ is called *algebraically dependent*, if there exists a non-zero polynomial A in m variables such that $A(d_1, \ldots, d_m) = 0$, see e.g. [129, 130]. A is called the *annihilator* of the ideal generated by the polynomials $\{d_1, \ldots, d_m\}$. The annihilator can be obtained by calculating the Gröbner basis of the ideal $\{y_1 - d_1(x_1, \ldots, x_n), \ldots, y_m - d_m(x_1, \ldots, x_n)\}$, if one chooses a monomial ordering in which $y_i \prec x_j \ \forall i, j$. A set of polynomials is called *algebraically independent*, if it is not algebraically dependent. Since for n variables at most n polynomials are algebraically independent, there can be at most n different denominator factors for each term in (4.5).

Algorithm 1 Leĭnartas' decomposition *of a rational function can be reached in two reduction steps [125]:*

1. *Use Hilbert's Nullstellensatz to decompose the denominator of r into several terms such that each term fulfills (i).*

2. *Calculate the annihilator for each term and use it to decompose each denominator to reach (ii).*

In contrast to iterated partial fractioning, these decomposition steps do not introduce new singularities. Appendix 4.B gives more details for this algorithm. A decomposition that fulfills requirements (i) and (ii) is not unique. In order to resolve this ambiguity, Refs. [99, 131] require additionally for each term (4.5), that the numerator $p_{\mathcal{S}}$ is reduced with respect to the ideal generated by the denominators $\{d_i | i \in \mathcal{S}\}$. We note that the algorithm of [131] assumes the input expression to be a single rational function $r = n/d$ with polynomials n and d and starts with a factorization of d.

Further ambiguities can arise due to spurious denominators which are not automatically removed. The algorithm in [131] for example does not guarantee a unique

result, if n and d are not coprime. However, common factors between numerator and denominator can always be eliminated by first performing a greatest-common-divisor computation.

In practical applications, one also encounters sums of rational functions, and it can be useful to decompose individual terms of the sum separately instead of combining them over a common denominator first. With the methods spelled out so far, uniqueness is not guaranteed in this approach, even in absence of any spurious denominator. Let us illustrate this phenomenon by considering an example where

$$r(x, y) = \frac{2x - y}{x(x + y)(x - y)}. \tag{4.6}$$

Then a Leĭnartas decomposition of r is given by

$$r(x, y) = \frac{1}{x(x + y)} + \frac{1}{(x - y)(x + y)}. \tag{4.7}$$

Another Leĭnartas decomposition is given by

$$r(x, y) = \frac{3}{2x(x + y)} + \frac{1}{2x(x - y)}. \tag{4.8}$$

If we consider the terms in Eqs. (4.7) and (4.8) separately, each of them is in Leĭnartas' decomposed form and the numerator is reduced with respect to the denominator, but the resulting representation is different for the respective sums. In order to resolve this ambiguity, some kind of "global" information needs to be incorporated into the decomposition of "local" terms. We will discuss a solution to this problem below, which does not necessarily require bringing the rational function into a common-denominator form first.

4.1.3 A wish-list for a "good" partial fractioning algorithm

Let us assume someone gives us a rational expression in any form, expanded, over a common denominator, or partially mixed. Then an "ideal" partial fraction decomposition would have the following properties:

(i) it should give a unique answer,

(ii) it should not introduce spurious denominator factors,

(iii) it should commute with summation,

(iv) it should eliminate spurious denominators if they are present in the input.

Note that requirement (iii) can be crucial if one aims at employing such a partial fraction algorithm in a system like `Form`. In such a case, one usually starts with fully expanded expressions, uses local replacement rules, and then wants to obtain a unique answer, such that cancellations can take place.

Unfortunately, there is no know solution to fulfill all of these points simultaneously. In the next section, we consider an algorithm that fulfills requirements (i), (ii) and (iii), and, in cases in which one knows which denominators are spurious in the final answer, also point (iv).

4.2 Multivariate partial fractions with polynomial reduction

4.2.1 Reduction algorithm

Let $\{d_1, ...d_m\}$ be the irreducible denominators of a rational function or a sum of rational functions with $d_i \in K[x_1, \ldots, x_n]$. Consider the ideal

$$I = \langle q_1 d_1(x_1, \ldots) - 1, \ldots, q_m d_m(x_1, \ldots) - 1 \rangle \,, \tag{4.9}$$

where $I \subset K[q_1, \ldots, q_m, x_1, \ldots, x_n]$ and q_i label inverse denominators. The main idea here is, that setting the generators of the ideal $q_i d_i(x_1, \ldots) - 1$ to zero, corresponds to the relation $q_i = 1/d_i(x_1, \ldots)$. If we rewrite a rational function r as a polynomial in the variables $q_1, \ldots, x_1, \ldots$ and reduce it with respect to the ideal I, we do not introduce new denominator factors and obtain a unique representation. Furthermore, whenever we encounter a product $q_i d_i$ it will be reduced to 1. By choosing a suitable monomial ordering, one can control further features of the reduced form as will be discussed in more detail in Section 4.2.2 and Appendix 4.B. Here, we only note that for any monomial ordering, which sorts first for the q_i and then for the x_i, denominators with disjoint zeros will be separated and it is justified to call the reduction a partial fraction decomposition. Using such a monomial ordering, we thus achieve a multivariate partial fraction decomposition with the following two steps: 1. calculate the Gröbner basis of the ideal I and 2. reduce the rational function with respect to this Gröbner basis. This reduction yields a unique remainder, which is the partial fractioned form of r. A complete algorithm to bring a rational function into a unique partial fractioned form can be formulated as follows (see also [127, 128]).

Algorithm 2 Multivariate partial fraction decomposition. *A rational function $r(x_1, \ldots) \in K[x_1, \ldots]$ can be decomposed into partial fractions using the following steps.*

1. *Bring the rational function into the form $n(x_1, \ldots)/d(x_1, \ldots)$ and cancel common factors in n and d such that they are coprime.*
2. *Factorize d over K. Let's call the irreducible factors of the denominator $d_i(x_1, \ldots)$ for $i = 1, \ldots, m$.*
3. *For each denominator factor $d_i(x_1, \ldots)$ introduce a new indeterminant q_i which represents the inverse of $d_i(x_1, \ldots)$, i.e. $q_i = 1/d_i(x_1, \ldots)$. Express all denominators in the problem in terms of the q_i such that the rational function becomes a polynomial $p \in K[q_1, \ldots, x_1, \ldots]$.*
4. *Calculate the Gröbner basis of the ideal I generated by $\{q_1 d_1(x_i) - 1, \ldots, q_m d_m(x_i) - 1\}$ using a monomial ordering which sorts first for the q_i and then for the x_i.*
5. *Find the fully reduced form of the polynomial p with respect to the Gröbner basis.*
6. *Replace back $q_i \to 1/d_i$.*

Step 1 eliminates spurious poles and ensures a unique final form. When operating on large sums, it may be useful to skip this step and operate on the individual terms of the sum separately. In this situation, one can still arrive at a unique output for

the sum when considering the decomposition of each term separately, but using the global set of denominators in the sum. For instance, for the example of Section 4.1.2, Algorithm 2 finds a unique form independent of the specific initial form of r (Eqs. (4.7) and (4.8)) once all possible denominators in the problem are specified. The difference to the standard Leĭnartas decomposition lies in the fact, that we specify by the monomial ordering which denominators are preferred in the partial fractioned result. The elimination of denominators that are known to be spurious, can then be achieved by a suitable choice of the monomial ordering; this will be discussed in the next section.

Step 6 is optional, of course. Leaving the denominators in abbreviated form can allow for more compact representations and as a preparation for an efficient numerical implementation.

4.2.2 Monomial ordering

The choice of monomial ordering has a crucial impact on the properties of the output of Algorithm 2 and the performance of its computation. We show in Appendix 4.B that the output form will satisfy Leĭnartas' requirement (i) and thus separate denominators with disjoint zeros as long as the monomial ordering orders all q_i before the x_i, while Leĭnartas' requirement (ii) may or may not be satisfied depending on further details.

The calculation of the Gröbner basis can be very challenging for practical applications of Algorithm 2, depending heavily on the choice of monomial ordering. Here we propose a specific monomial ordering which aims to provide good computational performance. We tested this ordering in various calculations of scattering amplitudes, and we were able to compute the Gröbner basis and partial fraction the required rational functions in all cases that we considered so far.

To motivate our choice of monomial ordering, let us go back to Eq. (4.3). Note that the prefactors in front of the denominators $x - f(y)$ and $x - g(y)$ do not depend on x. In the case where now $f(y) - g(y)$ is itself a valid denominator, this identity would therefore actually be a valid replacement rule and corresponds to a polynomial in the ideal I in Eq. (4.9). To ensure that this polynomial leads to the reduction (4.3), one can choose a monomial ordering, in which the inverse denominator variables q_1 and q_2 corresponding to $d_1 = x - f(y)$ and $d_2 = x - g(y)$, respectively, are "greater" than the inverse denominator variable q_3 corresponding to $d_3 = f(y) - g(y)$. This motivates the use of a block ordering, in which we group all denominators depending on x and y and all denominators depending on only x or only y.

Algorithm 3 Monomial block ordering. *A suitable monomial ordering for the ring $K[q_1, \ldots, q_m, x_1, \ldots, x_n]$ in Algorithm 2 can be constructed as follows.*

1. *Group the denominators $d_1, \ldots, d_m$ by their dependence on all variables $x_1, \ldots, x_n$, such that denominators which depend on the same set of variables form a group; each group will correspond to a block in the monomial ordering.*

2. *Sort the groups according to the number of variables they depend on; a group with denominators depending on fewer variables is considered "smaller" than a group with denominators depending on more variables.*

3. *In each group, sort the denominators according to their total degree.*

4. *Replace the denominators d_i by the corresponding inverse denominator variables q_i and add a last group containing the variables $x_1, \ldots, x_n$.*

5. *Let the sequence of groups of variables define the blocks of a monomial ordering. Within each block, use the "standard" degree reverse lexicographic ordering (degrevlex).*

Let us consider an example with the denominators

$$d_1 = x^2 + y,\ d_2 = x - y,\ d_3 = x + 1,\ d_4 = x^2 - 3,\ d_5 = y + 1,\ d_6 = y\,. \tag{4.10}$$

The ideal I is generated by the polynomials

$$\{q_1(x^2+y)-1, q_2(x-y)-1, q_3(x+1)-1, q_4(x^2-3)-1, q_5(y+1)-1, q_6 y-1\}. \tag{4.11}$$

In steps 1-3, we identify the three groups of denominators

$$\{\{d_1 = x^2+y,\ d_2 = x-y\}, \{d_4 = x^2-3,\ d_3 = x+1\}, \{d_5 = y+1,\ d_6 = y\}\}, \tag{4.12}$$

which gives in step 4

$$\{\{q_1, q_2\}, \{q_4, q_3\}, \{q_5, q_6\}, \{x, y\}\}. \tag{4.13}$$

This defines a monomial ordering with four blocks, see step 5, which would be used to calculate the Gröbner basis and the subsequent polynomial reductions.

Our proposal for the monomial ordering aims to reduce the computational effort of the decomposition and to prefer low degrees of the denominator and numerator polynomials. In our experiments, it allowed for a significantly faster calculation of the Gröbner basis than a global degree or a lexicographical ordering. We would like to point out that our choice of monomial order will in general only guarantee Leĭnartas' requirement (i) but not (ii). A lexicographical ordering could achieve a Leĭnartas decomposition fulfilling both requirements, but potentially at the price of significantly increased polynomial degrees. We give details and an example in Appendix 4.B.

4.2.3 Example for the algorithm

We consider again the rational expression in Eq. (4.6),

$$r = \frac{2x - y}{(x-y)y(x+y)}, \tag{4.14}$$

and apply our partial fraction algorithm to it. We identify three irreducible denominators and label their inverses according to

$$q_1 = \frac{1}{x-y}, \quad q_2 = \frac{1}{y}, \quad q_3 = \frac{1}{x+y}, \tag{4.15}$$

such that we can write r as a polynomial,

$$r = (2x - y) q_1 q_2 q_3\,. \tag{4.16}$$

Corresponding to the identification in Eq. (4.15), we consider the ideal

$$I = \langle q_1(x-y) - 1,\ q_2 y - 1,\ q_3(x+y) - 1\rangle\,. \tag{4.17}$$

With the monomial ordering defined by

$$\{\{q_3, q_1\},\ \{q_2\},\ \{x, y\}\}, \tag{4.18}$$

we obtain a Gröbner basis of I as

$$G = \{-1 + q_2 y, -1 + q_1 x - q_1 y, -1 + q_3 x + q_3 y, -q_1 q_2 + 2q_1 q_3 + q_2 q_3\}. \tag{4.19}$$

Reducing the polynomial representation of r in Eq. (4.16) with respect to G yields the reduced form

$$r = \frac{1}{2} q_1 q_2 + \frac{3}{2} q_2 q_3 \tag{4.20}$$

$$= \frac{1}{2(x-y)y} + \frac{3}{2y(x+y)}, \tag{4.21}$$

which is our partial fractioned result. Let us now assume we start with the equivalent expression from Eq. (4.7), i.e.

$$r = \frac{2}{y(x+y)} + \frac{1}{(x-y)(x+y)} = 2q_2 q_3 + q_1 q_2. \tag{4.22}$$

Reducing this expression with respect to G indeed yields exactly the same result as before, given by Eq. (4.20). Therefore, in this example, our algorithm recognizes that both input forms of r are equivalent, and gives a unique result. If we however start in another form, in which spurious denominators occur, one has to be careful.

Let us consider a different representation of the same rational expression r in (4.14), this time containing the additional spurious denominator x:

$$r = \frac{2}{y(x+y)} + \frac{1}{2x(x-y)} + \frac{1}{2x(x+y)}. \tag{4.23}$$

In this case we would identify four denominators and consider the ideal

$$I = \langle q_1(x-y) - 1,\ q_2 y - 1,\ q_3(x+y) - 1,\ q_4 x - 1 \rangle\,. \tag{4.24}$$

Our method produces in this case the block ordering

$$\{\{q_3, q_1\},\ \{q_2\},\ \{q_4\},\ \{x, y\}\}. \tag{4.25}$$

Calculating the corresponding Gröbner basis and reducing with respect to that basis yields

$$r = \frac{1}{2} q_1 q_4 + 2q_2 q_4 - \frac{3}{2} q_3 q_4\,. \tag{4.26}$$

We see that the spurious inverse denominator q_4 does not drop out, since we use a monomial ordering in which $q_4 \prec q_1, q_2, q_3$. However, if we would have chosen a different monomial ordering, in which q_4 is greater than all other q_i, the spurious denominator would drop out after reduction. In this way, one can locally eliminate denominators that are known to be spurious or add additional denominators to the problem without altering previous reductions.

4.2.4 Efficient reduction of factorized inputs

If the input expression is in a form with a single common denominator, i.e.

$$r = q_1^{\alpha_1} ... q_m^{\alpha_m} \times \mathcal{N}, \tag{4.27}$$

where $\mathcal{N}$ is a possibly lengthy numerator, it may be optimal from a performance perspective to just fully expand the polynomial prior to reduction. In this case, we propose the following guided scheme.

Algorithm 4 Iterated reductions. *The polynomial reduction of r in Eq. (4.27) with respect to I can be performed as follows.*

1. *Set $p = \mathcal{N}$ and $Q = \{q_1^{\alpha_1}, \ldots, q_m^{\alpha_m}\}$.*
2. *Identify the "smallest" inverse denominator factor q_i in Q according to the monomial ordering defined in Section 4.2.2. Set $p \leftarrow p \times q_i^{\alpha_i}$ and remove $q_i^{\alpha_i}$ from Q.*
3. *Replace p by its reduced form w.r.t. the Gröbner basis of the ideal I.*
4. *If Q is non-empty, goto step 2. Otherwise, stop and return p.*

The reason why this reduction scheme can be much faster than a "naive" direct reduction is, that the decomposed form of the common denominator $q_1^{\alpha_1}, \ldots, q_m^{\alpha_m}$ alone can result in huge expression, which only shortens once the numerator is taken into account. The iterative reduction of one denominator at a time avoids this intermediate expression swell because it avoids the clustering of many denominators at one reduction step.

In the `Mathematica` functions of our package, the iterated scheme above can be selected as an option. Our `Form` implementation of the polynomial reductions uses this scheme by default. We observed an additional speed-up in our implementation in `Mathematica` by partitioning the whole expression into smaller pieces and reducing these individually in step 2. An example with a comparison of timings for different sizes of these partitions can be found in our publication [88].

4.2.5 A comment on rational reconstructions

Symbolic manipulations of large rational expressions can be computationally expensive. Finite field sampling and rational reconstruction techniques allow to prevent intermediate expression swell and have become quite standard in high energy physics calculations today [94, 132–136]. The basic idea is to set the indeterminates to numerical values in prime fields, perform all complicated manipulations with machine-sized integers instead of rational functions, and reconstruct the final rational function of interest from many such samples. In this section, we would like to discuss the usage of information about the denominator structure for an improved reconstruction of rational functions. A major goal is to reduce the number of samples needed to reconstruct the rational functions, thus speeding up the computation. Furthermore, in applications involving linear relations between Feynman integrals, the partial fractioned forms are often particularly simple and it would be a significant advantage to directly reconstruct the partial fractioned form.

We first start with the following observation concerning the prediction of denominator factors in rational functions, which are to be reconstructed from numerical samples. Linear relations (integration-by-parts identities) between Feynman integrals typically involve only a small set of denominator factors. Moreover, choosing appropriate basis or master integrals can help to avoid spurious denominators in the calculation. In practice, the analysis of the denominator factors may be performed by considering only a small set of linear relations for a specific sector (set of distinct propagators) and setting subsector integrals (with fewer distinct propagators) to zero [137, 138]. This results in a list of possible denominator factors to be expected for a specific rational function. This knowledge helps to predict the denominator structure of the multivariate rational function e.g. by univariate reconstructions, see also [139].

Here, we propose a new method, which allows us to straight-forwardly guess denominator factors and their powers for a rational function, based on a list of candidate denominator factors and a small number of numerical probes (samples) of the rational function to reconstruct. Once the denominator is known or at least partial information about it, the full rational function can be reconstructed from (substantially) fewer samples. Let us assume we analyzed our rational functions and expect a list of irreducible denominator factors $d_1, \ldots, d_m$ in the result. We assume that the coefficient to be reconstructed is of the form

$$r = \frac{\mathcal{N}}{d_1^{\alpha_1} \cdots d_m^{\alpha_m}}, \tag{4.28}$$

where $\mathcal{N}$, d_1, ..., d_m are polynomials in $\mathbb{Q}[x_1, \ldots, x_n]$, and $\alpha_1, \ldots \in \mathbb{N}_0$.

Recipe 1 Denominator guess. *For a rational function, which is expected to be of the form (4.28) with known denominator factors $d_1(x_1, \ldots), \ldots$, the following construction provides a guess for the full denominator.*

1. *Find integer samples for all $x_1, \ldots, x_n$ such that all d_1, ..., d_m have a distinct, largest prime factor, which we denote by p_i, and each of these largest prime factors has multiplicity one. This requirement can be weakened but the stated form simplifies the following analysis.*

2. *Evaluate the rational function for the numerical values of the $x_1, \ldots, x_n$. In practice, this may mean e.g. linear system solving for several prime fields, Chinese remaindering and rational reconstruction. The result of this step is a number $r_{num} \in \mathbb{Q}$, which can be written in the form $r_{num} = n_{num}/d_{num}$ with $n_{num}, d_{num} \in \mathbb{Z}$.*

3. *Perform a prime factor decomposition of the integer number d_{num}. Due to Eq. (4.28), each factor $d_i^{\alpha_i}$ must contribute $p_i^{\alpha_i}$ to the prime factors in d_{num}. On the other hand, if we find a factor $p_i^{\alpha_i}$, we can take it as an indication that it was generated by $d_i^{\alpha_i}$ in the denominator. In this way, we can make a guess for the denominator just by counting the multiplicities of the p_i in the factorization of d_{num}.*

In step 3 our guess may be off due to the presence of a new denominator factor that was not in the candidate list or a factor p_i appearing in the coefficients of the numerator polynomial $\mathcal{N}$. One could imagine repeating the above construction for several samples of the indeterminates and combining this information to validate or correct the guess. In our experiments, we have just picked somewhat larger integers and were in fact not even faced with these problems for the cases that we checked.

The above method lets us therefore identify (parts of) the denominator of the expression we want to reconstruct. A robust way to use this guess for the full reconstruction of a rational function is to multiply all samples with this denominator and reconstruct the resulting expression as if it was a rational function. If the guess was accurate, only the numerator needs to be reconstructed, thereby reducing the number of required samples. We emphasize that this method will allow for a successful reconstruction of the result even if the guess was incomplete or inaccurate. After reconstruction, one can perform the partial fractioning as discussed in Section 4.2.

We successfully applied this method to integration-by-parts reductions of Feynman integrals for problems with up to three loops. Considering the reconstruction of just a single variable, we typically observe a reduction of the number of samples

by a factor of about two due to the guessed denominators. For a reduction problem with five variables, the iterated reconstruction of all variables resulted in an overall reduction of the number of samples by about a factor of 10.

As a next step, one can ask if it is possible to directly reconstruct the result in partial fractioned form. Indeed, assuming one knows all irreducible denominator factors of an expression beforehand, our method in Section 4.2 actually allows to systematically construct a basis of all monomials that can be expected in the final partial fractioned result, using a bound on the monomial degree in the construction. This, in principle, allows to match against an ansatz and reconstruct the partial fractioned form directly. We observed in our experiments that depending on the exact strategy the ansatz in partial fractioned form may require more samples to fix the free coefficients than the reconstruction in the common denominator representation along the lines described above. Furthermore, an incomplete list of denominator factors would prevent a successful fit of a partial fractioned ansatz as well as an insufficient degree of the ansatz. In contrast, the method for the reconstruction in the common-denominator form presented above is robust to incomplete denominator information.

4.2.6 Implementation in `Mathematica`

We implement the described algorithm in a `Mathematica` package, that can be downloaded using git:

```
git clone https://gitlab.msu.edu/vmante/multivariateapart.git
```

More information on the usage can be found in our original publication [88] in which we provide examples of the functionality of our package.

4.3 Conclusion and outlook

In this chapter, we discussed a method for the partial fraction decomposition of multivariate rational functions through polynomial reductions which has been published in Ref. [88]. The method does not introduce spurious singularities and allows for a straightforward implementation in `Form` using local replacement rules. We implemented our algorithms in a `Mathematica` package that is publicly available.

Our approach involves the construction of a special monomial ordering, which is optimized for computational performance and leads to results with comparably low degrees. We used this algorithm in several "real-life" applications, in which it helped to calculate Feynman amplitudes, in the presence of many kinematic variables, many denominators, or high polynomial degrees of the denominators. In several of our examples, the calculation of the Gröbner basis is highly non-trivial and became possible through our method to define the monomial ordering. The partial fractioned sum of terms lends itself to a straightforward and compiler-friendly implementation in numerical codes.

We discussed options for the reconstruction of rational functions from prime field samples. Here, we proposed a new idea to reconstruct the denominator of a rational function based on knowledge about possible denominator factors and a small number of numerical samples. This method has been successfully tested in the context of linear relations between Feynman integrals and reduced the number of samples required for the reconstruction of the full rational functions significantly. Our partial fraction decomposition provides a systematic approach to the direct reconstruction rational function in this representation. Future research might provide an optimized strategy

to further reduce the number of samples required to reconstruct complicated rational functions in this approach.

A possible future application of our methods to particle physics is the direct parametric integration of Feynman integrals [140, 141]. In this context, it is important to recognize potential cancellations between different terms and to avoid the introduction of spurious (non-linear) denominators, since they can prevent a successful integration. The algorithms discussed here provide a systematic approach to this problem. Further, particle physics calculations based on loop-tree duality [142, 143] or intersection theory [144] can benefit from our algorithms. Since our methods apply to general rational functions, they may be useful also for other areas of research unrelated to particle physics.

Appendix

4.A Polynomial reductions

In this appendix, we review some basic notions that can be found in any introductory textbook on the topic, see e.g. [129, 130].

Let us consider polynomials in the variables $x_1, \ldots, x_n$ with coefficients in the field K (e.g. the rational numbers). These polynomials form a *polynomial ring* $R = \mathbf{K}[x_1, \ldots, x_n]$.

A *monomial ordering* is a total order $\prec$ on the set of monomials

$$M \equiv \{x^\alpha \equiv x_1^{\alpha_1} \cdots x_n^{\alpha_n} | \alpha_i \in \mathbf{Z}_{\geq 0}\} \tag{4.29}$$

such that

(i) for all monomials x^α, x^β and x^γ: $x^\alpha \leq x^\beta \Rightarrow x^{\alpha+\gamma} \leq x^{\beta+\gamma}$,

(ii) $1 \leq x^\alpha \quad \forall \alpha$.

In many applications, in which the specific monomial ordering does not matter, one chooses the so-called *degree reverse lexicographic order* (degrevlex), which first compares the total degree of two monomials, and then, if the degrees are the same, uses a lexicographic comparison and reverses the outcome of the latter.

There is a more general way of defining a monomial ordering, which will be relevant to us. A monomial ordering is called a *block ordering*, if one can group the variables into two sets $\{x_1, \ldots, x_m\}$ and $\{y_1, \ldots, y_n\}$, such that

$$x^\alpha \prec y^\beta \quad \forall\, \alpha, \beta \text{ with } y^\beta \neq 1 \tag{4.30}$$

i.e. all monomials formed from variables from the first block are "smaller" than monomials formed from variables from the second block.

We call the "greatest" monomial of a polynomial p with respect to a monomial order the *leading monomial* of p. A term is a monomial multiplied by a coefficient, which is a non-zero rational number for our purposes. The *leading term* $\mathrm{LT}(p)$ of polynomial p is the term corresponding to the leading monomial.

Having defined a monomial ordering puts us in a position to discuss polynomial reductions. Given two polynomials p_1 and p_2 together with a monomial ordering $\prec$, we call p_1 reducible modulo p_2 if for some term t of p_1 there is a term u such that $t = u \cdot \mathrm{LT}(p_2)$. Then we say p_1 *reduces to* p_1' *modulo* p_2, where

$$p_1' = p_1 - u \cdot p_2 \tag{4.31}$$

The effect of the polynomial reduction is that a term in p_1 is replaced by a linear combination of "smaller" terms.

It is useful to introduce another concept. A set of polynomials $g_1, \ldots, g_m \in R$, the *generators*, define an *ideal* $I \subset R$ as the set of all their linear combinations, where the coefficients are polynomials themselves, $I = \{\sum_i f_i g_i \text{ with } f_i \in R\}$. We also use the notation $I = \langle g_1, \ldots, g_m \rangle$. The choice of generators is not unique, and

it is a non-trivial task to decide whether a polynomial is a member of a given ideal. It is clear that, if a polynomial reduces to zero modulo the generators of an ideal, this polynomial is a member of the ideal. The inverse, however, is not true and the remainder of a polynomial reduction will in general depend on the individual reduction steps.

It is possible to find a set of generators for an ideal, called a *Gröbner basis*, which allows one to find a unique remainder for the reduction of any polynomial modulo the generators. In this case, a reduction to zero occurs if and only if the polynomial is in the ideal. A Gröbner basis can be calculated algorithmically by adjoining specific differences of generators. The Gröbner basis depends on the choice of the monomial ordering and is unique if reduced with respect to itself.

4.B Leĭnartas' requirements and polynomial reductions

In this appendix, we revisit the two central decomposition steps in Algorithm 1 leading to Leĭnartas' decomposition, see Section 4.1.2 and consider under which circumstances they are reproduced by the polynomial reductions in Algorithm 2, see Section 4.2. As we will show, Algorithm 2 may or may not produce a Leĭnartas' decomposition, depending on the monomial ordering. If the monomial ordering sorts first for the q_i and then for the x_i, requirement (i) will be fulfilled, that is, the denominator zeros will be separated. If the q_i are sorted lexicographically, also requirement (ii), the algebraic independence of different denominator factors, will be guaranteed [128]. For degree-based orderings of the q_i, requirement (ii) is violated in general. This means in particular, that our monomial block ordering proposed in Section 4.2.2 guarantees only requirement (i) and not (ii), and will therefore not lead to a Leĭnartas decomposition. We emphasize, that an even more general choice of monomial ordering will ensure neither of the two requirements, but still allows for a unique output form.

First, we consider the requirement (i), i.e. that the denominators of each term shall have common zeros in $\overline{K}^n$. Let us assume we encounter a term which is not fully decomposed yet and has denominators $\{d_1(x_1,\ldots),\ldots,d_m(x_1,\ldots)\}$. By Hilbert's Nullstellensatz, a finite set of polynomials $\{d_1^{\alpha_1},\ldots,d_m^{\alpha_m}\}$ has no common zeros in $\overline{K}^n$ if and only if there exist polynomials $h_1,\ldots,h_m$, such that

$$1 = \sum_i h_i(x_1,\ldots)\, d_i^{\alpha_i}(x_1,\ldots). \tag{4.32}$$

Dividing this equation by $d_1^{\alpha_1}\cdots d_m^{\alpha_m}$ gives the decomposition [125]

$$\frac{1}{d_1^{\alpha_1}\cdots d_m^{\alpha_m}} = \sum_i \frac{h_i(x_1,\ldots)}{d_1^{\alpha_1}\cdots \hat{d}_i{}^{\alpha_i}\cdots d_m^{\alpha_m}}. \tag{4.33}$$

where $\hat{d}_i{}^{\alpha_i}$ means leaving $d_i^{\alpha_i}$ out in the product.

This decomposition step in Algorithm 1 has a direct analog in terms of a polynomial reduction in step 5 of Algorithm 2 for a suitable monomial ordering. Multiplying Eq. (4.32) by $q_1^{\alpha_1}\cdots q_m^{\alpha_1}$ and replacing $q_i d_i(x_1,\ldots) = 1$ gives

$$q_1^{\alpha_1}\cdots q_m^{\alpha_m} - \sum_i h_i(x_1,\ldots)\, q_1^{\alpha_1}\cdots \hat{q}_i{}^{\alpha_i}\cdots q_m^{\alpha_m} = 0, \tag{4.34}$$

where $\hat{q}_i{}^{\alpha_i}$ means leaving $q_i^{\alpha_i}$ out in the product. It is clear, that the polynomial on the lhs of Eq. (4.34) is a member of the ideal $I = \langle 1 - q_1 d_1(x_1,\ldots),\ldots\rangle$. Furthermore, $q_1^{\alpha_1}\cdots q_m^{\alpha_m}$ is the leading monomial for any monomial ordering which sorts first for all

of the $q_1, \ldots, q_m$ and then for the $x_1, \ldots, x_n$. In Algorithm 2, that leading monomial will be thus be replaced by the subleading terms on the lhs of Eq. (4.34), resulting in terms with fewer factors of q_i, that is, simpler denominators. A fully reduced term will therefore not have all factors $q_1 \cdots q_n$. This proves the above statements. We conclude that, for our choice of monomial ordering, the polynomial reduction in Algorithm 2 guarantees requirement (i) of Leĭnartas' decomposition, that is, the separation of independent denominator zeros.

Second, we consider requirement (ii), that is, the algebraic independence of the denominator factors. Let us assume that our decomposition contains a term with denominator $d_1^{\alpha_1} \cdots d_m^{\alpha_m}$, where the factors $\{d_1, \ldots, d_m\}$ are algebraically dependent. One can show that then also the polynomials $\{d_1^{\alpha_1}, \ldots, d_m^{\alpha_m}\}$ are algebraically dependent and there exists a non-zero annihilating polynomial $p(y_1, \ldots, y_m)$ with

$$p(d_1^{\alpha_1}, \ldots, d_m^{\alpha_m}) = 0 \tag{4.35}$$

after inserting the explicit expressions the $d_i(x_1, \ldots)$. In Algorithm 1, one can for example choose one of the monomials of p with smallest degree and substitute the remainder, i.e. one has

$$c_\beta (d^\alpha)^\beta = -\sum_{\gamma \in S} c_\gamma (d^\alpha)^\gamma, \tag{4.36}$$

where $d = (d_1, \ldots, d_m)$, α, β and γ are multi-indices in $\mathbb{N}^m$, with $\sum_i \beta_i \leq \sum_i \gamma_i$ for all β in the set of multi-indices S. Dividing by $c_\beta d^{\beta+1}$ gives the decomposition step [125]

$$\frac{1}{d_1^{\alpha_1} \cdots d_m^{\alpha_m}} = -\sum_{\gamma \in S} \frac{c_\gamma}{c_\beta} \prod_{i=1}^{m} \frac{d_i^{\alpha_i \gamma_i}}{d_i^{\alpha_i(\beta_i+1)}}. \tag{4.37}$$

Since $\sum_i \beta_i \leq \sum_i \gamma_i$ and $\beta \neq \gamma$, for each γ there exists an i such that $\beta_i + 1 \leq \gamma_i$ and the factor $d_i^{\beta_i+1}$ is removed from the denominator. Therefore, each term on the rhs of (4.37) depends on at least one denominator factor d_i less than the lhs.

The described decomposition step in Algorithm 1 may or may not have an analog in terms of a polynomial reduction in step 5 of Algorithm 2, depending on the monomial ordering. In general, for a degree based ordering of the q_i variables, either globally or in blocks like proposed here, a similar decomposition will *not* occur. In (4.37), the denominator degree may actually be higher on the rhs than on the lhs, and it may therefore not correspond to a polynomial reduction for such an ordering. A lexicographic ordering, on the other hand, *will* separate algebraically dependent denominators. To show this, we pick in Eq. (4.35) the unique exponent β' of p such that $(q^\alpha)^{\beta'}$ is minimal with respect to our monomial ordering. Multiplication with $(q^\alpha)^{\beta'+1}/(c_{\beta'})$ gives

$$q_1^{\alpha_1} \cdots q_m^{\alpha_m} + \sum_{\gamma \in S} \frac{c_\gamma}{c_{\beta'}} \prod_{i=1}^{m} d_i^{\alpha_i \gamma_i} q_i^{\alpha_i(\beta_i'+1)} = 0. \tag{4.38}$$

Replacing all products $q_i d_i(x_1, \ldots) = 1$ gives

$$q_1^{\alpha_1} \cdots q_m^{\alpha_m} + \sum_{\gamma \in S} \frac{c_\gamma}{c_{\beta'}} \prod_{i=1}^{m} d_i^{\max(\alpha_i(\gamma_i - \beta_i' - 1), 0)} q_i^{\max(\alpha_i(\beta_i' + 1 - \gamma_i), 0)} = 0. \tag{4.39}$$

Assuming a lexicographic ordering of the q_i with $q_1 \succ q_2 \succ \ldots$ implies that for each term γ there exists a $j = 1, \ldots, m$ such that $\beta_i' = \gamma_i$ for all $i = 1, \ldots, j$, $\beta_j' \prec \gamma_j$, the powers of q_i coincide with that of the first term for $i = 1, \ldots, j-1$, but q_j is removed.

This means that the first term in (4.39) is indeed the leading term. Since furthermore the polynomial on the lhs of (4.39) is a member of the ideal $I = \langle q_1 d_1(x_1, \ldots) - 1, \ldots \rangle$, the first term in (4.39) would be reduced in step 5 of Algorithm 2 for this ordering. We conclude that, for the block monomial ordering presented in our algorithm, the polynomial reduction in Algorithm 2 does not guarantee requirement (ii) of Leĭnartas' decomposition, that is, algebraically independent denominators. In contrast, a lexicographical ordering guarantees this requirement.

We would like to illustrate the impact of the monomial ordering on the decomposition with the following example. We consider the irreducible denominator factors

$$d_1 = x^3 + y^4, \quad d_2 = x + y^2, \quad d_3 = x^2 + y, \tag{4.40}$$

which share a common zero. We note that three denominator factors in two variables must be algebraically dependent on general grounds. Let us consider the ideal

$$I = \langle q_1 d_1(x, y) - 1, q_2 d_2(x, y) - 1, q_3 d_3(x, y) - 1 \rangle . \tag{4.41}$$

The monomial block ordering proposed in our algorithm gives

$$\{\{q_1, q_2, q_3\}, \{x, y\}\}. \tag{4.42}$$

Calculating the Gröbner basis of I with respect to this ordering, we see that the polynomial representation of $1/(d_1 d_2 d_3)$,

$$q_1 q_2 q_3, \tag{4.43}$$

is fully reduced already, despite the denominators d_1, d_2 and d_3 being algebraically dependent.

Next, let us consider a lexicographic ordering of the q_i according to

$$\{\{q_1\}, \{q_2\}, \{q_3\}, \{x, y\}\}. \tag{4.44}$$

In this case, the Gröbner basis computation of I reveals that $q_1 q_2 q_3$ is reducible. Alternatively, we can derive a reduction identity of type (4.39) as described above. Indeed, it is not difficult to calculate the annihilator

$$\begin{aligned} p(y_1, y_2, y_3) = {} & y_1^4 - 4y_1^3 y_2^2 - 4y_1^3 y_3 + 3y_1^3 + 6y_1^2 y_2^4 + 4y_1^2 y_2^2 y_3 - y_1^2 y_2^2 + 8y_1^2 y_2 y_3^2 \\ & - 6y_1^2 y_2 y_3 - 8y_1^2 y_2 - 2y_1^2 y_3^3 + 6y_1^2 y_3^2 - 2y_1^2 y_3 + 3y_1^2 - 4y_1 y_2^6 + 4y_1 y_2^4 y_3 \\ & - 7y_1 y_2^4 - 16y_1 y_2^3 y_3^2 + 12y_1 y_2^3 y_3 - 8y_1 y_2^3 + 4y_1 y_2^2 y_3^3 + 4y_1 y_2^2 y_3^2 + 36y_1 y_2^2 y_3 \\ & - 16y_1 y_2 y_3^3 - 18y_1 y_2 y_3^2 + 2y_1 y_2 y_3 - 5y_1 y_2 + 4y_1 y_3^4 + 2y_1 y_3^3 - y_1 y_3^2 + 2y_1 y_3 \\ & + y_2^8 - 4y_2^6 y_3 + 5y_2^6 + 8y_2^5 y_3^2 - 6y_2^5 y_3 - 2y_2^4 y_3^3 + 6y_2^4 y_3^2 - 2y_2^4 y_3 + 5y_2^4 \\ & - 16y_2^3 y_3^3 - 14y_2^3 y_3^2 - 2y_2^3 y_3 + 20y_2^2 y_3^4 + 6y_2^2 y_3^3 - 8y_2 y_3^5 + 5y_2 y_3^4 + y_3^6 - 2y_3^5 \end{aligned} \tag{4.45}$$

with $p(d_1(x, y), d_2(x, y), d_3(x, y)) = 0$ and identify $q_i d_i = 1$ modulo I to obtain

$$\begin{aligned} & q_1 q_2 q_3 - \tfrac{1}{2} q_1 q_2 - \tfrac{1}{2}(d_2^7 + 5d_2^5 + 5d_2^3) q_1 q_3^6 + (2d_2^5 + 3d_2^4 + d_2^3 + d_2^2) q_1 q_3^5 \\ & - (4d_2^4 + 3d_2^3 - 7d_2^2) q_1 q_3^4 + (d_2^3 + 8d_2^2 - 3d_2) q_1 q_3^3 - \tfrac{1}{2}(20d_2 + 5) q_1 q_3^2 + 4 q_1 q_3 \\ & - \tfrac{1}{2}(d_1^3 + 3d_1^2 + 3d_1) q_2 q_3^6 + (2d_1^2 + d_1 - 1) q_2 q_3^5 - \tfrac{1}{2}(6d_1 - 1) q_2 q_3^4 + (d_1 - 1) q_2 q_3^3 \\ & - 2 q_2 q_3^2 + \tfrac{1}{2}(4d_1^2 d_2 - 6d_1 d_2^3 + d_1 d_2 + 8d_1 + 4d_2^5 + 7d_2^3 + 8d_2^2 + 5) q_3^6 \\ & - (2d_1 d_2 - 3d_1 + 2d_2^3 + 6d_2^2 + 18d_2 + 1) q_3^5 - (4d_1 - 8d_2^2 + 2d_2 - 9) q_3^4 \\ & - (2d_2 - 8) q_3^3 = 0, \end{aligned} \tag{4.46}$$

where d_1, d_2, d_3 are meant to be replaced by their definitions (4.40). As we see, this gives a reduction identity for (4.43) since the first term is indeed the leading term in this ordering, such that the algebraically dependent denominators are decomposed. However, we also see that this decomposition leads to a significant increase in the degrees of the polynomials.

Part II

Radiative corrections to Compton processes

5 Leading-order QED corrections to the $\gamma p \to p l^- l^+$ process

This chapter is based on three articles [27, 52, 53], which were all published in Physical Review D. In the first publication, Ref. [52], we study the one-loop soft-photon corrections to the BH process, corresponding to the reaction $\gamma p \to l^+ l^- p$. In a subsequent work [53], we extend that calculation from the soft-photon approximation to a full next-to-leading-order calculation, taking into account all one-loop QED corrections including full dependence on the lepton mass. The main objective of both studies was the calculation of radiative corrections to the ratio of cross sections for muon vs electron pair production. As described in Section 1.2.2, a measurement of this ratio can potentially serve as a test of lepton universality as suggested in Ref. [51]. The authors propose to perform such measurement slightly above the di-muon production threshold (but below the two-pion threshold) and relate it with a measurement below the di-muon production threshold. They find, that the discrepancy between the different extracted proton charge radii at that time amounts to an effect of 0.2% on the ratio. In Refs. [52, 53] we showed that the inclusion of radiative corrections is mandatory to be able to interpret data from such experiments. In our analysis, we found that the effect of radiative corrections is of the order 1% on the cross section ratio, and thus significantly larger than the 0.2% effect that amounts for the different proton charge radii.

In Ref. [27], we extended our study to include radiative corrections in addition to the BH process also to the TCS process. While in Refs. [52, 53] we study kinematic regions, in which the BH process is the dominant contribution, in Ref. [27] we study the reaction $\gamma p \to e^- e^+ p$ also for small values of the invariant dilepton mass, such that the TCS amplitude becomes larger and the interference between BH and TCS is not negligible. By measuring the forward-backward and the beam spin asymmetry, one is able to access the real and imaginary part of the TCS amplitude and thus test various theoretical models describing the amplitude. In Ref. [27] we study the TCS process in two energy regimes, which we describe with two different models. For low energies, we model the amplitude in terms of the Born contribution and the first excitation of the proton, the $\Delta(1232)$ resonance. For high energies, when the timelike photon has large virtuality, we express the amplitude in terms of GPDs. In both cases, we study the impact of radiative corrections on the cross section and the two asymmetries, which allow to access the TCS amplitude.

The outline of the chapter is as follows. In Section 5.1, we introduce the contributing BH and TCS amplitudes to the $\gamma p \to l^- l^+ p$ reaction at tree level and define the relevant kinematic variables. In Section. 5.2, we describe in detail the two different models for the double virtual Compton amplitude. In Sections 5.3.1, 5.3.2 and 5.3.3, we calculate the virtual one-loop QED corrections due to vacuum polarization, as well as due to photons attached to the lepton lines of the BH and TCS amplitudes. In both cases we calculate the corrections on the level of the amplitude, allowing for the

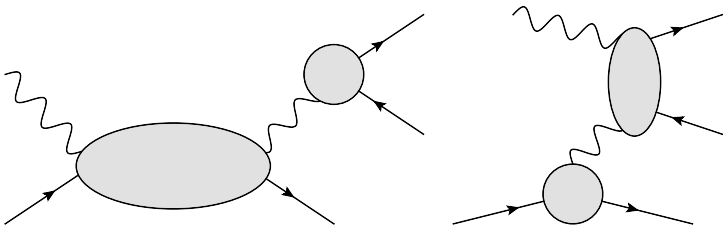

FIGURE 5.1.1: TCS (left panel) and BH (right panel) processes. The blob on the proton line denotes the nucleon structure, whereas the blob on the lepton line denotes the QED amplitude, including radiative corrections.

calculation of polarized cross sections. In Section 5.4, we calculate the soft-photon emission. We distinguish between two different experimental setups, corresponding to the measurement of the recoil proton or the dilepton pair. Including the soft-photon radiation gives infrared finite results for the observables. In Section 5.5, we present our numerical results and show the effect of the radiative corrections on the cross sections as well as on the forward-backward and photon beam helicity asymmetries. We show results both in the $\Delta(1232)$ resonance region as well as in the kinematical regime of the CLAS12@JLab TCS experiment [26]. For the latter, we show the sensitivity of the cross section and asymmetries on the underlying GPD parameterization. We also show the effect of radiative corrections on the ratio of cross sections motivated for the test of lepton universality. We conclude in Section 5.6 and give technical details in three appendices.

5.1 Bethe-Heitler and timelike Compton Scattering processes at tree level

In this chapter we consider the process

$$\gamma(q) + N(p) \to l^-(l_-) + l^+(l_+) + N(p'), \tag{5.1}$$

where the quantities in brackets denote the four-momenta of the particles. We distinguish between two different contributions to (5.1), which are called the Bethe-Heitler (BH) process and the timelike Compton scattering process (TCS). We show the corresponding Feynman diagrams in Fig 5.1.1.

The process (5.1) is defined in terms of three kinematic invariants,

$$(p+q)^2 = W^2, \qquad (l_+ + l_-)^2 = s_{ll}, \qquad (p'-p)^2 = t, \tag{5.2}$$

and two angles θ_l and ϕ_l, which are defined in the rest-frame of the dilepton pair, with the polar angle θ_l defined relative to the center-of-mass (c.m.) direction of $q' \equiv l_+ + l_-$.

The matrix element of the BH process at leading order is given by

$$\mathcal{M}_0^{\rm BH} = \frac{ie^3}{t}\bar{u}(l_-)\left[\gamma^\mu \frac{(\not{l}_- - \not{q} + m_l)}{(l_- - q)^2 - m_l^2}\gamma^\nu + \gamma^\nu \frac{(\not{q} - \not{l}_+ + m_l)}{(q - l_+)^2 - m_l^2}\gamma^\mu\right] v(l_+) \\ \times \varepsilon_\mu(q)\bar{N}(p')\Gamma_\nu(t)N(p), \tag{5.3}$$

where m denotes the mass of the lepton and where the electromagnetic vertex Γ_ν for the proton is expressed as:

$$\Gamma_\nu(t) = F_D(t)\gamma_\nu + iF_P(t)\frac{\sigma_{\nu\alpha}\Delta^\alpha}{2M}, \tag{5.4}$$

with momentum transfer to the proton $\Delta \equiv p' - p$, satisfying $\Delta^2 = t$, with M the proton's mass, and with F_D (F_P) the Dirac (Pauli) proton form factors (FFs) respectively.

The general TCS matrix element is given by

$$\mathcal{M}_0^{\mathrm{TCS}} = -\frac{ie^3}{s_{ll}} \bar{N}(p') M^{\mu\nu} N(p) \varepsilon_\mu(q) \bar{u}(l_-) \gamma_\nu v(l_+), \tag{5.5}$$

where $M^{\mu\nu}$ is the Compton tensor which will be specified below, and which depends on the model used to describe the interaction with the proton.

The unpolarized, fully differential cross section $d\sigma_0$ is given by

$$\frac{d\sigma_0}{dt\, ds_{ll}\, d\Omega_{ll}^*} = \frac{1}{(2\pi)^4} \frac{1}{64} \frac{\beta}{(2ME_\gamma)^2} \overline{\sum_i} \sum_f |\mathcal{M}_0|^2 , \tag{5.6}$$

where E_γ is the lab energy of the initial photon, which is related to W as $E_\gamma = (W^2 - M^2)/(2M)$, and Ω_{ll}^* is the solid angle of the lepton pair in the l^+l^- center-of-mass frame, in which the lepton velocity is denoted by

$$\beta = \sqrt{1 - \frac{4m_l^2}{s_{ll}}}. \tag{5.7}$$

The tree-level amplitude $\mathcal{M}_0$ is given by the sum of BH and TCS amplitudes,

$$\mathcal{M}_0 = \mathcal{M}_0^{\mathrm{BH}} + \mathcal{M}_0^{\mathrm{TCS}}. \tag{5.8}$$

In Eq. (5.6), we average over all polarizations in the initial state and sum over the polarizations in the final state.

In the following, we will consider two different experimental setups. In the case in which one wants to measure the forward-backward asymmetry of the dilepton pair, one needs to measure the pair. In that case the differential cross-section is given by Eq. (5.6).

In an experimental setup when only the recoil proton is measured, one has to integrate (5.6) over the lepton angles:

$$\frac{d\sigma_0}{dt\, ds_{ll}} = \frac{1}{(2\pi)^4} \frac{1}{64} \frac{\beta}{(2ME_\gamma)^2} \cdot \int d\Omega_{ll} \overline{\sum_i} \sum_f |\mathcal{M}_0|^2 . \tag{5.9}$$

In that case, the kinematical invariant t is in one-to-one relation with the recoiling proton lab momentum $\vec{p'}$ (or energy E') as follows:

$$|\vec{p'}| = 2M\sqrt{\tau(1+\tau)}, \tag{5.10}$$

$$E' = M(1+2\tau), \tag{5.11}$$

whereas the invariant s_{ll} is then determined from the recoiling proton lab scattering angle as:

$$\cos\theta_{p'} = \frac{s_{ll} + 2(W^2 + M^2)\tau}{2(s - M^2)\sqrt{\tau(1+\tau)}}. \tag{5.12}$$

5.2 Models for the doubly virtual Compton amplitude

The doubly virtual Compton tensor $M^{\mu\nu}$ entering Eq. (5.5) is calculated from the process

$$\gamma^*(q) + N(p) \to \gamma^*(q') + N(p'). \tag{5.13}$$

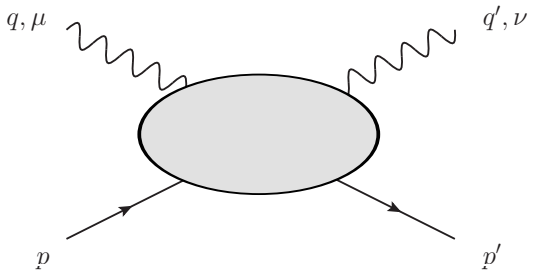

FIGURE 5.2.1: Diagram representing the doubly virtual Compton process.

We show the Feynman diagram for this process in Fig. 5.2.1. The blob in this diagram represents the interaction of the incoming and outgoing photons with the nucleon. In the following we use the average photon ($\bar{q}$) and proton (P) momenta,

$$\bar{q} = \frac{1}{2}(q + q'), \qquad P = \frac{1}{2}(p + p'). \tag{5.14}$$

Although in this chapter we study the process for a real initial photon, we will indicate below the extension to the general case with two off-shell photons, which we will use also in the subsequent chapter in which we study the double-virtual case.

The general doubly virtual Compton tensor $M^{\mu\nu}$ can be constructed using q^μ, q'^μ, p^μ, $g^{\mu\nu}$ and γ^μ as building blocks. From these blocks, one finds 34 independent tensors with two indices. Using gauge invariance it was shown that the number of independent amplitudes can be reduced from 34 to 18 [3]. The latter number corresponds with the minimal number of helicity amplitudes for a parity conserving process, which can be determined by accounting for the possible helicity states of the photons (3) and fermions (2). However, it was realized in Ref. [3], that there is in general a problem in such representation. For specific kinematical points, the 18 tensors become linearly dependent and therefore do not form a basis at these specific points anymore. As a result, the corresponding Compton amplitudes display kinematic singularities at these points. To bypass this problem, Tarrach introduced an overcomplete basis by introducing three additional tensors which do not have any kinematical constraints and are valid in the whole phase space. It was realized in Ref. [145] that the kinematic singularities and constraints of the Compton amplitude in a minimal basis are due to the Born terms, in which the intermediate state in the Compton process in Fig. 5.2.1 is a nucleon, and that for the non-Born contributions a minimal tensor basis consisting of 18 structures free of kinematical singularities and constraints exists.

To specify the doubly virtual Compton amplitude, we need to model the internal structure of the nucleon. In this work, we will consider two different models, which are tailored for applications in two different energy regimes. In a low-energy model, which is motivated for applications to describe the hadronic structure in precision atomic physics measurements such as the Lamb shift or hyperfine splitting in muonic Hydrogen, we consider the photons to interact with the nucleon and its lowest excitation, the $\Delta(1232)$ resonance. In a high-energy model, in which at least one of the photons is highly virtual, we use perturbative QCD which allows factorizing the Compton process on the nucleon in terms of a Compton amplitude on the quark convoluted with the amplitude to find the quarks inside the nucleon. The latter is parameterized through GPDs.

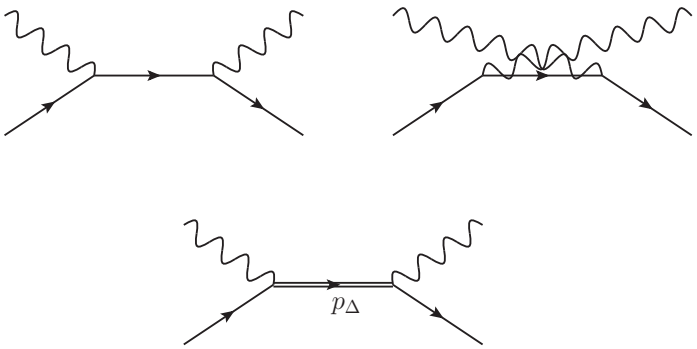

FIGURE 5.2.2: Born contribution (upper panel) and s-channel Δ-pole contribution (lower panel) to the Compton amplitude. While for the Born contribution only the sum of s and u- channel diagrams is gauge invariant, the s-channel Δ-pole contribution is gauge invariant by itself.

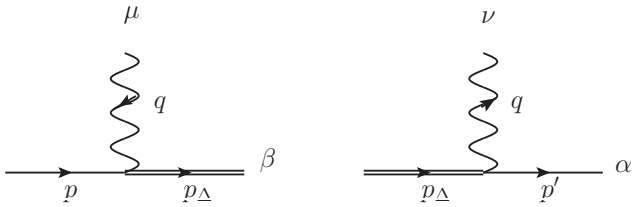

FIGURE 5.2.3: The $\gamma^* N\Delta$ vertex $\Gamma^{\beta\mu}_{\gamma N\Delta}$ (left diagram) and its adjoint, $\tilde{\Gamma}^{\alpha\nu}_{\gamma N\Delta}$ (right diagram).

5.2.1 Born term and Δ-pole model at low energies

At low photon energies, the leading Born (B) contribution to the Compton amplitude is described by two Feynman diagrams, shown in Fig. 5.2.2 (upper panel), in which a nucleon is propagating between both photon interactions. Its contribution to the tensor in Eq. (5.5) can be calculated as:

$$M_{\rm B}^{\mu\nu} = \Gamma_f^\nu \frac{\not{p} + \not{q} + M}{(p+q)^2 - M^2} \Gamma_i^\mu + \Gamma_i^\mu \frac{\not{p}' - \not{q} + M}{(p'-q)^2 - M^2} \Gamma_f^\nu, \tag{5.15}$$

where Γ_i^μ (Γ_f^ν) are the initial (final) state proton vertices, given by analogous expressions as Eq. (5.4) in which Δ is replaced by q ($-q'$) for Γ_i^μ (Γ_f^ν) respectively. Note that the FFs entering Γ_f^ν correspond with a timelike virtuality. For the numerical evaluation of these FFs we use the paramaterization of Ref. [146]. This parameterization allows the analytical continuation based on dispersion relations into the unphysical part of the timelike region, $0 < q'^2 < 4M^2$, in which no direct experimental extraction exists.

In addition to the Born term, we also evaluate the matrix element of the leading contribution due to the Δ resonance in the general case with two off-shell photons. The corresponding s-channel diagram is shown in Fig. 5.2.2 (lower panel) and its contribution to the tensor in Eq. (5.5) can be calculated as:

$$M_{s\Delta}^{\mu\nu} = \tilde{\Gamma}^{\alpha\nu}_{\gamma N\Delta}(p', p+q) \frac{(\not{p} + \not{q} + M_\Delta)(-g_{\alpha\beta} + \frac{1}{3}\gamma_\alpha\gamma_\beta)}{W^2 - M_\Delta^2 + iM_\Delta\Gamma_\Delta(W^2)} \Gamma^{\beta\mu}_{\gamma N\Delta}(p+q, p). \tag{5.16}$$

In Eq. (5.16), $\Gamma^{\beta\mu}_{\gamma N\Delta}$ and $\tilde{\Gamma}^{\alpha\nu}_{\gamma N\Delta}$ refer to the $\gamma^* N\Delta$ vertex function and its adjoint respectively. They are shown in Fig. 5.2.3 and can be expressed in terms of three transition form factors as [147]:

$$\Gamma^{\beta\mu}_{\gamma N\Delta}(p_\Delta, p) = \sqrt{\frac{3}{2}}\frac{(M_\Delta + M)}{MQ_+^2}\Big\{g_M(q^2)i\epsilon^{\beta\mu\kappa\lambda}(p_\Delta)_\kappa q_\lambda - g_E(q^2)(q^\beta p_\Delta^\mu - q\cdot p_\Delta g^{\beta\mu})\gamma_5 - g_C(q^2)\frac{1}{M_\Delta}\left[\not{p}_\Delta(q^\beta q^\mu - q^2 g^{\beta\mu}) - \gamma^\beta(q\cdot p_\Delta q^\mu - q^2 p_\Delta^\mu)\right]\gamma_5\Big\}, \tag{5.17}$$

and its adjoint:

$$\tilde{\Gamma}^{\alpha\nu}_{\gamma N\Delta}(p', p_\Delta) = -\sqrt{\frac{3}{2}}\frac{(M_\Delta + M)}{MQ_+'^2}\Big\{g_M(q'^2)i\epsilon^{\alpha\nu\kappa\lambda}(p_\Delta)_\kappa q'_\lambda - g_E(q'^2)(q'^\alpha p_\Delta^\nu - q'\cdot p_\Delta g^{\alpha\nu})\gamma_5 - g_C(q'^2)\frac{1}{M_\Delta}\gamma_5\left[\not{p}_\Delta(q'^\alpha q'^\nu - q'^2 g^{\alpha\nu}) - \gamma^\alpha(q'\cdot p_\Delta q'^\nu - q'^2 p_\Delta^\nu)\right]\Big\}, \tag{5.18}$$

where we defined $Q_\pm = \sqrt{(M_\Delta \pm M)^2 - q^2}$ and likewise $Q'_\pm = \sqrt{(M_\Delta \pm M)^2 - q'^2}$. Note that the FFs g_M, g_E, and g_C appearing in Eq. (5.17) have spacelike virtuality ($q^2 < 0$), whereas the corresponding ones in the adjoint vertex of Eq. (5.18) have timelike virtuality ($q'^2 > 0$).

The form factors g_M, g_E, and g_C can be expressed by the more conventional magnetic dipole (G_M^*), electric quadrupole (G_E^*), and Coulomb quadrupole (G_C^*) transition FFs as:

$$\begin{aligned} g_M &= \frac{Q_+}{M + M_\Delta}(G_M^* - G_E^*), \\ g_E &= -\frac{Q_+}{M + M_\Delta}\frac{2}{Q_-^2}\{(M_\Delta^2 - M^2 + q^2)G_E^* - q^2 G_C^*\}, \\ g_C &= \frac{Q_+}{M + M_\Delta}\frac{1}{Q_-^2}\{4M_\Delta^2 G_E^* - (M_\Delta^2 - M^2 + q^2)G_C^*\}, \end{aligned} \tag{5.19}$$

with the so-called Ash FFs parameterized, for spacelike virtuality $Q^2 = -q^2$, through the MAID2007 analysis as [148, 149]:

$$\begin{aligned} G_M^*(Q^2) &= 3.00(1 + 0.01Q^2)e^{-0.23Q^2}G_D(Q^2), \\ G_E^*(Q^2) &= 0.064(1 - 0.021Q^2)e^{-0.16Q^2}G_D(Q^2), \\ G_C^*(Q^2) &= 0.124\frac{1 + 0.12Q^2}{1 + 4.9Q^2/(4M^2)}\frac{4M_\Delta^2 e^{-0.23Q^2}G_D(Q^2)}{M_\Delta^2 - M^2}, \end{aligned} \tag{5.20}$$

with Q in GeV and the dipole FF $G_D(Q^2) = 1/(1 + Q^2/0.71)^2$. For small timelike virtualities, $0 < q'^2 < (M_\Delta - M)^2$, we can extrapolate the expressions for spacelike virtualities by the substitution $Q^2 \to -q'^2$.

5.2.2 High-energy timelike Compton Scattering in terms of GPDs

For deeply-virtual Compton scattering, in which at least one of the photons has large virtuality, we can express the doubly virtual Compton tensor using perturbative QCD in terms of GPDs. At leading order in the large virtuality, the deeply virtual Compton tensor can be calculated through the handbag diagrams, shown in Fig. 5.2.4. These handbag diagrams express the factorization of the process in terms of the Compton

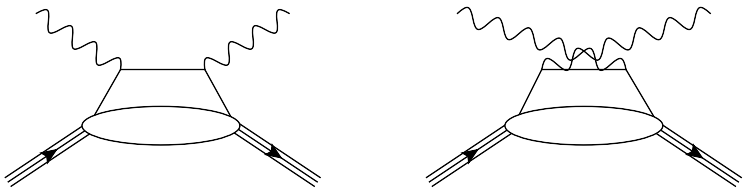

FIGURE 5.2.4: Handbag diagrams for the doubly virtual Compton amplitude. The single (composite) lines represent quarks (nucleons) respectively. The blobs represent the GPDs.

amplitude on the quark convoluted with the amplitude to find the quark in the nucleon, which is parameterized through the GPDs.

To describe the deeply-virtual Compton process with two virtual photons, it is convenient to define the Lorentz invariants ξ and ξ' as:

$$\xi \equiv -\frac{\Delta \cdot \bar{q}}{2P \cdot \bar{q}} = \frac{-q^2 + q'^2}{2(W^2 - M^2) - q^2 - q'^2 + t}, \tag{5.21}$$

$$\xi' \equiv -\frac{\bar{q}^2}{2P \cdot \bar{q}} = \frac{-q^2 - q'^2 + t/2}{2(W^2 - M^2) - q^2 - q'^2 + t}. \tag{5.22}$$

To calculate the handbag diagrams, we first express the four-momenta P^μ and $\bar{q}^\mu$ in terms of the lightlike four-vectors $\tilde{p}$ and n, with $\tilde{p} \cdot n = 1$,

$$P^\mu = \tilde{p}^\mu + \frac{\bar{M}^2}{2} n^\mu, \tag{5.23}$$

$$\bar{q}^\mu = -\tilde{\xi}' \tilde{p}^\mu - \frac{\bar{q}^2}{2\tilde{\xi}'} n^\mu, \tag{5.24}$$

with $\bar{M}^2 = M^2 - t/4$. The variables $\tilde{\xi}$ and $\tilde{\xi}'$ are related to the invariants ξ and ξ' introduced in Eqs. (5.21,5.22):

$$\tilde{\xi} = \xi \frac{1 + \tilde{\xi}'^2 \bar{M}^2/\bar{q}^2}{1 - \tilde{\xi}'^2 \bar{M}^2/\bar{q}^2}, \tag{5.25}$$

$$\tilde{\xi}' = \xi' \frac{2}{1 + \sqrt{1 - 4\xi'^2 \bar{M}^2/\bar{q}^2}}. \tag{5.26}$$

We notice that the difference between the tilded quantities $\tilde{\xi}, \tilde{\xi}'$ of Eqs. (5.25, 5.26) and the quantities ξ, ξ' of Eqs. (5.21, 5.22) involve kinematical corrections due to the target mass M and momentum tranfer t. In the following, we will consider the Bjorken limit $\bar{q}^2 \gg \bar{M}^2$, in which

$$\tilde{\xi} \to \xi, \qquad \tilde{\xi}' \to \xi'. \tag{5.27}$$

With these kinematic definitions, the double deeply virtual Compton scattering (DDVCS) tensor at leading twist-2 can be expressed as [28]:

$$M^{\mu\nu}_{\text{DDVCS}} = \frac{1}{2}(-g_{\mu\nu})_\perp \int_{-1}^{1} dx \left[\frac{1}{x - \xi' + i\epsilon} + \frac{1}{x + \xi' - i\epsilon} \right]$$

$$\times \left\{ H(x,\xi,t) \not{n} + E(x,\xi,t) i\sigma^{\alpha\beta} n_\alpha \frac{\Delta_\beta}{2M} \right\}$$
$$+ \frac{i}{2} (\varepsilon_{\nu\mu})_\perp \int_{-1}^{1} dx \left[\frac{1}{x-\xi'+i\epsilon} - \frac{1}{x+\xi'-i\epsilon} \right]$$
$$\times \left\{ \tilde{H}(x,\xi,t) \not{n} \gamma_5 + \tilde{E}(x,\xi,t) \gamma_5 \frac{\Delta \cdot n}{2M} \right\}, \tag{5.28}$$

where

$$(-g_{\mu\nu})_\perp = -g_{\mu\nu} + \tilde{p}_\mu n_\nu + \tilde{p}_\nu n_\mu,$$
$$(\varepsilon_{\nu\mu})_\perp = \varepsilon_{\nu\mu\alpha\beta} n^\alpha \tilde{p}^\beta, \tag{5.29}$$

and where the lightlike four-vectors $\tilde{p}$ and n are obtained from Eqs. (5.23,5.24) as:

$$n^\mu = \frac{1}{\tilde{\xi}' \bar{M}^2/2 - \bar{q}^2/(2\tilde{\xi}')} \left\{ \tilde{\xi}' P^\mu + \bar{q}^\mu \right\},$$
$$\tilde{p}^\mu = \frac{-1}{\tilde{\xi}' \bar{M}^2 - \bar{q}^2/\tilde{\xi}'} \left\{ \bar{q}^2/\tilde{\xi}' P^\mu + \bar{M}^2 \bar{q}^\mu \right\}. \tag{5.30}$$

Furthermore in Eq. (5.28), H, E, $\tilde{H}$, and $\tilde{E}$ are the GPDs, which depend on the two quark momentum fractions x and ξ, and on the momentum transfer t.

One can apply the above formula of Eq. (5.28) for the DDVCS tensor to two experimentally important limits. The first is the deeply-virtual Compton scattering (DVCS) process, in which the final photon is real ($q'^2 = 0$), and the intial photon's virtuality is large, i.e. $Q^2 = -q^2 \gg -t$, for which one has:

$$\text{DVCS}: \qquad \xi = \xi' = \frac{x_B/2}{1 - x_B/2}, \tag{5.31}$$

with Bjorken variable $x_B \equiv Q^2/(2p \cdot q)$. The second limit is the timelike Compton scattering (TCS) process with initial photon real ($q^2 = 0$), and large timelike virtuality, i.e. $q'^2 \gg -t$, for which one has:

$$\text{TCS}: \qquad \xi = -\xi' = \frac{q'^2}{4ME_\gamma - q'^2}. \tag{5.32}$$

The TCS amplitude can then be obtained by using the expression for the DDVCS tensor of Eq. (5.28) in the TCS limit in Eq. (5.5).

In the following, we will consider the observables for the TCS process on an unpolarized nucleon at small momentum transfer $-t \ll q'^2$. For these observables, the dominant contribution arises from the structure-function H, which is normalized to the proton Dirac FF $F_D(t)$. When studying the influence of the radiative corrections on the TCS observables at small values of $-t$, we will therefore neglect the contribution of the GPDs E, $\tilde{H}$ and $\tilde{E}$ in our study below. For the numerical evaluation in this work, we will use the GPD parametrizations from the VGG model [150–153], summarized in Ref. [154], in which

$$H(x,\xi,t) = \frac{4}{9} H^u_{\text{DD}}(x,\xi,t) + \frac{1}{9} H^d_{\text{DD}}(x,\xi,t) + D(\frac{x}{\xi}, t). \tag{5.33}$$

The parameterization is based on a double-distribution (DD) ansatz for the (x,ξ)-dependence of the up (down) quark [1] GPDs H^u_{DD} (H^d_{DD}), with parameter values $b_v = 1$

[1] The small s-quark GPD contribution is neglected throughout this work.

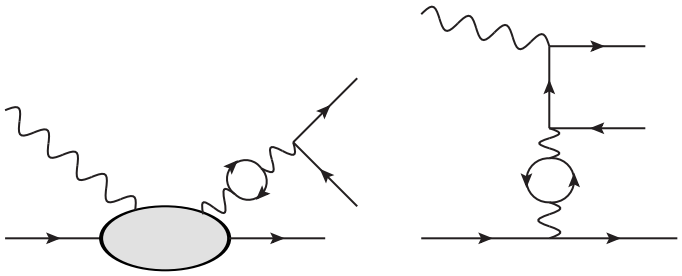

FIGURE 5.3.1: Vacuum polarization contributing to the TCS and BH processes (left and right panels, respectively).

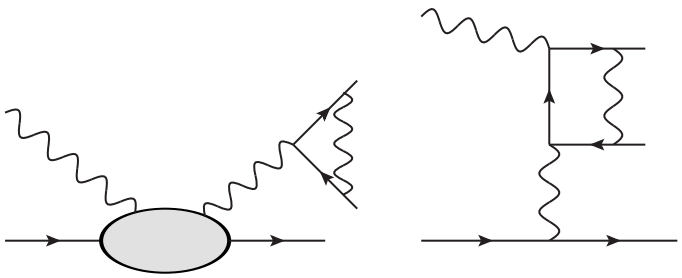

FIGURE 5.3.2: Left panel: vertex correction to the TCS process. Right panel: box diagram contributing to the corrections on the lepton side of the BH process.

($b_s = 5$) for valence (sea) quarks respectively, and on a Reggeized ansatz for the t-distribution, which was found to give a global description of existing DVCS data [155, 156]. Furthermore, we added an isoscalar so-called D-term contribution in Eq. (5.33), which only depends on the two variables x/ξ and t, and which is directly related to the subtraction function in a dispersive framework for the Compton amplitude. For its evaluation, we use the dispersive estimate of Ref. [157].

5.3 Virtual corrections to timelike Compton scattering

In this section, we calculate the one-loop QED corrections contributing to the TCS and the BH processes. We distinguish between three types of contributions: the vacuum polarization diagrams, shown in Fig. 5.3.1, the vertex correction contributing to the TCS process, shown in the left panel of Fig. 5.3.2, and the set of one-loop corrections on the lepton side contributing to the BH process. For the latter we show one sample diagram in the right panel of Fig. 5.3.2.

In the following, we will discuss the calculation of all three types of contributions separately.

5.3.1 Vacuum polarization at first order

We start our discussion of the first-order radiative corrections with the vacuum polarization process, which is shown to first order in Fig. 5.3.3. The photon propagator can be written as:

$$D^{\mu\nu}(q) = D_0^{\mu\nu}(q) + D_0^{\mu\alpha}(q)\Pi_{\alpha\beta}(q)D_0^{\beta\nu}(q), \tag{5.34}$$

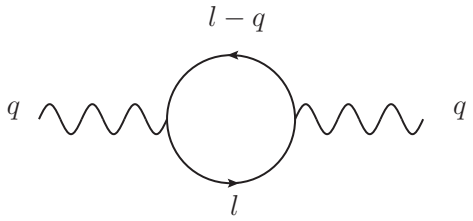

FIGURE 5.3.3: Vacuum polarization diagram. The fermion loop can be either electrons or muons.

where $D_0^{\mu\nu}$ is the leading order photon propagator

$$D_0^{\mu\nu} = \frac{-g^{\mu\nu}}{q^2}, \tag{5.35}$$

and $\Pi_{\alpha\beta}$ is the vacuum polarization, which is given at first order in $\alpha_{\rm em} \equiv e^2/(4\pi)$ by

$$\Pi^{\mu\nu}(q) = -ie^2 \int \frac{d^4l}{(2\pi)^4} \frac{\mathrm{Tr}\left[\gamma^\mu(\not{l}-\not{k}+m_l)\gamma^\nu(\not{l}+m_l)\right]}{[(l-k)^2-m_l^2][l^2-m_l^2]}, \tag{5.36}$$

where m_l is the mass of the lepton in the loop. Due to gauge-invariance, $q_\mu\Pi^{\mu\nu} = q_\nu\Pi^{\mu\nu} = 0$, and the vacuum polarization can be decomposed as

$$\Pi^{\mu\nu}(q) = (-g^{\mu\nu}q^2 + q^\mu q^\nu)\Pi(q^2). \tag{5.37}$$

The scalar function $\Pi(q^2)$ has an UV divergence. In dimensional regularisation, it is given by [158]

$$\Pi(q^2) = -\frac{\alpha_{\rm em}}{3\pi}\left[\frac{1}{\epsilon_{\rm UV}} - \gamma_E + \ln\left(\frac{4\pi\mu^2}{m_l^2}\right) - \left(v^2 - \frac{8}{3}\right) + \frac{v}{2}(v^2-3)\ln\left(\frac{v+1}{v-1}\right)\right], \tag{5.38}$$

where we defined $v^2 \equiv 1 - 4m_l^2/q^2$. In the following we consider muons and electrons in the fermion loop.

The UV-divergence (in limit $\epsilon_{\rm UV} \to 0+$) in Eq. (5.38) is removed by the renormalization constant Z_3 as follows:

$$\tilde{\Pi}(q^2) = \Pi(q^2) - (Z_3 - 1). \tag{5.39}$$

In the on-shell scheme this constant is fixed by requiring that the renormalized vacuum polarization $\tilde{\Pi}(q^2)$ has a pole with residue 1 at $q^2 = 0$,

$$Z_3 = 1 + \Pi(q^2 = 0). \tag{5.40}$$

The renormalized vacuum polarization is then given by

$$\tilde{\Pi}(q^2) = \frac{\alpha_{\rm em}}{3\pi}\left[\left(v^2 - \frac{8}{3}\right) + \frac{v}{2}(3-v^2)\ln\left(\frac{v+1}{v-1}\right)\right], \tag{5.41}$$

and the renormalized photon propagator by

$$\tilde{D}^{\mu\nu}(q) = \frac{-g^{\mu\nu}}{q^2}\left[1 + \tilde{\Pi}(q^2)\right] + \frac{q^\mu q^\nu \tilde{\Pi}(q^2)}{q^4}. \tag{5.42}$$

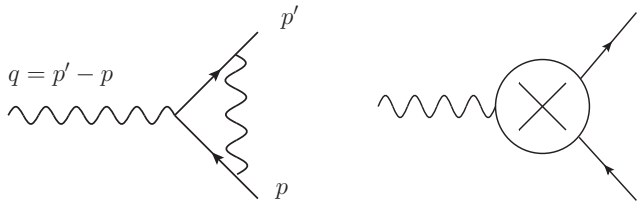

FIGURE 5.3.4: One-loop QED correction to the vertex (left panel) and the counterterm to remove its UV divergence (right panel).

Note that, due to gauge invariance, only the term proportional to $g^{\mu\nu}$ contribute to the BH and TCS amplitudes, such that the corrections factorize:

$$\mathcal{M}^{\text{TCS}}_{\text{vac pol}} = \tilde{\Pi}(s_{ll})\mathcal{M}^{\text{TCS}}, \qquad \mathcal{M}^{\text{BH}}_{\text{vac pol}} = \tilde{\Pi}(t)\mathcal{M}^{\text{BH}}. \tag{5.43}$$

For the evaluation of $\tilde{\Pi}(s_{ll})$, we need to perform an analytic continuation of Eq. (5.41),

$$\tilde{\Pi}(s_{ll}) = \frac{\alpha_{\text{em}}}{3\pi}\left(v^2 - \frac{8}{3}\right) + \frac{\alpha_{\text{em}}}{3\pi}\begin{cases} \frac{\tilde{v}}{2}(v^2-3)\left[2\arctan\tilde{v} - \pi\right] & 0 < s_{ll} < 4m_l \\ \frac{v}{2}(3-v^2)\left[\ln\left(\frac{1+v}{1-v}\right) - i\pi\right] & s_{ll} \geq 4m_l^2, \end{cases} \tag{5.44}$$

where $\tilde{v} \equiv iv = \sqrt{4m_l^2/s_{ll} - 1}$.

5.3.2 Vertex correction to the TCS amplitude

Next, we consider the one-loop QED corrections to the process

$$\gamma^*(q) \to l^+(p) + l^-(p'), \tag{5.45}$$

shown in Fig. 5.3.4.

The corresponding matrix element can be expressed in terms of two form factors, F_D^e and F_P^e, called Dirac and Pauli electron form factors respectively,

$$\Gamma^\mu(q^2) = F_D^e(q^2)\gamma^\mu + iF_P^e(q^2)\sigma^{\mu\nu}\frac{q_\nu}{2m_l}. \tag{5.46}$$

To first order in α_{em}, the Dirac form factor F_D^e is divergent. In dimensional regularisation it can be expressed as [158]

$$\begin{aligned} F_D^e(q^2) = \left(\frac{\alpha_{\text{em}}}{4\pi}\right)\Bigg\{ & \left[\frac{1}{\epsilon_{\text{IR}}} - \gamma_E + \ln\left(\frac{4\pi\mu^2}{m_l^2}\right)\right]\frac{1+v^2}{v}\ln\left(\frac{v+1}{v-1}\right) \\ & + \left[\frac{1}{\epsilon_{\text{UV}}} - \gamma_E + \ln\left(\frac{4\pi\mu^2}{m_l^2}\right)\right] + \frac{v^2+1}{2v}\ln\left(\frac{v+1}{v-1}\right)\ln\left(\frac{v^2-1}{4v^2}\right) \\ & + \frac{2v^2+1}{v}\ln\left(\frac{v+1}{v-1}\right) + \frac{1+v^2}{v}\left[\text{Li}_2\left(\frac{v+1}{2v}\right) - \text{Li}_2\left(\frac{v-1}{2v}\right)\right]\Bigg\}. \end{aligned} \tag{5.47}$$

The Pauli form factor F_P^e is finite and is given by

$$F_P^e(q^2) = -\frac{\alpha_{\text{em}}}{4\pi}\frac{v^2-1}{v}\ln\left(\frac{v-1}{v+1}\right), \tag{5.48}$$

where v is defined in the same way as below Eq. (5.38).

As can be seen from Eq. (5.47), F_D^e has an UV divergence, as well as an IR divergence (in limit $\epsilon_{\text{IR}} \to 0-$). The UV divergence gets removed by the on-shell

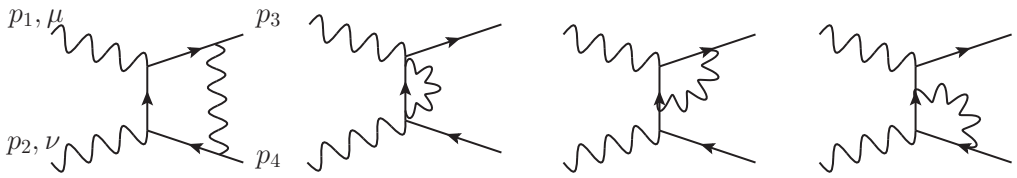

FIGURE 5.3.5: Diagrams contributing to the one loop corrections for the process $\gamma^*(p_1) + \gamma^*(p_2) \to l^-(p_3) + l^+(p_4)$. We don't show the crossed diagrams, which can be obtained by replacing p_3 and p_4.

subtraction scheme, in which the vertex counterterm is defined to fix the electron charge e at $q^2 = 0$. One finds at $q^2 = 0$ the renormalization constant

$$\begin{aligned} Z_1 &= 1 - F_D^e(0) \\ &= 1 - \frac{\alpha_{\rm em}}{4\pi}\left\{\left[\frac{1}{\epsilon_{\rm UV}} - \gamma_E + \ln\left(\frac{4\pi\mu^2}{m_l^2}\right)\right] + 2\left[\frac{1}{\epsilon_{\rm IR}} - \gamma_E + \ln\left(\frac{4\pi\mu^2}{m_l^2}\right)\right] + 4\right\}. \end{aligned} \tag{5.49}$$

This leads to the renormalized (on-shell) form factor

$$\tilde{F}_D^e(q^2) = F_D^e(q^2) - F_D^e(0). \tag{5.50}$$

For the case when the momentum transfer q^2 becomes timelike, i.e. $q^2 > 0$, one has to perform an analytic continuation of both form factors.

To calculate the corrections to the dVCS matrix element, we just have to contract Γ^μ with the dVCS tensor. Adding the vacuum polarization correction of Eq. (5.43), this yields the one-loop radiative correction to the TCS amplitude:

$$\mathcal{M}^{\rm TCS}_{\text{1-loop}} = -\frac{ie^3}{s_{ll}}\bar{N}(p')M^{\mu\nu}N(p)\varepsilon_\mu(q)\bar{u}(l_-)\tilde{\Gamma}_\nu(s_{ll})v(l_+) + \mathcal{M}^{\rm TCS}_{\text{vac pol}}, \tag{5.51}$$

where $\tilde{\Gamma}_\nu$ denotes the renormalized vertex, and where we indicated that the momentum transfer which appears in the Compton tensor is given by t. The remaining IR divergence in Eq. (5.47) will be discussed in Section 5.4.

5.3.3 One-loop corrections to the BH process

In order to calculate the one-loop diagrams contributing to the BH process, we consider corrections to the sub-process

$$\gamma^*(p_1) + \gamma^*(p_2) \to l^-(p_3) + l^+(p_4), \tag{5.52}$$

with two off-shell photons with momenta p_1 and p_2. We show the contributing diagrams in Fig. 5.3.5. We use the standard definition of Mandelstam variables

$$s_{ll} = (p_1 + p_2)^2, \quad t_{ll} = (p_1 - p_3)^2, \tag{5.53}$$

and denote the virtualities of the photons by

$$p_1^2 = t_1, \quad p_2^2 = t_2. \tag{5.54}$$

In order to construct a general tensor basis, we use p_1^μ, p_2^μ, p_3^μ, $g^{\mu\nu}$ and γ^μ as building blocks. In this way, we find 34 independent tensors T_i with two indices to expand

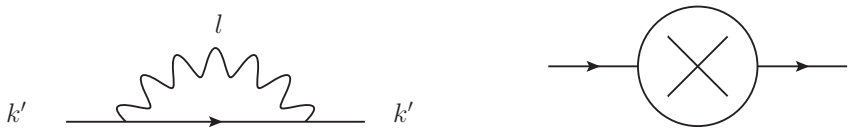

FIGURE 5.3.6: Left panel: Lepton self-energy diagram with $k'^2 = s'$. Right panel: counterterm for fermion self energy

the one-loop amplitude. However, as discussed in Section 5.2.1, we can reduce the number of amplitudes from 34 to 21 amplitudes, which are gauge invariant and free of any kinematic singularities, such that we can write

$$M^{\mu\nu}_{\gamma^*\gamma^*\to l\bar{l}}(p_1^2, p_2^2, s_{ll}, t_{ll}) = \sum_{i=1,..,21} B_i(p_1^2, p_2^2, s_{ll}, t_{ll})\tau_i^{\mu\nu}, \tag{5.55}$$

where the $\tau_i^{\mu\nu}$ denote the tensor basis introduced in Ref. [3] and are shown for completeness in Appendix 5.B, and B_i the corresponding invariant amplitudes. More details how to achieve this decomposition will be given in Section 5.3.3.

Using Eq. (5.55) and adding the contribution from vacuum polarization, the one-loop matrix element corresponding to the BH process with the incoming photon on-shell can be calculated by contracting with the photon polarization vector and the proton line as follows:

$$\mathcal{M}^{\text{BH}}_{\text{1-loop}} = \frac{ie^3}{t}\bar{u}(l_-)M^{\mu\nu}_{\gamma^*\gamma^*\to l\bar{l}}(0, t, s_{ll}, t_{ll})\; v(l_+)\varepsilon_\mu(q)\bar{N}(p')\Gamma_\nu(t)N(p) + \mathcal{M}^{\text{BH}}_{\text{vac pol}}, \tag{5.56}$$

where we now can identify $t_{ll} = (q - l_-)^2$, $t_1 = 0$ and $t_2 = t$.

UV renormalization and counterterms

To subtract UV divergences, we use as before the on-shell renormalization scheme. In addition to the vertex counterterm, that has been calculated in Section 5.3.2, we also need the counterterm from the fermion self-energy, which we show in Fig. 5.3.6 to first order. The corresponding amplitude is given by

$$-i\Sigma(\not{k}') = -e^2\mu^{4-d}\int \frac{d^dl}{(2\pi)^d}\frac{\gamma^\alpha(\not{k}' + \not{l} + m_l)\gamma_\alpha}{((k'+l)^2 - m_l^2)\, l^2}. \tag{5.57}$$

It can be reduced to

$$\begin{aligned}\Sigma(\not{k}') &= \frac{\alpha_{\text{em}}}{4\pi}\left\{\left[\frac{1}{\epsilon_{\text{UV}}} - \gamma_E + \ln(4\pi)\right](4m_l - \not{k}') - \not{k}\left[1 + \frac{m_l^2}{s'} + \frac{m_l^4 - (s')^2}{(s')^2}\ln\left(1 - \frac{s'}{m_l^2}\right)\right]\right. \\ &\quad \left. + 2m_l\left[3 + \frac{2(m_l^2 - s')}{s'}\ln\left(1 - \frac{s'}{m_l^2}\right)\right]\right\},\end{aligned} \tag{5.58}$$

where $s' \equiv (k')^2$. For $\not{k}' = m_l$, we find

$$\Sigma(m_l) = m_l\frac{\alpha_{\text{em}}}{4\pi}\left\{3\left[\frac{1}{\epsilon_{\text{UV}}} - \gamma_E + \ln(4\pi)\right] + 4 - 3\ln\left(\frac{m_l^2}{\mu^2}\right)\right\}. \tag{5.59}$$

The on-shell renormalization condition fixes the pole at $(k')^2 = m_l^2$ with residue equal to one. This gives the wave-function renormalization constant Z_2 and the mass renormalization constant Z_m as follows:

$$Z_2 = 1 + \left.\frac{d\,\Sigma(\not{k}')}{d\not{k}'}\right|_{\not{k}'=m_l}, \tag{5.60}$$

$$(1 - Z_m) Z_2 m_l = \Sigma(m_l). \tag{5.61}$$

The evaluation of $\Sigma(k')$ and its derivative results in the following renormalization constants:

$$\begin{aligned} Z_2 &= 1 - \frac{\alpha_{\text{em}}}{4\pi}\left\{\left[\frac{1}{\epsilon_{\text{UV}}} - \gamma_E + \ln\left(\frac{4\pi\mu^2}{m_l^2}\right)\right] + 2\left[\frac{1}{\epsilon_{\text{IR}}} - \gamma_E + \ln\left(\frac{4\pi\mu^2}{m_l^2}\right)\right] + 4\right\}, \\ Z_2 Z_m &= 1 - \frac{\alpha_{\text{em}}}{4\pi}\left\{4\left[\frac{1}{\epsilon_{\text{UV}}} - \gamma_E + \ln\left(\frac{4\pi\mu^2}{m_l^2}\right)\right] + 2\left[\frac{1}{\epsilon_{\text{IR}}} - \gamma_E + \ln\left(\frac{4\pi\mu^2}{m_l^2}\right)\right] + 8\right\}. \end{aligned} \tag{5.62}$$

The renormalized self-energy is therefore given by

$$\tilde{\Sigma}(k') = \Sigma(k') - (Z_2 - 1)\not{k}' + (Z_2 Z_m - 1) m_l, \tag{5.63}$$

and, plugging in Z_2 and Z_m explicitly, we find

$$\begin{aligned} \tilde{\Sigma}(k') = -\frac{\alpha_{\text{em}}}{4\pi}\Bigg\{ &(\not{k}' - m_l)\left[-2\left[\frac{1}{\epsilon_{\text{IR}}} - \gamma_E + \ln\left(\frac{4\pi\mu^2}{m_l^2}\right)\right]\right. \\ &\left. -3 + \frac{m_l^2}{s'} + \left(\frac{m_l^4}{(s')^2} - 1\right)\ln\left(1 - \frac{s'}{m_l^2}\right)\right] \\ &+ m_l\left[\left(\frac{m_l^2}{s'} - 1\right) + \left(3 + \frac{m_l^4}{(s')^2} - 4\frac{m_l^2}{s'}\right)\ln\left(1 - \frac{s'}{m_l^2}\right)\right]\Bigg\} \\ \equiv\ & (\not{k}' - m_l)\tilde{\Sigma}_1(s') + m_l\tilde{\Sigma}_2(s'). \end{aligned} \tag{5.64}$$

Calculation of the amplitudes

We calculate the one-loop corrections to the process (5.52) using the setup described in Chapter 3. First, we use `QGRAF` to generate all contributing diagrams in a symbolic representation. In `Form`, we implement Feynman rules using Feynman gauge. We use PV tensor reductions to express the amplitude in terms of scalar integrals. Next, we use `Reduze 2` to generate IBP identities which can be applied in `Form`. Using the anti-commutation relation of the Dirac matrices together with the Dirac equation, we are now able to express the amplitude in terms of the aforementioned 34 tensors as a sum over scalar integrals with coefficients that are rational functions in all external scales and the space-time dimension $d = 4 - 2\epsilon$. For the on-shell case, in which $t_1 = 0$, we encounter seven master integrals which are all given in Appendix 5.A

The next step is to reduce the 34 amplitudes to the 21 ones as given in Eq. (5.55). This is achieved in two steps. First, we reduce the 34 tensors to the 18 gauge-invariant ones by inverting the relations between the T_i and the τ_i. This is done by expressing all T_i for $i \in \{2, 3, 6, 7, 9, 10, 12, 13, 15, 16, 18, 19, 20, 21, 22, 24, 28, 30\}$ in terms of τ_i for $i = 1 \ldots, 18$ and the remaining T_i (see also Appendix 5.B). One could now assume that the amplitude would depend not only on these 18 τ_i, but also the remaining T_i. However, gauge invariance requires that the dependence on the remaining T_i drops

out completely. This is indeed the case and establishes a highly non-trivial check on the calculation of the amplitude.

Due to the replacement of the T_i in terms of τ_i, one introduces a spurious singularity at the kinematic point $p_1 \cdot p_2 = (s_{ll} - t_1 - t_2)/2 = 0$, which has its origin in the fact that at this point some τ_i become linearly dependent, as mentioned in Section 5.2. In the second step, we want to get rid of this spurious singularity. As mentioned before, Tarrach gives a recipe for how to achieve that [3]. By introducing three new tensors, namely τ_{19}, τ_{20} and τ_{21}, one can absorb the singularity into the definition of these new tensors. Explicitly, introducing the new tensors results in a shift in the other amplitudes, which displays a singularity at $p_1 \cdot p_2$, as follows:

$$
\begin{aligned}
B_2' &= B_2 + \frac{2(P_{12}\cdot P_{34})^2}{p_1\cdot p_2} B_{19}, & B_3' &= B_3 + 2\frac{t_1 t_2}{p_1\cdot p_2} B_{19},\\
B_4' &= B_4 - P_{12}\cdot P_{34}\frac{t_1+t_2}{p_1\cdot p_2} B_{19}, & B_5' &= B_5 - P_{12}\cdot P_{34}\frac{t_1-t_2}{p_1\cdot p_2},\\
B_{10}' &= B_{10} + \frac{t_1-t_2}{4p_1\cdot p_2} B_{20} + \frac{t_1+t_2}{4p_1\cdot p_2} B_{21}, & B_{14}' &= B_{14} - \frac{t_1-t_2}{2p_1\cdot p_2} B_{20} - \frac{t_1+t_2}{2p_1\cdot p_2} B_{21},\\
B_{15}' &= B_{15} + \frac{P_{12}\cdot P_{34}}{p_1\cdot p_2} B_{20}, & B_{16}' &= B_{16} + \frac{P_{12}\cdot P_{34}}{p_1\cdot p_2} B_{21},
\end{aligned}
\tag{5.65}
$$

where $P_{12} = (p_1 - p_2)/2$ and $P_{34} = (p_3 - p_4)/2$. Note that, in principle, B_{19}, B_{20} and B_{21} can be freely chosen. However, in order to get rid of the spurious singularity, one has to choose the amplitudes B_{19}, B_{20} and B_{21} in such a way, that they cancel the singularity at $p_1 \cdot p_2$ for the eight amplitudes on the lhs of Eq. (5.65). Then the new amplitudes, B_i for $i = 1, \ldots 21$ corresponding to to the decomposition in Eq. (5.55), are free from constraints and singularities.

The next question is therefore, how to choose B_{19}, B_{20} and B_{21}. For that purpose, we find the partial fraction algorithm introduced in Section 4 extremely helpful. Let us clarify this. In total, we find in our calculation due to IBP reductions and due to the reduction to the 18 gauge-invariant tensors, the following set of denominators:

$$
\begin{aligned}
&\{s_{ll} - 2\,s_{ll}\,t_{ll} + s_{ll}^2\,t_{ll} + s_{ll}\,t_{ll}^2 - s_{ll}\,t_1 - s_{ll}\,t\,t_1 + t_1^2 - s_{ll}\,t_2 - s_{ll}\,t\,t_2 - 2\,t_1\,t_2 + s_{ll}\,t_1\,t_2 + t_2^2,\\
&1 - 2\,s_{ll} + s_{ll}^2 - 2\,t_{ll} + 2\,s_{ll}\,t_{ll} + t_{ll}^2 - 4\,t_1 + 2\,t_2 - 2\,s_{ll}\,t_2 - 2\,t\,t_2 + t_2^2,\\
&1 - 2\,s_{ll} + s_{ll}^2 - 2\,t_{ll} + 2\,s_{ll}\,t_{ll} + t_{ll}^2 + 2\,t_1 - 2\,s_{ll}\,t_1 - 2\,t\,t_1 + t_1^2 - 4\,t_2,\\
&2 - s_{ll} - t_{ll} + t_1 + t_2, 1 - s_{ll} - t_{ll} + t_1 + t_2, s_{ll}^2 - 2\,s_{ll}\,t_1 + t_1^2 - 2\,s_{ll}\,t_2 - 2\,t_1\,t_2 + t_2^2,\\
&s_{ll} - t_1 - t_2, 1 - 2\,t_{ll} + t_{ll}^2 - 2\,t_2 - 2\,t\,t_2 + t_2^2, 1 - 2\,t_{ll} + t_{ll}^2 - 2\,t_1 - 2\,t_{ll}\,t_1 + t_1^2,\\
&t_{ll}, -1 + t, s_{ll}, 4 - s_{ll}, t_2, t_1\},
\end{aligned}
\tag{5.66}
$$

where we set $m_l^2 = 1$ and where, as mentioned above, $s_{ll} - t_1 - t_2$ is spurious. Now, choosing a monomial order in which the denominator $s_{ll} - t_1 - t_2$ is "greater" than all other denominators, we achieve a decomposition of the amplitudes B_i' of the form

$$
B_i' = \frac{1}{s_{ll} - t_1 - t_2} X + Y. \tag{5.67}
$$

Comparing with Eq. (5.65), we can then try to choose B_{19}, B_{20} and B_{21} such, that the term X in the above equation gets cancelled. Indeed, in that way we are able to determine B_{19}, B_{20} and B_{21} such that the singularity at $p_1 \cdot p_2$ is cancelled for all eight B_i' appearing in Eq. (5.65). Furthermore, by choosing a monomial ordering in which not only $s_{ll} - t_1 - t_2$ is greater than the other denominators, but also t_1 and t_2, we find an even better representation, which is also free from singularities in the limit $t_{1,2} \to 0$. In conclusion, our result can be applied for real-photon kinematics. Finally, let us note that the partial fractioned result is reduced in size by a factor of

seven on average compared to the factorized form. Some individual amplitudes are even reduced by a factor of 20 to 30.

5.3.4 Soft-photon approximation and IR structure

After performing the on-shell renormalization, the amplitude does not contain any UV divergence anymore but still is IR divergent. We checked that the amplitude has the correct infrared structure, which can be calculated using the soft-photon approximation. This approximation is defined by the scaling of the loop momenta: we only account for the regions of integration where the loop momentum l scales with respect to a small parameter λ (small compared to all external scales and masses) as:

$$l \sim \lambda. \tag{5.68}$$

We then calculate all contributions only up to order λ. The resulting corrections factorize, for TCS and BH amplitude separately, in terms of the corresponding tree-level amplitude. It follows, that the soft-photon approximation is a gauge-invariant subset of the full one-loop corrections. In the present case, only two terms contribute in this limit: for the BH process the two box diagrams and for the TCS process the vertex correction, calculated in Section 5.3.2.

In the soft-photon approximation, the amplitude corresponding to the BH box diagram shown in the right panel of Fig. 5.3.2, is given by

$$\mathcal{M}^{\mathrm{BH}}_{\mathrm{box}} = ie^2 4(l_+ \cdot l_-)\mathcal{M}^{\mathrm{BH}}_0 \mu^{4-d} \int \frac{d^d l}{(2\pi)^d} \frac{1}{[(l-l_-)^2 - m_l^2][(l+l_+)^2 - m_l^2][l^2]} + \mathcal{O}(\lambda). \tag{5.69}$$

A similar identity is valid for the crossed box diagram. Thus, the virtual soft-photon one-loop amplitude for the BH process is given by

$$\mathcal{M}^{\mathrm{BH}}_{\mathrm{soft}} = \frac{-e^2}{4\pi^2}(l_- \cdot l_+) C_0\left(m_l^2, (l_- + l_+)^2, m_l^2; 0, m_l^2, m_l^2\right) \mathcal{M}^{\mathrm{BH}}_0, \tag{5.70}$$

with the three-point function

$$\begin{aligned} C_0\left(m_l^2, s_{ll}, m_l^2, 0, m_l^2, m_l^2\right) = \frac{1}{s_{ll}\beta}\Bigg\{ &\left[\frac{1}{\epsilon_{\mathrm{IR}}} - \ln\left(\frac{m_l^2}{\bar{\mu}^2}\right)\right] \ln\left(\frac{\beta-1}{\beta+1}\right) \\ &+2\,\mathrm{Li}_2\left(\frac{\beta-1}{2\beta}\right) + \ln^2\left(\frac{\beta-1}{2\beta}\right) - \frac{1}{2}\ln^2\left(\frac{\beta-1}{\beta+1}\right) - \frac{\pi^2}{6}\Bigg\}, \end{aligned} \tag{5.71}$$

where $\bar{\mu}^2 = \mu^2 \frac{4\pi}{e^{\gamma_E}}$. Eq. (5.71) is valid in the Euclidean region, i.e. for $s_{ll} < 0$. Note that the same formula applies for the TCS amplitude in the soft-photon limit:

$$\mathcal{M}^{\mathrm{TCS}}_{\mathrm{soft}} = \frac{-e^2}{4\pi^2}(l_- \cdot l_+) C_0\left(m_l^2, (l_- + l_+)^2, m_l^2; 0, m_l^2, m_l^2\right) \mathcal{M}^{\mathrm{TCS}}_0, \tag{5.72}$$

In order to get the full IR structure, we also have to take into account infrared divergences stemming from counterterms. Extracting the IR divergent pieces of the vertex counterterm (Eq. (5.47)) as well as the self-energy counterterm (Eq. (5.64)), we find for the full correction, after performing an analytic continuation of Eq. (5.71) to $s_{ll} > 4m_l^2$, on the level of the cross section

$$d\sigma_{\mathrm{s;v}} = d\sigma_0 \left(\delta^{\mathrm{IR}}_{\mathrm{s;v}} + \delta_{\mathrm{s;v}}\right), \tag{5.73}$$

with the IR divergent part

$$\delta_{\mathrm{s;v}}^{\mathrm{IR}} = \frac{-\alpha_{\mathrm{em}}}{\pi}\left[\left(\frac{1+\beta^2}{2\beta}\right)\ln\left(\frac{1-\beta}{1+\beta}\right)+1\right]\left[\frac{1}{\epsilon_{\mathrm{IR}}}-\gamma_E+\ln\left(\frac{4\pi\mu^2}{m_l^2}\right)\right], \tag{5.74}$$

and the finite part

$$\delta_{\mathrm{s;v}} = \frac{-\alpha_{\mathrm{em}}}{\pi}\left(\frac{1+\beta^2}{2\beta}\right)\left\{2\,\mathrm{Li}_2\left(\frac{2\beta}{\beta+1}\right)+\frac{1}{2}\ln^2\left(\frac{1-\beta}{1+\beta}\right)-\pi^2\right\}. \tag{5.75}$$

5.4 Soft-photon bremsstrahlung

As the virtual corrections are IR divergent, we need to account for soft bremsstrahlung corresponding to diagrams, in which an additional soft photon is emitted from an external fermion line. Denoting the momentum of the fermion line with l and the momentum of the soft photon by k_γ, it corresponds to the amplitude

$$\mathcal{M}_s = \pm e Q_f \frac{\varepsilon^* \cdot l}{k_\gamma \cdot l}\mathcal{M}_0, \tag{5.76}$$

with the $+$ sign, if the fermion is outgoing and the $-$ sign if it is incoming, where Q_f denotes the charge of the lepton, and where $\mathcal{M}_0$ denotes the amplitude without photon emission.

To evaluate the soft bremsstrahlung contribution to the cross section, one has to integrate over the unobserved soft-photon phase space. It is easiest to perform this integral in the reference frame $\mathcal{S}$ where the maximum soft-photon energy ΔE_s is isotropic. The frame $\mathcal{S}$ depends on the specific experimental conditions. It is in general given by the rest frame of the soft photon and the unobserved particle(s) in the process. Without specifying $\mathcal{S}$ for the moment, let us write down the soft-photon phase space integral for this process:

$$d\sigma_{s;r} = -\,d\sigma_0 \frac{e^2}{(2\pi)^3}\int_{|\vec{k}_\gamma|<\Delta E_s}\frac{d^3\vec{k}}{2k_\gamma^0}\left\{\frac{m_l^2}{(k_\gamma\cdot l_+)^2}+\frac{m_l^2}{(k_\gamma\cdot l_-)^2}-\frac{2(l_+\cdot l_-)}{(k_\gamma\cdot l_+)(k_\gamma\cdot l_-)}\right\}, \tag{5.77}$$

where the maximal soft-photon energy ΔE_s depends on the frame and will be specified below. We can easily perform the integration for the first two terms in Eq. (5.77), which yields the expression

$$\begin{aligned} d\sigma_{s;r} = d\sigma_0 \frac{-\alpha_{\mathrm{em}}}{\pi}\Bigg\{&-\left[\frac{1}{\epsilon_{\mathrm{IR}}}-\gamma_E+\ln\left(\frac{4\pi\mu^2}{4(\Delta E_s)^2}\right)\right] \\ &+\frac{1}{2\tilde{\beta}_-}\ln\left(\frac{1-\tilde{\beta}_-}{1+\tilde{\beta}_-}\right)+\frac{1}{2\tilde{\beta}_+}\ln\left(\frac{1-\tilde{\beta}_+}{1+\tilde{\beta}_+}\right)-\frac{1}{2\pi}I_{-+}\Bigg\}, \end{aligned} \tag{5.78}$$

where $\tilde{\beta}_-$, $\tilde{\beta}_+$ are the lepton velocities, defined in the frame $\mathcal{S}$

$$\tilde{\beta}_\mp = \left(1-m_l^2/\tilde{E}_\mp^2\right)^{1/2}, \tag{5.79}$$

where $\tilde{E}_\mp$ are the corresponding lepton energies, which also depend on the system $\mathcal{S}$ in which the soft photon integral is calculated and will be specified below.

Furthermore, in Eq. (5.78) the integral I_{-+} is due to the interference between soft-photon emissions from the l^- and l^+ lines. It has been worked out e.g. in Ref. [159] and is given by

$$\begin{aligned} I_{-+} &\equiv \int_{|\vec{k}_\gamma|<\Delta E_s} \frac{d^3\vec{k}_\gamma}{k_\gamma^0} \frac{l_-\cdot l_+}{(k\cdot l_-)(k\cdot l_+)} \\ &= 4\pi \frac{\eta\, l_-\cdot l_+}{(\eta\, l_-)^2 - l_+^2} \Bigg\{ -\frac{1}{2}\ln\left(\frac{(\eta l_-)^2}{l_+^2}\right)\left[\frac{1}{\epsilon_{\rm IR}} - \gamma_E + \ln\left(\frac{4\pi\mu^2}{4(\Delta E_s)^2}\right)\right] \\ &+ \left[\frac{1}{4}\ln^2\left(\frac{u_0-|\vec{u}|}{u_0+|\vec{u}|}\right) + {\rm Li}_2\left(1-\frac{u_0+|\vec{u}|}{v}\right) + {\rm Li}_2\left(1-\frac{u_0-|\vec{u}|}{v}\right)\right]_{u=l_+}^{u=\eta l_-} \Bigg\}, \end{aligned} \tag{5.80}$$

where

$$\eta \equiv \frac{l_-\cdot l_+}{m_l^2} + \sqrt{\left(\frac{l_-\cdot l_+}{m_l^2}\right)^2 - 1} = \frac{1+\beta}{1-\beta}, \tag{5.81}$$

$$v \equiv \frac{(\eta^2-1)m_l^2}{2\,(\eta l_- - l_+)_0} = \frac{\beta s_{ll}}{2(\tilde{E}_- - \frac{1-\beta}{1+\beta}\tilde{E}_+)}, \tag{5.82}$$

with β given in Eq. (5.7).

In general, we can divide the soft-photon contribution of Eq. (5.78) in an IR divergent piece ($\delta_{\rm s;r}^{\rm IR}$) and a finite piece ($\delta_{\rm s;R}$) as follows:

$$d\sigma_{s;r} = d\sigma_0 \left(\delta_{\rm s;r}^{\rm IR} + \delta_{\rm s;r}\right), \tag{5.83}$$

where the IR divergent piece is given by

$$\delta_{\rm s;r}^{\rm IR} = \left(\frac{-\alpha_{\rm em}}{\pi}\right)\left[\left(\frac{1+\beta^2}{2\beta}\right)\ln\left(\frac{1+\beta}{1-\beta}\right) - 1\right]\left[\frac{1}{\epsilon_{\rm IR}} - \gamma_E + \ln\left(\frac{4\pi\mu^2}{m_l^2}\right)\right], \tag{5.84}$$

and the finite part $\delta_{\rm s;r}$ by

$$\begin{aligned} \delta_{\rm s;r} = \left(\frac{-\alpha_{\rm em}}{\pi}\right) \Bigg\{ &\ln\left(\frac{4(\Delta E_s)^2}{m_l^2}\right)\left[1 - \left(\frac{1+\beta^2}{2\beta}\right)\ln\left(\frac{1+\beta}{1-\beta}\right)\right] + \frac{1}{2\tilde{\beta}_-}\ln\left(\frac{1-\tilde{\beta}_-}{1+\tilde{\beta}_-}\right) \\ &+ \frac{1}{2\tilde{\beta}_+}\ln\left(\frac{1-\tilde{\beta}_+}{1+\tilde{\beta}_+}\right) - \left(\frac{1+\beta^2}{2\beta}\right)\left[\frac{1}{4}\ln^2\left(\frac{1-\tilde{\beta}_-}{1+\tilde{\beta}_-}\right) - \frac{1}{4}\ln^2\left(\frac{1-\tilde{\beta}_+}{1+\tilde{\beta}_+}\right)\right. \\ &+ {\rm Li}_2\left(1-\left(\frac{1+\beta}{1-\beta}\right)\frac{\tilde{E}_-}{v}(1+\tilde{\beta}_-)\right) + {\rm Li}_2\left(1-\left(\frac{1+\beta}{1-\beta}\right)\frac{\tilde{E}_-}{v}(1-\tilde{\beta}_-)\right) \\ &\left. - {\rm Li}_2\left(1-\frac{\tilde{E}_+}{v}(1+\tilde{\beta}_+)\right) - {\rm Li}_2\left(1-\frac{\tilde{E}_+}{v}(1-\tilde{\beta}_+)\right)\right]\Bigg\}. \end{aligned} \tag{5.85}$$

In the ultrarelativistic limit for the leptons, i.e. $\beta \approx 1$, $\tilde{\beta}_\mp \approx 1$, which is a very good approximation for the production of an e^-e^+ pair, the above expression simplifies considerably. Using

$$v \approx s_{ll}/(2\tilde{E}_-), \tag{5.86}$$

we obtain in this limit for the finite part

$$\delta_{\rm s;r} \approx \left(\frac{\alpha_{\rm em}}{\pi}\right)\left\{\ln\left(\frac{(\Delta E_s)^2}{\tilde{E}_-\tilde{E}_+}\right)\left[\ln\left(\frac{s_{ll}}{m_l^2}\right) - 1\right] + \frac{1}{2}\ln^2\left(\frac{s_{ll}}{m_l^2}\right)\right.$$

$$- \frac{1}{2}\ln^2\left(\frac{\tilde{E}_-}{\tilde{E}_+}\right) - \frac{\pi^2}{3} + \mathrm{Li}_2\left(1 - \frac{s_{ll}}{4\tilde{E}_-\tilde{E}_+}\right)\Bigg\}. \tag{5.87}$$

Note that the IR divergent pieces from virtual and real corrections, i.e. Eqs. (5.74) and (5.84), exactly cancel on the level of the cross section, thus giving an IR finte result.

5.4.1 Measurement of the recoil proton

We will now specify the system $\mathcal{S}$, in which we actually performed the integration, and derive expressions for ΔE_s and $\tilde{E}_\pm$, depending on the experimental setup. First, let us consider the case in which the recoil proton is measured and the dilepton pair remains unobserved. In this case the soft-photon integral is performed in the rest frame of the dilepton pair and the soft-photon. In this system, the energies of the dilepton pair are given by

$$\tilde{E}_\pm = \frac{\sqrt{s_{ll}}}{2}, \tag{5.88}$$

such that the soft-photon integral given in Eq. (5.85) simplifies to

$$\delta_{\mathrm{s;r}} = \left(\frac{-\alpha_{\mathrm{em}}}{\pi}\right)\Bigg\{\ln\left(\frac{4\Delta E_s^2}{m_l^2}\right)\left[1 + \left(\frac{1+\beta^2}{2\beta}\right)\ln\left(\frac{1-\beta}{1+\beta}\right)\right] + \frac{1}{\beta}\ln\left(\frac{1-\beta}{1+\beta}\right) + \\ + \left(\frac{1+\beta^2}{2\beta}\right)\left[2\,\mathrm{Li}_2\left(\frac{2\beta}{1+\beta}\right) + \frac{1}{2}\ln^2\left(\frac{1-\beta}{1+\beta}\right)\right]\Bigg\}. \tag{5.89}$$

In order to derive a formula for the soft-photon energy cut-off ΔE_s, we define the missing mass p_m of the system as:

$$p_m^2 = (l_+ + l_- + k_\gamma)^2 = s_{ll} + 2p_m E_s, \tag{5.90}$$

$$E_s = \frac{p_m^2 - s_{ll}}{2p_m}, \tag{5.91}$$

where E_s denotes the soft-photon energy in the rest frame of the dilepton pair and soft photon.

In the case of a proton measurement, the missing mass p_m is experimentally determined from the quantity

$$p_m^2 = (q + p - p')^2 = 4M\tau\left(E_\gamma\sqrt{\frac{1+\tau}{\tau}}\cos\theta_{p'} - E_\gamma - M\right), \tag{5.92}$$

where τ is determined from the lab proton momentum by Eq. (5.10), and $\theta_{p'}$ is the experimentally measured recoil proton scattering angle in the laboratory frame.

For the process without radiation, this angle is given by Eq. (5.12), which can be equivalently obtained from Eq. (5.92) by the replacement $p_m^2 \to s_{ll}$ as follows:

$$s_{ll} = 4M\tau\left(E_\gamma\sqrt{\frac{1+\tau}{\tau}}\cos\theta_{p'}|_{\text{no rad}} - E_\gamma - M\right). \tag{5.93}$$

Combining Eqs. (5.92) and (5.93), we can express the soft-photon energy of Eq. (5.91) approximately as:

$$E_{\mathrm{s}} = \frac{2ME_\gamma\sqrt{\tau(1+\tau)}}{\sqrt{s_{ll}}}\left[\cos\theta_{p'} - \cos\theta_{p'}|_{\text{no rad}}\right]. \tag{5.94}$$

Consequently, the experimental recoiling proton angular resolution, denoted as $\Delta\theta_{p'}$, determines the maximum value ΔE_s of the undetected soft-photon energy, which enters the radiative correction of Eq. (5.89), as:

$$\Delta E_s = \frac{2ME_\gamma\sqrt{\tau(1+\tau)}}{\sqrt{s_{ll}}}\sin\theta_{p'}\,\Delta\theta_{p'}. \tag{5.95}$$

5.4.2 Measurement of the dilepton pair

We will now consider the second case, in which the recoil proton remains unobserved and a measurement of the dilepton pair is performed. For that purpose, it will be convenient to express the lepton energies in terms of the lepton angles θ_l and ϕ_l in the l^-l^+ rest frame as defined in [15]. First, note that the energies of the dilepton pair can be expressed as:

$$\tilde{E}_\mp = \frac{p_m\cdot l_\mp}{\sqrt{p_m^2}} \approx \frac{1}{M}(q+p-q')\cdot l_\mp. \tag{5.96}$$

Eq. (5.96) then allows to express the dilepton energies $\tilde{E}_\mp$ in terms of invariants and the angle θ_l as follows:

$$\tilde{E}_\mp = \frac{1}{4M}\left\{(W^2-M^2-s_{ll}) \pm [(W^2-M^2-s_{ll})^2 - 4M^2 s_{ll}]^{1/2}\beta\cos\theta_l\right\}. \tag{5.97}$$

To evaluate the finite soft-photon cross section corrections of Eq. (5.85) or Eq. (5.87), we need again to express the maximal soft-photon energy ΔE_s, defined in the frame $\vec{p}_m = 0$ in terms of the experimental resolutions using

$$\Delta E_s = \Delta\left(\frac{p_m^2-M^2}{2\sqrt{p_m^2}}\right) \approx \frac{\Delta p_m^2}{2M}, \tag{5.98}$$

where to first order we have used $p_m^2 \approx M^2$ in the denominator, and where Δp_m^2 denotes the resolution in the missing mass squared. For the case of detecting the dilepton pair, the lab energies ($E_\mp$), the scattering angle between the pair (θ_{ll}^{Lab}), and the angle between the incoming photon q and the virtual photon q' ($\theta_{\gamma\gamma}^{Lab}$) are measured. These four parameters are in correspondence with the kinematic quantities s_{ll}, t, θ_l, and ϕ_l introduced in the cross section expression of Eq. (5.6). In the Lab frame, the missing mass squared can be expressed, neglecting the lepton mass in the kinematics, as

$$\begin{aligned} p_m^2 =& (q-q'+p)^2 \\ =& M^2 - 2q\cdot q' + s_{ll} + 2p\cdot(q-q') \\ =& \Big[M^2 + 2ME_\gamma + 2E_-E_+(1-\cos\theta_{ll}) \\ &+ 2E_\gamma|\vec{q}'|\cos\theta_{\gamma\gamma} - 2(E_\gamma+M)(E_+ + E_-)\Big]_{\text{Lab}}. \end{aligned}$$

Accounting for the finite resolutions in the Lab quantities, and adding their contributions quadratically, we can express the maximal soft-photon energy ΔE_s as:

$$\begin{aligned} \Delta E_s =& \frac{1}{M}\Big[\Big(-(E_\gamma+M) + E_+(1-\cos\theta_{ll}) + (E_- + E_+\cos\theta_{ll})\frac{E_\gamma}{|\vec{q}'|}\cos\theta_{\gamma\gamma}\Big)^2(\Delta E_-)^2 \\ &+ \Big(-(E_\gamma+M) + E_-(1-\cos\theta_{ll}) + (E_+ + E_-\cos\theta_{ll})\frac{E_\gamma}{|\vec{q}'|}\cos\theta_{\gamma\gamma}\Big)^2(\Delta E_+)^2 \end{aligned}$$

$$+ E_-^2 E_+^2 (1 - \frac{E_\gamma}{|\vec{q}'|} \cos\theta_{\gamma\gamma})^2 \sin^2\theta_{ll} (\Delta\theta_{ll})^2 + E_\gamma^2 |\vec{q}'|^2 \sin^2\theta_{\gamma\gamma} (\Delta\theta_{\gamma\gamma})^2 \Big]^{1/2}_{\text{Lab}}. \tag{5.99}$$

As is evident from Eq. (5.99), the evaluation of the soft-photon radiative correction depends on the specific experimental resolutions. For the purpose of illustrating the size of these corrections, we will provide predictions below, where the soft-photon cut-off energy ΔE_s is chosen to be in the one to few percent range of the beam energy, as a realistic value. For our predictions in the low-energy region ($E_\gamma \simeq 0.36$ GeV), we will show the corrections for $\Delta E_s = 0.01$ GeV, whereas for the high-energy region ($E_\gamma \simeq 6.8$ GeV), we will show the results for $\Delta E_s = 0.05$ GeV.

5.5 Results and discussion

5.5.1 Observables

We implement all one-loop corrected amplitudes in a `C++` code and use our setup to study the radiative corrections to the $\gamma p \to e^- e^+ p$ process in both, low- and high-energy regimes. For both kinematical situations, we study the effect of these corrections on the cross section, on the forward-backward asymmetry A_{FB}, as well as on the beam spin asymmetry $A_\odot$. These asymmetries are respectively defined as

$$A_{FB} = \frac{d\sigma_{\theta_l,\phi_l} - d\sigma_{\pi-\theta_l,\phi_l+\pi}}{d\sigma_{\theta_l,\phi_l} + d\sigma_{\pi-\theta_l,\phi_l+\pi}}, \tag{5.100}$$

$$A_\odot = \frac{d\sigma^+ - d\sigma^-}{d\sigma^+ + d\sigma^-}, \tag{5.101}$$

where $d\sigma_{\theta_l,\phi_l}$ in A_{FB} stands for the unpolarized cross section measured at lepton angles θ_l and ϕ_l (in the $l^- l^+$ rest frame), and where $d\sigma^\pm$ in $A_\odot$ stand for the polarized cross sections for circular photon polarization ± 1 respectively.

Because of the opposite symmetry of the BH and TCS amplitudes (Fig. 5.1.1) under charge conjugation (odd versus even number of photon couplings to the lepton charge), the asymmetry A_{FB}, which interchanges the kinematics for l^- and l^+, allows for a direct assessment of the interference term between the BH and the real part of the TCS amplitude. The BH and TCS processes separately yield a zero asymmetry. While A_{FB} is proportional to the real part of the BH-TCS interference, $A_\odot$ is proportional to the imaginary part of this interference. Note however, that the complex TCS amplitude by itself also yields a contribution to $A_\odot$, which is usually very small unless the real part of the TCS amplitude becomes comparable in size to the BH amplitude. The observables A_{FB} and $A_\odot$ are thus complementary in accessing the complex TCS amplitude experimentally and in testing theoretical models.

In addition to the two asymmetries, we also use our setup to study the effect of radiative corrections on the ratio R of cross sections of muon- vs electron-pair production. This ratio was studied in Ref. [51] and is defined as

$$R(s_{ll}, s_{ll}^0) \equiv \frac{[\sigma_0(\mu^+\mu^-)]\,(s_{ll}) + [\sigma_0(e^+e^-)](s_{ll})}{[\sigma_0(e^+e^-)](s_{ll}^0)}, \tag{5.102}$$

which depends on the invariant mass of the lepton pair s_{ll}, and a reference point s_{ll}^0 below the di-muon threshold to which the measurement is normalized. Note, that for this observable the cross sections have to be integrated over the lepton angles, since only the recoil proton is measured. For this setup, we neglect the contribution due to the TCS amplitude since we choose a kinematical regime, in which the BH

contribution is dominant. The motivation behind such measurement of cross section ratios is to test lepton universality. As we will see, the ratio R is sensitive to a difference between the coupling of the electron and the muon to the nucleon. Measuring R allows one to test, if the coupling to the nucleon is universal for both lepton flavors or not.

5.5.2 Results for TCS observables in the $\Delta(1232)$ region

We firstly study the importance of the radiative corrections on the $\gamma p \to e^- e^+ p$ observables in the low-energy kinematical region. The $\gamma p \to e^- e^+ p$ process was studied in Ref. [15] in the $\Delta(1232)$ resonance region at small values of s_{ll} and $-t$. In this limit, the TCS amplitude approaches the forward real Compton scattering amplitude, for which a full dispersive calculation based on empirical structure functions exists [160]. It was found in [15] that around $W = 1.25$ GeV the full TCS cross section integrated over the dilepton angles is reproduced by a Born + Δ-pole model for the TCS amplitude, as discussed in Section 5.2.1, within an accuracy of 5% or better. Therefore, we consider the Born + $\Delta(1232)$-pole model to be realistic enough as a model for the TCS amplitude around the $\Delta(1232)$-pole in the near forward direction in order to study the effect of the QED radiative corrections on this reaction. In the following, we will show the effect of the radiative corrections on the $\gamma p \to e^- e^+ p$ cross section, as well as on the two asymmetries A_{FB} and $A_\odot$ for a c.m. energy of $W = 1.25$ GeV.

In the upper-left panel of Fig. 5.5.1, we show the s_{ll} dependence of the unpolarized $\gamma p \to e^- e^+ p$ observables for in-plane dilepton kinematics ($\theta_l = 0^\circ$ and $\phi_l = 0^\circ$) in the $\Delta(1232)$ region and for a small value of $-t$. One notices that the TCS amplitude increases the cross section in this kinematical region by 50% or more, and that the forward-backward asymmetry A_{FB}, which depends linearly on the TCS amplitude reaches values larger than 30%. We see that the first-order QED radiative corrections yield a 5 - 8% correction on the $\gamma p \to e^- e^+ p$ cross section in this kinematical range. However, we also notice that in comparing the complementary forward (δ_F for $\theta_l = \phi_l = 0^\circ$) and backward ($\delta_B$ for $\theta_l = \phi_l = 180^\circ$) kinematics, these correction factors are nearly the same, such that the asymmetry A_{FB} is to good approximation unaffected by the first-order QED radiative corrections. This makes A_{FB} an ideal observable to extract the real part of the TCS amplitude.

Until recently, the only proof-of-principle experiment of the forward-backward asymmetry of the $\gamma p \to e^- e^+ p$ process was conducted by Alvensleben *et al.* at DESY [161]. It was performed at $W \simeq 2.2$ GeV in near-forward kinematics and aimed at an experimental verification of the Kramers-Kronig dispersion relation for the forward Compton amplitude. The Kramers-Kronig relation encompasses a fundamental connection between the photon absorption and scattering based on analyticity and unitarity and allows to evaluate the real part of the forward Compton scattering off protons through a dispersive integral over its imaginary part, which is evaluated using the empirical knowledge of the total photoabsorption cross sections. It was shown in a recent re-analysis of the Kramers-Kronig relation for forward Compton scattering [160], that the present database of the unpolarized photoabsorption cross section is not entirely consistent, and shows the largest discrepancies (in the 5 - 10% range) in the region of the $\Delta(1232)$ peak and in its higher-energy tail region. It was furthermore shown in [160] that these discrepancies in the world database also directly limit the obtained precision of the extracted Baldin sum rule value for the sum of proton electric and magnetic polarizabilities, $\alpha_{E1} + \beta_{M1}$. Being nearly unaffected by the first-order QED radiative corrections, our results show that the forward-backward asymmetry in the resonance region provides a direct measurement of the real part of

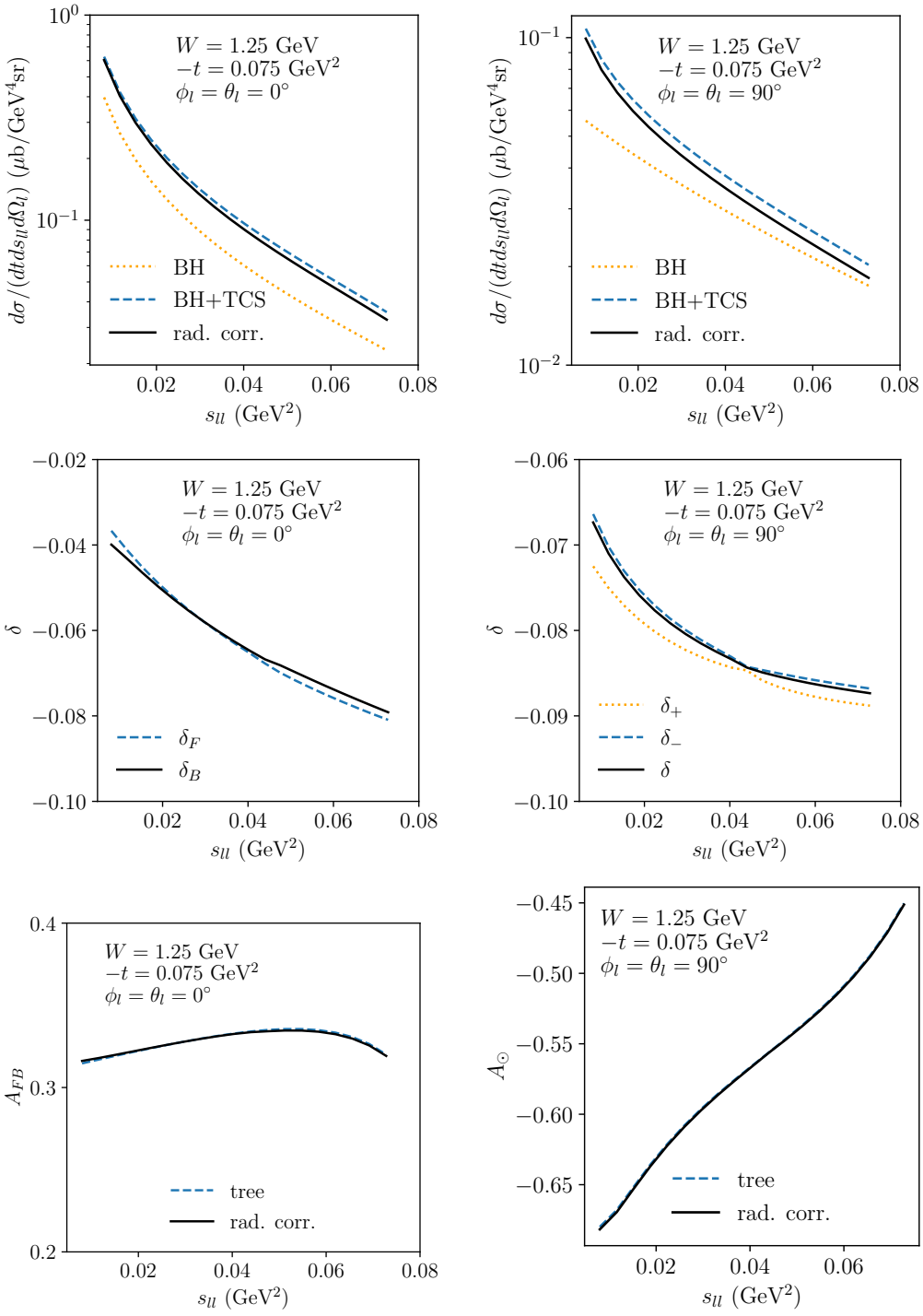

FIGURE 5.5.1: Upper panel: s_{ll}-dependence of the $\gamma p \to e^- e^+ p$ unpolarized cross section for in-plane kinematics (left panel) and out-of-plane kinematics (right panel) of the $e^- e^+$ pair. We show results for BH, BH+TCS, using a Born + $\Delta(1232)$-pole model for TCS, and including first-order QED radiative corrections with a soft-photon energy of $\Delta E_s = 0.01$ GeV. Middle panel: correction factor for forward (δ_F) and backward (δ_B) cross sections for in-plane kinematics (left panel) and $\delta_\pm$ for polarized cross sections for out-of-plane kinematics (right panel). Lower panel: sensitivity of the TCS amplitude on A_{FB} (left panel) and $A_\odot$ (right panel). The radiative correction are negligible on these observables (solid and dashed curves nearly overlapping).

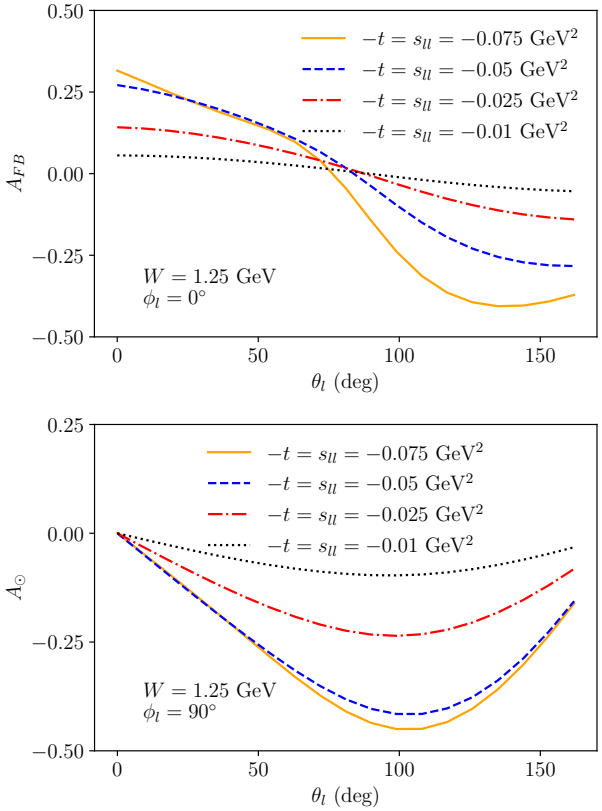

FIGURE 5.5.2: Dependence of the forward-backward asymmetry (upper panel) and photon beam helicity asymmetry (lower panel) on the lepton angle θ_l for different values of s_{ll} and t. The effect of the radiative corrections on both observables is negligibly small.

the near-forward Compton amplitude and thus has the potential to settle the existing discrepancies in the Compton database.

In the right panel of Fig. 5.5.1 we show the corresponding dilepton mass dependence of the $\gamma p \to e^- e^+ p$ observables for a circularly polarized photon beam for out-of-plane dilepton kinematics ($\theta_l = \phi_l = 90°$). As before we see that the first-order QED radiative corrections yield a 7 - 9% correction on the $\gamma p \to e^- e^+ p$ cross section in this kinematical range. The small cusp in the curves of $\delta^\pm$ around $s_{ll} \approx 0.044$ GeV^2 is due to the muon threshold in the vacuum polarization. This gives a contribution with different sign for the cross sections $d\sigma^\pm$. For the corresponding photon helicity asymmetry $A_\odot$, which is directly proportional to the imaginary part of the BH-TCS interference, the first-order QED radiative corrections nearly drop out. For kinematics close to the $\Delta(1232)$-pole position, where the imaginary part of the TCS amplitude is maximal, we find a large value of the asymmetry, varying between -65% and -45%.

In Fig. 5.5.2 we show the dependence of both asymmetries in the $\Delta(1232)$ region on the lepton angle θ_l for fixed out-of-plane angle ϕ_l ($\phi_l = 0°$ for A_{FB} and $\phi_l = 90°$ for $A_\odot$) and different values of t and s_{ll}. We see that increasing the values of $-t$ and s_{ll} results in larger asymmetries due to the larger interference terms. We only show the radiatively corrected results in Fig. 5.5.2, as the difference between the tree-level result and the result including first-order QED radiative corrections is at the few per mille level on these asymmetries.

5.5.3 Results for high-energy TCS observables

In this section, we study the effect of the first-order QED radiative corrections on the cross section, as well as on the forward-backward and beam helicity asymmetries of the $\gamma p \to e^- e^+ p$ process in the high-energy, forward scattering regime in which the dilepton pair is produced with large virtuality. In this regime, a QCD factorization theorem allows modeling the TCS amplitude in terms of GPDs as described in Section 5.2.2. We present here results in the kinematics of a recent CLAS12@JLab experiment [162]. The latter is the first TCS experiment where data have been reported [163, 164] in the kinematical regime corresponding with an average c.m. energy of $W = 3.69$ GeV and a large dilepton invariant mass squared of $s_{ll} = 3.24$ GeV^2.

In the left panel of Fig. 5.5.3, we show the t-dependence of the unpolarized $\gamma p \to e^- e^+ p$ observables for in-plane dilepton kinematics ($\theta_l = 65°$ and $\phi_l = 0°$), corresponding with the CLAS12@JLab experimental conditions. One notices that the cross section and the forward-backward asymmetry show a sizeable sensitivity on the D-term contribution to the GPD parameterization, which contributes to the real part of the TCS amplitude. Comparing the GPD double distribution parameterization (shown by blue dashed curves in upper-left and lower-left panels in Fig. 5.5.3), which was used in a previous global analysis of DVCS data in the valence region [155, 156], we see that adding the dispersive estimate of Ref. [157] for the D-term contribution (dotted red curves) gives a sizeable contribution to the cross section. For the forward-backward asymmetry, which is directly proportional to the real part of the BH-TCS interference, it leads to a shift in the asymmetry by 10 - 20%. We see that the first-order QED radiative corrections yield a nearly 20% correction on the $\gamma p \to e^- e^+ p$ cross section, which is important to account for in the extraction of the Compton form factors. However, we also notice that in comparing the complementary forward and backward kinematics, these correction factors are nearly the same, such that the asymmetry A_{FB} is to good approximation unaffected by the first-order QED radiative corrections. This makes A_{FB} a gold-plated observable to extract the real part of the Compton form factor, and test its sensitivity to the D-term contribution in GPD parameterizations.

In the right panel of Fig. 5.5.3 we show the t-dependence of the $\gamma p \to e^- e^+ p$ observables for a circularly polarized photon beam for out-of-plane dilepton kinematics ($\theta_l = \phi_l = 90°$), corresponding with the CLAS12@JLab experimental conditions. We notice that in out-of-plane kinematics the sensitivity to the D-term in the GPD parameterization is very small, while the radiative correction on the polarized cross sections is also around 20%. In the corresponding photon beam helicity asymmetry $A_\odot$, which is directly proportional to the imaginary part of the BH-TCS interference, the first-order QED radiative corrections again nearly drop out. As the D-term is purely real, its effect on $A_\odot$ is very small and contributes only through the squared modulus of the complex TCS amplitude. The imaginary part of the latter is rather well constrained by the precise electron beam helicity asymmetry data for the corresponding DVCS process [155, 156]. As the non-perturbative part in both processes is the same, a direct comparison between the GPD predictions for DVCS and TCS beam helicity asymmetries at the same values of $-t$ and ξ, provides a stringent test of the applicability of the underlying QCD factorization theorem at these kinematics. Furthermore, as can be seen from the lower panel in Fig. 5.5.1, such test is basically unaffected by the first-order QED radiative corrections.

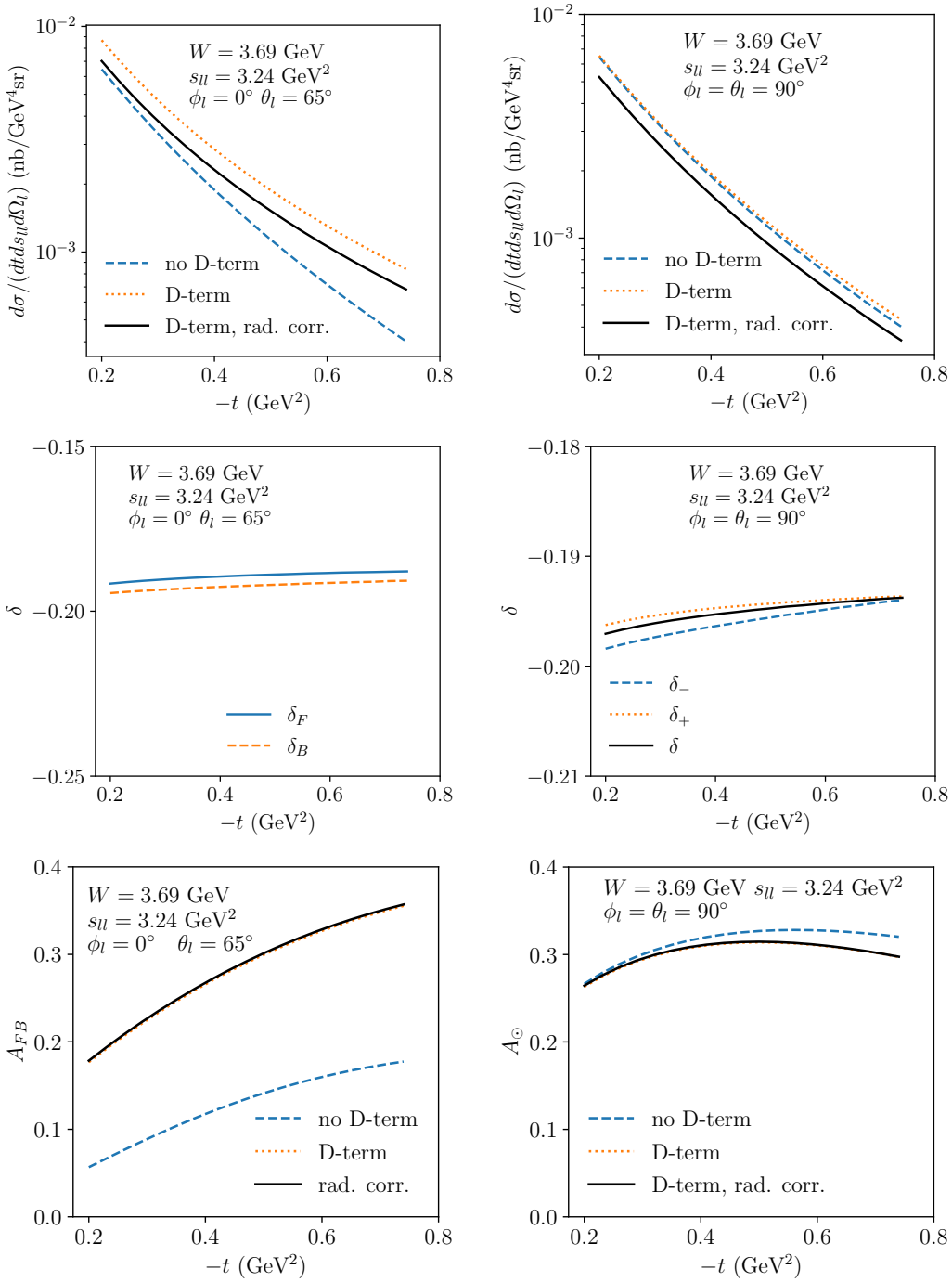

FIGURE 5.5.3: Upper panel: t-dependence of the $\gamma p \to e^- e^+ p$ unpolarized cross section for in-plane (left panel) and out-of-plane (right panel) kinematics of the dilepton pair, corresponding with the CLAS12@JLab experiment [163, 164]. We show our results for two GPD models and including the first-order QED radiative corrections, for a soft-photon energy of $\Delta E_s = 0.05$ GeV. Middle panel: radiative correction factor for forward (δ_F for $\theta_l = 65°$, $\phi_l = 0°$) and backward (δ_B for $\theta_l = 115°$, $\phi_l = 180°$) cross sections for in-plane kinematics (left panel) and correction factors $\delta_\pm$ for circular photon polarization ± 1 for out-of-plane kinematics (right panel). Lower panel: sensitivity of A_{FB} (left panel) and of $A_\odot$ (right panel) on the D-term contribution to the GPD. The radiative correction are negligible on these two observables (solid and dotted curves nearly overlapping).

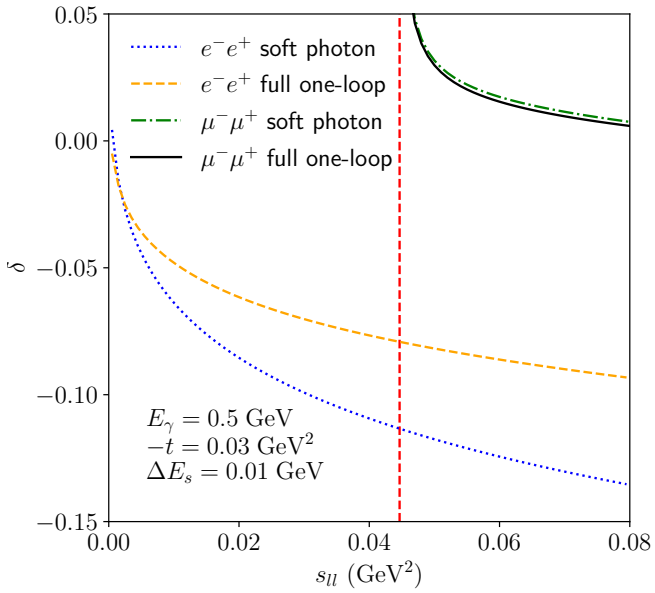

FIGURE 5.5.4: Comparison of first-order QED corrections to the cross section, including soft-photon bremsstrahlung with $\Delta E_s = 0.01$ GeV (solid lines), with the calculation in the soft-photon approximation (dashed lines). The vertical dashed red line indicates the muon-pair production threshold at $s_{ll} \approx 0.045$ GeV^2.

5.5.4 Results for the ratio of e^+e^- vs $\mu^+\mu^-$ production cross sections

In this section, we study the effect of radiative corrections on the ratio R of the electron- vs muon-production cross sections as defined in Eq. (5.102). We choose a kinematic region in which the BH cross section is dominant, such that we can neglect the TCS amplitude [51]. We perform the integration of the unpolarized BH cross section over the lepton angles numerically using `NIntergate` in `Mathematica`.

In Fig. 5.5.4 we show the radiative corrections to the cross section in the kinematical range of s_{ll} between 0 and 0.08 GeV^2 and compare with the result obtained in the soft-photon approximation in Ref. [52]. We indicate the muon threshold at $s_{ll} = 4m_\mu^2 \approx 0.045$ GeV^2 with a vertical dashed red line. We observe, that the corrections for electrons are negative of order 10 percent, while the corrections for muons are positive of order one percent. The difference between the full one-loop calculation and the soft-photon approximation comes from terms that are not proportional to the double logarithmic form $\ln^2(m_l^2/s_{ll})^2$.

In Fig. 5.5.5 we show the effect of the full one-loop radiative corrections on the ratio defined in Eq. (5.102), as well as the effect of taking into account higher-order soft-photon corrections. Those corrections can be incorporated by exponentiation of all double-logarithmic terms that appear in the soft-photon approximation [165]. More concretely, in the case under consideration the unpolarized cross section can be written as:

$$\left(\frac{d\sigma}{dtds_{ll}}\right) = \left(\frac{d\sigma}{dtds_{ll}}\right)_0 \times F\exp\left\{-\frac{\alpha_{\rm em}}{\pi}\left[\ln\left(\frac{4\Delta E_s^2}{m_l^2}\right) + \ln\left(\frac{1-\beta}{1+\beta}\right)\right]\left[1 + \frac{1+\beta^2}{2\beta}\ln\left(\frac{1-\beta}{1+\beta}\right)\right]\right\} \times \left\{1 + \left[\delta_{\text{1-Loop}} + \left(\frac{\alpha_{\rm em}}{\pi}\right)\frac{1+\beta^2}{4\beta}\ln^2\left(\frac{1-\beta}{1+\beta}\right)\right.\right.$$

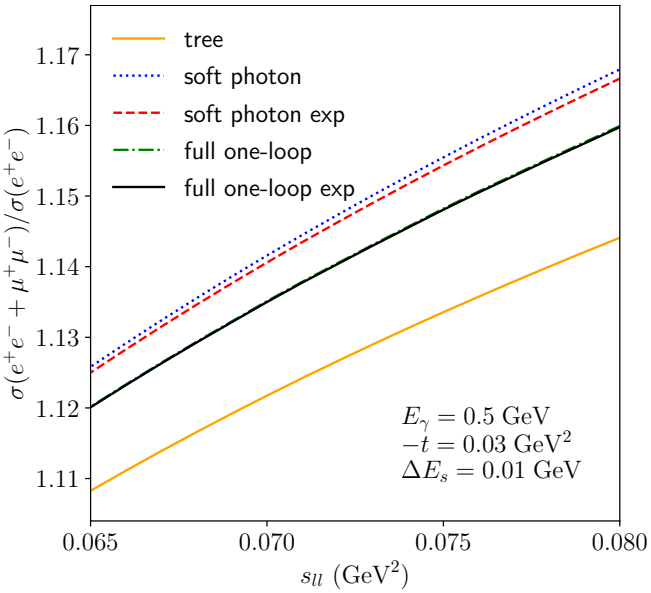

FIGURE 5.5.5: Effect of the one-loop radiative correction on the ratio $(d\sigma(e^+e^-) + d\sigma(\mu^+\mu^-))/d\sigma(e^+e^-)$, comparing with the soft-photon result of Ref. [52].

$$-\frac{\alpha_{\rm em}}{\pi}\left(\frac{1+\beta^2}{\beta}\mathrm{Li}_2\left(\frac{2\beta}{1+\beta}\right)+\frac{1-\beta}{\beta}\ln\left(\frac{1-\beta}{1+\beta}\right)\right)\Bigg]\Bigg\}$$
$$\equiv\left(\frac{d\sigma}{dtds_{ll}}\right)_0(1+\delta_{\rm exp})\,, \tag{5.103}$$

where $\delta_{\text{1-loop}}$ is the finite part of the one-loop virtual corrections and $\delta_{\rm exp}$ denotes the full, exponentiated correction. The normalization factor F arises due to the physical assumption that in an experiment the sum of all soft-photon energies is smaller than ΔE_s instead of requiring that each soft-photon energy is individually smaller than ΔE_s. Its leading correction from unity is given by [165]

$$F = 1 - \frac{\alpha^2}{3}\left[1+\left(\frac{1+\beta^2}{2\beta}\right)\ln\left(\frac{1-\beta}{1+\beta}\right)\right]^2 + ... \tag{5.104}$$

Taking radiative corrections into account, the ratio of Eq. (5.102) is now given by

$$R(s_{ll}, s_{ll}^0) \equiv \frac{\left[\sigma_0(\mu^+\mu^-)(1+\delta^\mu)\right](s_{ll}) + \left[\sigma_0(e^+e^-)(1+\delta^e)\right](s_{ll})}{\left[\sigma_0(e^+e^-)(1+\delta^e)\right](s_{ll}^0)}, \tag{5.105}$$

which depends on the measured invariant lepton mass s_{ll} and the reference point s_{ll}^0, to which the cross section is normalized. Taking into account exponentiation of soft photon corrections, δ^e and δ^μ are given by Eq. (5.103). One chooses $s_{ll}^0 < 4m_\mu^2$, such that the reference measurement is below the muon-pair-production threshold, and only electron pairs are created. As can be seen in Fig. 5.5.5, the exponentiation has a considerably smaller effect on the full one-loop calculation, than on the soft-photon approximation. Furthermore, the soft-photon approximation clearly overestimates the effect of radiative corrections in this calculation.

In Fig. 5.5.6 we show the differential cross section ratio R of Eq. (5.102), including full one-loop QED corrections (including the exponentiation of soft photon corrections) with $\Delta E_s = 0.01$ GeV. The radiative corrections to R are of the order of 1%. The red curve in Fig. 5.5.6 shows the scenario when lepton universality is

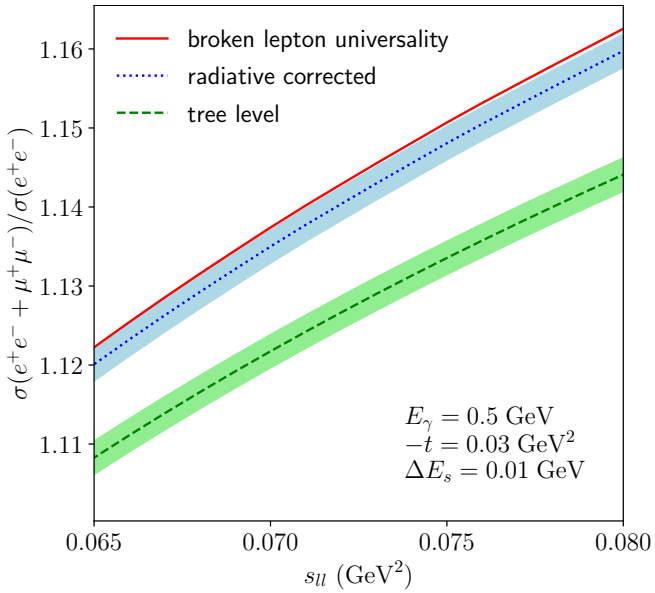

FIGURE 5.5.6: Ratio of cross sections between electron- and muon-pair production at tree level (dotted blue curve) with account of full one-loop QED corrections estimated using $\Delta E_s = 0.01$ GeV (green curve) with corresponding 3σ error bands. The dashed red curve denotes the scenario when lepton universality is broken with $G_E^\mu / G_E^e = 1.01$, including the one-loop radiative corrections.

violated by $G_E^\mu / G_E^e = 1.01$, which is an effect of order 0.2%. Following Ref. [51], we use 3σ bands around the curves, with the experimental resolution $\sigma = 7 \times 10^{-4}$. One sees from this plot, that the inclusion of radiative corrections is indispensable, since the ratio of cross sections, defined in Eq. (5.102), is shifted to higher values by more than the 3σ band. The statement that lepton universality can be tested with a 3σ confidence level remains true, if one adds radiative corrections as can be seen in Fig. 5.5.6.

5.6 Conclusions

In this chapter, we presented the first-order QED corrections on the lepton side contributing to the timelike Compton scattering process on a proton corresponding to the reaction $\gamma p \to l^- l^+ p$. This reaction contains contributions from both the BH amplitude, for which the dependence on the proton structure is parameterized through its spacelike elastic form factors, and from the TCS amplitude with initial real photon and final timelike photon. We calculated the first-order radiative corrections on the level of the amplitude, such that the individual sub-processes can be easily incorporated into different calculations. We studied the effect of radiative corrections in two different energy regimes. In the $\Delta(1232)$ resonance region the TCS amplitude was modeled as the sum of Born and $\Delta(1232)$-pole contributions, which was found to give a very good description of the near-forward kinematical regime. In the high-energy, near-forward regime we calculated the TCS amplitude in terms of GPDs, in the kinematics of a recent CLAS12@JLab experiment.

In the kinematics near the $\Delta(1232)$-resonance position, we found that the first-order QED radiative corrections on the $\gamma p \to e^- e^+ p$ cross section are in the 5 - 10% range, while in the high-energy kinematics of the CLAS12@JLab experiment, they

are in the 20% range. Their inclusion is thus important to extract the low-energy constants or Compton form factors from the $\gamma p \to e^- e^+ p$ process.

Besides the corrections on the unpolarized cross section, we also studied in both kinematical regimes the effect of the first-order radiative corrections on the forward-backward asymmetry A_{FB}, obtained by interchanging the kinematics of the produced dileptons, as well as on the photon beam helicity asymmetry $A_\odot$. While the asymmetry A_{FB} accesses the real part of the BH-TCS interference, the asymmetry $A_\odot$ accesses the imaginary part of the BH-TCS interference in the regime where the BH amplitude dominates. The asymmetries A_{FB} and $A_\odot$ are thus complementary in accessing experimentally the complex TCS amplitude.

We found that in both kinematical regimes the radiative corrections on these asymmetries are at the few per mille level only, although the radiative corrections on the $\gamma p \to e^- e^+ p$ cross sections are in the 10 - 20% range. The reason for the near cancellation of radiative corrections is that the corrections on the forward and backward cross sections as well as on both beam helicity cross sections are of the same size, and thus nearly cancel out in the corresponding ratios. This makes the A_{FB} and $A_\odot$ gold-plated observables to extract the real and imaginary parts of the TCS amplitude respectively.

In the $\Delta(1232)$ region, we find a value around +30% for the forward-backward asymmetry, which provides a good opportunity for a direct measurement of the real part of the near-forward Compton amplitude. This will also allow for a comparison with existing dispersive extractions, in which the real part of the forward Compton amplitude has been obtained as a dispersive integral over its imaginary part. At present, the latter extraction is limited in precision due to discrepancies in the world database for photoabsorption on a proton, especially in the $\Delta(1232)$ region, which also directly limits the obtained precision of the extracted Baldin sum rule value for the sum of proton electric and magnetic polarizabilities, $\alpha_{E1} + \beta_{M1}$.

In the kinematical regime of the CLAS12@JLab experiment, the measurement of both asymmetries A_{FB} and $A_\odot$ will allow to extract the Compton form factors from the TCS amplitude and compare them to the corresponding DVCS process with a spacelike initial photon and final real photon. As the non-perturbative part in both processes is the same, a direct comparison between the GPD predictions for DVCS and TCS observables provides a stringent test of the applicability of the underlying QCD factorization theorem at these kinematics. In particular, the forward-backward asymmetry is a very sensitive observable to extract the D-term contribution to the GPD parameterization, as it only contributes to the real part of the TCS amplitude. We found that a dispersive estimate of the D-term contribution leads to a shift in A_{FB} by 10 - 20%. The latter sensitivity will be interesting to test by the CLAS12@JLab TCS experiment (for first results see Ref. [26]) and is complementary to the information one extracts from the DVCS process when comparing cross sections for both electron and positron beams.

Additionally, we studied the first-order QED corrections to the ratio of dilepton production cross sections above and below $\mu^+\mu^-$ threshold for the Bethe-Heitler process. This ratio shows a sensitivity of 0.2%, when the difference between the larger proton charge radius extracted from the MAMI electron scattering from 2001 is used versus the smaller proton radius which results from the muonic hydrogen spectroscopy. Since the full one-loop radiative effects induce a correction around 1% on this same ratio, its inclusion is indispensable in this comparison.

In the next chapter, we will generalize our radiatively corrected calculations to the double virtual Compton scattering, in which the incoming photon has non-zero

spacelike virtuality while the outgoing photon has non-zero timelike virtuality, accessed through the $e^- p \to e^- p l^- l^+$ reaction. In the $\Delta(1232)$ region, it was shown that this process allows for an empirical determination of the remaining unknown low-energy structure constant entering the hadronic correction to the muonic hydrogen Lamb shift [15]. In the high-energy near-forward region, double deeply virtual Compton scattering allows extending the DVCS beam helicity asymmetry measurements of GPDs into the ERBL domain [28, 29]. Since in the present chapter we calculated all sub-parts of the amplitudes for off-shell particles, it will be straightforward to generalize our setup to the double virtual Compton observables.

Appendix

5.A Master integrals

In this appendix, we list analytic results for all scalar master integrals, which are needed for the calculation. The integrals $A_0(m_l^2)$ and $B_0\left(s_{ll}, m_l^2, m_l^2\right)$ are needed up to order ϵ, since they get multiplied by a factor proportional to $\frac{1}{\epsilon}$ from IBP identities. All other integrals are needed only up to order ϵ^0. All integrals, except for $C_0(t_{ll}, t, m_l^2, 0, m_l^2, m_l^2)$, can be found at http://qcdloop.fnal.gov/. General expressions for three-point functions can be found in Ref. [166].

We give the analytical results in the physical region, in which

$$s_{ll} > 4m_l^2, \quad t < 0, \quad t_{ll} < 0, \tag{5.106}$$

in terms of real-valued logarithms and dilogarithms for this region. We use the kinematical quantities

$$\beta_x = \sqrt{1 - \frac{4m_l^2}{x}}, \tag{5.107}$$

$$\lambda = \sqrt{-2t_{ll}\left(m_l^2 + t\right) + t_{ll}^2 + \left(m_l^2 - t\right)^2}. \tag{5.108}$$

In the following, we use the notation $\bar{\mu}^2 = \mu^2 \frac{4\pi}{e^{\gamma_E}}$ with $\epsilon = 2 - d/2$. To get the integral appearing in a calculation with the usual prefactor $1/(2\pi)^d$, one has to multiply our results by the factor $i/(4\pi)^2$.

The tadpole up to order ϵ is given by:

$$A_0\left(m_l^2\right) = m_l^2 \left\{ \frac{1}{\epsilon} + \left[1 - \ln\left(\frac{m_l^2}{\bar{\mu}^2}\right)\right] + \left[1 + \frac{\pi^2}{12} - \ln\left(\frac{m_l^2}{\bar{\mu}^2}\right) + \frac{1}{2}\ln^2\left(\frac{m_l^2}{\bar{\mu}^2}\right)\right]\epsilon \right\}. \tag{5.109}$$

The two-point function are given by:

$$B_0\left(t_{ll}, 0, m_l^2\right) = \frac{1}{\epsilon} + 2 - \ln\left(\frac{m_l^2}{\bar{\mu}^2}\right) + \frac{t_{ll} - m_l^2}{t_{ll}} \ln\left(\frac{m_l^2}{m_l^2 - t_{ll}}\right), \tag{5.110}$$

$$\begin{aligned} B_0\left(s_{ll}, m_l^2, m_l^2\right) = {} & \frac{1}{\epsilon} + \left\{ 2 - \ln\left(\frac{m_l^2}{\bar{\mu}^2}\right) + \beta_{s_{ll}} \left[i\pi - \ln\left(\frac{1+\beta_{s_{ll}}}{1-\beta_{s_{ll}}}\right)\right]\right\} \\ & + \epsilon \left\{ 4 + \frac{\pi^2}{12} - 2\ln\left(\frac{m_l^2}{\bar{\mu}^2}\right) + \frac{1}{2}\ln^2\left(\frac{m_l^2}{\bar{\mu}^2}\right) + \beta_{s_{ll}} \left[-\frac{2}{3}\pi^2 + \ln^2\left(\frac{1-\beta_{s_{ll}}}{2\beta_{s_{ll}}}\right)\right.\right. \\ & \left. + \ln\left(\frac{m_l^2}{\bar{\mu}^2}\right)\ln\left(\frac{1+\beta_{s_{ll}}}{1-\beta_{s_{ll}}}\right) - \frac{1}{2}\ln^2\left(\frac{1+\beta_{s_{ll}}}{1-\beta_{s_{ll}}}\right) - 2\ln\left(\frac{1+\beta_{s_{ll}}}{1-\beta_{s_{ll}}}\right) + 2\mathrm{Li}_2\left(\frac{\beta_{s_{ll}}-1}{2\beta_{s_{ll}}}\right)\right] \\ & \left. + i\pi\beta_{s_{ll}} \left[2 - \ln\left(\frac{m_l^2}{\bar{\mu}^2}\right) - \ln\left(\frac{1-\beta_{s_{ll}}}{1+\beta_{s_{ll}}}\right) + 2\ln\left(\frac{1-\beta_{s_{ll}}}{2\beta_{s_{ll}}}\right)\right]\right\}, \end{aligned} \tag{5.111}$$

$$B_0\left(t, m_l^2, m_l^2\right) = \frac{1}{\epsilon} + \left\{ 2 - \ln\left(\frac{m_l^2}{\bar{\mu}^2}\right) + \beta_t \ln\left(\frac{\beta_t - 1}{\beta_t + 1}\right)\right\}. \tag{5.112}$$

The three-point functions are given by:

$$C_0(t, s_{ll}, 0, m_l^2, m_l^2, m_l^2) = \frac{1}{2}\frac{1}{s_{ll}-t}\left\{\left[i\pi + \ln\left(\frac{1-\beta_{s_{ll}}}{1+\beta_{s_{ll}}}\right)\right]^2 + \ln^2\left(\frac{\beta_t - 1}{\beta_t + 1}\right)\right\}, \tag{5.113}$$

$$C_0(0, m_l^2, t_{ll}, m_l^2, m_l^2, 0) = \frac{-1}{m_l^2 - t_{ll}}\left\{\frac{\pi^2}{6} - \mathrm{Li}_2\left(\frac{t_{ll}}{m_l^2}\right)\right\}, \tag{5.114}$$

$$\begin{aligned}
C_0(t_{ll}, t, m_l^2, 0, m_l^2, m_l^2) \quad &= \frac{1}{\lambda}\left\{\frac{1}{2}\ln^2\left(\frac{-t_{ll}}{m_l^2 - t - t_{ll} + \lambda}\right) + \ln^2\left(\frac{-t_{ll}}{m_l^2 - t + t_{ll} + \lambda}\right)\right. \\
&-\frac{1}{2}\ln^2\left(\frac{-t_{ll}}{-m_l^2 + t - t_{ll} + \lambda}\right) - \frac{1}{2}\ln^2\left(\frac{m_l^2 - t - t_{ll} + \lambda}{m_l^2 - t + t_{ll} + \lambda}\right) \\
&-\ln\left(\frac{m_l^2 - t_{ll}}{m_l^2}\right)\ln\left(\frac{-m_l^2 + t - t_{ll} + \lambda}{m_l^2 - t + t_{ll} + \lambda}\right) \\
&+\ln(2)\ln\left(\frac{2\, t_{ll}^2\,(-m_l^2 + t - t_{ll} + \lambda)}{(m_l^2 - t + t_{ll} + \lambda)^2(m_l^2 - t - t_{ll} + \lambda)}\right) \\
&-\frac{1}{2}\ln^2\left(\frac{-m_l^2 t_{ll} - t t_{ll}\beta_t + t t_{ll} + m_l^4 + \lambda m_l^2 - m_l^2 t}{-t_{ll}\,(2m_l^2 + t\beta_t - t)}\right) \\
&-\frac{1}{2}\ln^2\left(\frac{-m_l^2 t_{ll} + t t_{ll}\beta_t + t t_{ll} + m_l^4 + \lambda m_l^2 - m_l^2 t}{-t_{ll}\,(2m_l^2 - t\beta_t - t)}\right) + \mathrm{Li}_2\left(\frac{m_l^2 - t + \lambda + t_{ll}}{2t_{ll}}\right) \\
&+\mathrm{Li}_2\left(\frac{-m_l^2 + t + \lambda + t_{ll}}{2t_{ll}}\right) - \mathrm{Li}_2\left(\frac{t_{ll}\,(2m_l^2 - t - t\beta_t)}{-m_l^4 + t m_l^2 - \lambda m_l^2 + t_{ll} m_l^2 - t t_{ll} - t t_{ll}\beta_t}\right) \\
&-\mathrm{Li}_2\left(\frac{-m_l^4 + t m_l^2 + \lambda m_l^2 + t_{ll} m_l^2 - t t_{ll} - t t_{ll}\beta_t}{t_{ll}\,(2m_l^2 - t - t\beta_t)}\right) \\
&-\mathrm{Li}_2\left(\frac{t_{ll}\,(2m_l^2 - t + t\beta_t)}{-m_l^4 + t m_l^2 - \lambda m_l^2 + t_{ll} m_l^2 - t t_{ll} + t t_{ll}\beta_t}\right) \\
&\left.-\mathrm{Li}_2\left(\frac{-m_l^4 + t m_l^2 + \lambda m_l^2 + t_{ll} m_l^2 - t t_{ll} + t t_{ll}\beta_t}{t_{ll}\,(2m_l^2 - t + t\beta_t)}\right)\right\}.
\end{aligned} \tag{5.115}$$

We also need the following four-point function:

$$\begin{aligned}
D_0(m_l^2, 0, t, m_l^2, t_{ll}, s_{ll}, 0, m_l^2, m_l^2, m_l^2) &= \frac{1}{s_{ll}\beta_{s_{ll}}(t_{ll} - m_l^2)}\left\{\frac{1}{\epsilon}\left[i\pi + \ln\left(\frac{1-\beta_{s_{ll}}}{1+\beta_{s_{ll}}}\right)\right]\right. \\
&-\frac{7}{6}\pi^2 - 2\ln\left(\frac{m_l^2 - t_{ll}}{m_l^2}\right)\left[i\pi + \ln\left(\frac{1-\beta_{s_{ll}}}{1+\beta_{s_{ll}}}\right)\right] - 2\ln\left(\frac{4\beta_{s_{ll}}}{(1+\beta_{s_{ll}})^2}\right)\left[i\pi + \ln\left(\frac{1-\beta_{s_{ll}}}{1+\beta_{s_{ll}}}\right)\right] \\
&-\ln\left(\frac{m_l^2}{\bar{\mu}^2}\right)\left[i\pi + \ln\left(\frac{1-\beta_{s_{ll}}}{1+\beta_{s_{ll}}}\right)\right] + \ln^2\left(\frac{2\,(\beta_t - \beta_{s_{ll}})}{(\beta_t - 1)\,(1+\beta_{s_{ll}})}\right) - \ln^2\left(\frac{\beta_t - 1}{\beta_t + 1}\right) \\
&+2\ln\left(\frac{2\,(\beta_t - \beta_{s_{ll}})}{(\beta_t - 1)\,(1+\beta_{s_{ll}})}\right)\left[-\ln\left(\frac{(\beta_t + 1)\,(1-\beta_{s_{ll}})}{(\beta_t - 1)\,(1+\beta_{s_{ll}})}\right) + \ln\left(\frac{\beta_t + 1}{\beta_t - 1}\right) + i\pi\right] \\
&+2\ln\left(\frac{1-\beta_{s_{ll}}}{1+\beta_{s_{ll}}}\right)\left[\ln\left(\frac{2\,(\beta_t - \beta_{s_{ll}})}{(\beta_t - 1)\,(\beta_{s_{ll}} + 1)}\right) + \ln\left(\frac{2\,(\beta_{s_{ll}} + \beta_t)}{(\beta_t + 1)\,(1+\beta_{s_{ll}})}\right)\right] + 2\ln\left(\frac{\beta_t - 1}{\beta_t + 1}\right) \\
&\times\ln\left(\frac{2\,(\beta_{s_{ll}} + \beta_t)}{(\beta_t + 1)\,(\beta_{s_{ll}} + 1)}\right) - 2\ln\left(\frac{2\,(\beta_{s_{ll}} + \beta_t)}{(\beta_t + 1)\,(\beta_{s_{ll}} + 1)}\right)\left[\ln\left(\frac{(\beta_t - 1)\,(1-\beta_{s_{ll}})}{(\beta_t + 1)\,(1+\beta_{s_{ll}})}\right) - i\pi\right] \\
&+\ln^2\left(\frac{2\,(\beta_{s_{ll}} + \beta_t)}{(\beta_t + 1)\,(1+\beta_{s_{ll}})}\right) - \mathrm{Li}_2\left(\frac{(1-\beta_{s_{ll}})^2}{(1+\beta_{s_{ll}})^2}\right) + 2\mathrm{Li}_2\left(\frac{(\beta_t - 1)\,(\beta_{s_{ll}} + 1)}{2\,(\beta_t - \beta_{s_{ll}})}\right)
\end{aligned}$$

$$+2\mathrm{Li}_2\left(\frac{(\beta_t+1)(\beta_{s_{ll}}+1)}{2(\beta_t+\beta_{s_{ll}})}\right)\Bigg\}. \tag{5.116}$$

In the expansion for small m_l^2, keeping only terms proportional to $\ln(m_l^2)$, all integrals simplify considerably. The two-point functions are given by:

$$B_0(t_{ll},0,m_l^2) = \frac{1}{\epsilon}+2-\ln\left(\frac{-t_{ll}}{m_l^2}\right)-\ln\left(\frac{m_l^2}{\bar{\mu}^2}\right), \tag{5.117}$$

$$\begin{aligned} B_0(s_{ll},m_l^2,m_l^2) = {}& \frac{1}{\epsilon}+\left[2+i\pi-\ln\left(\frac{s_{ll}}{\bar{\mu}^2}\right)\right] \\ & +\epsilon\left[(-2-i\pi)\ln\left(\frac{s_{ll}}{\bar{\mu}^2}\right)+\frac{1}{2}\ln^2\left(\frac{s_{ll}}{\bar{\mu}^2}\right)+4+2i\pi-\frac{7\pi^2}{12}\right]. \end{aligned} \tag{5.118}$$

The three-point functions are given by:

$$C_0(0,t,s_{ll},m_l^2,m_l^2,m_l^2) = \frac{1}{2(t-s_{ll})}\left[\pi^2+2i\pi\ln\frac{s_{ll}}{m_l^2}-\ln^2\frac{s_{ll}}{m_l^2}+\ln^2\frac{-t}{m_l^2}\right], \tag{5.119}$$

$$C_0(0,m_l^2,t_{ll},m_l^2,m_l^2,0) = \frac{1}{t_{ll}}\left[\frac{\pi^2}{3}+\frac{1}{2}\ln^2\frac{-t_{ll}}{m_l^2}\right], \tag{5.120}$$

$$C_0(t,m_l^2,t_{ll},m_l^2,m_l^2,0) = \frac{1}{2(t-t_{ll})}\left[\ln^2\frac{-t}{m_l^2}-\ln^2\frac{-t_{ll}}{m_l^2}-4\mathrm{Li}_2\left(\frac{t_{ll}-t}{t_{ll}}\right)\right]. \tag{5.121}$$

The four-point function for small lepton mass is given by:

$$\begin{aligned} D_0(m_l^2,0,t,t_{ll},s_{ll},0,m_l^2,m_l^2,m_l^2) = {}& \frac{1}{\epsilon}\frac{1}{s_{ll}t_{ll}}\left[i\pi-\ln\left(\frac{s_{ll}}{m_l^2}\right)\right] \\ & +\frac{1}{s_{ll}t_{ll}}\Bigg\{\ln\left(\frac{s_{ll}}{m_l^2}\right)\left[-2\ln\left(\frac{s_{ll}-t}{s_{ll}}\right)+2\ln\left(-\frac{t_{ll}}{s_{ll}}\right)+\ln\left(\frac{m_l^2}{\bar{\mu}^2}\right)-2i\pi\right] \\ & +\ln\left(\frac{s_{ll}-t}{s_{ll}}\right)\left[-2\ln\left(-\frac{t}{s_{ll}}\right)+2\ln\left(-\frac{t}{m_l^2}\right)+2i\pi\right] \\ & +2\ln^2\left(\frac{s_{ll}}{m_l^2}\right)+2\mathrm{Li}_2\left(\frac{s_{ll}}{s_{ll}-t}\right)+\ln^2\left(\frac{s_{ll}-t}{s_{ll}}\right)-2i\pi\ln\left(-\frac{t_{ll}}{s_{ll}}\right) \\ & -i\pi\ln\left(\frac{m_l^2}{\bar{\mu}^2}\right)-\ln^2\left(-\frac{t}{m_l^2}\right)-\frac{5\pi^2}{6}\Bigg\} \end{aligned} \tag{5.122}$$

5.B Tensor basis for the dVCS amplitude

In this appendix, we give the explicit tensors needed to calculated all helicity amplitudes contributing to the doubly virtual Compton scattering process. Note, that the same tensor structure also applies to the four-point helicity amplitude of the process

$$\gamma(p_1)+\gamma(p_2)\to l^-(p_3)+l^+(p_4) \tag{5.123}$$

considered Section 5.3.3, by exchanging

$$q\to p_1,\quad q'\to -p_2,\quad k\to -p_3,\quad k'\to p_4. \tag{5.124}$$

In the following, we consider the dVCS process as defined in Eq. (5.13). Forming tensors with two open indices from the building blocks, $g^{\mu\nu}$, q^μ, q'^μ and p^μ, one finds 34 different Lorentz structures:

$$T_1 = g^{\mu\nu}, \qquad T_2 = q^\mu q'^\nu,$$

$$
\begin{aligned}
T_3 &= q'^{\mu} q^{\nu}, & T_4 &= q^{\mu} q^{\nu} + q'^{\mu} q'^{\nu},\\
T_5 &= q^{\mu} q^{\nu} - q'^{\mu} q'^{\nu}, & T_6 &= P^{\mu} P^{\nu},\\
T_7 &= P^{\mu} q^{\nu} + P^{\nu} q'^{\mu}, & T_8 &= P^{\mu} q^{\nu} - P^{\nu} q'^{\mu},\\
T_9 &= P^{\mu} q'^{\nu} + P^{\nu} q^{\mu}, & T_{10} &= P^{\mu} q'^{\nu} - P^{\nu} q^{\mu},\\
T_{11} &= g^{\mu\nu} \not{q}, & T_{12} &= q^{\mu} q'^{\nu} \not{q},\\
T_{13} &= q'^{\mu} q^{\nu} \not{q}, & T_{14} &= \left(q^{\mu} q^{\nu} + q'^{\mu} q'^{\nu}\right) \not{q},\\
T_{15} &= \left(q^{\mu} q^{\nu} - q'^{\mu} q'^{\nu}\right) \not{q}, & T_{16} &= P^{\mu} P^{\nu} \not{q},\\
T_{17} &= \left(P^{\mu} q^{\nu} + P^{\nu} q'^{\mu}\right) \not{q}, & T_{18} &= \left(P^{\mu} q^{\nu} - P^{\nu} q'^{\mu}\right) \not{q},\\
T_{19} &= \left(P^{\mu} q'^{\nu} + P^{\nu} q^{\mu}\right) \not{q}, & T_{20} &= \left(P^{\mu} q'^{\nu} - P^{\nu} q^{\mu}\right) \not{q},\\
T_{21} &= P^{\mu} \gamma^{\nu} + P^{\nu} \gamma^{\mu}, & T_{22} &= P^{\mu} \gamma^{\nu} - P^{\nu} \gamma^{\mu},\\
T_{23} &= q^{\mu} \gamma^{\nu} + q'^{\nu} \gamma^{\mu}, & T_{24} &= q^{\mu} \gamma^{\nu} - q'^{\nu} \gamma^{\mu},\\
T_{25} &= q'^{\mu} \gamma^{\nu} + q^{\nu} \gamma^{\mu}, & T_{26} &= q'^{\mu} \gamma^{\nu} - q^{\nu} \gamma^{\mu},\\
T_{27} &= \left(P^{\mu} \gamma^{\nu} + P^{\nu} \gamma^{\mu}\right) \not{q} - \not{q} \left(P^{\mu} \gamma^{\nu} + P^{\nu} \gamma^{\mu}\right),\\
T_{28} &= \left(P^{\mu} \gamma^{\nu} - P^{\nu} \gamma^{\mu}\right) \not{q} - \not{q} \left(P^{\mu} \gamma^{\nu} - P^{\nu} \gamma^{\mu}\right),\\
T_{29} &= \left(q^{\mu} \gamma^{\nu} + q'^{\nu} \gamma^{\mu}\right) \not{q} - \not{q} \left(q^{\mu} \gamma^{\nu} + q'^{\nu} \gamma^{\mu}\right),\\
T_{30} &= \left(q^{\mu} \gamma^{\nu} - q'^{\nu} \gamma^{\mu}\right) \not{q} - \not{q} \left(q^{\mu} \gamma^{\nu} - q'^{\nu} \gamma^{\mu}\right),\\
T_{31} &= \left(q'^{\mu} \gamma^{\nu} + q^{\nu} \gamma^{\mu}\right) \not{q} - \not{q} \left(q'^{\mu} \gamma^{\nu} + q^{\nu} \gamma^{\mu}\right),\\
T_{32} &= \left(q'^{\mu} \gamma^{\nu} - q^{\nu} \gamma^{\mu}\right) \not{q} - \not{q} \left(q'^{\mu} \gamma^{\nu} - q^{\nu} \gamma^{\mu}\right),\\
T_{33} &= \gamma^{\mu} \gamma^{\nu} - \gamma^{\nu} \gamma^{\mu},\\
T_{34} &= \left(\gamma^{\mu} \gamma^{\nu} - \gamma^{\nu} \gamma^{\mu}\right) \not{q} + \not{q} \left(\gamma^{\mu} \gamma^{\nu} - \gamma^{\nu} \gamma^{\mu}\right).
\end{aligned}
\tag{5.125}
$$

In order to define gauge invariant amplitudes, one needs to take linear combinations from the tensor structures, such that the contraction with the photon momenta q^{ν} or $(q')^{\mu}$ yields zero. One finds 21 such structures given by [3]:

$$
\begin{aligned}
\tau_1 &= q \cdot q' \, T_1 - T_3,\\
\tau_2 &= (q \cdot q) \, (q' \cdot q') \, T_1 + q \cdot q' \, T_2 - \frac{1}{2} (q \cdot q + q' \cdot q') \, T_4 + \frac{1}{2} (q \cdot q - q' \cdot q') \, T_5,\\
\tau_3 &= (P \cdot \bar{q})^2 \, T_1 + q \cdot q' \, T_6 - P \cdot \bar{q} \, T_7,\\
\tau_4 &= P \cdot \bar{q} (q \cdot q + q' \cdot q') \, T_1 - P \cdot \bar{q} \, T_4 - \frac{q \cdot q + q' \cdot q'}{2} \, T_7 + \frac{q \cdot q - q' \cdot q'}{2} \, T_8 + q \cdot q' \, T_9,\\
\tau_5 &= - P \cdot \bar{q} (q \cdot q - q' \cdot q') \, T_1 + P \cdot \bar{q} \, T_5 + \frac{q \cdot q - q' \cdot q'}{2} \, T_7 - \frac{q \cdot q + q' \cdot q'}{2} \, T_8 + q \cdot q' \, T_{10},\\
\tau_6 &= P \cdot \bar{q} \, T_2 - \frac{q \cdot q + q' \cdot q'}{4} \, T_9 - \frac{q \cdot q - q' \cdot q'}{4} \, T_{10} - M \, T_{12} + M \frac{q \cdot q + q' \cdot q'}{4} \, T_{23}\\
&\quad - M \frac{q \cdot q - q' \cdot q'}{4} \, T_{24} + \frac{q \cdot q - q' \cdot q'}{8} \, T_{29} - \frac{q \cdot q + q' \cdot q'}{8} \, T_{30} - \frac{q \cdot q q' \cdot q'}{4} \, T_{33},\\
\tau_7 &= 8 \, T_{16} - 4 P \cdot \bar{q} \, T_{21} + P \cdot \bar{q} \, T_{34},\\
\tau_8 &= T_{19} + \frac{q \cdot q - q' \cdot q'}{2} \, T_{22} - P \cdot \bar{q} \, T_{23} + \frac{q \cdot q + q' \cdot q'}{8} \, T_{34},\\
\tau_9 &= T_{20} - \frac{q \cdot q + q' \cdot q'}{2} \, T_{22} + P \cdot \bar{q} \, T_{24} - \frac{q \cdot q - q' \cdot q'}{8} \, T_{34},\\
\tau_{10} &= - 8 q \cdot q' \, T_6 + 4 P \cdot \bar{q} \, T_7 + 4 M q \cdot q' \, T_{21} - 4 M P \cdot \bar{q} \, T_{25} - 2 P \cdot \bar{q} \, T_{32}\\
&\quad - 2 q \cdot q' P \cdot \bar{q} \, T_{33} + M q \cdot q' \, T_{34},\\
\tau_{11} &= T_{18} - q \cdot q' \, T_{22} + P \cdot \bar{q} \, T_{26},\\
\tau_{12} &= P \cdot \bar{q} \, T_4 - \frac{q \cdot q - q' \cdot q'}{2} \, T_8 - q \cdot q' \, T_9 - M \, T_{14} + M q \cdot q' \, T_{23} - M \frac{q \cdot q - q' \cdot q'}{2} \, T_{26}\\
&\quad - \frac{q \cdot q + q' \cdot q'}{4} \, T_{32} - q \cdot q' \frac{q \cdot q + q' \cdot q'}{4} \, T_{33},
\end{aligned}
$$

$$\begin{aligned}
\tau_{13} =&P\cdot\bar{q}\,T_5 - \frac{q\cdot q - q'\cdot q'}{2}\,T_8 + q\cdot q'\,T_{10} - M\,T_{15} + Mq\cdot q'\,T_{24} - M\frac{q\cdot q + q'\cdot q'}{2}\,T_{26}\\
&- \frac{q\cdot q - q'\cdot q'}{4}\,T_{32} - q\cdot q'\frac{q\cdot q - q'\cdot q'}{4}\,T_{33},\\
\tau_{14} =&2P\cdot\bar{q}\,T_8 - 2Mq\cdot q'\,T_{22} + 2MP\cdot\bar{q}\,T_{26} - q\cdot q'\,T_{27} + P\cdot\bar{q}\,T_{31},\\
\tau_{15} =&-(q\cdot q - q'\cdot q')\,T_7 + (q\cdot q + q'\cdot q')\,T_8 - 2q\cdot q'\,T_{10} - 2Mq\cdot q'\,T_{24} + M(q\cdot q - q'\cdot q')\,T_{25}\\
&+ M(q\cdot q + q'\cdot q')\,T_{26} - q\cdot q'\,T_{29} + \frac{q\cdot q + q'\cdot q'}{2}\,T_{31} + \frac{q\cdot q - q'\cdot q'}{2}\,T_{32},\\
\tau_{16} =&-(q\cdot q + q'\cdot q')\,T_7 + (q\cdot q - q'\cdot q')\,T_8 + 2q\cdot q'\,T_9 - 2Mq\cdot q'\,T_{23} + M(q\cdot q + q'\cdot q')\,T_{25}\\
&+ M(q\cdot q - q'\cdot q')\,T_{26} - q\cdot q'\,T_{30} + \frac{q\cdot q - q'\cdot q'}{2}\,T_{31} + \frac{q\cdot q + q'\cdot q'}{2}\,T_{32},\\
\tau_{17} =&-4P\cdot\bar{q}\,T_1 + 2\,T_7 + 4M\,T_{11} - 2M\,T_{25} + T_{32} + q\cdot q'\,T_{33},\\
\tau_{18} =&4\,T_{17} - 4P\cdot\bar{q}\,T_{25} + q\cdot q'\,T_{34},\\
\tau_{19} =&\frac{1}{q\cdot q'}(2(P\cdot\bar{q})^2\tau_2 + 2(q\cdot q)(q'\cdot q')\tau_3 - P\cdot\bar{q}(q\cdot q + q'\cdot q')\tau_4 - P\cdot\bar{q}(q\cdot q - q'\cdot q')\tau_5),\\
\tau_{20} =&\frac{1}{4q\cdot q'}((q\cdot q - q'\cdot q')\tau_{10} - 2(q\cdot q + q'\cdot q')\tau_{14} + 4P\cdot\bar{q}\tau_{15}),\\
\tau_{21} =&\frac{1}{4q\cdot q'}((q\cdot q + q'\cdot q')\tau_{10} - 2(q\cdot q - q'\cdot q')\tau_{14} + 4P\cdot\bar{q}\tau_{16}).
\end{aligned}$$

5.C Compton Tensor in Born+Δ approximation

In this appendix, we give the amplitudes contributing to the dVCS tensor in Born+Δ approximation for the low-energy model. In the Born approximation only ten different tensor structures contribute to the Compton tensor which are given by

$$\begin{aligned}
B_1 =&\frac{1}{M}\frac{1}{(q\cdot q')^2 - 4P\cdot\bar{q}}\Big[q\cdot q'\Big(F_D(q\cdot q)F_P(q'\cdot q') + F_D(q'\cdot q')F_P(q\cdot q)\\
&+ F_P(q\cdot q)F_P(q'\cdot q')\Big) + \frac{1}{M^2}(P\cdot\bar{q})^2F_P(q\cdot q)F_P(q'\cdot q')\Big],\\
B_3 =&\frac{4}{M}\frac{1}{(q\cdot q')^2 - 4P\cdot\bar{q}}\Big[F_D(q\cdot q)F_D(q'\cdot q') - \frac{1}{4M^2}q\cdot q'F_P(q\cdot q)F_P(q'\cdot q')\Big],\\
B_6 =&\frac{P\cdot\bar{q}}{M^3}\frac{1}{(q\cdot q')^2 - 4P\cdot\bar{q}}F_P(q\cdot q)F_P(q'\cdot q'),\\
B_7 =&-\frac{P\cdot\bar{q}}{2M^2}\frac{1}{(q\cdot q')^2 - 4P\cdot\bar{q}}F_P(q\cdot q)F_P(q'\cdot q'),\\
B_8 =&\frac{1}{2M^2}\frac{1}{(q\cdot q')^2 - 4P\cdot\bar{q}}\Big[q\cdot q'\Big(F_D(q\cdot q)F_P(q'\cdot q') + F_D(q'\cdot q')F_P(q\cdot q)\\
&+ 2F_P(q\cdot q)F_P(q'\cdot q')\Big) + \frac{2}{M^2}(P\cdot\bar{q})^2F_P(q\cdot q)F_P(q'\cdot q')\Big],\\
B_{10} =&\frac{1}{4M}\frac{1}{(q\cdot q')^2 - 4P\cdot\bar{q}}\Big[2F_D(q\cdot q)F_D(q'\cdot q') + F_D(q\cdot q)F_P(q'\cdot q')\\
&+ F_D(q'\cdot q')F_P(q\cdot q) + \frac{t}{4M^2}F_P(q\cdot q)F_P(q'\cdot q')\Big],\\
B_{14} =&\frac{1}{2M}\frac{1}{(q\cdot q')^2 - 4P\cdot\bar{q}}\Big[F_D(q'\cdot q')F_P(q\cdot q) - F_D(q\cdot q)F_P(q'\cdot q')\\
&- \frac{q\cdot q - q'\cdot q'}{4M^2}F_P(q\cdot q)F_P(q'\cdot q')\Big],
\end{aligned}$$

$$
\begin{aligned}
B_{17} =& \frac{P\cdot\bar{q}}{M}\frac{1}{(q\cdot q')^2-4P\cdot\bar{q}}\Big[F_D(q\cdot q)+F_P(q\cdot q))(F_D(q'\cdot q')+F_P(q'\cdot q')\Big],\\
B_{18} =& \frac{1}{8M^2}\frac{1}{(q\cdot q')^2-4P\cdot\bar{q}}\Big[-q\cdot q'\Big(F_D(q\cdot q)F_P(q'\cdot q')+F_D(q'\cdot q')F_P(q\cdot q)\Big)\\
&-\frac{2}{M^2}(P\cdot\bar{q})^2F_P(q\cdot q)F_P(q'\cdot q')\Big],\\
B_{21} =& -\frac{q\cdot q'}{4M^3}\frac{1}{(q\cdot q')^2-4P\cdot\bar{q}}F_P(q\cdot q)F_P(q'\cdot q'). \qquad (5.126)
\end{aligned}
$$

Although we implement the full amplitude for the $\Delta(1323)$ resonance, we only present the dominant contribution, given by the part that is proportional to the magnetic dipole form factor G_M^*. Pulling out a global prefactor, we decompose the dominant contribution of $\mathcal{M}_\Delta^{\mu\nu}$ as follows:

$$
\mathcal{M}_\Delta^{\mu\nu} = -\frac{3}{2}\frac{(M_\Delta+M)^2}{M^2Q_+^4}\frac{G_M^*(q^2)G_M^*(q'^2)}{W^2-M_\Delta^2+iM_\Delta\Gamma_\Delta(W^2)}\sum_{i=1}^{21}B_iT_i^{\mu\nu}, \qquad (5.127)
$$

The amplitudes are given by

$$
\begin{aligned}
B_1 =& \frac{1}{96M}\Big[16M^3M_\Delta-12M^2(q^2+q'^2)+24M^2W^2+8M^2t_\Delta+12M^4-8MM_\Delta(q^2+q'^2)\\
&+48MW^2M_\Delta-8Mt_\Delta M_\Delta-20W^2(q^2+q'^2)+3(q^2+q'^2)^2+28W^4+8W^2t_\Delta-3t_\Delta^2\Big],\\
B_2 =& \frac{1}{12M}\Big[-4MM_\Delta+q'^2+q^2-2W^2-t_\Delta\Big],\\
B_3 =& \frac{1}{12M}\Big[-4M^2-8MM_\Delta+3(q^2+q'^2)-4W^2-3t_\Delta\Big],\\
B_4 =& \frac{1}{24M}\Big[-4M^2-12MM_\Delta+4(q^2+q'^2)-8W^2-3t_\Delta\Big],\\
B_5 =& \frac{1}{24M}\Big[q^2-q'^2\Big],\\
B_6 =& \frac{1}{12M}\Big[8M^2+8W^2-3t_\Delta\Big],\\
B_7 =& \frac{1}{48M}\Big[-2M^2-4MM_\Delta-3(q^2+q'^2)-2W^2+3t_\Delta\Big],\\
B_8 =& \frac{1}{96M^2}\Big[-32M^3M_\Delta-28M^2(q^2+q'^2)-8M^2W^2+44M^2t_\Delta-52M^4+4Mt_\Delta M_\Delta\\
&-20W^2(q^2+q'^2)+3(q^2+q'^2)^2+28W^4+8W^2t_\Delta-3t_\Delta^2\Big],\\
B_9 =& 0,\\
B_{10} =& \frac{1}{96M}\Big[8M^2+4MM_\Delta+q'^2+3q^2-4W^2-3t_\Delta\Big],\\
B_{11} =& -\frac{1}{4M}\Big[q^2-q'^2\Big],\\
B_{12} =& \frac{1}{24M}\Big[8M^2-8W^2-3t_\Delta\Big],\\
B_{13} =& \frac{1}{8M}\Big[q^2-q'^2\Big],\\
B_{14} =& -\frac{1}{24M}q'^2,
\end{aligned}
$$

$$
\begin{aligned}
B_{15} &= \frac{1}{96M}\Big[-2M^2 - 5q'^2 + 3q^2 + 2W^2 + t_\Delta\Big],\\
B_{16} &= -\frac{1}{48M}\Big[4M^2 + 8W^2 - t_\Delta\Big],\\
B_{17} &= -\frac{1}{24M}\Big[M^4 - 2M^3 M_\Delta - M^2(q^2+q'^2) - 6M^2W^2 + MM_\Delta(q^2+q'^2)\\
&\qquad - 2MW^2M_\Delta - W^2(q^2+q'^2) + q^2q'^2 + W^4 + 3W^2t_\Delta\Big]\\
B_{18} &= -\frac{1}{384M}\Big[28M^4 - 4M^2(q^2+q'^2) - 56M^2W^2 - 4M^2t_\Delta + 4Mt_\Delta M_\Delta\\
&\qquad - 20W^2(q^2+q'^2) + 3(q'^2+q^2)^2 + 28W^4 + 8W^2t_\Delta - 3t_\Delta^2\Big],\\
B_{19} &= -\frac{1}{12M},\\
B_{20} &= \frac{t_\Delta - 2q'^2}{48M},\\
B_{21} &= \frac{4M^2 - 4MM_\Delta - t_\Delta}{48M},
\end{aligned}
\tag{5.128}
$$

where we defined $t_\Delta = (q-q')^2$.

6 Soft-photon corrections to the $e^-p \to e^-pl^-l^+$ process

This chapter is based on Ref. [16], in which we extended the calculation from the TCS process to the dVCS process on a proton. More specifically, we calculate the amplitudes contributing to the process $e^-p \to l^+l^-p$, where $l^- = \mu^-$ or $l^- = e^-$. We distinguish between three different contributions, the spacelike and timelike Bethe-Heitler process, and the aforementioned dVCS process. As described in Section 1.2.1, this most general case of a double-virtual Compton process can be useful to access the so-far unknown low-energy constant, which appears in the leading hadronic corrections to the muonic Hydrogen Lamb shift and hyperfine splitting. In this chapter, we will study the sensitivity on this low-energy constant using the same low-energy model for the Compton tensor as in the TCS case. Furthermore, we study the dVCS tensor also in a high-energy regime, again using GPDs, and show the sensitivity of the $e^-p \to l^+l^-p$ process on their parameterization. In both models, we calculate cross sections, as well as forward-backward and beam spin asymmetries. To provide a first estimate of the size of radiative corrections to these observables, we will use the soft-photon approximation. We distinguish between three different, gauge-invariant types of corrections, from which one contributes also to the VCS case, a second one contributes to the TCS case, both of which are obtained as limits of our present work, and a third type of correction, which is new for the double-virtual case. We study the size of these corrections on the level of unpolarized cross sections as well as on the forward-backward and beam spin asymmetries.

The outline of the present chapter is as follows. In Section 6.1, we introduce the relevant Feynman diagrams at tree level. In Section 6.2, we introduce the models we used to calculate the dVCS tensor. Since those have been presented already in the previous chapter, we will comment only on the additions we implemented going from the TCS to the dVCS case. In Section 6.3, we calculate the virtual radiative corrections in the soft-photon approximation from the three gauge-invariant types of contributions. We give analytic expressions for the finite as well as for the IR divergent parts of all three contributions in terms of a factorizing contribution on the level of cross section. In Section 6.4, we calculate the contribution to the cross sections due to soft-photon bremsstrahlung. Taking real radiation into account, we cross-check analytically the cancellation with the IR divergences from the virtual corrections. In Section 6.5, we show our results for the observables in both the low-energy and high-energy kinematical regimes. We conclude in Section 6.6. Technical details are discussed in two appendices.

6.1 Dilepton electroproduction at tree level

In this chapter, we study the dilepton electroproduction process

$$e^-(k) + N(p) \to e^-(k') + N(p') + l^-(l_-) + l^+(l_+), \tag{6.1}$$

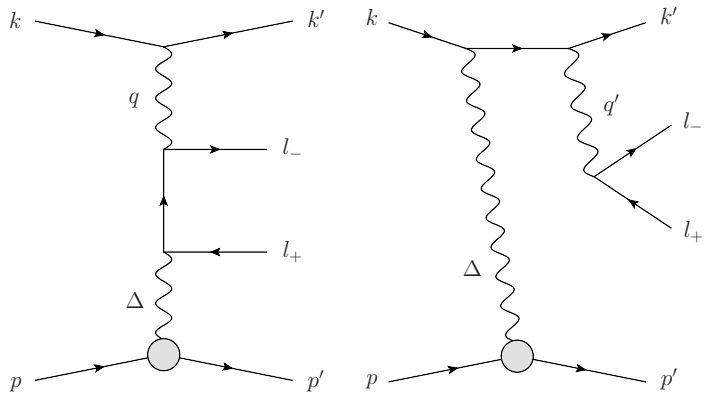

FIGURE 6.1.1: Tree level QED diagrams contributing to the $e^- p \to e^- p l^- l^+$ process. We distinguish between the spacelike (left) and the timelike (right) Bethe-Heitler processes. The crossed diagrams, for which in the spacelike process the order of the vertices on the produced dilepton line are interchanged, and for which in the timelike process the order of the vertices on the electron beam line are interchanged, are not shown.

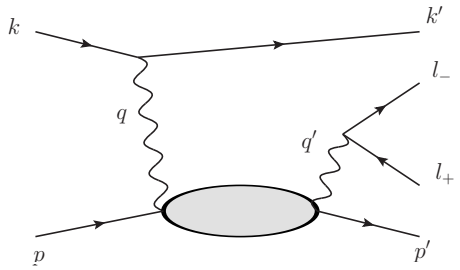

FIGURE 6.1.2: Tree level diagrams for the Compton scattering. The blob represents the (elastic and inelastic) interaction of the virtual photon with the nucleon.

as a probe of proton (N) structure, with $l^- = e^-$ or $l^- = \mu^-$, where the quantities in brackets denote the particle four-momenta. At tree level, we distinguish between three different contributions, which we denote as the spacelike (SL) and timelike (TL) Bethe-Heitler (BH) processes, see Fig. 6.1.1, as well as the double virtual Compton process (dVCS), see Fig. 6.1.2.

To specify the kinematics, it is useful to introduce the following four-momenta:

$$q = k - k', \quad q' = l_+ + l_-, \quad \Delta = p' - p. \tag{6.2}$$

The process (6.1) is defined by five kinematical invariants,

$$\begin{aligned} s &= (k+p)^2, & Q^2 &= -(k-k')^2, \\ W^2 &= (q+p)^2, & t &= \Delta^2, \\ s_{ll} &= q'^2, \end{aligned} \tag{6.3}$$

and three scattering angles,

$$\Phi,\ \theta_l^*,\ \phi_l^*, \tag{6.4}$$

where Φ denotes the angle of the initial electron plane relative to the production plane. Furthermore, the angle θ_l^* (ϕ_l^*) denotes the polar (azimuthal) angle respectively of

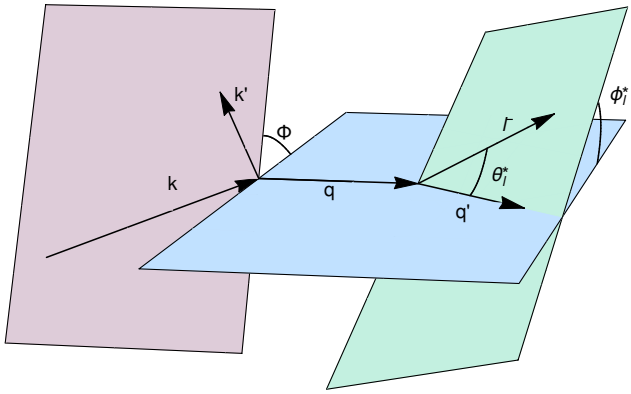

FIGURE 6.1.3: Planes defining the scattering angles which characterize the $e^- p \to e^- p l^- l^+$ process. The angles Φ and ϕ_l^* are defined with respect to the blue plane, which is the scattering plane of the virtual photons with four-momenta q and q'.

the negative charged lepton in the rest frame of the $l^- l^+$ lepton pair. In Fig. 6.1.3 we show the three different scattering planes defined by these angles.

We denote by m the mass of the electron, by m_l the mass of the produced leptons, and by M the mass of the proton. The on-shell relations of the external particles are therefore

$$k^2 = k'^2 = m^2, \quad l_-^2 = l_+^2 = m_l^2, \quad p^2 = p'^2 = M^2, \tag{6.5}$$

and the invariant s is obtained from the Lab electron beam energy E_e as $s = M^2 + m^2 + 2ME_e$.

The matrix element for the spacelike Bethe-Heitler (BH,SL) process (left diagram in Fig. 6.1.1) is given by

$$\begin{aligned}\mathcal{M}_{0;dir}^{\mathrm{BH,SL}} = & \frac{-ie^4}{Q^2 t}\bar{u}\left(k', h'\right)\gamma^\mu u\left(k, h\right) \\ & \times\bar{u}\left(l_-, h_-\right)\left[\gamma_\mu \frac{\not{l}_- - \not{q} + m_l}{(l_- - q)^2 - m_l^2}\gamma_\alpha + \gamma_\alpha \frac{\not{q} - \not{l}_+ + m_l}{(q - l_+)^2 - m_l^2}\gamma_\mu\right] v\left(l_+, h_+\right) \\ & \times\bar{N}\left(p', s'\right)\Gamma^\alpha(t) N\left(p, s\right), \end{aligned} \tag{6.6}$$

while the timelike Bethe-Heitler (BH,TL) process (right diagram in Fig. 6.1.1) is given by

$$\begin{aligned}\mathcal{M}_{0;dir}^{\mathrm{BH,TL}} = & \frac{ie^4}{s_{ll} t}\bar{u}\left(l_-, h_-\right)\gamma^\mu v\left(l_+, h_+\right) \\ & \times\bar{u}\left(k', h'\right)\left[\gamma_\mu \frac{\not{k}' + \not{q}' + m}{\left(k' + q'\right)^2 - m^2}\gamma_\alpha + \gamma_\alpha \frac{\not{k} - \not{q}' + m}{\left(k - q'\right)^2 - m^2}\gamma_\mu\right] u(k, h) \\ & \times\bar{N}\left(p', s'\right)\Gamma^\alpha(t) N\left(p, s\right). \end{aligned} \tag{6.7}$$

In Eqs. (6.6,6.7), $h(h')$ denote the helicities of the intial (scattered) electrons, h_- and h_+ are the helicities of the produced lepton pair, and $s(s')$ are the helicities of the intial (final) proton respectively. Furthermore, Γ^α is the electromagnetic nucleon vertex given by

$$\Gamma^\alpha(p', p) = F_1(t)\gamma^\alpha + F_2(t)\frac{i\sigma^{\alpha\alpha'}\Delta_{\alpha'}}{2M}, \tag{6.8}$$

where F_1 (F_2) are the Dirac (Pauli) form factors of the nucleon respectively.

The matrix element for the double virtual Compton scattering (dVCS) process (Fig. 6.1.2) is expressed as:

$$\begin{aligned}\mathcal{M}_{0;dir}^{\mathrm{dVCS}} &= \frac{ie^4}{Q^2 s_{ll}} \bar{u}\left(k',h'\right)\gamma_\mu u\left(k,h\right)\bar{u}\left(l_-,h_-\right)\gamma_\nu v\left(l_+,h_+\right)\\ &\times \bar{N}\left(p',s'\right)M^{\mu\nu}N\left(p,s\right),\end{aligned} \tag{6.9}$$

where $M^{\mu\nu}$ denotes the Compton tensor, which depends on the model to describe the interaction of photons with the nucleon, and which will be specified below.

In the case of e^-e^+ production, we have to take into account that the electrons with momenta k' and l_- are indistinguishable. Thus for e^-e^+ production, we have to consider, besides the direct (dir) contribution of Eqs. (6.6,6.7,6.9), also the contribution of all exchange (ex) diagrams where both electrons in the final state are interchanged. The Bethe-Heitler matrix elements corresponding with these exchange terms are given by (note that this only contributes in the case $m_l = m$):

$$\begin{aligned}\mathcal{M}_{0;ex}^{\mathrm{BH,SL}} &= \frac{ie^4}{(k-l_-)^2 t}\bar{u}\left(l_-,h_-\right)\gamma^\mu u\left(k,h\right)\\ &\times \bar{u}\left(k',h'\right)\left[\gamma_\mu \frac{\not{l}_- - \not{q} + m}{(l_- - q)^2 - m^2}\gamma_\alpha + \gamma_\alpha \frac{\not{k} - \not{q}' + m}{(k-q')^2 - m^2}\gamma_\mu\right] v\left(l_+,h_+\right)\\ &\times \bar{N}\left(p',s'\right)\Gamma^\alpha(t) N\left(p,s\right),\end{aligned} \tag{6.10}$$

$$\begin{aligned}\mathcal{M}_{0;ex}^{\mathrm{BH,TL}} &= \frac{ie^4}{(l_+ + k')^2 t}\bar{u}\left(k',h'\right)\gamma^\mu v\left(l_+,h_+\right)\\ &\times \bar{u}\left(l_-,h_-\right)\left[\gamma_\mu \frac{\not{k}' + \not{q}' + m}{(k'+q')^2 - m^2}\gamma_\alpha + \gamma_\alpha \frac{\not{q} - \not{l}_+ + m}{(q-l_+)^2 - m^2}\gamma_\mu\right] u(k,h)\\ &\times \bar{N}\left(p',s'\right)\Gamma^\alpha(t) N\left(p,s\right),\end{aligned} \tag{6.11}$$

and the exchange term corresponding with the dVCS matrix element is given by

$$\begin{aligned}\mathcal{M}_{0;ex}^{\mathrm{dVCS}} &= \frac{-ie^4}{(k-l_-)^2(l_+ + k')^2}\bar{u}\left(l_-,h_-\right)\gamma_\mu u\left(k,h\right)\bar{u}\left(k',h'\right)\gamma_\nu v\left(l_+,h_+\right)\\ &\times \bar{N}\left(p',s'\right)M^{\mu\nu}N\left(p,s\right).\end{aligned} \tag{6.12}$$

To ensure the Pauli principle, one has to anti-symmetrize the amplitude under exchange of both electrons in the final state. Therefore, the full matrix elements for the $e^-p \to e^-pe^-e^+$ process is obtained as difference between the amplitudes for direct (dir) and exchange (ex) diagrams as follows:

$$\begin{aligned}\mathcal{M}_0^{\mathrm{BH,SL}} &= \mathcal{M}_{0;dir}^{\mathrm{BH,SL}} - \mathcal{M}_{0;ex}^{\mathrm{BH,SL}},\\ \mathcal{M}_0^{\mathrm{BH,TL}} &= \mathcal{M}_{0;dir}^{\mathrm{BH,TL}} - \mathcal{M}_{0;ex}^{\mathrm{BH,TL}}\\ \mathcal{M}_0^{\mathrm{dVCS}} &= \mathcal{M}_{0;dir}^{\mathrm{dVCS}} - \mathcal{M}_{0;ex}^{\mathrm{dVCS}},\end{aligned} \tag{6.13}$$

while for $\mu^-\mu^+$ production only the direct diagrams contribute.

The fully differential cross section for the $e^-p \to e^-pl^-l^+$ process is given by

$$\begin{aligned}\left(\frac{\mathrm{d}\sigma}{\mathrm{d}Q^2\mathrm{d}W^2\mathrm{d}\Phi\mathrm{d}t\mathrm{d}s_{ll}\mathrm{d}\Omega_l^*}\right)_0 &= \frac{1}{(4\pi)^7}\frac{1}{2(s-M^2)^2}\frac{\beta}{[((W+M)^2+Q^2)((W-M)^2+Q^2)]^{\frac{1}{2}}}\\ &\times \overline{\sum_i}\sum_f \left|\mathcal{M}_0^{\mathrm{BH,SL}} + \mathcal{M}_0^{\mathrm{BH,TL}} + \mathcal{M}_0^{\mathrm{dVCS}}\right|^2,\end{aligned} \tag{6.14}$$

where $\mathrm{d}\Omega_l^*$ refers to the phase space of the produced lepton of the dilepton pair in the $l^- l^+$ rest frame, and where β is the lepton velocity in the $l^- l^+$ rest frame,

$$\beta = \sqrt{1 - \frac{4m_l^2}{s_{ll}}}. \tag{6.15}$$

6.2 Models for the double virtual Compton amplitude

Like in the case of TCS, we use two different models to calculate the dVCS amplitude. Both models are described in the previous chapter in Section 5.2. In the present section, we describe a few differences we implemented compared to the TCS case.

6.2.1 Low-energy model and low-energy expansion

For the low-energy model we use, as before, the Born and Δ-pole model as described in Section 5.2.1. However, in the present calculation, we only use the dominant contribution of the Δ-pole model coming from the magnetic dipole transition FF G_M^*. This corresponds with the leading term in the so-called δ-expansion [147] to calculate observables, i.e. we set $G_E^* = G_C^* = 0$.

In addition to the Born+Δ model, we furthermore use a low-energy expansion of the amplitude. The expansion of the helicity-averaged amplitude can be described by five independent tensors which are given, following the notations of [145], by

$$M^{\mu\nu} = \sum_{i=1,2,3,4,19} B_i(\nu, q^2, q'^2, q\cdot q')\, T_i^{\mu\nu}, \tag{6.16}$$

where $T_i^{\mu\nu}$ are the spin-independent and gauge invariant tensors, symmetric under exchange of the two virtual photons, and are given by

$$\begin{aligned}
T_1^{\mu\nu} &= -q\cdot q' g^{\mu\nu} + q'^{\mu} q^{\nu}\,, \\
T_2^{\mu\nu} &= (2M\nu)^2 \left(-g^{\mu\nu} + \frac{q'^{\mu}q^{\nu}}{q\cdot q'}\right) - 4q\cdot q' \left(P^{\mu} - \frac{q\cdot P}{q\cdot q'} q'^{\mu}\right)\left(P^{\nu} - \frac{q\cdot P}{q\cdot q'} q^{\nu}\right)\,, \\
T_3^{\mu\nu} &= q^2 q'^2 g^{\mu\nu} + q\cdot q' q^{\mu} q'^{\nu} - q^2\, q'^{\mu} q'^{\nu} - q'^2\, q^{\mu} q^{\nu}\,, \\
T_4^{\mu\nu} &= (2M\nu)(q^2 + q'^2)\left(g^{\mu\nu} - \frac{q'^{\mu}q^{\nu}}{q\cdot q'}\right) + 2\left(P^{\mu} - \frac{q\cdot P}{q\cdot q'} q'^{\mu}\right)\left(-q'^2 q^{\nu} + q\cdot q' q'^{\nu}\right) \\
&\quad + 2\left(P^{\nu} - \frac{q\cdot P}{q\cdot q'} q^{\nu}\right)\left(-q^2 q'^{\mu} + q\cdot q' q^{\mu}\right)\,, \\
T_{19}^{\mu\nu} &= 4q^2 q'^2 \left(P^{\mu} - \frac{q\cdot P}{q^2} q^{\mu}\right)\left(P^{\nu} - \frac{q\cdot P}{q'^2} q'^{\nu}\right)\,.
\end{aligned} \tag{6.17}$$

Furthermore, in Eq. (6.16), the invariant amplitudes B_i are functions of four Lorentz invariants, with $\nu \equiv q\cdot P/M$.

The non-Born part of the dVCS amplitudes, denoted as $\bar{B}_i$, can be expanded for small values of ν, q^2, q'^2, and $q\cdot q'$, with coefficients given by polarizabilities. The relations between these low-energy coefficients and the polarizabilities measured through real Compton scattering ($\gamma p \to \gamma p$) and virtual Compton scattering ($\gamma^* p \to \gamma p$) have been given in Ref. [12].

A special limit of the double virtual Compton process is given by its forward limit, denoted by VVCS, which corresponds with $q' = q$ and $p' = p$. This limit is of particular importance as it enters the two-photon hadronic corrections to the electronic and muonic hydrogen energy levels. The helicity averaged VVCS process

is described by two invariant amplitudes, denoted by T_1 and T_2, which are functions of the two kinematic invariants Q^2 and ν, as:

$$M^{\mu\nu}_{\rm VVCS} \equiv \frac{1}{\alpha_{\rm em}} \left\{ \hat{g}^{\mu\nu} T_1(\nu, Q^2) - \frac{\hat{p}^\mu \hat{p}^\nu}{M^2} T_2(\nu, Q^2) \right\}, \tag{6.18}$$

with $\hat{g}^{\mu\nu} \equiv g^{\mu\nu} - q^\mu q^\nu / q^2$, $\hat{p}^\mu \equiv p^\mu - p\cdot q / q^2\, q^\mu$. The optical theorem allows expressing the imaginary parts of T_1 and T_2 as:

$$\text{Im}\; T_1(\nu, Q^2) = \frac{e^2}{4M} F_1\,, \quad \text{Im}\; T_2(\nu, Q^2) = \frac{e^2}{4\nu} F_2\,, \tag{6.19}$$

where F_1, F_2 are the conventionally defined structure functions parameterizing inclusive electron-nucleon scattering, depending on Q^2 and $x \equiv Q^2/2M\nu$. The two-photon exchange correction to the μH Lamb shift can be expressed as a weighted double integral over Q^2 and ν of the forward amplitudes T_1 and T_2 [9]. Using the empirical input of F_1 and F_2, the ν dependence of T_2 can be fully reconstructed using an unsubtracted dispersion relation, whereas the dispersion relation for T_1 requires one subtraction, which can be chosen at $\nu = 0$ as $T_1(0, Q^2)$. The subtraction function is usually split in a Born part, corresponding with the nucleon intermediate state, and a remainder, so-called non-Born part, denoted by $\bar{T}_1(0, Q^2)$. The Born part can be expressed in terms of elastic form factors and is well known, see e.g. [167] for the corresponding expressions. The non-Born part cannot be fixed empirically so far. In general, one can however write down a low Q^2 expansion of $\bar{T}_1(0, Q^2)$ as:

$$\bar{T}_1(0, Q^2) = \beta_{M1} Q^2 + \frac{1}{2} T_1^{''}(0) Q^4 + \mathcal{O}(Q^6), \tag{6.20}$$

where the term proportional to Q^2 is empirically determined by the magnetic dipole polarizability β_{M1} [168]. Theoretical estimates for the subtraction term were given at order Q^4 in heavy-baryon chiral perturbation theory (HBChPT) [10], in BChPT, both at leading order due to πN loops, and at next-to-leading order, including both $\Delta(1232)$-exchange and $\pi\Delta$ loops [12, 13], as well as extracted from superconvergence sum rule (SR) relations [14]. The different estimates for $\bar{T}_1''(0)$ are compared in Table 6.2.1. Even for these theoretically well-motivated approaches, the spread among the different estimates is quite large. The resulting uncertainty due to this subtraction term constitutes at present the main uncertainty in the theoretical μH Lamb shift estimate. To reduce such model dependence, the dilepton electroproduction process on a proton has been proposed in [15] as an empirical way to determine $\bar{T}_1''(0)$.

As the forward VVCS process of Eq. (6.18) is a special case of Eq. (6.16), one can express the subtraction function entering the hadronic corrections to the μH energy levels as [12]:

$$\bar{T}_1(0, Q^2) = \alpha_{\rm em} Q^2 \left(\bar{B}_1 + Q^2 \bar{B}_3 \right), \tag{6.21}$$

where both non-Born amplitudes $\bar{B}_1, \bar{B}_3$ are understood in the forward limit ($q = q'$), i.e. $\bar{B}_i(0, q^2, q^2, q^2)$ for $i = 1, 3$. In order to specify $\bar{T}_1(0, Q^2)$ up to the Q^4 term, we use the low-energy expansion in $k \in \{q, q'\}$ of the amplitudes $\bar{B}_1, \bar{B}_3$ [12],

$$\begin{aligned} \bar{B}_1(0, q^2, q'^2, q\cdot q') &= \frac{1}{\alpha_{\rm em}} \left\{ \beta_{M1} - \frac{1}{6} \beta_{M2} q\cdot q' - \left(\beta'_{M1}(0) + \frac{\beta_{M1}}{8M^2} \right) (q^2 + q'^2) \right\} + \mathcal{O}(k^4), \\ \bar{B}_3(0, q^2, q'^2, q\cdot q') &= b_{3,0} + \mathcal{O}(k^2), \end{aligned} \tag{6.22}$$

where β_{M2} is the magnetic quadrupole polarizability determined from real Compton scattering [169], and $\beta'_{M1}(0)$ is the slope at $Q^2 = 0$ of the generalized magnetic dipole

Source	Ref.	$\frac{1}{2}\bar{T}_1''(0)$	$\alpha_{\rm em} b_{3,0}$
HBChPT	[10]	$[-1.01, -0.35]$	
πN loops		-0.06	0.001
$\pi\Delta$ loops		-0.10	-0.005
Δ exchange		-1.98	0.11
Total BChPT	[12]	-2.14 ± 0.98	0.11 ± 0.05
superconvergence SR	[14]	-0.47	3.96

TABLE 6.2.1: Estimates of the Q^4 term of the subtraction function $\bar{T}_1(0, Q^2)$ (second column) and of the dVCS low-energy constant $b_{3,0}$ (third column), both in units 10^{-4} fm^5, in different theoretical approaches [12]. The indicated range for the HBChPT result corresponds with the range given by Eq. (15) in Ref. [10].

polarizability which is accessed through virtual Compton scattering, see Ref. [7] for a recent review. While the terms of $\mathcal{O}(k^0)$ and $\mathcal{O}(k^2)$ in the low-energy structure of the amplitude $\bar{B}_1$ at $\nu = 0$ are empirically constrained from real or virtual Compton scattering, the low-energy constant $b_{3,0}$ is not determined empirically so far because the tensor structure $T_3^{\mu\nu}$ in Eq. (6.17) decouples when either the initial or final photon is real. As such the low-energy constant $b_{3,0}$ is the main unknown to date in the empirical determination of $\bar{T}_1''(0)$. Below, we study the sensitivity of the $e^- p \to e^- p l^- l^+$ process, including the soft-photon radiative corrections, to this low-energy constant.

6.2.2 High-energy double virtual Compton amplitude in terms of GPDs

For the high-energy regime, we use the same model as described in Section 5.2.2 based on perturbative QCD, in which the amplitude is expressed through GPDs, cf. Eq. (5.28). However, since we now consider two off-shell photons in the Compton amplitude, we have to ensure that for both incoming and outgoing virtual photons in the DDVCS process exact electromagnetic gauge invariance is satisfied. We therefore generalize the procedure introduced in Ref. [151] to add transversal correction terms which are formally of higher-twist as follows:

$$\begin{aligned} M^{\mu\nu}_{\rm DDVCS} = M^{\mu\nu}_{\rm DDVCS,tw-2} &- \frac{P^\mu}{2P\cdot\bar{q}}(\Delta_\perp)_\kappa M^{\kappa\nu}_{\rm DDVCS,tw-2} \\ &+ \frac{P^\nu}{2P\cdot\bar{q}}(\Delta_\perp)_\lambda M^{\mu\lambda}_{\rm DDVCS,tw-2} \\ &- \frac{P^\mu P^\nu}{4(P\cdot\bar{q})^2}(\Delta_\perp)_\kappa(\Delta_\perp)_\lambda M^{\kappa\lambda}_{\rm DDVCS,tw-2}, \end{aligned} \tag{6.23}$$

where the transverse part $\Delta_\perp$ of the four-momentum transfer to the nucleon is defined as

$$(\Delta_\perp)^\mu \equiv \Delta^\mu + 2\tilde{\xi}\,\tilde{p}^\mu - \tilde{\xi}\bar{M}^2\,n^\mu. \tag{6.24}$$

Using the identities

$$\begin{aligned} q_\mu M^{\mu\nu}_{\rm DDVCS,tw-2} &= \frac{1}{2}\,(\Delta_\perp)_\mu\; M^{\mu\nu}_{\rm DDVCS,tw-2}, \\ q'_\nu M^{\mu\nu}_{\rm DDVCS,tw-2} &= -\frac{1}{2}\,(\Delta_\perp)_\nu\; M^{\mu\nu}_{\rm DDVCS,tw-2}, \end{aligned} \tag{6.25}$$

one immediately verifies that both $q_\mu M^{\mu\nu}_{\rm DDVCS} = 0$ and $q'_\nu M^{\mu\nu}_{\rm DDVCS} = 0$.

Using the parameterization of Eq. (5.33) for the GPD H in terms of a double distribution and a D-term part, the evaluation of the amplitude in Eq. (5.28) involves a principle-value integral which can be evaluated numerically, for the case $0 < \xi' < \xi$, as:

$$\begin{aligned}\text{P.V.}\int_0^1 dx\,\frac{H^{\rm singlet}(x,\xi,t)}{x-\xi'} &= \int_0^1 dx\,\frac{H^{\rm singlet}_{DD}(x,\xi,t) - H^{\rm singlet}_{DD}(\xi',\xi,t)}{x-\xi'} \\ &+ 2\int_0^\xi dx\,\frac{D(x/\xi,t) - D(\xi'/\xi,t)}{x-\xi'} \\ &+ \ln\left(\frac{1-\xi'}{\xi'}\right) H^{\rm singlet}_{DD}(\xi',\xi,t) + \ln\left(\frac{\xi-\xi'}{\xi'}\right) 2D(\xi'/\xi,t),\end{aligned} \tag{6.26}$$

with the singlet GPD,

$$H^{\rm singlet}(x,\xi,t) \equiv H(x,\xi,t) - H(-x,\xi,t). \tag{6.27}$$

6.3 Virtual soft-photon corrections

In this section, we evaluate all one-loop virtual photon radiative corrections to the $e^- p \to e^- p l^- l^+$ process in the soft-photon approximation. From all soft-photon contributions, one can distinguish between the following three gauge-invariant subsets:

- class (a): soft photon attached to the beam electron line
- class (b): soft photon attached to the dilepton pair
- class (c): soft photon connecting the beam electron line with the dilepton line

We give analytical expressions for the corrections of all three types. Like in the previous chapter, we use dimensional regularization to regularize infrared divergences coming from the integration over the soft-photon loop momentum l. In addition to the diagrams with virtual soft photons, we also have to consider infrared divergent counterterms, which were calculated in the previous chapter using the on-shell renormalization scheme.

We will subsequently discuss the virtual radiative corrections to the spacelike BH process, the timelike BH process, and the double virtual Compton process.

6.3.1 Corrections to the spacelike Bethe-Heitler process

Contributions of class (a)

In this section, we calculate the soft-photon corrections for which the soft-photon is attached to the electron line. This corresponds to the left diagram in Fig. 6.3.1. In the following, we suppress helicity states in all spinors to make the formulas more compact and better readable. Using Feynman gauge, the first diagram in Fig. 6.3.1 is given by

$$\begin{aligned}\mathcal{M}_a^{\rm BH,SL} = &-\frac{e^6}{Q^2 t}\bar N(p')\,\Gamma^\alpha(t) N(p)\,\mu^{4-d} \\ &\times\int\frac{d^dl}{(2\pi)^d}\frac{\bar u(k')\,\gamma^\beta(\not k' + \not l + m)\gamma^\mu(\not k + \not l + m)\gamma_\beta u(k)}{[(k'+l)^2-m^2]\,[(k+l)^2-m^2]\,[l^2]}\end{aligned}$$

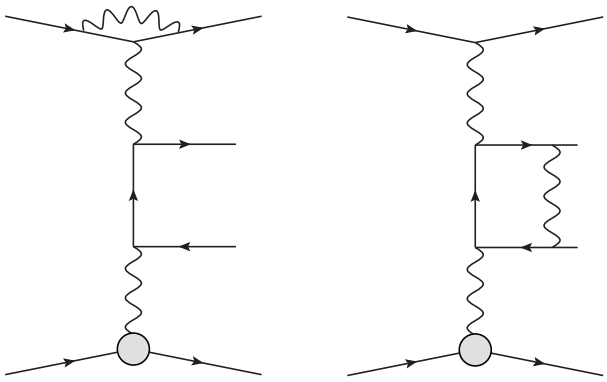

FIGURE 6.3.1: Virtual corrections of class (a) (left) and class (b) (right) to the spacelike BH process with two virtual photons. One also has to consider the corresponding counterterm diagrams. The crossed diagrams with l_- and l_+ interchanged yield the same correction.

$$\times \frac{\bar{u}\left(l_-\right)\gamma_\mu\left(\not{l}_- - \not{q} + m_l\right)\gamma_\alpha v\left(l_+\right)}{\left[\left(l_- - q\right)^2 - m_l^2\right]}, \tag{6.28}$$

which reduces in the soft-photon approximation to

$$\begin{aligned}\mathcal{M}_a^{\mathrm{BH,SL}} &= -ie^2 4(k\cdot k')\mathcal{M}_0^{\mathrm{BH,SL}}\mu^{4-d}\int \frac{d^d l}{(2\pi)^d}\frac{1}{\left[l^2+2k\cdot l\right]\left[l^2\right]\left[l^2+2k'\cdot l\right]} \\ &= \frac{e^2}{4\pi^2}(k\cdot k')C_0\left(m^2,\left(k-k'\right)^2,m^2;0,m^2,m^2\right)\mathcal{M}_0^{\mathrm{BH,SL}},\end{aligned} \tag{6.29}$$

with the three-point function C_0 given in Eq. (5.71).

In addition to the contribution of Eq. (6.29), we also have to include the vertex counterterm. We have shown the calculation of the one-loop vertex in Section 5.3.2 using the on-shell subtraction scheme. In the soft-photon approximation, one has to extract only the IR divergent piece of the full expression. From Eq. (5.47) we thus find for the vertex counterterm in the soft-photon approximation

$$\mathcal{M}_{\mathrm{ct;s}}^{\mathrm{BH,SL}} = -\frac{\alpha_{\mathrm{em}}}{2\pi}\left[\frac{1}{\epsilon_{\mathrm{IR}}} - \gamma_E + \ln\left(\frac{4\pi\mu^2}{m^2}\right)\right]\mathcal{M}_0^{\mathrm{BH,SL}}. \tag{6.30}$$

After adding the vertex counterterm to Eq. (6.29) and evaluating the three-point function, the infrared divergent part of the virtual correction to the cross section of the spacelike process is given by

$$\delta_{a,\mathrm{IR}}^{\mathrm{BH,SL}} = -\frac{\alpha_{\mathrm{em}}}{\pi}\left[\left(\frac{1+\beta_Q^2}{2\beta_Q}\right)\ln\left(\frac{\beta_Q-1}{\beta_Q+1}\right)+1\right]\left[\frac{1}{\epsilon_{\mathrm{IR}}} - \gamma_E + \ln\left(\frac{4\pi\mu^2}{m^2}\right)\right], \tag{6.31}$$

and the finite part by

$$\begin{aligned}\delta_a^{\mathrm{BH,SL}} = -\frac{\alpha_{\mathrm{em}}}{\pi}\left(\frac{1+\beta_Q^2}{2\beta_Q}\right)\Bigg\{&2\,\mathrm{Li}_2\left(\frac{\beta_Q-1}{2\beta_Q}\right)+\ln^2\left(\frac{\beta_Q-1}{2\beta_Q}\right) \\ &-\frac{1}{2}\ln^2\left(\frac{\beta_Q-1}{\beta_Q+1}\right)-\frac{\pi^2}{6}\Bigg\},\end{aligned} \tag{6.32}$$

where $\beta_Q = \sqrt{1+\frac{4m^2}{Q^2}}$.

Note that here and in the following, we define δ to be the correction on the level of the cross section, not the amplitude. This corresponds to taking twice the real part of the correction on the level of the amplitude.

For the crossed diagrams with l_- and l_+ interchanged we find the same result as in Eqs. (6.31) and (6.32). In the limit of a small electron mass, i.e. $m \ll Q^2$, the correction simplifies to

$$\begin{aligned}\delta_{a,\mathrm{IR}}^{\mathrm{BH,SL}} &= \frac{\alpha_{\mathrm{em}}}{\pi}\left[\ln\frac{Q^2}{m^2}-1\right]\left[\frac{1}{\epsilon_{\mathrm{IR}}}-\gamma_E+\ln\left(\frac{4\pi\mu^2}{m^2}\right)\right],\\ \delta_{a}^{\mathrm{BH,SL}} &= \frac{-\alpha_{\mathrm{em}}}{\pi}\left[\frac{1}{2}\ln^2\frac{Q^2}{m^2}-\frac{\pi^2}{6}\right].\end{aligned} \tag{6.33}$$

Contributions of class (b)

Here, we calculate all contributions to the spacelike process, for which the soft-photon is attached to the dilepton line. The Feynman diagram corresponding to this correction is shown in Fig. 6.3.1 on the right. The matrix element is given by

$$\begin{aligned}\mathcal{M}_b^{\mathrm{BH,SL}} = -\frac{e^6}{Q^2 t}\bar{N}\left(p'\right)\Gamma^{\alpha}(t)N\left(p\right)\bar{u}\left(k'\right)\gamma^{\mu}u\left(k\right)\mu^{4-d}\int\frac{d^dl}{(2\pi)^d}\frac{\bar{u}\left(l_-\right)\gamma^{\beta}\left(-\not{l}+\not{l}_-+m_l\right)}{\left[\left(l-l_-\right)^2-m_l^2\right]}\\ \times\frac{\gamma_{\mu}\left(-\not{l}+\not{l}_--\not{q}+m_l\right)\gamma_{\alpha}(-\not{l}-\not{l}_++m_l)\gamma_{\beta}v\left(l_+\right)}{[(l-l_-+q)^2-m_l^2][(l+l_+)^2-m_l^2]\left[l^2\right]},\end{aligned} \tag{6.34}$$

which in the soft-photon approximation reduces to

$$\begin{aligned}\mathcal{M}_b^{\mathrm{BH,SL}} &= ie^2 4(l_-\cdot l_+)\mathcal{M}_0^{\mathrm{BH,SL}}\mu^{4-d}\int\frac{d^dl}{(2\pi)^d}\frac{1}{\left[l^2-2l_-\cdot l\right]\left[l^2\right]\left[l^2+2l_+\cdot l\right]}\\ &= \frac{-e^2}{4\pi^2}(l_-\cdot l_+)C_0\left(m_l^2,\left(l_-+l_+\right)^2,m_l^2;0,m_l^2,m_l^2\right)\mathcal{M}_0^{\mathrm{BH,SL}}.\end{aligned} \tag{6.35}$$

As before for the class (a) contribution, we need to include counterterms. In addition to the infrared divergent piece of the vertex counterterm as given by Eq. (6.30), we also need the counterterm of the fermion self-energy. The full self-energy has been calculated in Section 5.3.3. In the soft-photon limit, in which we only extract the IR divergence from Eq. (5.64), we find

$$\tilde{\Sigma}_s(k') = \frac{\alpha_{\mathrm{em}}}{2\pi}\left(\not{k}'-m_l\right)\left[\frac{1}{\epsilon_{\mathrm{IR}}}-\gamma_E+\ln\left(\frac{4\pi\mu^2}{m_l^2}\right)\right]. \tag{6.36}$$

Adding the counterterms of the vertex and fermion self-energy to Eq. (6.35), we find for the total contribution the infrared divergent part

$$\delta_{b,\mathrm{IR}}^{\mathrm{BH,SL}} = \frac{\alpha_{\mathrm{em}}}{\pi}\left[\frac{1+\beta^2}{2\beta}\ln\left(\frac{1+\beta}{1-\beta}\right)-1\right]\left[\frac{1}{\epsilon_{\mathrm{IR}}}-\gamma_E+\ln\left(\frac{4\pi\mu^2}{m_l^2}\right)\right], \tag{6.37}$$

and the finite part

$$\delta_{b}^{\mathrm{BH,SL}} = -\frac{\alpha_{\mathrm{em}}}{\pi}\left(\frac{1+\beta^2}{2\beta}\right)\left[2\,\mathrm{Li}_2\left(\frac{2\beta}{\beta+1}\right)+\frac{1}{2}\ln^2\left(\frac{1-\beta}{1+\beta}\right)-\pi^2\right]. \tag{6.38}$$

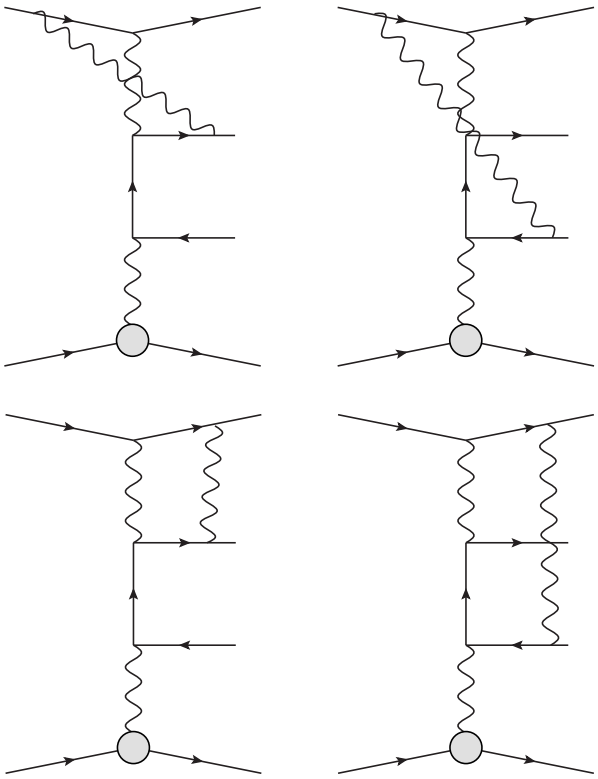

FIGURE 6.3.2: Virtual photon corrections of class (c) to the spacelike BH proces. The crossed diagrams with l_- and l_+ interchanged yield the same correction.

Note that this correction is exactly the same as in the TCS process, that was studied in the previous chapter, cf. Eq. (5.75). In the limit of small lepton masses, i.e. $m_l^2 \ll s_{ll}$, we find

$$\begin{aligned}\delta_{b,\mathrm{IR}}^{\mathrm{BH,SL}} &= \frac{\alpha_{\mathrm{em}}}{\pi}\left[\ln\frac{s_{ll}}{m_l^2}-1\right]\left[\frac{1}{\epsilon_{\mathrm{IR}}}-\gamma_E+\ln\left(\frac{4\pi\mu^2}{m_l^2}\right)\right],\\ \delta_{b}^{\mathrm{BH,SL}} &= -\frac{\alpha_{\mathrm{em}}}{\pi}\left[\frac{1}{2}\ln^2\frac{s_{ll}}{m_l^2}-\frac{2}{3}\pi^2\right].\end{aligned} \tag{6.39}$$

Contributions of class (c)

In this section, we calculate all diagrams, in which a soft-photon connects the electron line with the dilepton line. We show the contributing diagrams of this class in Fig. 6.3.2. For the contribution of class (c) no counterterms contribute.

The first diagram in Fig. 6.3.2 is calculated as

$$\begin{aligned}\mathcal{M}_{c_1}^{\mathrm{BH,SL}} = \frac{e^6}{t}\bar{N}(p')\,\Gamma^{\alpha}(t)N(p)\,\mu^{4-d}\int\frac{d^dl}{(2\pi)^d}\frac{\bar{u}(k')\,\gamma^{\mu}\left(\not{l}+\not{k}+m\right)\gamma^{\beta}u(k)}{\left[(l+k)^2-m^2\right]\left[(l+k-k')^2\right]\left[l^2\right]}\\ \times\frac{\bar{u}(l_-)\,\gamma_{\beta}\left(\not{l}_-+\not{l}+m_l\right)\gamma_{\mu}\left(\not{l}_--\not{q}+m_l\right)\gamma_{\alpha}v(l_+)}{\left[(l+l_-)^2-m_l^2\right]\left[(l_--q)^2-m_l^2\right]},\end{aligned} \tag{6.40}$$

which in the soft-photon limit can be reduced to

$$\mathcal{M}_{c_1}^{\mathrm{BH,SL}} = -ie^2 4(k\cdot l_-)\mu^{4-d}\mathcal{M}_0^{\mathrm{BH,SL}}\int\frac{d^dl}{(2\pi)^d}\frac{1}{\left[l^2\right]\left[l^2+2k\cdot l\right]\left[l^2+2l_-\cdot l\right]}$$

$$= \frac{e^2}{4\pi^2}(k\cdot l_-)C_0\left(m^2,(k-l_-)^2,m_l^2;0,m^2,m_l^2\right)\mathcal{M}_0^{\mathrm{BH,SL}}. \tag{6.41}$$

Evaluating the three-point function C_0, as given in Appendix 6.B, we find, that the infrared-divergent part is given by

$$\delta_{c_1,\mathrm{IR}}^{\mathrm{BH,SL}} = \frac{\alpha_{\mathrm{em}}}{\pi}\frac{k\cdot l_-}{\lambda_{kl_-}(k-l_-)^2}\ln\left(\frac{\gamma_{kl_-}^-(1-\gamma_{kl_-}^+)}{(1-\gamma_{kl_-}^-)\gamma_{kl_-}^+}\right)\left[\frac{1}{\epsilon_{\mathrm{IR}}}-\gamma_E+\ln\left(\frac{4\pi\mu^2}{m^2}\right)\right], \tag{6.42}$$

and the finite part by

$$\begin{aligned}\delta_{c_1}^{\mathrm{BH,SL}} = \frac{\alpha_{\mathrm{em}}}{\pi}\frac{k\cdot l_-}{\lambda_{kl_-}(k-l_-)^2}\Bigg\{&-\ln(-\lambda_{kl_-})\left[\ln\left(\frac{\gamma_{kl_-}^+-1}{\gamma_{kl_-}^+}\right)+\ln\left(\frac{\gamma_{kl_-}^-}{\gamma_{kl_-}^--1}\right)\right]\\&+\frac{1}{2}\ln^2\left(-\gamma_{kl_-}^+\right)-\frac{1}{2}\ln^2\left(\gamma_{kl_-}^-\right)-\frac{1}{2}\ln^2\left(1-\gamma_{kl_-}^+\right)+\frac{1}{2}\ln^2\left(\gamma_{kl_-}^--1\right)\\&-\mathrm{Li}_2\left(\frac{1-\gamma_{kl_-}^-}{\lambda_{kl_-}}\right)-\mathrm{Li}_2\left(\frac{\gamma_{kl_-}^+}{\lambda_{kl_-}}\right)+\mathrm{Li}_2\left(\frac{\gamma_{kl_-}^+-1}{\lambda_{kl_-}}\right)+\mathrm{Li}_2\left(\frac{\gamma_{kl_-}^-}{\lambda_{kl_-}}\right)\\&-\ln\left(\frac{\gamma_{kl_-}^-(1-\gamma_{kl_-}^+)}{(1-\gamma_{kl_-}^-)\gamma_{kl_-}^+}\right)\ln\left(\frac{-(k-l_-)^2}{m^2}\right)\Bigg\},\end{aligned} \tag{6.43}$$

where

$$\lambda_{kl_-} = \frac{2\sqrt{(k\cdot l_-)^2-m^2m_l^2}}{(k-l_-)^2},\quad \gamma_{kl_-}^{\pm} = \left[\frac{m_l^2-k\cdot l_-}{(k-l_-)^2}\pm\frac{\lambda_{kl_-}}{2}\right]. \tag{6.44}$$

We now consider two limits for this correction, in which the above expressions simplify. The first limit corresponds to the case, when the electron mass is small compared to all other scales. In this limit, we find for the infrared divergent contribution

$$\delta_{c_1,\mathrm{IR}}^{\mathrm{BH,SL}} = \frac{\alpha_{\mathrm{em}}}{\pi}\ln\left(\frac{2k\cdot l_-}{m\,m_l}\right)\left[\frac{1}{\epsilon_{\mathrm{IR}}}-\gamma_E+\ln\left(\frac{4\pi\mu^2}{m^2}\right)\right], \tag{6.45}$$

and for the finite contribution

$$\begin{aligned}\delta_{c_1}^{\mathrm{BH,SL}} = \frac{\alpha_{\mathrm{em}}}{2\pi}\Bigg\{&\frac{1}{2}\ln^2\left(\frac{m^2}{2k\cdot l_-}\right)-\frac{1}{2}\ln^2\left(\frac{2k\cdot l_-}{2k\cdot l_--m_l^2}\right)+\frac{1}{2}\ln^2\left(\frac{m_l^2}{2k\cdot l_--m_l^2}\right)\\&-\ln\left(\frac{4(k\cdot l_-)^2}{m^2m_l^2}\right)\ln\left(\frac{2k\cdot l_-}{m^2}\right)+\mathrm{Li}_2\left(\frac{2k\cdot l_--m_l^2}{2k\cdot l_-}\right)-\mathrm{Li}_2\left(\frac{m_l^2}{2k\cdot l_-}\right)+\frac{\pi^2}{6}\Bigg\}.\end{aligned} \tag{6.46}$$

If in addition to $m^2 \ll k\cdot l_-$, also $m_l = m$, i.e. considering electron pair production, we find

$$\begin{aligned}\delta_{c_1,\mathrm{IR}}^{\mathrm{BH,SL}} &= \frac{\alpha_{\mathrm{em}}}{\pi}\ln\left(\frac{2k\cdot l_-}{m^2}\right)\left[\frac{1}{\epsilon_{\mathrm{IR}}}-\gamma_E+\ln\left(\frac{4\pi\mu^2}{m^2}\right)\right],\\ \delta_{c_1}^{\mathrm{BH,SL}} &= -\frac{\alpha_{\mathrm{em}}}{\pi}\left\{\frac{1}{2}\ln^2\frac{2k\cdot l_-}{m^2}-\frac{\pi^2}{6}\right\}.\end{aligned} \tag{6.47}$$

We now turn to the second diagram in the first row of Fig. 6.3.2. It can be related to the previous one using Eq. (6.41) with the replacement $l_- \to l_+$ together with a sign change,

$$\mathcal{M}_{c_2}^{\mathrm{BH,SL}} = \frac{-e^2}{4\pi^2}(k\cdot l_+)C_0\left(m^2,(k-l_+)^2,m_l^2;0,m^2,m_l^2\right)\mathcal{M}_0^{\mathrm{BH,SL}}. \tag{6.48}$$

Therefore, the correction on the level of the cross section is given by

$$\delta_{c_2,\mathrm{IR}}^{\mathrm{BH,SL}} = -\delta_{c_1,\mathrm{IR}}^{\mathrm{BH,SL}}\Big|_{l_-\to l_+}, \quad \delta_{c_2}^{\mathrm{BH,SL}} = -\delta_{c_1}^{\mathrm{BH,SL}}\Big|_{l_-\to l_+}. \tag{6.49}$$

The first diagram in the second row of Fig. 6.3.2 is given by

$$\begin{aligned}\mathcal{M}_{c_3}^{\mathrm{BH,SL}} = \frac{e^6}{t}\bar{N}\left(p'\right)\Gamma^{\alpha}(t)N\left(p\right)\mu^{4-d}\int\frac{d^dl}{(2\pi)^d}\frac{\bar{u}\left(k'\right)\gamma^{\beta}\left(\not{l}+\not{k}'+m\right)\gamma^{\mu}u\left(k\right)}{\left[(l+k')^2-m^2\right]\left[(l-k+k')^2\right]\left[l^2\right]}\\ \times\frac{\bar{u}\left(l_-\right)\gamma_{\beta}\left(\not{l}_- - \not{l}+m_l\right)\gamma_{\mu}\left(\not{l}_- - \not{q}+m_l\right)\gamma_{\alpha}v\left(l_+\right)}{\left[(l-l_-)^2-m_l^2\right]\left[(l_- -q)^2-m_l^2\right]},\end{aligned} \tag{6.50}$$

which reduces to

$$\begin{aligned}\mathcal{M}_{c_3}^{\mathrm{BH,SL}} &= -ie^2 4(k'\cdot l_-)\mu^{4-d}\mathcal{M}_0^{\mathrm{BH,SL}}\int\frac{d^dl}{(2\pi)^d}\frac{1}{\left[l^2+2k'l\right]\left[l^2-2l_-l\right]\left[l^2\right]}\\ &= \frac{e^2}{4\pi^2}(k'\cdot l_-)C_0\left(m^2,\left(k'+l_-\right)^2,m_l^2;0,m^2,m_l^2\right)\mathcal{M}_0^{\mathrm{BH,SL}}.\end{aligned} \tag{6.51}$$

In this case, the second argument of the three-point function is positive. Therefore, an analytic continuation of this function to the timelike region has to be performed. This yields

$$\delta_{c_3,\mathrm{IR}}^{\mathrm{BH,SL}} = \frac{\alpha_{\mathrm{em}}}{\pi}\frac{(k'\cdot l_-)}{\tilde{\lambda}_{k'l}(k'+l_-)^2}\ln\left(\frac{\tilde{\gamma}_{k'l_-}^{-}(1-\tilde{\gamma}_{k'l_-}^{+})}{(1-\tilde{\gamma}_{k'l_-}^{-})\tilde{\gamma}_{k'l_-}^{+}}\right)\left[\frac{1}{\epsilon_{\mathrm{IR}}}-\gamma_E+\ln\left(\frac{4\pi\mu^2}{m^2}\right)\right], \tag{6.52}$$

and

$$\begin{aligned}\delta_{c_3}^{\mathrm{BH,SL}} =& \frac{\alpha_{\mathrm{em}}}{\pi}\frac{(k'\cdot l_-)}{\tilde{\lambda}_{k'l}(k'+l_-)^2}\left\{\frac{1}{2}\ln^2\left(\frac{\tilde{\lambda}_{k'l}}{1-\tilde{\gamma}_{k'l_-}^{+}}\right)+\ln^2\left(1-\tilde{\gamma}_{k'l_-}^{-}\right)-\ln^2\left(\tilde{\gamma}_{k'l_-}^{-}\right)\right.\\ &+\ln^2\left(\tilde{\gamma}_{k'l_-}^{+}\right)-\ln^2\left(1-\tilde{\gamma}_{k'l_-}^{+}\right)+\mathrm{Li}_2\left(\frac{\tilde{\lambda}_{k'l}}{1-\tilde{\gamma}_{k'l_-}^{-}}\right)+\mathrm{Li}_2\left(-\frac{\tilde{\gamma}_{k'l_-}^{-}}{\tilde{\lambda}_{k'l}}\right)\\ &+\frac{1}{2}\ln^2\left(\frac{\tilde{\lambda}_{k'l}}{\tilde{\gamma}_{k'l_-}^{-}}\right)+\mathrm{Li}_2\left(\frac{\tilde{\lambda}_{k'l}}{\tilde{\gamma}_{k'l_-}^{+}}\right)+\mathrm{Li}_2\left(\frac{\tilde{\gamma}_{k'l_-}^{+}-1}{\tilde{\lambda}_{k'l}}\right)-\frac{5\pi^2}{3}\\ &\left.-\ln\left(\frac{\tilde{\gamma}_{k'l_-}^{-}(1-\tilde{\gamma}_{k'l_-}^{+})}{(1-\tilde{\gamma}_{k'l_-}^{-})\tilde{\gamma}_{k'l_-}^{+}}\right)\ln\left(\frac{(k'+l)^2}{m^2}\right)\right\},\end{aligned} \tag{6.53}$$

where

$$\tilde{\lambda}_{k'l_-} = \frac{2\sqrt{(k'\cdot l_-)^2-m^2m_l^2}}{(k'+l_-)^2}, \quad \tilde{\gamma}_{k'l_-}^{\pm} = \left[\frac{m_l^2+k'\cdot l_-}{(k'+l_-)^2}\pm\frac{\tilde{\lambda}_{k'l_-}}{2}\right]. \tag{6.54}$$

We consider the two limits like before. In the limit of a small electron mass, we find for the infrared divergent contribution

$$\delta_{c_3,\mathrm{IR}}^{\mathrm{BH,SL}} = \frac{-\alpha_{\mathrm{em}}}{\pi}\ln\left(\frac{2k'\cdot l_-}{m\,m_l}\right)\left[\frac{1}{\epsilon_{\mathrm{IR}}}-\gamma_E+\ln\left(\frac{4\pi\mu^2}{m^2}\right)\right], \tag{6.55}$$

and for the finite contribution

$$\delta_{c_3}^{\mathrm{BH,SL}} = \frac{\alpha_{\mathrm{em}}}{2\pi}\left\{\frac{1}{2}\ln^2\left(\frac{2k'l_-}{m_l^2}\right)-\ln^2\left(\frac{2k'l_-}{m^2}\right)+\ln^2\left(\frac{2k'l_-}{2k'l_-+m_l^2}\right)-\ln^2\left(\frac{m_l^2}{2k'l_-+m_l^2}\right)\right.$$

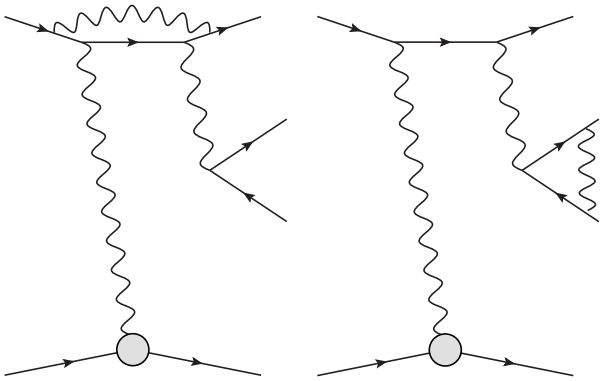

FIGURE 6.3.3: Virtual corrections of class (a) (left) and class (b) (right) to the timelike BH process. One also has to consider the corresponding counter-term diagrams. For the correction, the crossed diagrams with Δ and q' interchanged yield the same result.

$$+\frac{1}{2}\ln^2\left(\frac{4(k'l_-)^2}{m^2(2k'l_-+m_l^2)}\right)+\ln\left(\frac{m^2m_l^2}{4(k'l_-)^2}\right)\ln\left(\frac{m^2}{2k'l_-+m_l^2}\right)$$
$$+\mathrm{Li}_2\left(-\frac{m_l^2}{2k'l_-}\right)+\mathrm{Li}_2\left(\frac{2k'l_-}{2k'l_-+m_l^2}\right)-\frac{3}{2}\pi^2\Big\}. \tag{6.56}$$

Considering electron production, $m_l = m$, we find

$$\delta_{c_3,\mathrm{IR}}^{\mathrm{BH,SL}} = -\frac{\alpha_{\mathrm{em}}}{\pi}\ln\left(\frac{2k'\cdot l_-}{m^2}\right)\left[\frac{1}{\epsilon_{\mathrm{IR}}}-\gamma_E+\ln\left(\frac{4\pi\mu^2}{m^2}\right)\right],$$
$$\delta_{c_3}^{\mathrm{BH,SL}} = \frac{\alpha_{\mathrm{em}}}{\pi}\left\{\frac{1}{2}\ln^2\frac{2k'\cdot l_-}{m^2}-\frac{2}{3}\pi^2\right\}. \tag{6.57}$$

For the second diagram in the second row of Fig. 6.3.2, we can derive the correction in the soft-photon approximation from the previous result, leading to

$$\delta_{c_4}^{\mathrm{BH,SL}} = -\delta_{c_3}^{\mathrm{BH,SL}}\Big|_{l_-\to l_+}. \tag{6.58}$$

Note that from Eqs. (6.47), (6.49), (6.57) and (6.58) we can see that the sum of all class (c) corrections is *anti-symmetric* with respect to interchanging $l^+ \leftrightarrow l^-$. This is in contrast to the contributions of class (a) and (b), which are *symmetric* with respect to the interchange of l^+ and l^-.

6.3.2 Corrections to the timelike Bethe-Heitler process

In this section, we give the soft-photon corrections for the timelike process, which lead to exactly the same corrections as in the spacelike process.

The first diagram in Fig. 6.3.3 is given by

$$\mathcal{M}_a^{\mathrm{BH,TL}} = \frac{e^6}{s_{ll}t}\bar{N}(p')\,\Gamma^\alpha(t)N(p)\,\bar{u}(l_-)\,\gamma^\mu v(l_+)\,\mu^{4-d}$$
$$\times\int\frac{d^dl}{(2\pi)^d}\frac{\bar{u}(k')\,\gamma_\beta\left(\not{k}'+\not{l}+m\right)\gamma_\mu\left(\not{k}'+\not{q}'+\not{l}+m\right)\gamma_\alpha\left(\not{k}+\not{l}+m\right)\gamma^\beta u(k)}{[(k'+l)^2-m^2]\,[(k'+q'+l)^2-m^2]\,[(k+l)^2-m^2]\,[l^2]}, \tag{6.59}$$

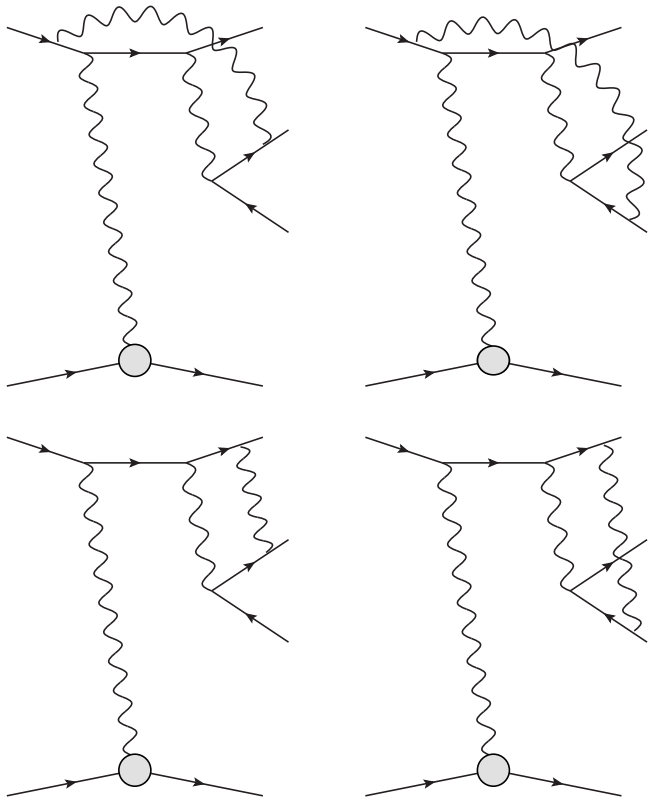

FIGURE 6.3.4: Contributing diagrams from class (c) for the timelike Bethe-Heitler process. The crossed diagrams with Δ and q' interchanged yield the same result.

which in the soft-photon limit reduces to

$$\begin{aligned}\mathcal{M}_a^{\mathrm{BH,TL}} &= -ie^2 4(k\cdot k')\mu^{4-d}\mathcal{M}_0^{\mathrm{BH,TL}}\int\frac{d^dl}{(2\pi)^d}\frac{1}{[l^2]\,[l^2+2k\cdot l]\,[l^2+2k'\cdot l]}\\ &= \frac{e^2}{4\pi^2}(k\cdot k')C_0\left(m^2,(k-k')^2,m^2;0,m^2,m^2\right)\mathcal{M}_0^{\mathrm{BH,TL}}.\end{aligned} \tag{6.60}$$

After adding the counterterms, on the level of the cross section, the same correction as for the spacelike process is found:

$$\delta_a^{\mathrm{BH,TL}} = \delta_a^{\mathrm{BH,SL}}. \tag{6.61}$$

By the same argument, the second diagram in Fig. 6.3.3, including counterterms, yields the same correction as for the spacelike process from Eqs. (6.37) and (6.38):

$$\delta_b^{\mathrm{BH,TL}} = \delta_b^{\mathrm{BH,SL}}. \tag{6.62}$$

The same argument also applies to the four diagrams of class (c), shown in Fig. 6.3.4, which yield the same correction as for the spacelike process:

$$\begin{aligned}\delta_{c_1}^{\mathrm{BH,TL}} &= \delta_{c_1}^{\mathrm{BH,SL}}, \quad \delta_{c_2}^{\mathrm{BH,TL}} = \delta_{c_2}^{\mathrm{BH,SL}},\\ \delta_{c_3}^{\mathrm{BH,TL}} &= \delta_{c_3}^{\mathrm{BH,SL}}, \quad \delta_{c_4}^{\mathrm{BH,TL}} = \delta_{c_4}^{\mathrm{BH,SL}}.\end{aligned} \tag{6.63}$$

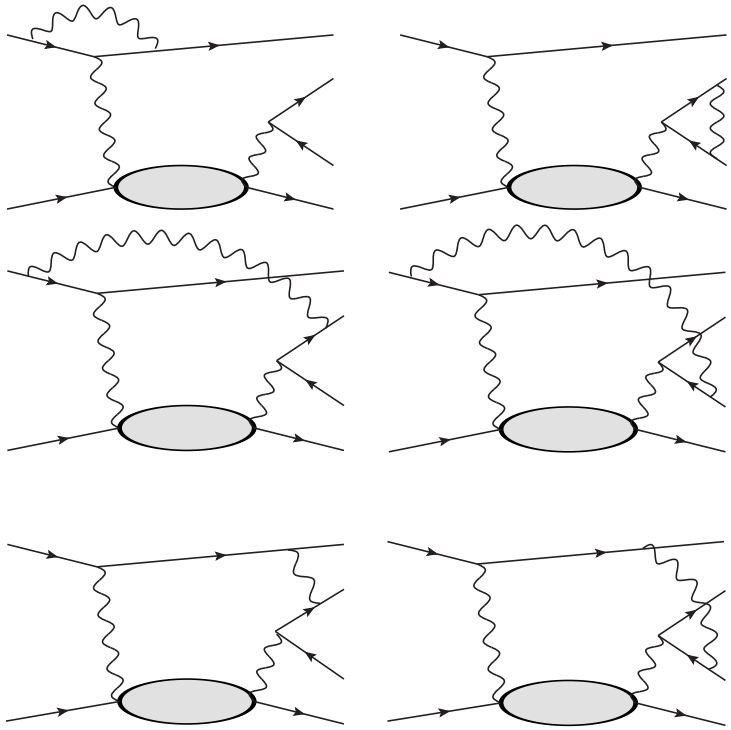

FIGURE 6.3.5: Virtual corrections of class (a) (top left), class (b) (top right), and class (c) (lower two rows) to the dVCS process. One also has to consider the corresponding counter-term diagrams. The crossed diagrams with q and q' interchanged yield the same result.

6.3.3 Corrections to the Compton process

In this section, we derive the corrections for the Compton scattering, which in the soft-photon limit lead again to the same results as before for space-like and time-like Bethe-Heitler process. Therefore, on the level of the cross section, the correction in the soft-photon approximation can be factorized for the total process, and is given by

$$\begin{aligned} \delta_a^{\mathrm{dVCS}} &= \delta_a^{\mathrm{BH,SL}}, \quad \delta_b^{\mathrm{dVCS}} = \delta_b^{\mathrm{BH,SL}}, \\ \delta_{c1}^{\mathrm{dVCS}} &= \delta_{c1}^{\mathrm{BH,SL}}, \quad \delta_{c2}^{\mathrm{dVCS}} = \delta_{c2}^{\mathrm{BH,SL}}, \\ \delta_{c3}^{\mathrm{dVCS}} &= \delta_{c3}^{\mathrm{BH,SL}}, \quad \delta_{c4}^{\mathrm{dVCS}} = \delta_{c4}^{\mathrm{BH,SL}}. \end{aligned} \tag{6.64}$$

6.3.4 Sum of all virtual soft-photon corrections

Adding all contributions from classes (a), (b) and (c), we define the virtual soft-photon corrections on the cross section as

$$d\sigma_{s;v} = d\sigma_0(1 + \delta_{s;v}). \tag{6.65}$$

The correction can be separated in the IR divergent contribution

$$\begin{aligned} \delta_{s;v}^{\mathrm{IR}} = \frac{\alpha_{\mathrm{em}}}{\pi} \Bigg\{ \Bigg[\frac{1}{\epsilon_{\mathrm{IR}}} - \gamma_E + \ln\left(\frac{4\pi\mu^2}{m^2}\right) \Bigg] \\ \times \left[\ln\left(\frac{Q^2}{m^2}\right) + \ln\left(\frac{2k\cdot l_-}{m\, m_l}\right) - \ln\left(\frac{2k\cdot l_+}{m\, m_l}\right) - \ln\left(\frac{2k'\cdot l_-}{m\, m_l}\right) + \ln\left(\frac{2k'\cdot l_+}{m\, m_l}\right) - 1 \right] \end{aligned}$$

$$+\left[\left(\frac{1+\beta}{1-\beta}\right)\ln\left(\frac{1+\beta}{1-\beta}\right)-1\right]\left[\frac{1}{\epsilon_{\mathrm{IR}}}-\gamma_E+\ln\left(\frac{4\pi\mu^2}{m_l^2}\right)\right]\Bigg\}, \tag{6.66}$$

and the finite contribution

$$\delta_{s;v}=\delta_a+\delta_b+\delta_{c_1}+\delta_{c_2}+\delta_{c_3}+\delta_{c_4}. \tag{6.67}$$

For convenience of the reader, we summarize all formulas derived in the previous sections:

$$\delta_a=-\frac{\alpha_{\mathrm{em}}}{\pi}\left\{\frac{1}{2}\ln^2\left(\frac{Q^2}{m^2}\right)-\frac{\pi^2}{6}\right\}, \tag{6.68}$$

$$\delta_b=-\frac{\alpha_{\mathrm{em}}}{\pi}\left(\frac{1+\beta^2}{2\beta}\right)\left\{2\,\mathrm{Li}_2\left(\frac{2\beta}{\beta+1}\right)+\frac{1}{2}\ln^2\left(\frac{1-\beta}{1+\beta}\right)-\pi^2\right\}, \tag{6.69}$$

$$\begin{aligned}\delta_{c_1}=\frac{\alpha_{\mathrm{em}}}{2\pi}\Bigg\{&\frac{1}{2}\ln^2\left(\frac{m^2}{2k\cdot l_-}\right)-\frac{1}{2}\ln^2\left(\frac{2k\cdot l_-}{2k\cdot l_- - m_l^2}\right)\\&+\frac{1}{2}\ln^2\left(\frac{m_l^2}{2k\cdot l_- - m_l^2}\right)-\ln\left(\frac{4(k\cdot l_-)^2}{m^2m_l^2}\right)\ln\left(\frac{2k\cdot l_-}{2k\cdot l_- - m_l^2}\right)\\&+\mathrm{Li}_2\left(\frac{2k\cdot l_- - m_l^2}{2k\cdot l_-}\right)-\mathrm{Li}_2\left(\frac{m_l^2}{2k\cdot l_-}\right)+\frac{\pi^2}{6}\Bigg\},\end{aligned} \tag{6.70}$$

$$\delta_{c_2}=-\delta_{c_1}\Big|_{l_-\to l_+}, \tag{6.71}$$

$$\begin{aligned}\delta_{c_3}=\frac{\alpha_{\mathrm{em}}}{2\pi}\Bigg\{&\frac{1}{2}\ln^2\left(\frac{2k'\cdot l_-}{m_l^2}\right)+\ln^2\left(\frac{2k'\cdot l_-}{2k'\cdot l_- + m_l^2}\right)-\ln^2\left(\frac{m_l^2}{2k'\cdot l_- + m_l^2}\right)\\&+\frac{1}{2}\ln^2\left(\frac{4(k'\cdot l_-)^2}{m^2(2k'\cdot l_- + m_l^2)}\right)-\ln^2\left(\frac{2k'\cdot l_-}{m^2}\right)\\&+\ln\left(\frac{m^2m_l^2}{4(k'\cdot l_-)^2}\right)\ln\left(\frac{m^2}{2k'\cdot l_- + m_l^2}\right)+\mathrm{Li}_2\left(\frac{-m_l^2}{2k'\cdot l_-}\right)\\&+\mathrm{Li}_2\left(\frac{2k'\cdot l_-}{2k'\cdot l_- + m_l^2}\right)-\frac{3}{2}\pi^2\Bigg\},\end{aligned} \tag{6.72}$$

$$\delta_{c_4}=-\delta_{c_3}\Big|_{l_-\to l_+}. \tag{6.73}$$

In the case of e^-e^+ production, the formula simplifies significantly to

$$\begin{aligned}\delta_{s;v}=-\frac{\alpha_{\mathrm{em}}}{2\pi}\Bigg\{&\ln^2\left(\frac{Q^2}{m^2}\right)+\ln^2\left(\frac{s_{ll}}{m^2}\right)-\ln^2\left(\frac{2k'\cdot l_-}{m^2}\right)+\ln^2\left(\frac{2k'\cdot l_+}{m^2}\right)\\&+\ln^2\left(\frac{2k\cdot l_-}{m^2}\right)-\ln^2\left(\frac{2k\cdot l_+}{m^2}\right)-\frac{5}{3}\pi^2\Bigg\}.\end{aligned} \tag{6.74}$$

6.4 Soft-photon bremsstrahlung

Like in the TCS case discussed in Section 5.4, we need to include soft bremstrahlung to cancel the IR divergences of the virtual soft-photon corrections. On the level of the cross section, the IR divergences cancel, resulting in a finite physical result. Since in the present chapter, we study the process in which the proton remains unobserved, while the dilepton pair is measured, the bremstrahlung integral has to be performed in the rest frame of the unobserved proton and soft-photon. Defining the missing

momentum $p_m \equiv p' + k_\gamma$, this frame is defined by the condition $\vec{p}_m = 0$. The bremstrahlung contribution to the cross section is then given by

$$d\sigma_{s;r} = d\sigma_0 \frac{-e^2}{(2\pi)^3} \int_{|\vec{k}_\gamma|<\Delta E_s} \frac{d^3\vec{k}_\gamma}{2k_\gamma^0} \left\{ \frac{m_l^2}{(k_\gamma\cdot l_+)^2} + \frac{m_l^2}{(k_\gamma\cdot l_-)^2} + \frac{m^2}{(k_\gamma\cdot k)^2} + \frac{m^2}{(k_\gamma\cdot k')^2} \right.$$
$$- \frac{2l_+\cdot l_-}{(k_\gamma\cdot l_+)(k_\gamma\cdot l_-)} - \frac{2k'\cdot l_+}{(k_\gamma\cdot k')(k_\gamma\cdot l_+)} + \frac{2k'\cdot l_-}{(k_\gamma\cdot k')(k_\gamma\cdot l_-)}$$
$$\left. - \frac{2k'\cdot k}{(k_\gamma\cdot k)(k_\gamma\cdot k')} - \frac{2k\cdot l_-}{(k_\gamma\cdot k)(k_\gamma\cdot l_-)} + \frac{2k\cdot l_+}{(k_\gamma\cdot k)(k_\gamma\cdot l_+)} \right\}, \quad (6.75)$$

where the maximal soft-photon energy in that frame is denoted by ΔE_s. The expression after performing the integration in Eq. (6.75) is lengthy and complicated in the general case. Here, we give explicit results only in the limit of a small electron mass, i.e. we only keep the logarithmic dependence on m. For the IR divergent contribution, we then find

$$\delta_{\mathrm{s;r}}^{\mathrm{IR}} = -\frac{\alpha_{\mathrm{em}}}{\pi} \left\{ \left[\frac{1}{\epsilon_{\mathrm{IR}}} - \gamma_E + \ln\left(\frac{4\pi\mu^2}{m^2}\right) \right] \right.$$
$$\times \left[\ln\left(\frac{Q^2}{m^2}\right) + \ln\left(\frac{2k\cdot l_-}{m\, m_l}\right) - \ln\left(\frac{2k'\cdot l_-}{m\, m_l}\right) + \ln\left(\frac{2k'\cdot l_+}{m\, m_l}\right) - \ln\left(\frac{2k\cdot l_+}{m\, m_l}\right) - 1 \right]$$
$$\left. + \left[\left(\frac{1+\beta^2}{2\beta}\right) \ln\left(\frac{1+\beta}{1-\beta}\right) - 1 \right] \left[\frac{1}{\epsilon_{\mathrm{IR}}} - \gamma_E + \ln\left(\frac{4\pi\mu^2}{m_l^2}\right) \right] \right\}, \quad (6.76)$$

while for the finite part we find

$$\delta_{\mathrm{s;r}} \equiv \delta_a^{\mathrm{s;r}} + \delta_b^{\mathrm{s;r}} + \delta_c^{\mathrm{s;r}}, \quad (6.77)$$

where

$$\delta_a^{\mathrm{s;r}} = -\frac{\alpha_{\mathrm{em}}}{\pi} \left\{ \ln\left(\frac{4(\Delta E_s)^2}{m^2}\right) \left[1 - \ln\left(\frac{Q^2}{m^2}\right) \right] + \frac{1}{2}\ln\left(\frac{m^2}{4\tilde{E}'^2}\right) + \frac{1}{2}\ln\left(\frac{m^2}{4\tilde{E}^2}\right) \right.$$
$$\left. + \frac{1}{4}\ln^2\left(\frac{4\tilde{E}'^2}{m^2}\right) + \frac{1}{4}\ln^2\left(\frac{4\tilde{E}^2}{m^2}\right) + \mathrm{Li}_2\left(1 - \frac{4\tilde{E}\tilde{E}'}{Q^2}\right) + \frac{\pi^2}{3} \right\}, \quad (6.78)$$

$$\delta_b^{\mathrm{s;r}} = -\frac{\alpha_{\mathrm{em}}}{\pi} \left\{ \ln\left(\frac{4(\Delta E_s)^2}{m_l^2}\right) \left[1 - \left(\frac{1+\beta^2}{2\beta}\right) \ln\left(\frac{1+\beta}{1-\beta}\right) \right] + \frac{1}{2\tilde{\beta}_-} \ln\left(\frac{1-\tilde{\beta}_-}{1+\tilde{\beta}_-}\right) \right.$$
$$+ \frac{1}{2\tilde{\beta}_+} \ln\left(\frac{1-\tilde{\beta}_+}{1+\tilde{\beta}_+}\right) - \left(\frac{1+\beta^2}{2\beta}\right) \left[\frac{1}{4}\ln^2\left(\frac{1-\tilde{\beta}_-}{1+\tilde{\beta}_-}\right) - \frac{1}{4}\ln^2\left(\frac{1-\tilde{\beta}_+}{1+\tilde{\beta}_+}\right) \right.$$
$$+ \mathrm{Li}_2\left(1 - \left(\frac{1+\beta}{1-\beta}\right)\frac{\tilde{E}_-}{v}(1+\tilde{\beta}_-)\right) + \mathrm{Li}_2\left(1 - \left(\frac{1+\beta}{1-\beta}\right)\frac{\tilde{E}_-}{v}(1-\tilde{\beta}_-)\right)$$
$$\left. \left. - \mathrm{Li}_2\left(1 - \frac{\tilde{E}_+}{v}(1+\tilde{\beta}_+)\right) - \mathrm{Li}_2\left(1 - \frac{\tilde{E}_+}{v}(1-\tilde{\beta}_+)\right) \right] \right\}, \quad (6.79)$$

$$\delta_c^{\mathrm{s;r}} = -\frac{\alpha_{\mathrm{em}}}{\pi} \left\{ \ln\left(\frac{4(\Delta E_s)^2}{m^2}\right) \ln\left(\frac{k'\cdot l_-}{k\cdot l_-}\right) - \mathrm{Li}_2\left(1 - \frac{\tilde{E}'}{k'\cdot l_-}\left(\tilde{E}_- - \sqrt{\tilde{E}_-^2 - m_l^2}\right)\right) \right.$$
$$+ \mathrm{Li}_2\left(1 - \frac{\tilde{E}}{k\cdot l_-}\left(\tilde{E}_- - \sqrt{\tilde{E}_-^2 - m_l^2}\right)\right) - \mathrm{Li}_2\left(1 - \frac{\tilde{E}'}{k'\cdot l_-}\left(\tilde{E}_- + \sqrt{\tilde{E}_-^2 - m_l^2}\right)\right)$$
$$\left. + \mathrm{Li}_2\left(1 - \frac{\tilde{E}}{k\cdot l_-}\left(\tilde{E}_- + \sqrt{\tilde{E}_-^2 - m_l^2}\right)\right) \right\} - \left(l_- \to l_+\right). \quad (6.80)$$

In the above, we defined

$$v \equiv \frac{\beta s_{ll}}{2(\tilde{E}_- - \frac{1-\beta}{1+\beta}\tilde{E}_+)}, \quad \tilde{\beta}_\mp = \left(1 - m_l^2/\tilde{E}_\mp^2\right)^{1/2}, \tag{6.81}$$

where $\tilde{E}_\pm$ denotes the energy of the lepton with momentum $l^\pm$ in the rest frame of the soft-photon and recoil proton, and we denote by $\tilde{E}$ ($\tilde{E}'$) the energy of the electron with momentum k (k') in the same system.

Adding Eqs. (6.66) and (6.76), we verify that the IR divergences from real and virtual soft-photon corrections cancel on the level of cross section.

As mentioned before, the integration of the soft-photon bremsstrahlung is performed up to a small energy cut-off ΔE_s. This cut-off can be related to the experimental resolution of the detector. In the frame with $\vec{p}_m = 0$, we find

$$\Delta E_s = \Delta \left(\frac{p_m^2 - M^2}{2\sqrt{p_m^2}} \right) \approx \frac{\Delta p_m^2}{2M}, \tag{6.82}$$

where to first order we have used $p_m^2 \approx M^2$ in the denominator, and where Δp_m^2 denotes the resolution in the missing mass squared. In order to express ΔE_s in terms of Lab quantities, one needs to calculate the missing mass in that frame. Neglecting the lepton masses, we find

$$\begin{aligned} p_m^2 = (q - q' + p)^2 &= M^2 + s_{ll} - Q^2 - 2q \cdot q' + 2p \cdot (q - q') \\ &= \Big[M^2 + 2Mq^0 + 4E_- E_+ \sin^2 \theta_{ll}/2 \\ &\quad - 4EE' \sin^2 \theta_{kk'}/2 + 2|\vec{q}||\vec{q}'| \cos \theta_{\gamma\gamma} \\ &\quad - 2(q^0 + M)(E_+ + E_-) \Big]_{\text{Lab}}, \end{aligned} \tag{6.83}$$

where all quantities on the rhs have to be given in the Lab frame, where $\theta_{kk'}$ denotes the scattering angle between the incoming electron with momentum k and the outgoing with momentum k', and where θ_{ll} denotes the Lab angle between the lepton pair momenta. Eqs. (6.82) and (6.83) allow one to express the maximal soft-photon energy ΔE_s (defined in the system $\vec{p}_m = 0$) in terms of Lab quantities and detector resolutions.

In the following, it will be convenient to express the energies $\tilde{E}_\pm$, $\tilde{E}$ and $\tilde{E}'$ in terms of kinematic invariants. For the case of a large lepton mass, for which the formulas are lengthy and complicated, we use the expressions given in Appendix 6.A and then boost to the rest frame of the recoiled proton and soft-photon to calculate the energies numerically. In the case of electron-pair production in which we can neglect the mass m compared to other quantities, the formulas become more compact. In that case, we also find more compact expressions for the bremstrahlung corrections. We find

$$\begin{aligned} \delta_{s;r} = -\frac{\alpha_{\text{em}}}{\pi} \Bigg\{ & \ln\left(\frac{4(\Delta E_s)^2}{m^2}\right) \left[2 - \ln\left(\frac{Q^2}{m^2}\right) - \ln\frac{s_{ll}}{m^2} + \ln\frac{k' \cdot l_-}{k \cdot l_-} - \ln\frac{k' \cdot l_+}{k \cdot l_+} \right] \\ & - \frac{1}{2}\left[\ln\frac{4\tilde{E}_+^2}{m^2} + \ln\frac{4\tilde{E}_-^2}{m^2} + \ln\frac{4\tilde{E}^2}{m^2} + \ln\frac{4\tilde{E}'^2}{m^2} \right] \\ & + \frac{1}{4}\left[\ln^2\frac{4\tilde{E}_-^2}{m^2} + \ln^2\frac{4\tilde{E}_+^2}{m^2} + \ln^2\frac{4\tilde{E}^2}{m^2} + \ln^2\frac{4\tilde{E}'^2}{m^2} \right] \\ & + \text{Li}_2\left(1 - \frac{4\tilde{E}_-\tilde{E}_+}{s_{ll}}\right) + \text{Li}_2\left(1 - \frac{4\tilde{E}\tilde{E}'}{Q^2}\right) + \text{Li}_2\left(1 - \frac{2\tilde{E}'\tilde{E}_+}{k' \cdot l_+}\right) \end{aligned}$$

$$- \mathrm{Li}_2\left(1 - \frac{2\tilde{E}'\tilde{E}_-}{k'\cdot l_-}\right) + \mathrm{Li}_2\left(1 - \frac{2\tilde{E}\tilde{E}_-}{k\cdot l_-}\right) - \mathrm{Li}_2\left(1 - \frac{2\tilde{E}\tilde{E}_+}{k\cdot l_+}\right) + \frac{2}{3}\pi^2\Bigg\}. \tag{6.84}$$

The energies $\tilde{E}_\pm$, $\tilde{E}$ and $\tilde{E}'$ in the rest frame of the recoil proton + soft photon are given by

$$\begin{aligned}
\tilde{E}_\mp &= \frac{p_m\cdot l_\mp}{\sqrt{p_m^2}} \approx \frac{1}{M}(q+p-q')\cdot l_\mp \\
&= \frac{1}{4M}\left\{(W^2-M^2-s_{ll}) \pm [(W^2-M^2-s_{ll})^2 - 4M^2 s_{ll}]^{1/2}\beta\cos\theta_l^*\right\}, \qquad (6.85)\\
\tilde{E} &= \frac{p_m\cdot k}{\sqrt{p_m^2}} \approx \frac{1}{M}(q+p-q')\cdot k \\
&= \frac{1}{2M\left((W^2-M^2+Q^2)^2+4M^2Q^2\right)}\Bigg\{Q^2\Big[t(W^2+M^2+Q^2) - 2M^2(Q^2+s_{ll})\Big] \\
&+ (s-M^2)\Big[(W^2-M^2)(W^2-M^2+Q^2-s_{ll}+t) + Q^2(-s_{ll}-t+4M^2)\Big] \\
&+ 2Q\cos(\Phi)\Big[s\left(s-M^2-Q^2\right) - W^2\left(s-M^2\right)\Big]^{1/2} \\
&\times\Big[-t(W^2-M^2)(W^2-M^2+Q^2-s_{ll}+t) - M^2\Big((Q^2-s_{ll}+t)^2+4s_{ll}Q^2\Big)\Big]^{1/2}\Bigg\}, \qquad (6.86)
\end{aligned}$$

$$\tilde{E}' = \tilde{E} - \frac{W^2-M^2-s_{ll}+t}{2M}. \tag{6.87}$$

6.5 Results

6.5.1 Observables

We implement all amplitudes in our `C++` code to calculate numerically helicity amplitudes and interference terms. We use our setup to study the $e^-p \to e^-pl^-l^+$ process, including the first-order radiative corrections in both, the low- and high-energy regimes. For both cases, we study the effect of these corrections in the soft-photon approximation on the cross section, on the forward-backward asymmetry A_{FB}, as well as on the beam spin asymmetry $A_\odot$. These asymmetries are defined in analogy to the asymmetries in the TCS case (cf. Eqs. (5.100) and (5.101)) as

$$A_{FB} = \frac{d\sigma_{\theta_l^*,\phi_l^*} - d\sigma_{\pi-\theta_l^*,\phi_l^*+\pi}}{d\sigma_{\theta_l^*,\phi_l^*} + d\sigma_{\pi-\theta_l^*,\phi_l^*+\pi}}, \tag{6.88}$$

$$A_\odot = \frac{d\sigma^+ - d\sigma^-}{d\sigma^+ + d\sigma^-}, \tag{6.89}$$

where $d\sigma_{\theta_l^*,\phi_l^*}$ in A_{FB} stands for the unpolarized cross section measured at lepton angles θ_l^* and ϕ_l^* (defined in the l^-l^+ rest frame), and where $d\sigma^\pm$ in $A_\odot$ stand for the polarized cross sections for a polarized electron beam with helicity $\pm 1/2$ respectively. In the following we show plots ranging from $\theta_l^* = -180°$ to $\theta_l^* = +180°$. This allows us to show forward and backward cross sections economically in one plot, since $d\sigma(\theta_l^*, \phi_l^* + \pi) = d\sigma(-\theta_l^*, \phi_l^*)$. The forward-backward asymmetry can therefore also be written as:

$$A_{FB} = \frac{d\sigma(\theta_l^*,\phi_l^*) - d\sigma(\pi-\theta_l^*,\pi+\phi_l^*)}{d\sigma(\theta_l^*,\phi_l^*) + d\sigma(\pi-\theta_l^*,\pi+\phi_l^*)} = \frac{d\sigma(\theta_l^*,\phi_l^*) - d\sigma(\theta_l^*-\pi,\phi_l^*)}{d\sigma(\theta_l^*,\phi_l^*) + d\sigma(\theta_l^*-\pi,\phi_l^*)}, \tag{6.90}$$

and, including radiative correction explicitly, it is given by

$$A_{FB} = \frac{d\sigma_0(\theta_l^*)(1+\delta(\theta_l^*)) - d\sigma_0(\theta_l^*-\pi)(1+\delta(\theta_l^*-\pi))}{d\sigma_0(\theta_l^*)(1+\delta(\theta_l^*)) + d\sigma_0(\theta_l^*-\pi)(1+\delta(\theta_l^*-\pi))}. \tag{6.91}$$

From Eq. (6.91) one can see that corrections that are symmetric under the interchange $l^- \leftrightarrow l^+$, corresponding with $\theta_l^* \leftrightarrow \theta_l^* - \pi$, drop out in the ratio. Therefore, to first order, only corrections of class (c) give a contribution to the asymmetry:

$$A_{FB} = \frac{A_{FB}^0 + \delta_c/(1+\delta_a+\delta_b)}{1 + A_{FB}^0\,\delta_c/(1+\delta_a+\delta_b)} \approx A_{FB}^0 + \delta_c\left(1 - (A_{FB}^0)^2\right), \tag{6.92}$$

where A_{FB}^0 denotes the uncorrected asymmetry.

On the other hand, the radiatively corrected beam spin asymmetry, given by

$$A_\odot = \frac{d\sigma^+(1+\delta^+) - d\sigma^-(1+\delta^-)}{d\sigma^+(1+\delta^+) + d\sigma^-(1+\delta^-)}, \tag{6.93}$$

does not get modified in the soft-photon approximation, since the corrections are the same for both helicity cross sections, i.e. $\delta^+ = \delta^-$, and therefore drop out in the ratio.

In the following, we show our numerical results for the $e^- p \to e^- p l^- l^+$ observables including the first order soft-photon radiative corrections.

6.5.2 Results for dVCS observables in the $\Delta(1232)$ region

In this section, we show our results in the low-energy regime in which we choose the center-of-mass energy $W = 1.25$ GeV. We model the dVCS amplitude in terms of the Born amplitude and the first proton excitation, the $\Delta(1232)$ resonance. As was found in Ref. [15], this model can reproduce the full calculation based on empirical structure functions from Ref. [160] with an accuracy in the few per-cent range for the process $\gamma p \to e^- e^+ p$ (i.e. for a real photon). Therefore, we can safely assume that the Born + Δ-pole model describes the dVCS amplitude sufficiently well also in the virtual-photon process for sufficiently small photon virtualities.

For the dVCS model to be also accurate for the $e^- p \to e^- p e^- e^+$ process, in which we need to anti-symmetrize the full amplitude under exchange of both final electrons as given by Eq. (6.13), we choose the kinematics in such a way that also for the exchange dVCS amplitude the c.m. energy $W_{\rm ex}$ remains in the $\Delta(1232)$ resonance region, and the photon virtualities entering the exchange process remain sufficiently small. As can be seen from Fig. 6.5.1 (left panel), for the choice of an electron beam of 0.6 GeV, we find that $W_{\rm ex}$ (blue dotted curve) is roughly of the same magnitude as W (dashed red curve), varying between 1.18 and 1.33 GeV as function of θ_e^*. Note, that a larger electron beam energy leads to a larger value of $W_{\rm ex}$. From the right panel of Fig. 6.5.1, we furthermore see that both photon virtualities in the exchange dVCS amplitude, denoted by $Q_{\rm ex}$ (blue dotted curve) and $s_{ll,\rm ex}$ (green dash-dashed curve), are both below 0.18 GeV^2 for the full range of the lepton angle θ_e^*. We are thus in a kinematic regime where we can study the sensitivity of the full amplitude to the low-energy constant $b_{3,0}$ described in Section 6.2.1.

Having studied the appropriate kinematics to describe both, the direct and the exchange dVCS amplitude, within the same model, we next explore the sensitivity of the $e^- p \to e^- p l^- l^+$ observables on the low-energy constant $b_{3,0}$ introduced in the low-energy expansion of Eq. (6.22). This low-energy constant is the main unknown in the determination of the $\mathcal{O}(Q^4)$ term of the subtraction function $\bar{T}_1(0, Q^2)$ entering the theoretical calculation of the μH Lamb shift.

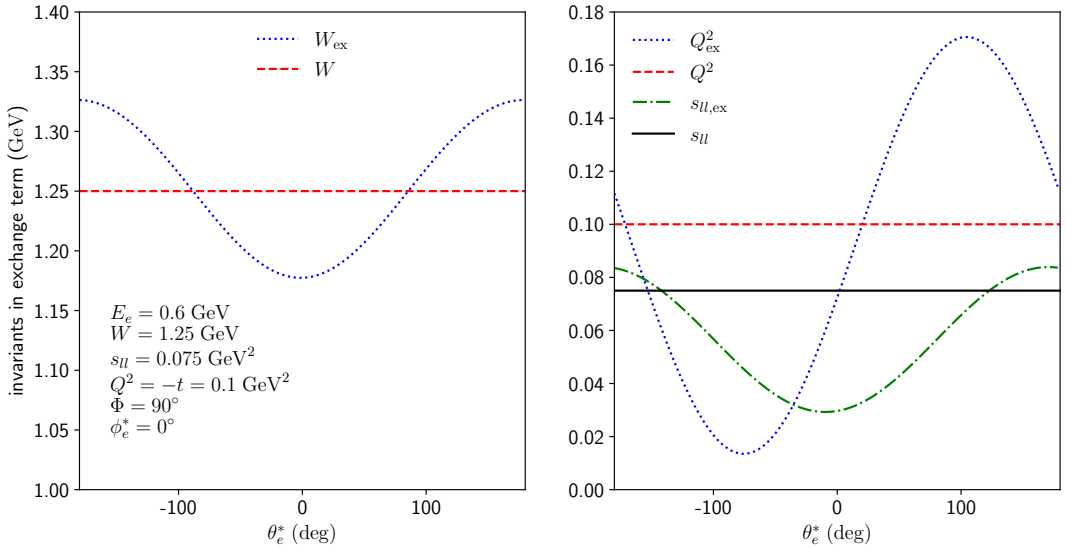

FIGURE 6.5.1: Kinematic quantities entering the exchange dVCS amplitude for the $e^-p \to e^-pe^-e^+$ process in the $\Delta(1232)$ region. In the left panel we show the c.m. energy W_{ex}, as function of θ_e^*, compared with the value $W = 1.25$ GeV of the direct process. In the right panel we compare the θ_e^* dependence of both photon virtualities in the exchange dVCS amplitude with their constant values for the direct dVCS amplitude.

In Fig. 6.5.2, we show the dependence on the lepton angle θ_l^* of the $e^-p \to e^-pl^-l^+$ differential cross section (upper panels), the forward-backward asymmetry (middle panels) as well as the beam spin asymmetry (lower panels) for both e^-e^+ and $\mu^-\mu^+$ production (left and right panels respectively). We choose the kinematics as in Fig. 6.5.1. As can be seen from the upper panel, the interference between the dVCS process with the BH process amplifies the cross section for both e^-e^+ and $\mu^-\mu^+$ production by roughly a factor of two as compared with the BH process itself. Furthermore, the spread between the different theoretical estimates for the low-energy constant $b_{3,0}$, as shown in Table 6.2.1, increases the cross sections additionally by approximately 15% in both cases.

We also study the effect of the soft-photon radiative corrections on the cross section, as given by Eqs. (6.67) to (6.73), (6.77) to (6.80) and (6.84). For the real soft-photon emission correction, we choose the soft-photon energy cut-off of $\Delta E_s = 0.01$ GeV, which corresponds to approximately 1.5% of the lepton beam energy. As can be seen from Fig. 6.5.2, the effect of the first-order radiative corrections is found to be quite sizeable on the level of cross sections. In the case of e^-e^+ production, the effect leads to a decrease of the cross section by around 30%, whereas for $\mu^-\mu^+$ production it leads to a decrease of the order of 15%. Therefore, although the cross section by itself has a relatively high sensitivity on the low-energy constant $b_{3,0}$, for an experimental extraction of $b_{3,0}$ the inclusion of the radiative corrections is imperative. Comparable importance of the radiative corrections was also found in the extraction of the proton generalized polarizabilities from the cross sections of the VCS process $e^-p \to e^-p\gamma$ [7, 158].

The situation is different for the asymmetries. For the forward-backward asymmetry A_{FB}, we find for the kinematics of Fig. 6.5.2 only a small sensitivity to the dVCS amplitude and its underlying hadronic model. However, this is mainly due to

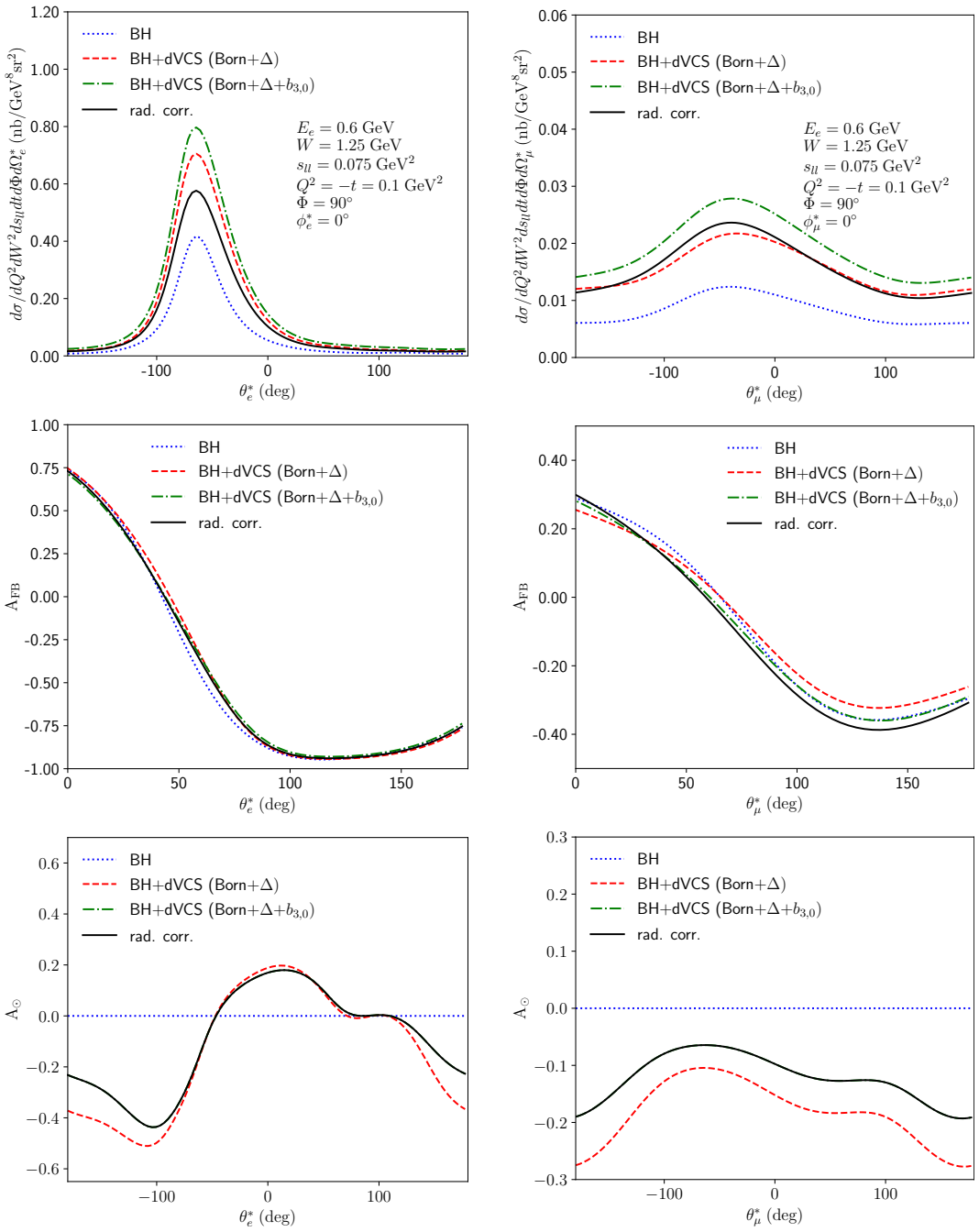

FIGURE 6.5.2: θ_l^* dependence of the $e^-p \to e^-pl^-l^+$ cross section (upper panels), forward-backward asymmetry (middle panels) and beam spin asymmetry (lower panels) for e^-e^+ production (left panels) and $\mu^-\mu^+$ production (right panels) in the $\Delta(1232)$ region, for $\Phi = 90°$. The curves show the predictions for BH and BH + dVCS for two models showing the sensitivity to the low-energy constant $b_{3,0}$. The black solid curves show the effect of the radiative corrections, for the hadronic model of the green dashed-dotted curves (these curves exactly coincide in the lower panels).

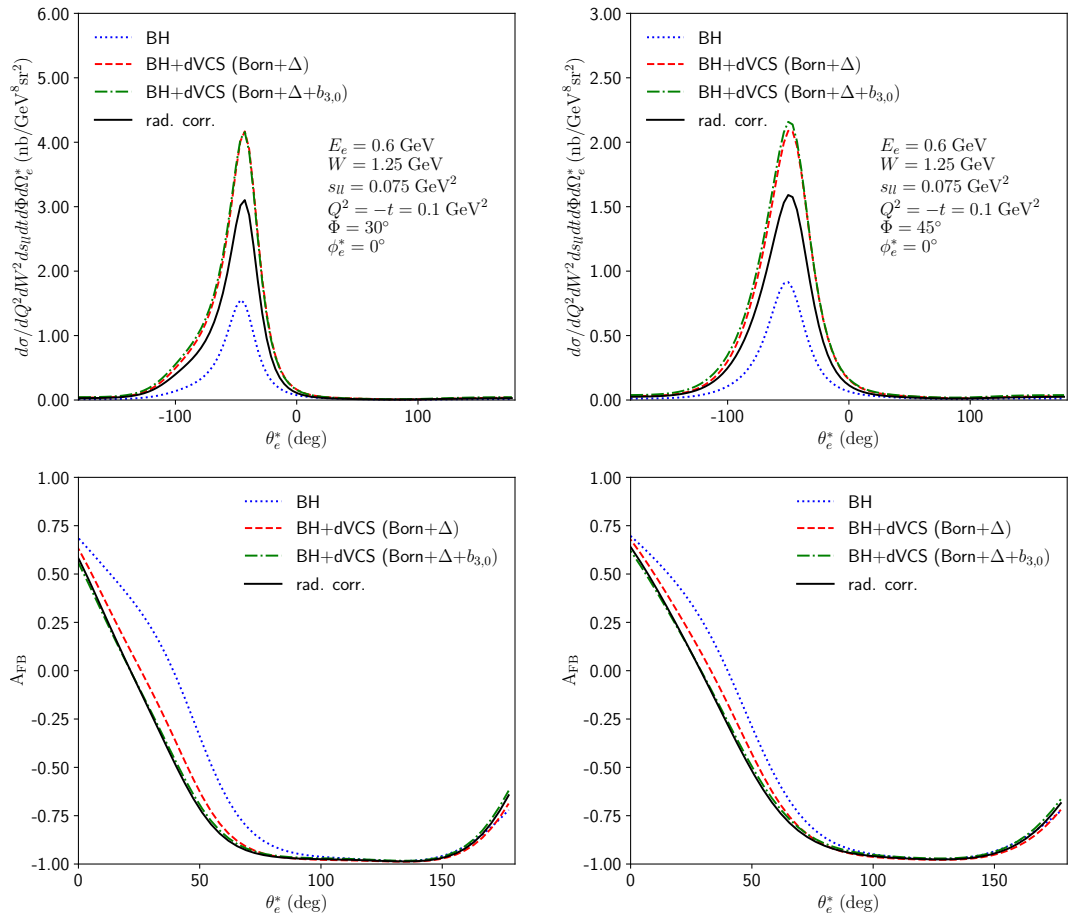

FIGURE 6.5.3: θ_e^* dependence of the $e^-p \to e^-pe^-e^+$ cross section (upper panels) and forward-backward asymmetry (lower panels) in the $\Delta(1232)$ region for $\Phi = 30°$ (left panels) and $\Phi = 45°$ (right panels). Curve conventions as in Fig. 6.5.2.

the choice of $\Phi = 90°$, for which the forward-backward asymmetry is completely dominated by the BH process. The sensitivity can be increased by varying Φ. In Fig. 6.5.3 we show the cross sections and forward-backward asymmetries for the same kinematics, but for smaller angles between the $(\vec{k}, \vec{k}')$ and $(\vec{q}, \vec{q}')$ scattering planes in Fig. 6.1.3: $\Phi = 30°$ and $\Phi = 45°$. For these cases, we find a 20% shift of the forward-backward asymmetry for the case including the Δ-resonance compared to the BH process by itself. Including the range of theoretical values for the dVCS low-energy constant $b_{3,0}$, we find a further shift of the asymmetry of up to 5% on A_{FB}, while the inclusion of radiative corrections is found to have a very small effect, around or below the 1% range on A_{FB}.

For the beam spin asymmetry, we find a significantly higher sensitivity on $b_{3,0}$ than for the forward-backward asymmetry, as shown in the lower panels of Fig. 6.5.2. Note, that the result for Born + Δ-pole + $b_{3,0}$ (green dashed-dotted curves) and the result which in addition also includes the radiative corrections (black solid curves) coincide since in the soft-photon approximation the radiative corrections drop out in the ratio of cross sections calculated for $A_\odot$, as discussed above. Including the range of theoretical values for the dVCS low-energy constant $b_{3,0}$, leads to a shift in $A_\odot$ up to around 15% for e^-e^+ production and up to around 10% for $\mu^-\mu^+$ production.

As A_{FB} and $A_\odot$ are basically not affected by the radiative corrections, a combined analysis of the cross section, A_{FB} and $A_\odot$ holds promise to extract the dVCS low-energy constant $b_{3,0}$.

In Fig. 6.5.4 we show in more detail how the radiative corrections to the $e^-p \to e^-pe^-e^+$ process vary when the initial photon approaches the real photon limit, i.e. $Q^2 \to 0$. In this limit, only the class (b) corrections contribute. We choose the kinematics comparable to the case shown in the previous chapter, in which we studied the effect of radiative corrections for the process $\gamma p \to e^-e^+p$. There, we found corrections of roughly 8% for the full set of one-loop QED corrections (cf. Fig. 5.5.1) for the kinematics shown in Fig. 6.5.4. In the soft-photon approximation, the corrections are somewhat over-estimated, as can be seen from the blue dotted curve corresponding with a correction of roughly 13%. Comparing the blue dotted curve with the red dashed-dotted one, we see that for quasi-real photons with the virtuality of 10^{-4} to 10^{-3} GeV^2 the inclusion of all corrections is important, and the description as a real photon underestimates the corrections by $10-15$%. Note, that in the region around $Q^2 \approx 0.03$ GeV^2 the two outgoing electrons with momenta k' and l_- are becoming collinear. This explains the spiked behavior in the red dashed-dotted curve since the logarithm with the argument proportional to the scalar product $k' \cdot l_-$ is becoming large.

In Fig. 6.5.5 (upper panels), we study in more detail the relative size of the radiative corrections due to the three different diagram classes (a), (b) and (c). While for e^-e^+ production the corrections due to class (a) and (b) are dominant and negative, for $\mu^-\mu^+$ production the main correction arises from class (a) as it involves the vertex correction on the beam electron, whereas the corrections between the produced $\mu^-\mu^+$ pair are small and positive. Comparing left and right panels, one can clearly see that the biggest difference between e^-e^+ and $\mu^-\mu^+$ production is due to the corrections of class (b), which correspond with the corrections from the produced dilepton pair. Furthermore, Fig. 6.5.5 illustrates, as mentioned above, that the corrections of class (a) and (b) are symmetric under the interchange of l^+ and l^-, corresponding to the angular shift $\theta_l^* \to \theta_l^* - \pi$, while class (c) is anti-symmetric. As only class (c) contributes to the forward-backward asymmetry to lowest order, the smallness of the corrections of class (c) also explains why the A_{FB} is largely unaffected by the radiative corrections.

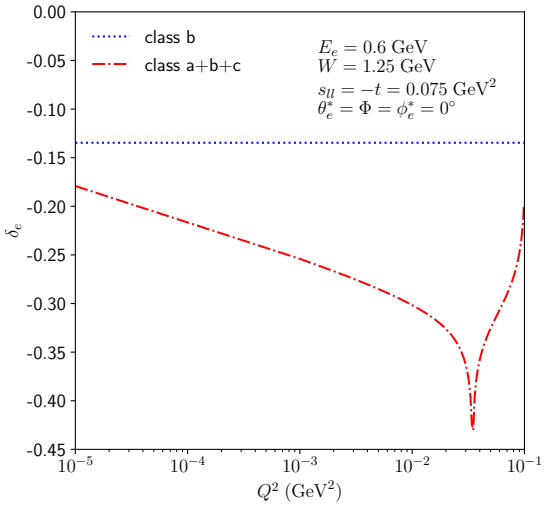

FIGURE 6.5.4: Radiative corrections for the $e^-p \to e^-pe^-e^+$ process in the $\Delta(1232)$ region in the limit $Q^2 \to 0$ for the comparable kinematic setup as was studied before for the $\gamma p \to e^-e^+p$ process in Chapter 5. The corrections are for soft-photon cut-off energy of $\Delta E_s = 0.01$ GeV.

Furthermore, in Fig. 6.5.5 (lower panels), we show the sum of all three types of corrections also for a twice larger value of the soft-photon cut-off energy ΔE_s. One notices the positive contribution to the cross section correction δ upon increasing the value of ΔE_s.

6.5.3 Results for high-energy DDVCS observables

In this section, we show our results for the $e^-p \to e^-pl^-l^+$ observables in the high-energy regime, in which we use GPDs to model the dVCS amplitude in the deeply virtual regime, the so-called DDVCS process, as described in Section 5.2.2. We will explore the sensitivity of this process to the modeling of the GPDs, in particular the D-term contribution, and quantify the effect of the radiative corrections in the soft-photon approximation.

As is conventional in the high-energy regime, we give the differential cross section with respect to the Bjorken scaling variable instead of the c.m. energy W describing the Compton process. Therefore, in this section we show differential cross sections with respect to the quantity ξ, which is related to the kinematical invariants through Eq. (5.21). The cross section differential w.r.t. ξ is related to the cross section differential w.r.t. W^2 as:

$$\left(\frac{\mathrm{d}\sigma}{\mathrm{d}Q^2\mathrm{d}\xi\mathrm{d}\Phi\mathrm{d}t\mathrm{d}s_{ll}\mathrm{d}\Omega_l^*}\right) = \left(\frac{Q^2+s_{ll}}{2\xi^2}\right)\left(\frac{\mathrm{d}\sigma}{\mathrm{d}Q^2\mathrm{d}W^2\mathrm{d}\Phi\mathrm{d}t\mathrm{d}s_{ll}\mathrm{d}\Omega_l^*}\right). \tag{6.94}$$

In Fig. 6.5.6 we show a comparison of $e^-p \to e^-pl^-l^+$ cross sections for e^-e^+ production (left panels) vs $\mu^-\mu^+$ production (right panels). The cross sections are shown for an incoming electron beam energy of 11 GeV, which corresponds to the experimental setup of the CLAS12@JLab experiment and of the SoLID@JLab project. We show the cross section for $\xi = 0.175$, $Q^2 = 2.75$ GeV^2, $-t = 0.25$ GeV^2, $\Phi = 90°$ and for three values of the dilepton invariant mass s_{ll}. While for e^-e^+ production one observes a pronounced peak around $\theta_e^* \approx -20°$ for all three cross sections, the cross sections for $\mu^-\mu^+$ production appear flatter. Furthermore, the cross sections for e^-e^+ production are 4 to 15 times larger than the cross sections for $\mu^-\mu^+$ production at the

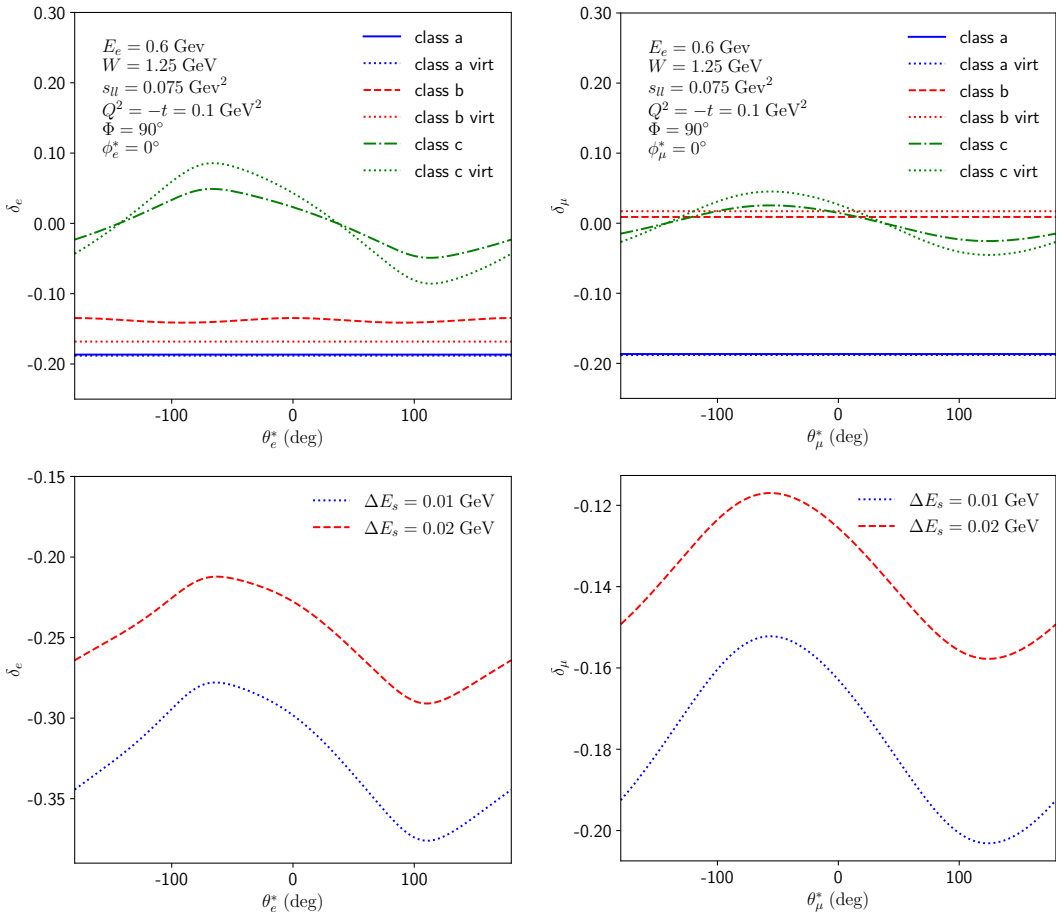

FIGURE 6.5.5: Upper panels: θ_l^* dependence of the radiative corrections to the $e^-p \to e^-pl^-l^+$ cross section in the $\Delta(1232)$ region for e^-e^+ production (left) and $\mu^-\mu^+$ production (right), for the different classes of radiative corrections for $\Delta E_s = 0.01$ GeV. Lower panels: θ_l^* dependence of the total radiative correction for different values of ΔE_s for both e^-e^+ production (left) and $\mu^-\mu^+$ production (right).

same value of s_{ll}. This significant difference is due to the contribution of the exchange diagrams, which only contribute to e^-e^+ production to satisfy the Pauli principle. Naively, one would expect the cross sections to be of roughly the same magnitude, since even for $s_{ll} = 0.5$ GeV^2 the dilepton invariant mass is 10 times larger than the $\mu^-\mu^+$ production threshold, such that effects from the lepton mass don't play a crucial role. However, the anti-symmetrization of the final-state electrons for e^-e^+ production yields a large contribution of the exchange diagrams, which increases with increasing values of s_{ll}.

Furthermore, one can see from Fig. 6.5.6 that the BH process again serves as an amplifier of the dVCS process, and the BH+dVCS cross section is roughly 50% larger than the BH cross section. The cross section therefore has a strong sensitivity to the underlying GPD model. In particular, through such interference, the D-term contribution to the GPD, using the dispersive estimate of Ref. [157], decreases the cross section by up to approximately 20% (green dashed-dotted curves vs red dashed curves).

In order to use the $e^-p \to e^-pl^-l^+$ as a tool to access the DDVCS amplitude, it is important to quantify the radiative corrections, which is an aim of this work. In Fig. 6.5.6 we show the impact of the radiative corrections on the cross section. For the real soft-photon emission correction, we choose the soft-photon energy cut-off of $\Delta E_s = 0.05$ GeV, which is roughly 1% of the $e-p$ center-of-mass energy $\sqrt{s} = 4.64$ GeV (corresponding to an electron beam of 11 GeV). We see from Fig. 6.5.6 that the soft-photon radiative corrections are very sizeable in the DDVCS regime, decreasing the cross sections by up to 50% for e^-e^+ production and by up to 35% for $\mu^-\mu^+$ production (black solid curves vs green dashed-dotted curves).

In Fig. 6.5.7 we show the θ_l^* dependence of the soft-photon radiative correction factor on the $e^-p \to e^-pl^-l^+$ cross section in more detail, for the three values of s_{ll}, corresponding to the cross sections shown in Fig 6.5.6. As mentioned above, using $\Delta E_s = 0.05$ GeV, the corrections in the DDVCS regime vary between -60% and -45% for e^-e^+ production, while for $\mu^-\mu^+$ production they are slightly smaller and vary between -45% and -30%.

In Fig. 6.5.8 (upper panels) we show the relative size of the corrections to the unpolarized cross sections stemming from the three different classes of diagrams for the central value of the squared dilepton mass, $s_{ll} = 1.0$ GeV^2. We show both, the virtual corrections (labeled "virt"), corresponding with Eqs. (6.67) to (6.73), as well as the virtual + real soft-photon corrections, with the real corrections given by Eqs. (6.77) to (6.80) and (6.84).

While the corrections of class (a) are just constant and negative, the corrections of class (b) and (c) have a non-trivial dependence on the dilepton scattering angle θ_l^*. For class (b) this dependence is coming entirely from the real photon emission correction since the dilepton energies in the soft-photon frame depend on the lepton scattering angle θ_l^*, see Eq. (6.85). Comparing the soft-photon radiative corrections to e^-e^+ and $\mu^-\mu^+$ production we see that the largest difference is again coming from class (b), which is expected since it is most sensitive to the lepton mass m_l. Let us note that, as discussed before for the low-energy case, classes (a) and (b) are symmetric with respect to the interchange l^+ and l^-, while class (c) is anti-symmetric. Therefore to first order, only class (c) contributes to the A_{FB}.

In the lower panels of Fig. 6.5.8, we show the sum of all corrections for two different values of the soft-photon energy cutoff of $\Delta E_s = 0.05$ GeV (blue dotted curve) and $\Delta E_s = 0.1$ GeV (red dashed curve). The difference between both curves is a constant proportional to $\ln \Delta E_s^2/m^2$. For the twice higher value of the soft-photon energy, we find in absolute values smaller corrections shifted by approximately 10%.

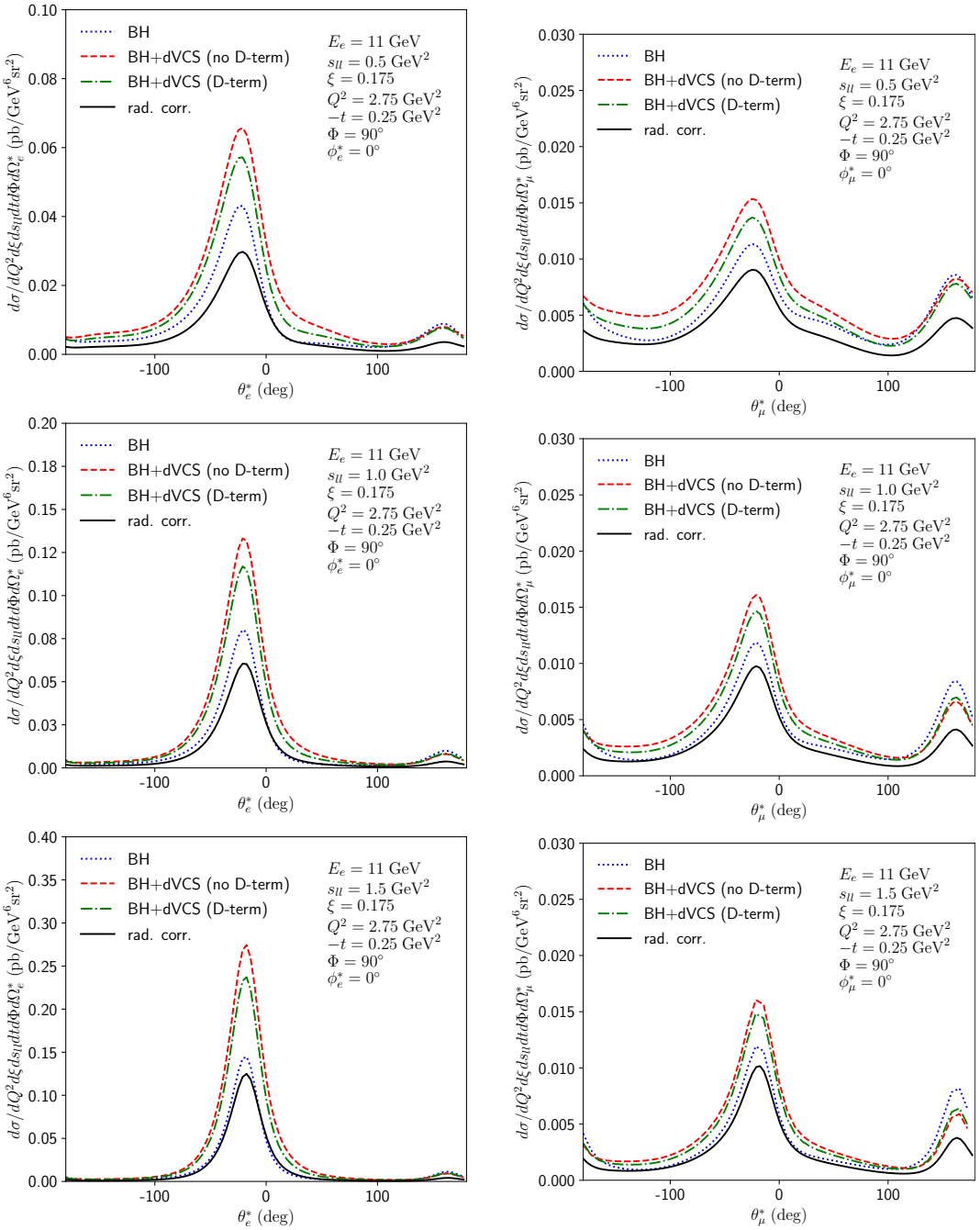

FIGURE 6.5.6: θ_l^* dependence of the $e^-p \to e^-pl^-l^+$ cross section in the DDVCS regime for e^-e^+ production (left panels) and $\mu^-\mu^+$ production (right panels), for different values of the dilepton invariant mass s_{ll}. The curves show the predictions for BH and BH + dVCS for two models showing the sensitivity to the D-term in the GPD parameterization. The black solid curves show the effect of the radiative corrections, for the hadronic model of the green dashed-dotted curves.

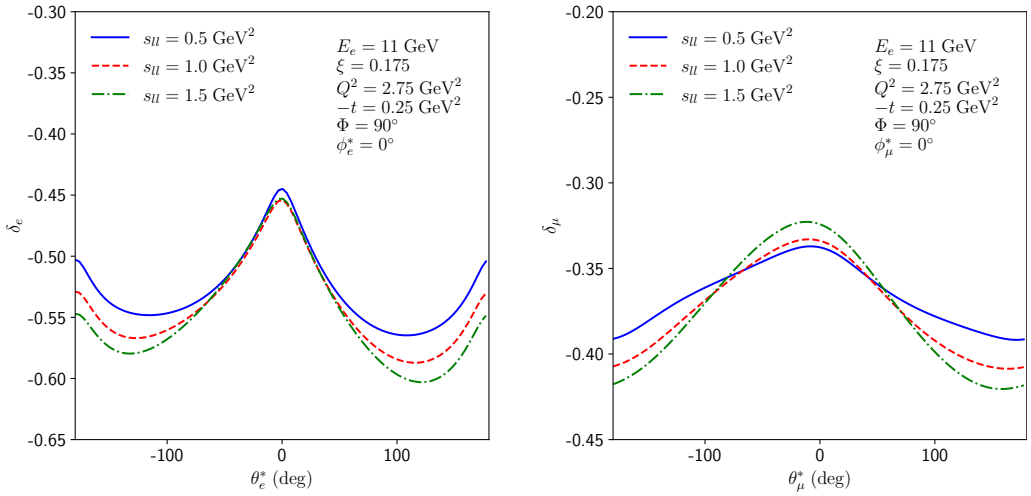

FIGURE 6.5.7: θ_l^* dependence on the soft-photon radiative corrections to the $e^-p \to e^-pl^-l^+$ cross section in the DDVCS regime, for different values of s_{ll}. Left (right) panel is for e^-e^+ ($\mu^-\mu^+$) production respectively. The corrections are for a soft-photon cut-off energy of $\Delta E_s = 0.05$ GeV.

Furthermore, we see that the sum of all corrections is in absolute value smaller by more than 10% for $\mu^-\mu^+$ production compared to e^-e^+ production. As mentioned above the difference is coming mainly from corrections of class (b) which are (in absolute value) smaller for $\mu^-\mu^+$ production.

In Fig. 6.5.9, we show the soft-photon radiative corrections for the $e^-p \to e^-pe^-e^+$ process, for roughly the same kinematics as in the previous chapter where we studied the effect of radiative corrections for the timelike Compton scattering (TCS) process, $\gamma p \to e^-e^+p$, with an on-shell incoming photon (cf. Fig. 5.5.3). In the soft-photon approximation, the corrections to that process are equivalent to that of class (b) studied in the present chapter. Therefore, we find for corrections of class (b) the same order of magnitude of approximately -25 % as in the TCS case (blue dotted curve). Including also corrections of class (a) and (c) we find that the corrections increase with increasing Q^2 values, varying from -35 % to -50 % when varying Q^2 from 10^{-5} GeV^2 to 10^{-1} GeV^2 (red dashed curve). Furthermore, one observes around $Q^2 = 1$ GeV^2 the same spiked behavior as in the low-energy case in Fig. 6.5.4. The reason is again that in this kinematics the two outgoing electrons with momenta k' and l_- become collinear which leads to a large logarithm in the corrections of type (c). For an experiment, such kinematic region should be avoided.

In Fig. 6.5.10, we show a comparison of both, beam spin and forward-backward asymmetries in the DDVCS regime, both for e^-e^+ and $\mu^-\mu^+$ production, and for a dilepton invariant mass squared of $s_{ll} = 1.0$ GeV^2.

Studying the DDVCS process in this energy regime is of particular interest as it allows to extend the DVCS beam spin asymmetry measurements of GPDs into the so-called ERBL domain [28, 29]. The $A_\odot$ is proportional to the imaginary part of the DDVCS amplitude of Eq. (5.28), and allows to access the GPDs directly unlike the real part of the amplitude which depends on a convolution integral over the GPDs. The numerator of the $A_\odot$ directly yields for both the cases $\xi' > 0$ ($Q^2 > q'^2$) and $\xi' < 0$ ($Q^2 < q'^2$):

$$\sigma^+ - \sigma^- = c\, H^{\text{singlet}}(\xi', \xi, t) + ..., \tag{6.95}$$

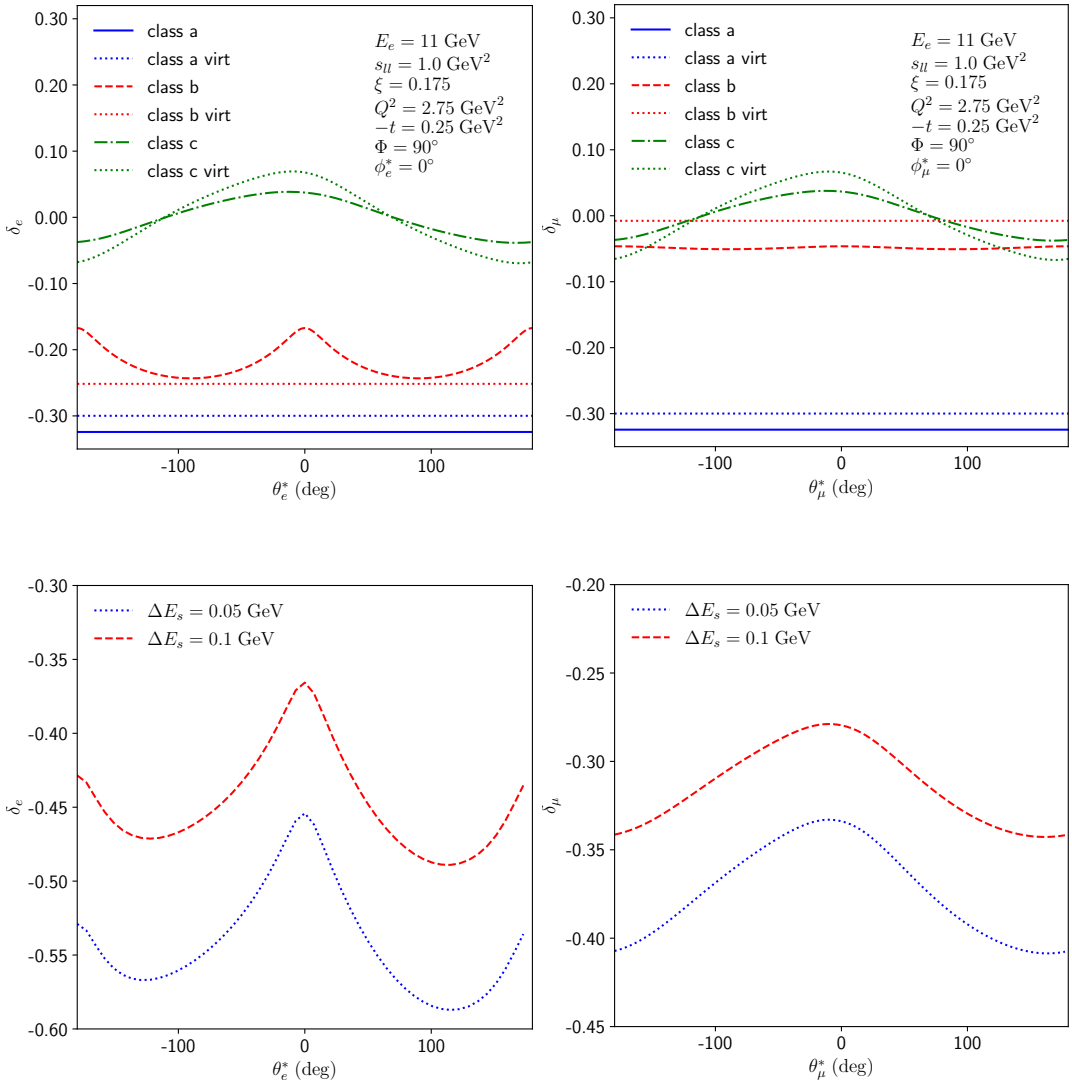

FIGURE 6.5.8: Upper panels: θ_l^* dependence of the radiative corrections to the $e^-p \to e^-pl^-l^+$ cross section in the DDVCS regime for e^-e^+ production (left) and $\mu^-\mu^+$ production (right), for the different classes of radiative corrections for $\Delta E_s = 0.05$ GeV. Lower panels: θ_l^* dependence of the total radiative correction for different values of ΔE_s for both e^-e^+ production (left) and $\mu^-\mu^+$ production (right).

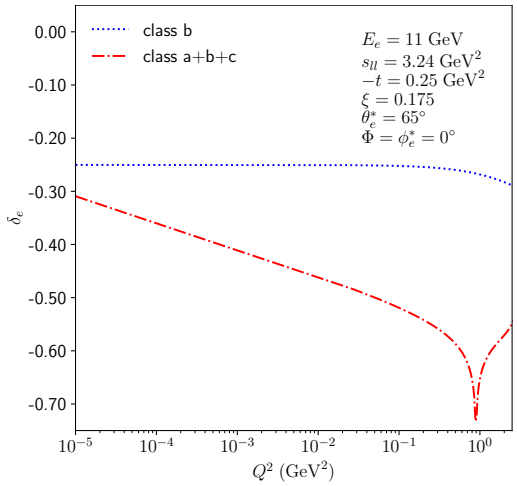

FIGURE 6.5.9: Radiative correction for the $e^-p \to e^-pe^-e^+$ process in the TCS limit $Q^2 \to 0$ in a kinematic setup comparable to Chapter 5.

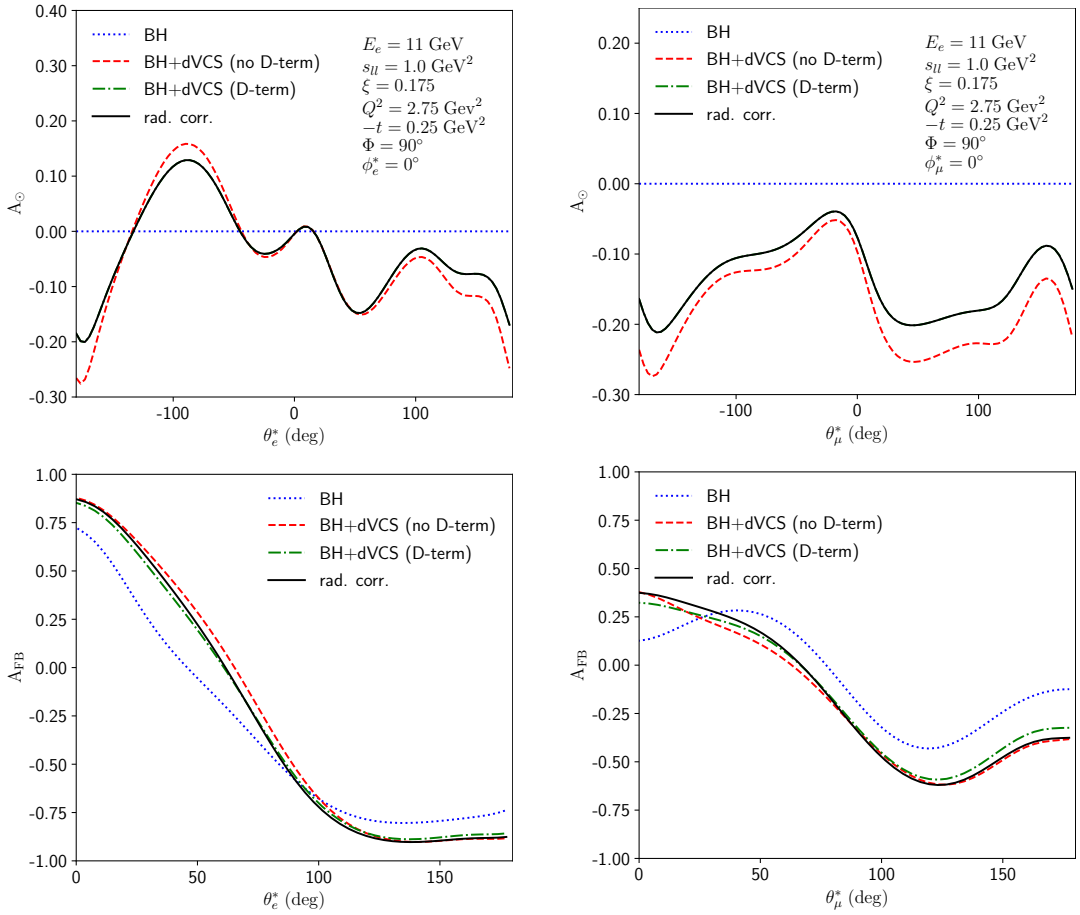

FIGURE 6.5.10: θ_l^* dependence of the $e^-p \to e^-pl^-l^+$ beam spin asymmetry $A_\odot$ (upper panels) and forward-backward asymmetry A_{FB} (lower panels) in the DDVCS regime, for e^-e^+ production (left) and $\mu^-\mu^+$ production (right). Curve conventions as in Fig. 6.5.6.

with $-\xi < \xi' < \xi$. In Eq. (6.95) c is a known factor, originating from the BH amplitude dependent on the nucleon elastic form factors, and the ellipses stand for the subdominant contribution of GPDs beyond H^{singlet}.

As H^{singlet} is an odd function in its first argument, we thus see that the $A_\odot$ for the DDVCS process changes sign when crossing the point $\xi' = 0$. The $A_\odot$ for the DVCS and TCS limits have the same magnitude but opposite signs, expressing the fact that the GPD information content in both limits is the same.

Given that the real BH process does not yield a beam spin asymmetry by itself, we see from Fig. 6.5.10 that $A_\odot$ has a significant sensitivity to the GPDs, yielding asymmetries between -25% and +10% for $e^- e^+$ production and between -25% and -5% for $\mu^- \mu^+$ production. The difference between both cases is mainly due to the effect of anti-symmetrization in both outgoing electrons for $e^- e^+$ production. Furthermore, unlike the DVCS and TCS cases, the $A_\odot$ for DDVCS is also sensitive to the D-term contribution to the GPD, as it also yields a contribution to the imaginary part of the DDVCS amplitude. By comparing the red dashed and black solid curves in Fig. 6.5.10, we notice that the sensitivity to the D-term induces a change of the $A_\odot$ by 5% or more over a large angular range. As noticed above, the radiative correction drops out of the $A_\odot$ in the soft-photon approximation.

We also show the forward-backward asymmetry in Fig. 6.5.10, and notice that the anti-symmetrization induces already a large effect for the BH process itself (blue dotted curves in Fig. 6.5.10). Adding the dVCS contribution changes the forward-backward asymmetry by up to 25% over a large angular range, while the effect of radiative corrections (black solid curves) is in the few percent range only. The sensitivity on the D-term for the forward-backward asymmetry is much smaller, comparing the curve including the D-term (green dot-dashed line) and the curve excluding the D-term (red dashed line) we find a difference of up to approximately 5%.

For the calculation of the $e^- p \to e^- p e^- e^+$ cross sections shown in Fig. 6.5.6 (left panels) and the corresponding asymmetries shown in Fig. 6.5.10 (left panels) we have to ensure that the model used for the dVCS amplitude is applicable for both the direct and the exchange terms. In Fig. 6.5.11 we show the two photon virtualities entering the dVCS tensor for the exchange diagrams. One can see that in the kinematics considered one of the two virtualities is around or above 2 GeV^2 for nearly all lepton angles, which corresponds with the lower limit for which the QCD-factorization in terms of GPDs is expected to hold. This justifies the use of the handbag description of Section 5.2.2 in terms of GPDs also for the exchange term.

Furthermore in Fig. 6.5.11 (right panel) we show the scaling variables entering the DDVCS tensor for the exchange diagrams. While ξ_{ex} and $\tilde{\xi}_{\text{ex}}$ both are roughly constant as function of the dilepton angle, close to the value of $\xi = 0.175$ for the direct diagram, one notices a large angular variation for ξ'_{ex} and $\tilde{\xi}'_{\text{ex}}$. Compared to the constant value $\xi' = 0.0758$ entering the direct diagram, ξ'_{ex} varies between -0.08 and 0.08. Thus the $e^- p \to e^- p e^- e^+$ process has the unique feature, due to the anti-symmetrization in both outgoing electrons, that by varying the dilepton angle θ_e^* one performs a systematic scan in the scaling variable ξ'_{ex} in the ERBL domain of the GPDs.

In Fig. 6.5.12 we also show the dilepton momenta and scattering angles measured in the Lab frame as a function of the dilepton rest frame angle θ_l^*. From the left panel of that figure, it becomes clear, that most of the region is experimentally accessible. Except for angles around 0° and ±180°, over most of the dilepton angular range the lepton momenta are larger than 0.1 GeV, which makes it quite feasible to detect the particles. The scattering angles measured in the Lab system are shown in the right panel in Fig. 6.5.12. In the region where the Lab momenta of the dilepton pair are

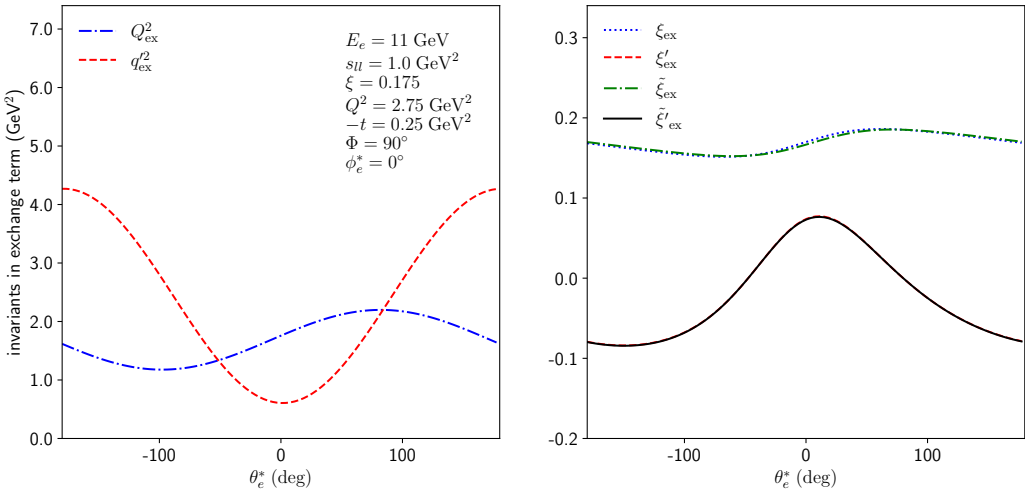

FIGURE 6.5.11: Left panel: photon virtualities entering the dVCS amplitude in the exchange diagrams of the $e^-p \to e^-pe^-e^+$ process for the kinematics of Fig. 6.5.10. Right panel: scaling variables entering the GPDs for the exchange diagrams.

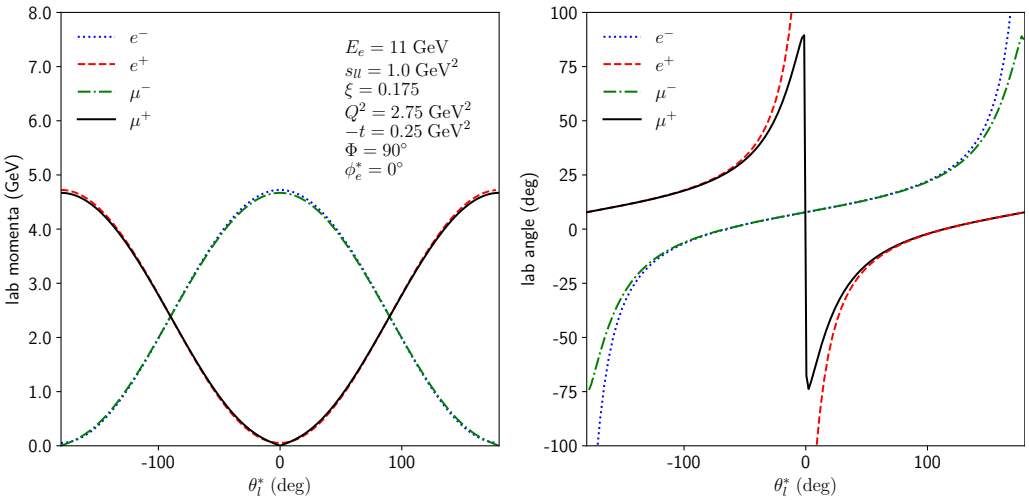

FIGURE 6.5.12: Lab momenta (left panel) and Lab scattering angles (right panel) of the dilepton pair as function of dilepton rest frame angle θ^*_l for the kinematics of Fig. 6.5.10.

larger than 0.1 GeV, they range from $-50°$ to $50°$. This initial study seems promising for a measurement of the $e^-p \to e^-pe^-e^+$ process over a large range of scattering angles.

6.6 Conclusions

In this chapter, we studied the soft-photon radiative corrections to the process $e^-p \to e^-pl^-l^+$, where $l = e$ or $l = \mu$. The process contains two distinct contributions: firstly the space- and time-like Bethe-Heitler processes which only depend on the nucleon elastic form factors, and secondly the double virtual Compton scattering process. The latter is sensitive to the underlying hadronic model describing the virtual photon-nucleon interaction, and a measurement of $e^-p \to e^-pl^-l^+$ observables can therefore be used to test and study nucleon structure models. Here, we studied the $e^-p \to e^-pl^-l^+$ process in two different energy regimes.

In the low-energy regime, in which the center-of-mass energy of the dVCS amplitude is close to the $\Delta(1232)$-resonance, and in which both photon virtualities are typically below or around 0.1 GeV^2, we described the interaction using a Δ-pole model together with a low-energy expansion of the dVCS amplitude. This regime is motivated to better constrain the hadronic corrections to precision atomic spectroscopy. In particular for the muonic Hydrogen Lamb shift, the main hadronic unknown to date results from a low-energy nucleon structure constant, denoted by $b_{3,0}$, which enters the empirical determination of the $\mathcal{O}(Q^4)$ term in the subtraction function $T_1(0, Q^4)$ of the forward double virtual Compton amplitude. We found that the spread between the different theoretical estimates for the low-energy constant $b_{3,0}$ increases the $e^-p \to e^-pl^-l^+$ cross section by approximately 15% both for e^-e^+ and $\mu^-\mu^+$ production. Furthermore, we also found that the beam spin asymmetry and the forward-backward asymmetry, resulting from an interchange in the kinematics of the produced dilepton pair, are sensitive to the low-energy constant $b_{3,0}$. For the beam spin asymmetry the range of theoretical values for this low-energy constant leads to a shift in the asymmetry up to 15% for e^-e^+ production, and up to around 10% for $\mu^-\mu^+$ production. A measurement of the $e^-p \to e^-pl^-l^+$ observables in this low-energy regime is thus promising to extract the nucleon structure constant, which could help to reduce the main uncertainty in the theoretical μH Lamb shift estimate.

For the high-energy deeply-virtual regime, we modeled the dVCS amplitude in terms of GPDs. We studied the sensitivity of the $e^-p \to e^-pl^-l^+$ process to the modeling of the GPDs, in particular the so-called D-term contribution. In kinematics of future experiments at JLab, we found that dispersive estimates for the D-term contribution to the GPDs induce around 20% change in the $e^-p \to e^-pl^-l^+$ cross section. Furthermore, we also found a large sensitivity to the GPD model for the beam spin as well as the forward-backward asymmetry. The beam spin asymmetry is of particular interest as it does not involve any convolution over GPDs, but is directly proportional to the GPDs, mostly in a linear way, through interference with the BH process. For the $e^-p \to e^-pe^-e^+$ process, the beam spin asymmetry has the unique feature, due to the anti-symmetrization in both outgoing electrons, that by varying the dilepton angle one performs a systematic scan in the average quark momentum fraction in the ERBL domain of the GPDs, due to the exchange term.

In order to use the $e^-p \to e^-pl^-l^+$ process in either the low-energy or high-energy regimes as a probe of nucleon structure, we also studied the QED radiative corrections on the observables, in the soft-photon approximation. We found that the radiative corrections have a large impact on the cross sections. In the low-energy regime, we

find that these corrections lead to a decrease of the cross section of up to 30% for e^-e^+ production, and around 15% for $\mu^-\mu^+$ production. In the high-energy deeply-virtual regime, the corrections even range up to 50% for e^-e^+ production, and around 35% for $\mu^-\mu^+$ production in JLab kinematics. For the forward-backward and beam spin asymmetries, the situation is different. For the A_{FB} the radiative corrections were found to affect the asymmetry only around or below the 1% level, whereas the beam spin asymmetry is not affected at all in the soft-photon approximation. A combined analysis of the cross section and both asymmetries thus holds promise to access the hadronic structure information in both regimes.

A next step to interpret future measurements of $e^-p \to e^-pl^-l^+$ observables, would consist in performing a full one-loop radiative correction calculation, beyond the soft-photon approximation. Such calculation can build upon the work of Refs. [27, 53] (which were presented in the previous chapter), in which such study was performed for the related $\gamma p \to l^-l^+p$ process. The latter study has shown that the soft-photon approximation can be expected to somewhat over-estimate the full one-loop corrections on the cross sections, while the beam spin and forward-backward asymmetries remain nearly unaffected by the radiative corrections.

Appendix

6.A Kinematics in $\gamma^* p$ rest frame

In this appendix, we derive expressions for the four-momenta in the rest frame of the proton and the momentum transfer of the scattered electron, i.e. the frame in which

$$\vec{q} = \vec{k} - \vec{k}' = -\vec{p}. \tag{6.96}$$

We align this system along the z-axis, such that the energy of the virtual photon with momentum q is given by

$$q^0_{cm} = \frac{W^2 - M^2 - Q^2}{2W}, \tag{6.97}$$

and the z-component of the three-momentum by

$$q_{cm} \equiv q_z = \frac{1}{2W}\left[\left((W+M)^2 + Q^2\right)\left((W-M)^2 + Q^2\right)\right]^{1/2}. \tag{6.98}$$

The energy of the incoming electron with momentum k is given by

$$k^0 = \frac{s - M^2 - m^2 - Q^2}{2W}. \tag{6.99}$$

In order to write down the three-momentum $\vec{k}$, we define r_k, which is the magnitude of the three-momentum in x- and y-direction:

$$\begin{aligned} r_k = \frac{Q}{2W q_{cm}} \Big[& s(s - M^2 - Q^2) - W^2(s - M^2) \\ & - m^2\left((W^2 - M^2)^2/Q^2 + 2s + W^2 + M^2\right) + m^4\Big]^{1/2}, \end{aligned} \tag{6.100}$$

such that $\vec{k}$ is given by

$$\begin{aligned} k_x &= r_k \cos\Phi \\ k_y &= r_k \sin\Phi \\ k_z &= \frac{WQ^2 + q^0_{cm}(s - m^2 - M^2 - Q^2)}{2q_{cm}W}. \end{aligned} \tag{6.101}$$

Using these quantities, we can write down the momenta of the incoming and outgoing electron k and k' as

$$k = \begin{pmatrix} k^0 \\ r_k \cos\Phi \\ r_k \sin\Phi \\ k_z \end{pmatrix} \qquad k' = \begin{pmatrix} k^0 - q^0_{cm} \\ r_k \cos\Phi \\ r_k \sin\Phi \\ k_z - q_{cm} \end{pmatrix}. \tag{6.102}$$

The energy of the photon with momentum q' is given by

$$q'^0_{cm} = \frac{W^2 - M^2 + s_{ll}}{2W}, \tag{6.103}$$

and its three-momentum by

$$q'_{cm} \equiv |\vec{q'}_{cm}| = \frac{1}{2W}\left[\left((W+M)^2 - s_{ll}\right)\left((W-M)^2 - s_{ll}\right)\right]^{1/2}. \tag{6.104}$$

The angle $\theta_{\gamma\gamma}$ is defined as the angle between the two virtual photons with momenta q and q'. It can be calculated in terms of invariants as follows:

$$\begin{aligned} 2q_{cm}q'_{cm}\cos(\theta_{\gamma\gamma}) = &\frac{(W^2 - M^2 - Q^2)(W^2 - M^2 + s_{ll})}{2W^2} \\ &+ t - s_{ll} + Q^2. \end{aligned} \tag{6.105}$$

We can now write down the four-momentum of l_-:

$$l_- = \begin{pmatrix} \frac{q'^0_{cm}}{2}\left(1 + \frac{q'_{cm}}{q'^0_{cm}}\beta\cos\theta^*_l\right) \\ \frac{q'^0_{cm}}{2}\left(\beta\cos\theta^*_l + \frac{q'_{cm}}{q'^0_{cm}}\right)\sin(\theta_{\gamma\gamma}) + \frac{\sqrt{s_{ll}}}{2}\beta\sin\theta^*_l\cos\phi^*_l\cos(\theta_{\gamma\gamma}) \\ \frac{\sqrt{s_{ll}}}{2}\beta\sin\theta^*_l\sin\phi^*_l \\ \frac{q'^0_{cm}}{2}\left(\beta\cos\theta^*_l + \frac{q'_{cm}}{q'^0_{cm}}\right)\cos(\theta_{\gamma\gamma}) - \frac{\sqrt{s_{ll}}}{2}\beta\sin\theta^*_l\cos\phi^*_l\sin(\theta_{\gamma\gamma}) \end{pmatrix}. \tag{6.106}$$

The momentum l_+ of the other lepton can be obtained via the transformation

$$\cos\theta^*_l \to -\cos\theta^*_l, \quad \cos\phi^*_l \to -\cos\phi^*_l, \quad \sin\phi^*_l \to -\sin\phi^*_l. \tag{6.107}$$

The momentum p of the incoming proton is aligned to the z-axis. The energy and the z-component are given by

$$p^0 = \sqrt{M^2 + q^2_{cm}}, \quad p_z = -q_{cm}. \tag{6.108}$$

The momentum p' of the outgoing proton can be calculated using energy-momentum conservation. The energy and three-momentum are given by

$$p'^0 = \sqrt{M^2 + |\vec{q'}|^2}, \qquad \vec{p'} = -\vec{q'}. \tag{6.109}$$

Having derived all four-momenta in the $\gamma^* p$ center-of-mass frame, one can easily perform a Lorentz transformation to get the four-momenta in any other system. In particular, one can perform the boost to the recoil proton + soft-photon rest frame, which is needed to calculate the soft-photon integrals from Section 6.4.

6.B Three-point function

In this appendix we give analytic expressions for the three-point function which we need for the virtual soft-photon corrections of type (c), the three-point function with two different masses m and m_l. Up to zeroth order in ϵ, it is given by

$$\begin{aligned} &C_0\left(m^2, s, m_l^2; 0, m^2, m_l^2\right) = \\ &\quad \frac{1}{2\lambda}\Bigg\{\left[\frac{1}{\epsilon_{\mathrm{IR}}} - \ln\left(\frac{s}{\bar{\mu}^2}\right)\right]\ln(x_+x_-) - \ln\left(-\frac{\lambda}{s}\right)\left(\ln(x_+) + \ln(x_-)\right) \end{aligned}$$

$$+\frac{1}{2}\ln^2\left(-\gamma^+\right)+\frac{1}{2}\ln^2\left(\gamma^- -1\right)-\frac{1}{2}\ln^2\left(-\gamma^-\right)+\frac{1}{2}\ln^2\left(1-\gamma^+\right)$$
$$-\mathrm{Li}_2\left(\frac{s-s\gamma^-}{\lambda}\right)-\mathrm{Li}_2\left(\frac{s\gamma^+}{\lambda}\right)+\mathrm{Li}_2\left(\frac{s\gamma^+ - s}{\lambda}\right)+\mathrm{Li}_2\left(\frac{s\gamma^-}{\lambda}\right)\Bigg\}, \quad (6.110)$$

with

$$\lambda=\sqrt{(-s+m^2+m_l^2)^2-4m^2m_l^2}, \qquad \gamma_\pm=\frac{1}{2}\left[1+\frac{m_l^2-m^2}{s}\pm\frac{\lambda}{s}\right],$$
$$x_-=\frac{-\gamma_-}{1-\gamma_-}, \qquad x_+=\frac{\gamma_+-1}{\gamma_+}, \quad (6.111)$$

and $\bar{\mu}^2=\mu^2\frac{4\pi}{e^{\gamma_E}}$. The expression is valid in the space-like region with $s<0$.

Part III

Mixed EW-QCD corrections to the Drell-Yan process

7 Calculation of the master integrals with two masses

This chapter is based on Ref. [84], in which we computed the two-loop two-mass master integrals for the mixed EW-QCD corrections to Drell-Yan production. These master integrals can be cast into a canonical dln form, depending on algebraic, unrationalizable letters. In total, the definition of the master integrals involves three square roots at once which can *not* be rationalized simultaneously [109, 170]. Thus, the standard algorithm of integrating the differential equation in terms of Goncharov polylogarithms fails and one needs new methods. We have discussed a new approach to tackle this type of differential equations in Section 2.7 and in Ref [84] we applied these techniques for the first time. We showed for the first time, that it is still possible to integrate the differential equation, despite those algebraic letters, in terms of multiple polylogarithms for the present case. Therefore, the result of this work is not only of phenomenological interest, but also interesting from a mathematical point of view.

The outline of this chapter is as follows. In Section 7.1, we define a normal form basis with $\epsilon\,\mathrm{d}\ln$ differential equations for the two-loop master integrals for the mixed EW-QCD corrections to Drell-Yan production with two massive internal lines and discuss a partial rationalization of the roots appearing in the integral basis definition. In Section 7.2, we discuss in detail how to use the methods introduced in Section 2.8 in the present case to integrate the differential equation. We introduce the initial alphabet and show how it can be simplified using our algorithm. In Section 7.3, we review the analytic continuation of multiple polylogarithms and outline our procedure to filter multiple polylogarithms with undesirable analytic properties out of our ansätze. In Section 7.4, we present results for the most complicated two-loop mixed EW-QCD Drell-Yan master integrals. In particular, we highlight the notable analytic features of the solution for the six-line integral. We conclude in Section 7.5, and, for clarity, we give the set of complete $\epsilon\,\mathrm{d}\ln$ differential equations for the two-loop master integrals considered here in Appendix 7.A.

7.1 An ϵ basis for the Drell-Yan master integrals with two massive lines

In this chapter, we are primarily concerned with neutral-current lepton pair production in quark-antiquark annihilation,

$$q(p_1) + \bar{q}(p_2) \to \ell^-(p_3) + \ell^+(p_4), \tag{7.1}$$

where all external particles are taken massless and on their mass shell. The master integrals for the two-loop mixed EW-QCD corrections to the above process involving zero or one mass (Family A and Family C from Table 7.1.1) have been already calculated in Ref. [107] using the standard approach of differential equations. However, the most complicated master integrals are those with two internal lines of mass m, where,

Family A	Family C	Family E
k_1^2	k_1^2	k_1^2
k_2^2	k_2^2	$k_2^2 - m^2$
$(k_1 - k_2)^2$	$(k_1 - k_2)^2$	$(k_1 - k_2)^2$
$(k_1 - p_1)^2$	$(k_1 - p_1)^2$	$(k_1 - p_1)^2$
$(k_2 - p_1)^2$	$(k_2 - p_1)^2$	$(k_2 - p_1)^2$
$(k_1 - p_1 - p_2)^2$	$(k_1 - p_1 - p_2)^2$	$(k_1 - p_1 - p_2)^2$
$(k_2 - p_1 - p_2)^2$	$(k_2 - p_1 - p_2)^2 - m^2$	$(k_2 - p_1 - p_2)^2 - m^2$
$(k_1 - p_3)^2$	$(k_1 - p_3)^2$	$(k_1 - p_3)^2$
$(k_2 - p_3)^2$	$(k_2 - p_3)^2$	$(k_2 - p_3)^2$

TABLE 7.1.1: Integral families for the master integrals which appear in the differential equations for the two-loop mixed EW-QCD Drell-Yan master integrals with two massive internal lines.

depending on the parent Feynman diagram, m may refer to either m_W or m_Z. In particular, as mentioned above, some integral topologies for this case actually contain master integrals with unrationalizable symbol letters in their ϵ-decoupled differential equations. In total, we encounter 17 master integrals with two massive internal lines and we consider a single integral family based on the two-loop planar double box with two massive internal lines (Family E from Table 7.1.1). For completeness, we will also give definitions for those normal form integrals from family A and B, which appear on the right-hand sides of the ϵ-decoupled differential equations for the master integrals with two massive internal lines.

To obtain a closed system of differential equations for the two-loop two-mass master integrals, we need to consider in total 36 integrals. Our notation for Feynman integrals in this section is exactly that of Ref. [107] (i.e. dots for doubled propagators, heavy lines for massive propagators, numerator insertions written in square brackets, and $\bar{\text{F}}{:}x$ for the crossed version of sector x from family F). As usual, we define the kinematic invariants as

$$s = (p_1 + p_2)^2, \qquad t = (p_1 - p_3)^2, \qquad u = (p_2 - p_3)^2, \qquad p_1^2 = p_2^2 = p_3^2 = p_4^2 = 0\,. \tag{7.2}$$

In the following, we keep the dependence on the internal mass parameter m implicit for the sake of brevity and since it is clear from the thick-line notation. We build up the normal form basis out of the following 36 Feynman integrals:

$\mathbf{f}_1^{\bar{\text{A}}:38} =$ 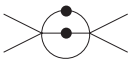 (t) $\mathbf{f}_2^{\text{C}:97} =$  (s) $\mathbf{f}_3^{\text{C}:76} =$ 

$\mathbf{f}_4^{\text{C}:69} =$ 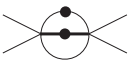 (s) $\mathbf{f}_5^{\text{C}:69} =$ 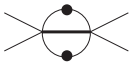 (s) $\mathbf{f}_6^{\text{A}:53} =$ 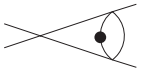 (s)

$\mathbf{f}_7^{\bar{\text{A}}:53} =$ 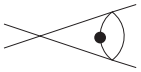 (t) $\mathbf{f}_8^{\text{C}:212} =$ 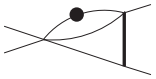 (t) $\mathbf{f}_9^{\text{E}:99} =$  (s)

$\mathbf{f}_{10}^{\text{E}:71} =$ 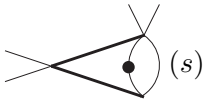 (s) $\mathbf{f}_{11}^{\text{E}:78} =$ 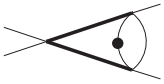 (s) $\mathbf{f}_{12}^{\text{E}:78} =$ 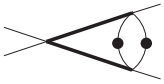 (s)

$\mathbf{f}_{13}^{\bar{\mathrm{A}}:174} =$ 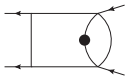 (t,s) $\mathbf{f}_{14}^{\mathrm{C}:372} =$ 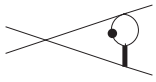 (t) $\mathbf{f}_{15}^{\mathrm{C}:244} =$ 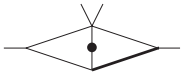 (t)

$\mathbf{f}_{16}^{\mathrm{C}:117} =$ 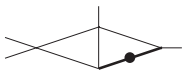 (s) $\mathbf{f}_{17}^{\mathrm{C}:117} =$ 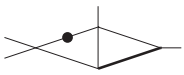 (s) $\mathbf{f}_{18}^{\mathrm{C}:341} =$ 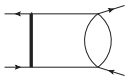 (s,t)

$\mathbf{f}_{19}^{\mathrm{C}:341} =$ 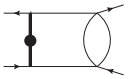 (s,t) $\mathbf{f}_{20}^{\mathrm{C}:213} =$ 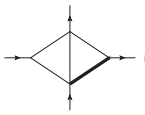 (s,t) $\mathbf{f}_{21}^{\mathrm{C}:213} =$ 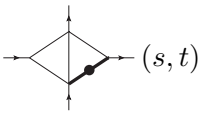 (s,t)

$\mathbf{f}_{22}^{\mathrm{E}:115} =$ 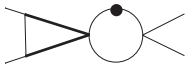 (s) $\mathbf{f}_{23}^{\mathrm{E}:103} =$  (s) $\mathbf{f}_{24}^{\mathrm{E}:87} =$ 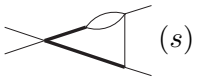 (s)

$\mathbf{f}_{25}^{\mathrm{E}:79} =$ 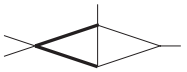 (s) $\mathbf{f}_{26}^{\mathrm{E}:214} =$ 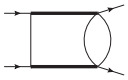 (s,t) $\mathbf{f}_{27}^{\mathrm{E}:214} =$ 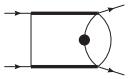 (s,t)

$\mathbf{f}_{28}^{\mathrm{C}:245} =$ 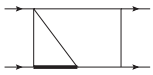 (s,t) $\mathbf{f}_{29}^{\mathrm{C}:245} =$ 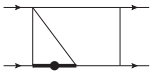 (s,t) $\mathbf{f}_{30}^{\mathrm{E}:119} =$ 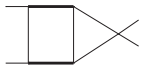 (s)

$\mathbf{f}_{31}^{\mathrm{E}:343} =$ 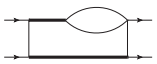 (s,t) $\mathbf{f}_{32}^{\mathrm{E}:215} =$ 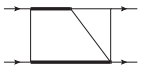 (s,t) $\mathbf{f}_{33}^{\mathrm{E}:247} =$  (s,t)

$\mathbf{f}_{34}^{\mathrm{E}:247} =$ 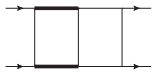 $\left[(k_2-p_3)^2\right](s,t)$ $\mathbf{f}_{35}^{\mathrm{E}:247} =$ 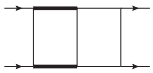 $\left[(k_1-p_1)^2\right](s,t)$

$$\mathbf{f}_{36}^{\mathrm{E}:247} = \quad \left[(k_1-p_1)^2(k_2-p_3)^2\right](s,t). \tag{7.3}$$

From the general principles discussed in Ref. [97], one can readily cast (7.3) above into a normal form basis for the integrals of interest.[1] Abbreviating the three square roots which appear as

$$r_1 = \sqrt{s\,(s-4\,m^2)}\,, \tag{7.4}$$

$$r_2 = \sqrt{-s\,t\,\left(4m^2(m^2+t)-s\,t\right)}\,, \tag{7.5}$$

$$r_3 = \sqrt{s\,\left(t^2(s-4\,m^2)+m^2\,s\,(m^2-2\,t)\right)}\,, \tag{7.6}$$

we find:

$\mathbf{m}_1 = \epsilon^2\,t\,\mathbf{f}_1^{\bar{\mathrm{A}}:38}$,

[1] Due to the presence of unrationalizable square roots, the available public software packages for the construction of a normal form basis of integrals [99, 171, 172] are not applicable to the problem at hand.

$$
\begin{aligned}
\mathbf{m}_2 &= \epsilon^2\, s\, \mathbf{f}_2^{\mathrm{C:97}},\\
\mathbf{m}_3 &= \epsilon(1-\epsilon)\, m^2\, \mathbf{f}_3^{\mathrm{C:76}},\\
\mathbf{m}_4 &= \epsilon^2\, s\, \mathbf{f}_4^{\mathrm{C:69}},\\
\mathbf{m}_5 &= 2\,\epsilon^2(s-m^2)\mathbf{f}_4^{\mathrm{C:69}} + \epsilon^2(s-m^2)\mathbf{f}_5^{\mathrm{C:69}},\\
\mathbf{m}_6 &= \epsilon^3\, s\, \mathbf{f}_6^{\mathrm{A:53}},\\
\mathbf{m}_7 &= \epsilon^3\, t\, \mathbf{f}_7^{\bar{\mathrm{A}}:53},\\
\mathbf{m}_8 &= \epsilon^3\, t\, \mathbf{f}_8^{\mathrm{C:212}},\\
\mathbf{m}_9 &= \epsilon^2\, s\, r_1 \mathbf{f}_9^{\mathrm{E:99}},\\
\mathbf{m}_{10} &= \frac{\epsilon(1-\epsilon)m^2\, s}{4\, r_1}\mathbf{f}_3^{\mathrm{C:76}} - \frac{\epsilon^2\, s(s-3\,m^2)}{2\, r_1}\mathbf{f}_4^{\mathrm{C:69}} - \frac{\epsilon^2\, s(s-m^2)}{4\, r_1}\mathbf{f}_5^{\mathrm{C:69}} + \frac{\epsilon^2(1-2\,\epsilon)m^2\, s}{r_1}\mathbf{f}_{10}^{\mathrm{E:71}},\\
\mathbf{m}_{11} &= \epsilon^3\, s\, \mathbf{f}_{11}^{\mathrm{E:78}},\\
\mathbf{m}_{12} &= -\frac{\epsilon(1-\epsilon)m^2\, s}{r_1}\mathbf{f}_3^{\mathrm{C:76}} + \frac{3\,\epsilon^3\, s(s-2\,m^2)}{r_1}\mathbf{f}_{11}^{\mathrm{E:78}} + \frac{\epsilon^2\, m^4\, s}{r_1}\mathbf{f}_{12}^{\mathrm{E:78}},\\
\mathbf{m}_{13} &= \epsilon^3\, s\, t\, \mathbf{f}_{13}^{\bar{\mathrm{A}}:174},\\
\mathbf{m}_{14} &= \epsilon^3\, m^2\, t\, \mathbf{f}_{14}^{\mathrm{C:372}},\\
\mathbf{m}_{15} &= \epsilon^3\, m^2\, t\, \mathbf{f}_{15}^{\mathrm{C:244}},\\
\mathbf{m}_{16} &= \epsilon^3\, m^2\, s\, \mathbf{f}_{16}^{\mathrm{C:117}},\\
\mathbf{m}_{17} &= \epsilon^3\, s^2\, \mathbf{f}_{17}^{\mathrm{C:117}},\\
\mathbf{m}_{18} &= \epsilon^3(1-2\,\epsilon)\, t\, \mathbf{f}_{18}^{\mathrm{C:341}},\\
\mathbf{m}_{19} &= 3\,\epsilon^3(1-2\,\epsilon)\, m^2\, \mathbf{f}_{18}^{\mathrm{C:341}} + \epsilon^2(1-2\,\epsilon)\, m^2\, (m^2+t)\mathbf{f}_{19}^{\mathrm{C:341}},\\
\mathbf{m}_{20} &= \epsilon^4\, (s+t)\mathbf{f}_{20}^{\mathrm{C:213}},\\
\mathbf{m}_{21} &= \epsilon^3\, m^2\, (s+t)\mathbf{f}_{21}^{\mathrm{C:213}},\\
\mathbf{m}_{22} &= \epsilon^3\, s^2\, \mathbf{f}_{22}^{\mathrm{E:115}},\\
\mathbf{m}_{23} &= \epsilon^3(1-2\,\epsilon)\, s\, \mathbf{f}_{23}^{\mathrm{E:103}},\\
\mathbf{m}_{24} &= \epsilon^3(1-2\,\epsilon)\, s\, \mathbf{f}_{24}^{\mathrm{E:87}},\\
\mathbf{m}_{25} &= \epsilon^4\, s\, \mathbf{f}_{25}^{\mathrm{E:79}},\\
\mathbf{m}_{26} &= \epsilon^3(1-2\,\epsilon)\, s\, \mathbf{f}_{26}^{\mathrm{E:214}},\\
\mathbf{m}_{27} &= \epsilon^3\, r_2\, \mathbf{f}_{27}^{\mathrm{E:214}},\\
\mathbf{m}_{28} &= \epsilon^4\, s\, t\, \mathbf{f}_{28}^{\mathrm{C:245}},\\
\mathbf{m}_{29} &= 2\,\epsilon^4\, m^2\, s\, \mathbf{f}_{28}^{\mathrm{C:245}} + \epsilon^3\, m^2\, s\, (m^2+t)\mathbf{f}_{29}^{\mathrm{C:245}},\\
\mathbf{m}_{30} &= \epsilon^4\, s\, r_1\, \mathbf{f}_{30}^{\mathrm{E:119}},\\
\mathbf{m}_{31} &= \epsilon^3(1-2\,\epsilon)\, r_2\, \mathbf{f}_{31}^{\mathrm{E:343}},\\
\mathbf{m}_{32} &= \epsilon^4\, r_3\, \mathbf{f}_{32}^{\mathrm{E:215}},\\
\mathbf{m}_{33} &= \epsilon^4\, s\, r_2\, \mathbf{f}_{33}^{\mathrm{E:247}},\\
\mathbf{m}_{34} &= \epsilon^4\, s^2\, \mathbf{f}_{34}^{\mathrm{E:247}},\\
\mathbf{m}_{35} &= 2\,\epsilon^4\, t\, r_1\, \mathbf{f}_{32}^{\mathrm{E:215}} - \epsilon^4\, s\, t\, r_1\, \mathbf{f}_{33}^{\mathrm{E:247}} + \epsilon^4\, s\, r_1\, \mathbf{f}_{35}^{\mathrm{E:247}},\\
\mathbf{m}_{36} &= 2\,\epsilon^4\, t\, \mathbf{f}_{20}^{\mathrm{C:213}} + \epsilon^3\, s\, t\, \mathbf{f}_{22}^{\mathrm{E:115}} - \frac{1}{2}\epsilon^3\, s\, \mathbf{f}_{23}^{\mathrm{E:103}} - \frac{1}{2}\epsilon^4\, s\, (s-2\,m^2)\mathbf{f}_{30}^{\mathrm{E:119}} + \epsilon^4\, s\, t\, \mathbf{f}_{32}^{\mathrm{E:215}}\\
&\quad - \frac{1}{2}\epsilon^4\, s\, t\, (s-2\,m^2)\mathbf{f}_{33}^{\mathrm{E:247}} + \frac{1}{2}\epsilon^4\, s\, (s-2\,m^2)\mathbf{f}_{35}^{\mathrm{E:247}} + \epsilon^4\, s\, \mathbf{f}_{36}^{\mathrm{E:247}}. \qquad (7.7)
\end{aligned}
$$

For $\mathbf{m}_1, \ldots, \mathbf{m}_{36}$, we employ the integration measure

$$\left(\frac{\Gamma(1-\epsilon)s^{\epsilon}}{i\pi^{2-\epsilon}}\right)^2 \int \mathrm{d}^{4-2\epsilon}k_1 \int \mathrm{d}^{4-2\epsilon}k_2 \tag{7.8}$$

with $\epsilon = (4-d)/2$, which allows us to consider our integrals to be functions of two dimensionless kinematic variables. For instance,

$$\mathbf{m}_1 = \frac{\Gamma^5(1-\epsilon)\Gamma(1+2\epsilon)}{\Gamma(1-3\epsilon)}\left(-\frac{t}{s}\right)^{-2\epsilon}. \tag{7.9}$$

One achieves a rationalization of two of the three roots, r_1 and r_2, with the parametrization [173]

$$s = -\frac{m^2(1-w)^2}{w} \qquad \text{and} \qquad t = -\frac{m^2 w\,(1+z)^2}{z\,(1+w)^2}, \tag{7.10}$$

and we hereafter work primarily with the variables w and z. It is immediate from Eq. (7.7) that, in the (w,z) representation, the *only* normal form integral which involves a square root in its definition is $\mathbf{m}_{32}$. Indeed, we see from (7.10) and Appendix A of Ref. [173] that

$$r_1 = -\frac{m^2(1-w)(1+w)}{w}, \tag{7.11}$$

$$r_2 = -\frac{m^4(1-w)(1-z)(1+z)}{z(1+w)}, \tag{7.12}$$

$$r_3 = \frac{m^4(1-w)}{w\,z(1+w)}\sqrt{(1+w^2z^2)(w+z)^2 + 2w\,z(w-z)^2 + 4w\,z^2(1+w^2)} \tag{7.13}$$

in the region $s > 4\,m^2$ (see also Section 7.3.1 for a detailed discussion of the (w,z) parametrization).

In the following, we will replace r_1, r_2 and r_3 according to (7.11)-(7.13) in the normal form definitions $\mathbf{m}_1, \ldots, \mathbf{m}_{36}$ and use these partially rationalized expressions. Note that only the definition of $\mathbf{m}_{32}$ involves the root

$$r \equiv \sqrt{(1+w^2z^2)(w+z)^2 + 2w\,z(w-z)^2 + 4w\,z^2(1+w^2)} \tag{7.14}$$

in the prefactor, which is real valued for $s > 4\,m^2$, which is the region of phase-space we are primarily concerned with. Using these definitions, it is straightforward to obtain the differential equations in the ϵ-decoupled form. We used `Reduze 2` [113, 114, 174, 175] to compute the integration-by-parts identities required to derive the differential equations.

7.2 Integrating the symbol

In this section, we discuss in more detail how the methods discussed in Section 2.8 are applied to the EW-QCD Drell-Yan master integrals with two massive internal lines. At the outset, before performing any simplification of the symbol alphabet, we find the rational alphabet

$$\begin{aligned}\mathcal{L}_R = \{&1-w, -w, 1+w, 1-w+w^2, 1-z, -z, 1+z,\\ &1-w\,z, 1+w^2\,z, -z-w^2, z-w\}\end{aligned} \tag{7.15}$$

and the intrinsically algebraic alphabet

$$\mathcal{L}_A = \{r, -(1-w)(z-w)(1-w\,z) + r\,(1+w),$$

$$-(1-w)\left(4w\,z+(w+z)(1+w\,z)\right)-r\,(1+w), r^2-2w\,z^2(1-w)^2+r\,(w+z)(1+w\,z),$$
$$r^2(1-z)^2+2z^2(z+w^2)(1+w^2z)+r\,(1-z)(1+z)\left(2w\,z-(w+z)(1+w\,z)\right)\}, \tag{7.16}$$

where r is given in Eq. (7.14). Note that r already appears as a letter in Eq. (7.16). However, there are also two rather complicated-looking symbol letters with terms involving r^2. The next step, is to use the simplification algorithm introduced in Section 2.8.3 to simplify (7.16). Considering ansätze up to degree four, we find the following candidates for algebraic letters for the differential equation:

$$\tilde{\mathcal{L}}_A = \Big\{r, \frac{1}{2}(2+z-w+w\,z(w+z)+r), \frac{1}{2}(2w^2+z-w+w\,z(w+z)+r),$$
$$\frac{1}{2}(-(w+z)(1-w\,z)+r), \frac{1}{2}(-(z-w)(1+w\,z)+r)\Big\}. \tag{7.17}$$

The overall factors of $1/2$ in Eq. (7.17) are judiciously chosen after the fact to prevent the appearance of explicit factors of 2 in our Li function arguments. The presence of this factor can be understood in light of the factorization property: one can easily check that all letters in $\tilde{\mathcal{L}}_A$ after multiplication with their conjugate, indeed factorize over the rational part of the alphabet without the presence of the factor 2 in this product. In order to find the correct normalization, one can run the above algorithm first adding the letter 2 in the rational part of the alphabet.

Using our heuristic approach to algebraic function factorization, we immediately find that the non-trivial elements of $\mathcal{L}_A$ can indeed be expressed as power products of letters drawn from the candidates in $\tilde{\mathcal{L}}_A$ from Eq. (7.17):

$$-(1-w)(z-w)(1-w\,z)+r\,(1+w) =$$
$$\frac{2(-w)(1+z)(-z-w^2)(2+z-w+w\,z(w+z)+r)}{2w^2+z-w+w\,z(w+z)+r},$$
$$-(1-w)\left(4w\,z+(w+z)(1+w\,z)\right)-r\,(1+w) =$$
$$\frac{8(-w)^2(-z)(1+z)^3(1+w^2\,z)(2w^2+z-w+w\,z(w+z)+r)}{(2+z-w+w\,z(w+z)+r)(-(w+z)(1-w\,z)+r)(-(z-w)(1+w\,z)+r)},$$
$$r^2-2w\,z^2(1-w)^2+r\,(w+z)(1+w\,z) =$$
$$\frac{(-z)^2(2+z-w+w\,z(w+z)+r)^2(2w^2+z-w+w\,z(w+z)+r)^2}{8(1+z)^2(1+w^2\,z)^2(-(w+z)(1-w\,z)+r)^2(-(z-w)(1+w\,z)+r)^{-2}},$$
$$r^2(1-z)^2+2z^2(z+w^2)(1+w^2z)+r\,(1-z)(1+z)\left(2w\,z-(w+z)(1+w\,z)\right)$$
$$=\frac{2(-z)^2(1+w^2\,z)^2(-(w+z)(1-w\,z)+r)^2}{(-(z-w)(1+w\,z)+r)^2}. \tag{7.18}$$

In summary, we define the full symbol alphabet for the two-massive-line Drell-Yan integrals, $\mathcal{L}=\mathcal{L}_R\cup\tilde{\mathcal{L}}_A$, in terms of positive definite letters for physical phase space points which satisfy $-1<w<0$ and $w<z<-w^2$ (this component of (w,z) space corresponds to part of the $s>4m^2$ region, see Section 7.3.1 for details). From Eqs. (7.15) and (7.17), we have:

$$\mathcal{L}=\{l_1,\ldots,l_{16}\}$$
$$=\Big\{1-w,-w,1+w,1-w+w^2,1-z,-z,1+z,1-w\,z,1+w^2\,z,-z-w^2,$$
$$z-w,r,\frac{1}{2}(2+z-w+w\,z(w+z)+r),\frac{1}{2}(2w^2+z-w+w\,z(w+z)+r),$$

$$\frac{1}{2}\big(-(w+z)(1-w\,z)+r\big), \frac{1}{2}\big(-(z-w)(1+w\,z)+r\big)\Big\}. \tag{7.19}$$

We express the differential equation in terms of this new alphabet and, for completeness, present it in Appendix 7.A.

Using the improved representation of the alphabet we are able to match the differential equation against an ansatz of multiple polylogarithms, cf. Section 2.8. For the integration through to weight four, it is enough to consider power products of symbol letters up to a total degree nine. In the next section, we will comment on what additional constraints we put on our ansatz to get a result with real-valued and monodromy-free functions only.

7.3 Analytic continuation and optimization of the functional bases

In this section, we review the salient features of the (w, z) representation for the mixed EW-QCD corrections to Drell-Yan production introduced in Section 7.1 above, as well as subtleties one encounters when analytically continuing multiple polylogarithms. Our primary goal in Section 7.3.1 is to motivate the analysis of Section 7.3.2, where we show how we avoid all explicit analytic continuations and $+i\,0$ prescriptions by selecting only well-behaved, monodromy-free Li functions in our ansatz. However, we also find it useful to review the fundamentals of analytic continuation of Feynman integrals as well as some details relevant to our specific representation.

7.3.1 Analytic continuation

Feynman's $+i\,0$ prescription for the propagators determines the value of a given Feynman integral in a specific region of phase space unambiguously. In principle, one could imagine solving the Feynman integral in each region of phase space separately. Alternatively, one can try to solve the integral in one region and then use the solution to obtain a result for it in a neighboring region by analytic continuation. The latter method is of particular interest for the method of differential equations, since it typically involves regularity conditions in some regions of phase space, and one needs to transport this knowledge to the region of interest.

If we want to continue a specific representation of the solution based on just the solution itself (without reference to the original Feynman integral), we need to make sure Feynman's $+i\,0$ prescription is maintained by appropriate complex values of the kinematic parameters. It is essential to observe that the analytic continuation is along a path in complex phase space and that the $+i\,0$ prescriptions must be respected for all points along this path, not just for the start and endpoint. This is in general non-trivial and needs to be checked for the representation at hand.

What is commonly referred to as "analytic continuation" in the physics literature should really be regarded as a two-step procedure in general:

(i) The actual analytic continuation in the mathematical sense: given a solution for one region, derive a solution for a connected region in some representation.

(ii) A possible change of functional representation in the new region such that no explicit $+i\,0$ prescription is necessary.

We will now work out the details for our current application.

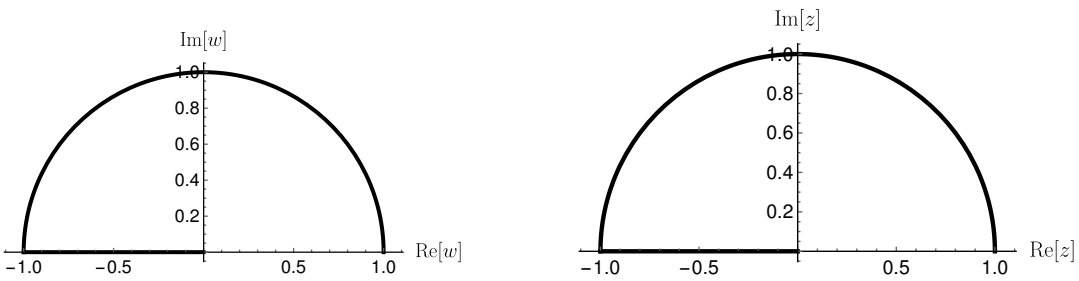

FIGURE 7.3.1: The (w, z) representation of the physical phase space has two main components which merge at the point of non-analyticity $w = z = -1$, corresponding to the two-mass threshold at $s = 4\,m^2$. The line segments on the negative real axes of w space (left) and z space (right) are half-open intervals which correspond to the above-threshold region; the points $w = 0$ and $z = 0$ are approached in the $s \to \infty$ limit. The semi-circular domains in the upper w and z half-planes correspond to the below-threshold region; the point $w = 1$ corresponds to the phase space boundary point $s = 0$ and $z = 1$ corresponds to the phase space boundary point $s = -t = 2\,m^2$. Note that the upper endpoint of z depends parametrically on w both above and below the two-mass threshold.

The Euclidean region for the mixed EW-QCD two-loop integrals is given by $s < 0$, $t < 0$ and $m^2 > 0$.[2] Considering other regions of phase space, we observe that the Feynman propagator prescription can effectively be implemented by the replacements $s \to s + i\,0$, $t \to t + i\,0$, since these are external scales, and $m^2 \to m^2 - i\,0$, since this is an internal scale. The $+i\,0$ prescription is relevant for s (t) whenever s (t) is positive. For the discussion of w and z, we will see that it is sufficient to view m^2 as being normalized to 1 without any imaginary part.

Let us focus on the (w, z) parametrization of our integrals in the physical region of phase space, $s > 0$, $t < 0$ and $m^2 > 0$. It was noted in [173] that the (w, z) representation has a point of non-analyticity at the physical two-mass threshold $s = 4\,m^2$ and a rather different character depending on whether s is above or below this threshold. We find it natural to adopt the definitions

$$w = -\frac{\sqrt{s} - \sqrt{s - 4\,m^2}}{\sqrt{s} + \sqrt{s - 4\,m^2}}, \tag{7.20}$$

$$z = -\frac{\sqrt{4\,m^4 - t\,(s - 4\,m^2)} - \sqrt{-t(s - 4\,m^2)}}{\sqrt{4\,m^4 - t\,(s - 4\,m^2)} + \sqrt{-t(s - 4\,m^2)}}\,. \tag{7.21}$$

We can see from the above that w and z are real variables which satisfy $-1 < w < 0$ and $-1 < z < -w^2$ in the region $s > 4\,m^2$. With our choices (7.20) and (7.21), we find that the Feynman prescription implies $w \to w + i\,0$ and $z \to z + i\,0$ in this region. On the other hand, both w and z become pure phases in the region $0 < s < 4\,m^2$. Therefore, it makes sense to explicitly extract their real and imaginary parts,

$$w = 1 - \frac{s}{2\,m^2} + \sqrt{1 - \left(1 - \frac{s}{2\,m^2}\right)^2}\,i\,, \tag{7.22}$$

[2] For non-planar topologies with four massless external legs, also cuts in u must be taken into account, which may actually prevent the existence of a Euclidean region with $s + t + u = 0$ [176].

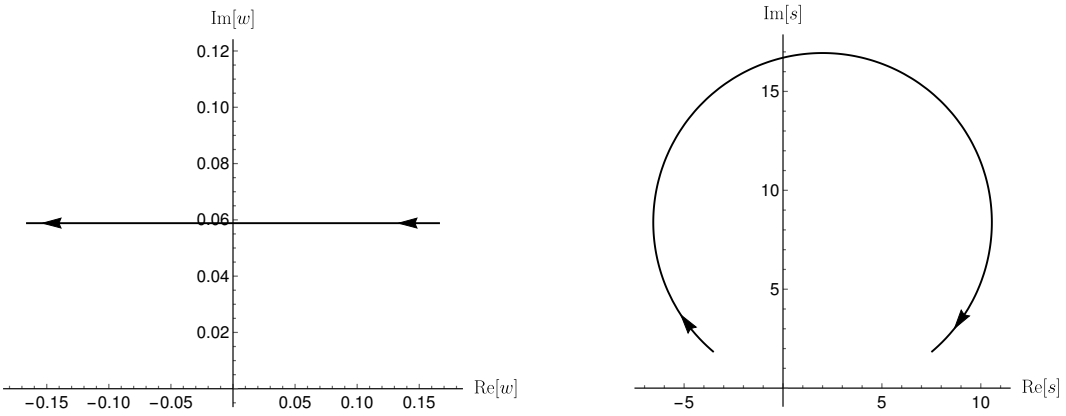

FIGURE 7.3.2: The path in w space prescribed by Eq. (7.24) for $w_{(0)} = 1/6$ and $\delta = 1/17$ (left) induces a nearly semi-circular path in s space (right) which respects the $+i\,0$ prescription for s. Note that, for fixed t and m^2, this straight-line path in w determines a nearly straight-line path in z as well.

$$z = -1 - \frac{t\,(4\,m^2 - s)}{2\,m^4} + \sqrt{1 - \left(-1 - \frac{t\,(4\,m^2 - s)}{2\,m^4}\right)^2}\,i\,, \tag{7.23}$$

to emphasize that, in the below-threshold region, the imaginary parts of w and z are fixed in terms of the real parts of w and z. In particular, we can deduce from Eqs. (7.22) and (7.23) that $\mathrm{Re}[w]$ and $\mathrm{Re}[z]$ satisfy $-1 < \mathrm{Re}[w] < 1$ and $-1 < \mathrm{Re}[z] < 1 - 2\,(\mathrm{Re}[w])^2$ in the below-threshold region. A visualization of the full physical phase space in the (w, z) representation is given in Figure 7.3.1.

In the following, we will study how to analytically continue solutions between different regions in s. In practice, we work with simple straight-line paths in the complex (w, z) space, checking after the fact that the chosen paths of analytic continuation always preserve the $+i\,0$ prescription for the original kinematic variables. In what follows, we carefully go through typical elementary examples of analytic continuation to clearly illustrate the subtleties for our Li functions, which one must be wary of to avoid introducing errors.

First, let us illustrate the importance of taking into account the complete path of analytic continuation rather than just the start and endpoint. Consider the analytic continuation of $\ln\,(w^2)$ along a straight-line path from $w_i = w_{(0)} + i\,\delta$ to $w_e = -w_{(0)} + i\,\delta$, for real $w_{(0)}$ and δ such that $0 < w_{(0)} < 1$ and $0 < \delta < w_{(0)}$ (see Figure 7.3.2). Such a path allows one to connect solutions for $s < 0$ with solutions for $s > 4\,m^2$. Naively, one might be tempted to erroneously implement the analytic continuation as $\ln\,(w_i^2) = \ln\,(w_{(0)}^2) = \ln\,((-w_{(0)})^2) = \ln\,(w_e^2)$ and incorrectly conclude that the analytic continuation is trivial along the chosen path. The problem here, is that the logarithm is a multi-valued function and one must therefore carefully check whether or not the specified path of analytic continuation forces the polynomial function argument to cross the branch cut of the logarithm on the negative real axis, $(-\infty, 0)$. In the absence of any branch cut crossings, knowledge of the endpoint of the path is sufficient. However, in the presence of one or more branch cut crossings, the function leaves its principal Riemann sheet and one must add an appropriate monodromy contribution, taking into account the details of the path of analytic continuation.

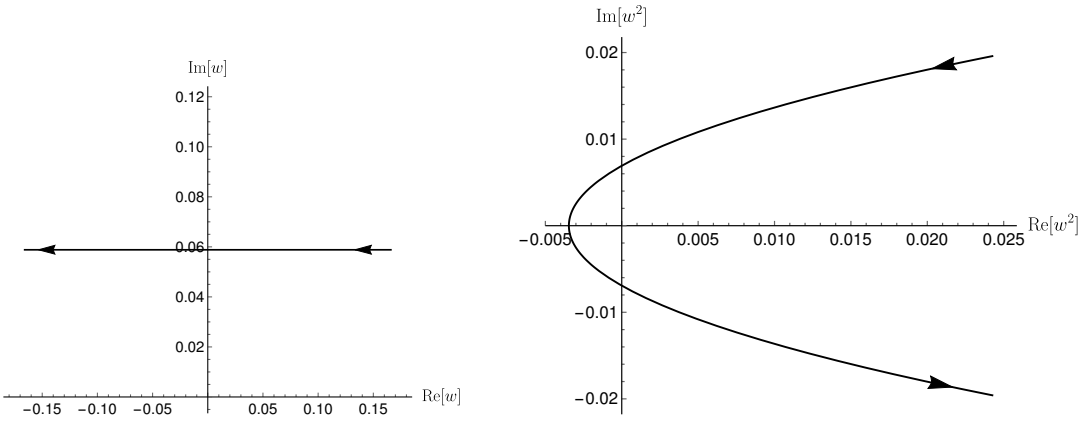

FIGURE 7.3.3: The path in w space prescribed by Eq. (7.24) for $w_{(0)} = 1/6$ and $\delta = 1/17$ (left) induces an essentially hyperbolic path in w^2 space (right) which crosses the negative real axis at $-\delta^2$.

Let us spell out in detail how to correctly analytically continue solutions valid for different values of s. We parametrize our chosen path in w space as

$$w(v) = (1 - 2v)\, w_{(0)} + \delta\, i, \tag{7.24}$$

with a parameter $v \in [0, 1]$. We then have

$$w^2(v) = (1 - 2\,v)^2 w_{(0)}^2 - \delta^2 + 2\,(1 - 2\,v)\,\delta\, w_{(0)}\, i \tag{7.25}$$

for the argument of $\ln(w^2)$. As depicted in Figure 7.3.3, our path in w space takes $w^2(v)$ from just above the point $w_{(0)}^2 - \delta^2$ on the positive real axis to just below the point $w_{(0)}^2 - \delta^2$ and, crucially, it passes through the negative real axis at $w(1/2) = \delta\, i$. The monodromy contribution to $\ln(w^2)$ in this case is well-known to be simply $2\pi i$, due to the fact that our path induces just one counter-clockwise branch cut crossing. Therefore, the analytically continued function is $\ln(w^2) + 2\pi i$ in a neighborhood of the endpoint of our chosen path. This conclusion may be quickly checked by rewriting the function $\ln(w^2)$ as $2\ln(w)$ in the Euclidean region where $0 < \mathrm{Re}[w] < 1$ before carrying out the analytic continuation along our chosen path. When the function is viewed in this alternative way, no branch cut crossing is induced and one can simply rewrite the function to explicitly extract its imaginary part: for $\mathrm{Im}[w] > 0$, $2\ln(w) = 2\big(\ln(-w) + \pi i\big) = 2\ln(-w) + 2\pi i = \ln(w^2) + 2\pi i$. In the two-step picture mentioned above we thus have

$$\ln(w^2) \xrightarrow[\text{(i) } w(v)]{} \ln(w^2) + 2\pi i \underset{\text{(ii)}}{=} \ln(w^2) + 2\pi i \tag{7.26}$$

or

$$\ln(w^2) = 2\ln(w) \xrightarrow[\text{(i) } w(v)]{} 2\ln(w) \qquad \underset{\text{(ii)}}{=} 2\ln(-w) + 2\pi i = \ln(w^2) + 2\pi i \tag{7.27}$$

Depending on the type of representation we consider, either the analytic continuation (i) or the rewriting of the function to be independent of $+i\,0$ prescriptions (ii) is trivial in this example.

The relevant monodromy contributions become more complicated for higher-weight Li functions. Already for Li_2, a new feature emerges: moving across its branch

cut on the positive real axis, $(1,\infty)$, onto a Riemann sheet other than the principal one actually exposes the existence of a hidden branch point at 1. To see this, consider Euler's identity for the dilogarithm of $1-w^2$,

$$\mathrm{Li}_2(1-w^2) = -\mathrm{Li}_2(w^2) - \ln(w^2)\ln(1-w^2) + \frac{\pi^2}{6}. \tag{7.28}$$

The representation furnished by the right-hand side of (7.28) and the above discussion of $\ln(w^2)$ make it clear that $\mathrm{Li}_2(1-w^2)$ has non-trivial monodromy for the path $w(v)$ defined above in Eq. (7.24). For the path $w(v)$, we find:

$$\begin{aligned}\mathrm{Li}_2(1-w^2) &= -\mathrm{Li}_2(w^2) - \ln(w^2)\ln(1-w^2) + \frac{\pi^2}{6} \\ &\xrightarrow[w(v)]{} -\mathrm{Li}_2(w^2) - \Big(\ln(w^2) + 2\pi i\Big)\ln(1-w^2) + \frac{\pi^2}{6} \\ &= \mathrm{Li}_2(1-w^2) - 2\pi i \ln(1-w^2),\end{aligned} \tag{7.29}$$

This implies that $\mathrm{Li}_2(1-w^2)$ picks up a monodromy contribution of $-2\pi i\ln(1-w^2)$ due to the branch point at $w=1$, despite the fact the function is continuous at that point on the principal sheet.

When considering general analytic continuations of $\mathrm{Li}_{n_1,\ldots,n_k}$ functions, one must take into account all function arguments to obtain the monodromy contributions as one moves along the path of analytic continuation. Building on the work of Goncharov [177], it was shown in [178] how one can easily compute the monodromy of an arbitrary Li function in terms of monodromies of simple logarithms using the coproduct. In particular, the presence of a monodromy contribution can be detected by studying the first entry of the symbol. For our master integrals, the sheer number of distinct branch cut crossings that can arise from the arguments of the various Li functions renders the analytic continuation between different regions rather involved in practice. While our final goal is to obtain representations in terms of well-behaved, monodromy-free Li functions for a given kinematic region, we find it convenient to also employ auxiliary representations for the purpose of analytic continuations.

If available, a representation in terms of G functions with the kinematic variables in the argument avoids many of the subtleties involved in the continuation described above. For the integrals with unrationalizable alphabets, however, this is not an option. For such cases, we find it useful to use expansions around regular and singular points [179] for the continuation. For this part of the analysis, we do not include the unrationalizable root of $\mathbf{m}_{32}$ in (7.38) in the definition of our basis in order to work with rational differential equations. Using high-precision numerical evaluations for two expansion points with an overlapping region of convergence and the PSLQ algorithm [102], one can effectively transport analytic integration constants.

What has been discussed so far allows us to construct a functional basis for a given region of phase space, integrate the symbol in terms of these functions, and relate solutions for different regions by analytic continuation in order to fix the integration constants. We will now discuss how to construct domain-restricted but well-behaved ansätze of multiple polylogarithms, which don't require an explicit $+i\,0$ prescription and perform well numerically.

7.3.2 Optimizing the bases of multiple polylogarithms

Starting from a Duhr-Gangl-Rhodes basis of multiple polylogarithms for the integrals $\vec{\mathbf{m}}$, we wish to remove Li functions that have suboptimal analytic properties for

physical kinematics. In the following we will restrict ourselves to the region above the two-mass threshold, i.e. $s > 4\,m^2$. To proceed, we must determine under what conditions the logarithms of the letters either diverge or move off of their principal Riemann sheets. We find that, in practice, it is simplest to use Eqs. (7.20) and (7.21) above threshold, and the `Mathematica` function `Reduce` to work out how various constraints on polynomials of w and z map back to conditions on the original and more familiar kinematic variables, s, t, and m^2. To check whether it is possible for a given function to live without a $+i\,0$ prescription, we must first understand for what values of s, t, and m^2 the letters vanish or become negative:

- $\ln(l_1) = \ln(1-w)$ diverges at the phase space boundary point $s = 0$.
- $\ln(l_2) = \ln(-w)$ has no issues for $m^2 > 0$, except at the phase space boundary point $s = 0$ where it becomes ill-defined.
- $\ln(l_3) = \ln(1+w)$ diverges at the two-mass threshold $s = 4\,m^2$.
- $\ln(l_4) = \ln(1-w+w^2)$ diverges at the one-mass threshold $s = m^2$.
- $\ln(l_5) = \ln(1-z)$ diverges at the phase space boundary point $s = -t = 2\,m^2$.
- $\ln(l_6) = \ln(-z)$ has no issues for $m^2 > 0$, except at the phase space boundary point $s = -t = 2\,m^2$ where it becomes ill-defined.
- $\ln(l_7) = \ln(1+z)$ diverges at the phase space boundary where $t = 0$ and at the two-mass threshold $s = 4\,m^2$.
- $\ln(l_8) = \ln(1-w\,z)$ diverges at the two-mass threshold $s = 4\,m^2$.
- $\ln(l_9) = \ln(1+w^2\,z)$ diverges at the phase space boundary $s = -t$ for $0 \leq s \leq 2\,m^2$ and at the two-mass threshold $s = 4\,m^2$.
- $\ln(l_{10}) = \ln(-z-w^2)$ diverges at the phase space boundary $s = -t$ for $s \geq 2\,m^2$ and, in particular, at $s = 4\,m^2$.
- $\ln(l_{11}) = \ln(z-w)$ diverges when $t = -m^2$ for $s \geq m^2$ and, in particular, at $s = 4\,m^2$. $\ln(l_{11})$ is also not analytic at $s = -\frac{4\,m^2 t}{m^2-t}$ for $-m^2 \leq t \leq 0$.
- $\ln(l_{12}), \ldots, \ln(l_{16})$ do not diverge anywhere for $s > 4m^2$

Due to the absence of u dependence in our planar double boxes, we expect them to have a regular limit as u approaches 0. We see from the above that for $s > 2\,m^2$ (thus also $s > 4\,m^2$) regularity for $u \to 0$ suggests the absence of $\ln(l_{10})$ at weight one. Of course, we wish to achieve that also the higher weight basis functions lack logarithmic singularities (and are thus monodromy-free) as $l_{10} \to 0$ for $s > 4\,m^2$. This can be achieved by imposing an appropriate first-entry condition [178, 180–182] on the symbol to select suitable functions: we remove all Li functions, which have the letter l_{10} in the first entry of their symbols, from our ansatz. The only additional logarithm with a spurious singularity in the physical region for $s > 4\,m^2$ is $\ln(l_{11})$, which can also be dealt with by imposing an additional first-entry condition on l_{11}.

Since all 16 letters evaluate to real numbers for $s > 4\,m^2$, we can impose a further restriction on our ansatz, namely, we only allow real-valued functions. After filtering our ansatz with these two constraints (monodromy-free and real-valued functions only) we find in total 478 candidates for the Li_n functions. We proceed analogously to filter the set of $\mathrm{Li}_{2,1}$, $\mathrm{Li}_{3,1}$, and $\mathrm{Li}_{2,2}$ function argument pairs which survive the first-entry condition and are real-valued. In total, we find 41 admissible candidates for the $\mathrm{Li}_{2,1}$ functions, 516 $\mathrm{Li}_{2,2}$ and 960 $\mathrm{Li}_{3,1}$ functions.

7.4 Weight-four multiple polylogarithms for Drell-Yan master integrals

Having build our ansatz as described in the previous section, we apply the techniques introduced in Sections 2.8 and 7.3.2 to explicitly integrate the $\epsilon\,\mathrm{d}\ln$ form for $\{\mathbf{m}_1,\ldots,\mathbf{m}_{36}\}$, (7.38), in the physical region above the two-mass threshold ($s > 4\,m^2$) through to weight four in terms of real-valued and monodromy-free Li functions. To our knowledge, this is the first time a complete solution in terms of standard multiple polylogarithms has been found for a multi-loop Feynman integral with an $\epsilon\,\mathrm{d}\ln$ differential equation containing provably unrationalizable symbol letters. We fix our integration constants using a variety of established techniques, such as direct evaluation in Feynman parameters, exploiting regular kinematic limits of the differential equations, and exploiting kinematic limits where particular integrals are power-suppressed and must therefore vanish (see Section 5.2 of [173]).

Due to the significant length of our results, we refrain from presenting them explicitly in the text. It is worth pointing out that our choice of alphabet, Eq. (7.19), produces remarkably simple integration constants. E.g. for $\mathbf{m}_{36}$ we find

$$\frac{3}{2}\zeta_3 - \frac{3}{2}\pi^3 i \tag{7.30}$$

at weight three and

$$\frac{1335349}{32}\zeta_2^2 - 116\,\zeta_3\,\pi i \tag{7.31}$$

at weight four.

In lieu of our explicit analytic results, it is straightforward to obtain high-precision numerical results for our master integrals using `GiNaC`. For the randomly chosen physical phase space point

$$\left(s, t, m^2\right) = (17, -7, 6241/1681)\,. \tag{7.32}$$

we find for the most complicated master integrals with two massive internal lines

$$\begin{aligned}\mathbf{m}_{32} \approx\ & \epsilon^3(0.066537984962080530758\ldots - 27.508245870011457529\ldots\, i)\\ & + \epsilon^4(51.615607433806381131\ldots - 149.06326619542437190\ldots\, i) + \mathcal{O}\left(\epsilon^5\right),\end{aligned} \tag{7.33}$$

$$\begin{aligned}\mathbf{m}_{33} \approx\ & \epsilon^2(10.163316917366188927\ldots + 6.2974465571355440423\ldots\, i)\\ & + \epsilon^3(33.914009430201406423\ldots + 4.6486595371603574921\ldots\, i)\\ & + \epsilon^4(163.17321004422879959\ldots - 128.72756457117576796\ldots\, i) + \mathcal{O}\left(\epsilon^5\right),\end{aligned} \tag{7.34}$$

$$\begin{aligned}\mathbf{m}_{34} \approx\ & \epsilon^2(-9.3166453894096456380\ldots - 4.6722528592943756861\ldots\, i)\\ & + \epsilon^3(-12.274144284891231677\ldots - 11.270075866466130873\ldots\, i)\\ & + \epsilon^4(-51.057330106861359687\ldots + 87.629800828432935443\ldots\, i) + \mathcal{O}\left(\epsilon^5\right),\end{aligned} \tag{7.35}$$

$$\mathbf{m}_{35} \approx \epsilon^4(6.9039856473317646358\ldots - 0.013343873471826080269\ldots\, i) + \mathcal{O}\left(\epsilon^5\right), \tag{7.36}$$

$$\begin{aligned}\mathbf{m}_{36} \approx\ & \epsilon^3(-4.7564239669560836801\ldots + 4.0753242804814306037\ldots\, i)\\ & + \epsilon^4(-8.5216864119748844907\ldots - 13.318764764536663942\ldots\, i) + \mathcal{O}\left(\epsilon^5\right).\end{aligned} \tag{7.37}$$

Using the finite integral method [107, 183, 184] and `SecDec 3` [185], we were able to independently check these numerical results to a few decimal digits.

We find, that a double precision evaluation of all 36 master integrals $m_1, \ldots, m_{36}$ at the point (7.32) using `GiNaC` takes 0.5 seconds on one Intel E3-1275 CPU core. The performance in this central point in phase space is therefore not much worse than what is encountered for Feynman integrals involving rational alphabets, see *e.g.* the discussion in [105]. Therefore, we expect the functional representation discussed here to be well-suited for direct usage in Monte-Carlo programs.

7.5 Outlook

In this chapter, we considered irreducible Feynman integrals that appear in the calculation of the mixed EW-QCD two-loop corrections to the Drell-Yan process. These integrals satisfy $\epsilon\,\mathrm{d}\ln$ differential equations with non-rational symbol letters. We developed a new technique, which allowed us to simplify the differential equation. We were then able to find an analytic solution in terms of standard multiple polylogarithms, even in the presence of unrationalizable symbol letters. The results have been published in Ref. [84]. In the next chapter, we will use these master integrals to calculate the mixed EW-QCD two-loop amplitude and evaluate it numerically.

Appendix

7.A Differential equations for the Drell-Yan masters with two massive lines

In terms of the symbol letters $\{l_1, \ldots, l_{16}\}$ defined in (7.19), the system of differential equations for $\mathbf{m}_1, \ldots, \mathbf{m}_{36}$ in (7.7) can be cleanly written in differential form:

$$\epsilon^{-1}\mathrm{d}\mathbf{m}_1 = \mathbf{m}_1\Big[4\,\mathrm{d}\ln(l_1) - 4\,\mathrm{d}\ln(l_2) + 4\,\mathrm{d}\ln(l_3) + 2\,\mathrm{d}\ln(l_6) - 4\,\mathrm{d}\ln(l_7)\Big],$$

$$\epsilon^{-1}\mathrm{d}\mathbf{m}_2 = \mathbf{m}_2\Big[2\,\mathrm{d}\ln(l_1) - \mathrm{d}\ln(l_2)\Big],$$

$$\epsilon^{-1}\mathrm{d}\mathbf{m}_3 = \mathbf{m}_3\Big[4\,\mathrm{d}\ln(l_1) - 2\,\mathrm{d}\ln(l_2)\Big],$$

$$\epsilon^{-1}\mathrm{d}\mathbf{m}_4 = \mathbf{m}_4\Big[6\,\mathrm{d}\ln(l_1) - 3\,\mathrm{d}\ln(l_2)\Big] + \mathbf{m}_5\Big[\mathrm{d}\ln(l_2) - \mathrm{d}\ln(l_4)\Big],$$

$$\epsilon^{-1}\mathrm{d}\mathbf{m}_5 = \mathbf{m}_4\Big[12\,\mathrm{d}\ln(l_1) - 6\,\mathrm{d}\ln(l_2)\Big] + \mathbf{m}_5\Big[4\,\mathrm{d}\ln(l_1) + 2\,\mathrm{d}\ln(l_2) - 4\,\mathrm{d}\ln(l_4)\Big],$$

$$\epsilon^{-1}\mathrm{d}\mathbf{m}_6 = 0,$$

$$\epsilon^{-1}\mathrm{d}\mathbf{m}_7 = \mathbf{m}_7\Big[4\,\mathrm{d}\ln(l_1) - 4\,\mathrm{d}\ln(l_2) + 4\,\mathrm{d}\ln(l_3) + 2\,\mathrm{d}\ln(l_6) - 4\,\mathrm{d}\ln(l_7)\Big],$$

$$\begin{aligned}\epsilon^{-1}\mathrm{d}\mathbf{m}_8 = {}& \mathbf{m}_1\Big[-\mathrm{d}\ln(l_3) - \frac{1}{2}\mathrm{d}\ln(l_6) + \frac{1}{2}\mathrm{d}\ln(l_8) + \frac{1}{2}\mathrm{d}\ln(l_{11})\Big] \\ & + \mathbf{m}_3\Big[\mathrm{d}\ln(l_3) + \frac{1}{2}\mathrm{d}\ln(l_6) - \frac{1}{2}\mathrm{d}\ln(l_8) - \frac{1}{2}\mathrm{d}\ln(l_{11})\Big] \\ & + \mathbf{m}_8\Big[4\,\mathrm{d}\ln(l_1) - \mathrm{d}\ln(l_2) + 2\,\mathrm{d}\ln(l_3) + \mathrm{d}\ln(l_6) + 2\,\mathrm{d}\ln(l_7) - 2\,\mathrm{d}\ln(l_8) - 2\,\mathrm{d}\ln(l_{11})\Big],\end{aligned}$$

$$\epsilon^{-1}\mathrm{d}\mathbf{m}_9 = \mathbf{m}_2\Big[-\mathrm{d}\ln(l_2)\Big] + \mathbf{m}_9\Big[2\,\mathrm{d}\ln(l_1) - 2\,\mathrm{d}\ln(l_3)\Big],$$

$$\begin{aligned}\epsilon^{-1}\mathrm{d}\mathbf{m}_{10} = {}& \mathbf{m}_3\Big[-\frac{1}{4}\mathrm{d}\ln(l_2)\Big] + \mathbf{m}_4\Big[\frac{3}{2}\mathrm{d}\ln(l_2)\Big] + \mathbf{m}_5\Big[-\frac{3}{4}\mathrm{d}\ln(l_2)\Big] \\ & + \mathbf{m}_{10}\Big[4\,\mathrm{d}\ln(l_1) - \mathrm{d}\ln(l_2) - 2\,\mathrm{d}\ln(l_3)\Big],\end{aligned}$$

$$\epsilon^{-1}\mathrm{d}\mathbf{m}_{11} = \mathbf{m}_{11}\Big[6\,\mathrm{d}\ln(l_1) - 3\,\mathrm{d}\ln(l_2)\Big] + \mathbf{m}_{12}\Big[\mathrm{d}\ln(l_2)\Big],$$

$$\epsilon^{-1}\mathrm{d}\mathbf{m}_{12} = \mathbf{m}_3\Big[-2\,\mathrm{d}\ln(l_2)\Big] + \mathbf{m}_{11}\Big[3\,\mathrm{d}\ln(l_2)\Big] + \mathbf{m}_{12}\Big[4\,\mathrm{d}\ln(l_1) - \mathrm{d}\ln(l_2) - 2\,\mathrm{d}\ln(l_3)\Big],$$

$$\begin{aligned}\epsilon^{-1}\mathrm{d}\mathbf{m}_{13} = {}& \mathbf{m}_1\Big[-3\,\mathrm{d}\ln(l_2) - 3\,\mathrm{d}\ln(l_7) + \frac{3}{2}\,\mathrm{d}\ln(l_9) + \frac{3}{2}\,\mathrm{d}\ln(l_{10})\Big] \\ & + \mathbf{m}_6\Big[6\,\mathrm{d}\ln(l_1) + 6\,\mathrm{d}\ln(l_3) + 3\,\mathrm{d}\ln(l_6) - 3\,\mathrm{d}\ln(l_9) - 3\,\mathrm{d}\ln(l_{10})\Big]\end{aligned}$$

$$
\begin{aligned}
&+ \mathbf{m}_{13}\Big[2\,\mathrm{d}\ln(l_1) - 4\,\mathrm{d}\ln(l_2) + 2\,\mathrm{d}\ln(l_3) + \mathrm{d}\ln(l_6) - 4\,\mathrm{d}\ln(l_7) + \mathrm{d}\ln(l_9) + \mathrm{d}\ln(l_{10})\Big],\\
\epsilon^{-1}\mathrm{d}\mathbf{m}_{14} &= \mathbf{m}_3\Big[\mathrm{d}\ln(l_3) + \frac{1}{2}\mathrm{d}\ln(l_6) - \frac{1}{2}\mathrm{d}\ln(l_8) - \frac{1}{2}\mathrm{d}\ln(l_{11})\Big]\\
&+ \mathbf{m}_7\Big[3\,\mathrm{d}\ln(l_2) + 6\,\mathrm{d}\ln(l_7) - 3\,\mathrm{d}\ln(l_8) - 3\,\mathrm{d}\ln(l_{11})\Big]\\
&+ \mathbf{m}_{14}\Big[4\,\mathrm{d}\ln(l_1) - \mathrm{d}\ln(l_2) + 2\,\mathrm{d}\ln(l_7) - \mathrm{d}\ln(l_8) - \mathrm{d}\ln(l_{11})\Big],\\
\epsilon^{-1}\mathrm{d}\mathbf{m}_{15} &= \mathbf{m}_1\Big[-\mathrm{d}\ln(l_2) - 2\,\mathrm{d}\ln(l_7) + \mathrm{d}\ln(l_8) + \mathrm{d}\ln(l_{11})\Big]\\
&+ \mathbf{m}_3\Big[2\,\mathrm{d}\ln(l_3) + \mathrm{d}\ln(l_6) - \mathrm{d}\ln(l_8) - \mathrm{d}\ln(l_{11})\Big]\\
&+ \mathbf{m}_8\Big[4\,\mathrm{d}\ln(l_2) + 8\,\mathrm{d}\ln(l_7) - 4\,\mathrm{d}\ln(l_8) - 4\,\mathrm{d}\ln(l_{11})\Big] + \mathbf{m}_{15}\Big[4\,\mathrm{d}\ln(l_1) - 2\,\mathrm{d}\ln(l_2)\Big],\\
\epsilon^{-1}\mathrm{d}\mathbf{m}_{16} &= \mathbf{m}_2\Big[\mathrm{d}\ln(l_2) - \mathrm{d}\ln(l_4)\Big] + \mathbf{m}_3\Big[\mathrm{d}\ln(l_1) - \frac{1}{6}\mathrm{d}\ln(l_2) - \frac{1}{3}\mathrm{d}\ln(l_4)\Big]\\
&+ \mathbf{m}_4\Big[6\,\mathrm{d}\ln(l_1) - 3\,\mathrm{d}\ln(l_2)\Big] + \mathbf{m}_5\Big[-\mathrm{d}\ln(l_1) + \frac{2}{3}\mathrm{d}\ln(l_2) - \frac{1}{6}\mathrm{d}\ln(l_4)\Big]\\
&+ \mathbf{m}_6\Big[-2\,\mathrm{d}\ln(l_2) + 2\,\mathrm{d}\ln(l_4)\Big] + \mathbf{m}_{16}\Big[6\,\mathrm{d}\ln(l_1) - \frac{7}{3}\mathrm{d}\ln(l_2) - \frac{2}{3}\mathrm{d}\ln(l_4)\Big]\\
&+ \mathbf{m}_{17}\Big[4\,\mathrm{d}\ln(l_1) - \frac{2}{3}\mathrm{d}\ln(l_2) - \frac{4}{3}\mathrm{d}\ln(l_4)\Big],\\
\epsilon^{-1}\mathrm{d}\mathbf{m}_{17} &= \mathbf{m}_2\Big[\mathrm{d}\ln(l_2) - \mathrm{d}\ln(l_4)\Big] + \mathbf{m}_3\Big[\frac{1}{3}\mathrm{d}\ln(l_2) - \frac{1}{3}\mathrm{d}\ln(l_4)\Big]\\
&+ \mathbf{m}_5\Big[-\frac{1}{3}\mathrm{d}\ln(l_2) + \frac{1}{3}\mathrm{d}\ln(l_4)\Big] + \mathbf{m}_6\Big[-2\,\mathrm{d}\ln(l_2) + 2\,\mathrm{d}\ln(l_4)\Big]\\
&+ \mathbf{m}_{16}\Big[\frac{2}{3}\,\mathrm{d}\ln(l_2) - \frac{2}{3}\,\mathrm{d}\ln(l_4)\Big] + \mathbf{m}_{17}\Big[4\,\mathrm{d}\ln(l_1) - \frac{2}{3}\,\mathrm{d}\ln(l_2) - \frac{4}{3}\,\mathrm{d}\ln(l_4)\Big],\\
\epsilon^{-1}\mathrm{d}\mathbf{m}_{18} &= \mathbf{m}_4\Big[4\,\mathrm{d}\ln(l_1) + 4\,\mathrm{d}\ln(l_3) + 2\,\mathrm{d}\ln(l_6) - 2\,\mathrm{d}\ln(l_9) - 2\,\mathrm{d}\ln(l_{10})\Big]\\
&+ \mathbf{m}_5\Big[-\mathrm{d}\ln(l_1) - \mathrm{d}\ln(l_3) - \frac{1}{2}\mathrm{d}\ln(l_6) + \frac{1}{2}\mathrm{d}\ln(l_9) + \frac{1}{2}\mathrm{d}\ln(l_{10})\Big]\\
&+ \mathbf{m}_7\Big[-4\,\mathrm{d}\ln(l_1) - 4\,\mathrm{d}\ln(l_3) - 2\,\mathrm{d}\ln(l_6) + 2\,\mathrm{d}\ln(l_9) + 2\,\mathrm{d}\ln(l_{10})\Big]\\
&+ \mathbf{m}_{18}\Big[\mathrm{d}\ln(l_2) + 4\,\mathrm{d}\ln(l_7) - 3\,\mathrm{d}\ln(l_8) + \mathrm{d}\ln(l_9) + \mathrm{d}\ln(l_{10}) - 3\,\mathrm{d}\ln(l_{11})\Big]\\
&+ \mathbf{m}_{19}\Big[-2\,\mathrm{d}\ln(l_1) - \mathrm{d}\ln(l_8) + \mathrm{d}\ln(l_9) + \mathrm{d}\ln(l_{10}) - \mathrm{d}\ln(l_{11})\Big],\\
\epsilon^{-1}\mathrm{d}\mathbf{m}_{19} &= \mathbf{m}_4\Big[-12\,\mathrm{d}\ln(l_1) + 3\,\mathrm{d}\ln(l_2) - 6\,\mathrm{d}\ln(l_3) + 6\,\mathrm{d}\ln(l_4) - 3\,\mathrm{d}\ln(l_6) + 6\,\mathrm{d}\ln(l_7)\Big]\\
&+ \mathbf{m}_5\Big[3\,\mathrm{d}\ln(l_1) - \mathrm{d}\ln(l_2) + 2\,\mathrm{d}\ln(l_3) - \frac{3}{2}\mathrm{d}\ln(l_4) + \mathrm{d}\ln(l_6) - 2\,\mathrm{d}\ln(l_7)\Big]\\
&+ \mathbf{m}_7\Big[12\,\mathrm{d}\ln(l_1) - 6\,\mathrm{d}\ln(l_4)\Big]\\
&+ \mathbf{m}_{18}\Big[12\,\mathrm{d}\ln(l_1) - 6\,\mathrm{d}\ln(l_2) - 6\,\mathrm{d}\ln(l_4) - 12\,\mathrm{d}\ln(l_7) + 6\,\mathrm{d}\ln(l_8) + 6\,\mathrm{d}\ln(l_{11})\Big]
\end{aligned}
$$

$$
\begin{aligned}
&+ \mathbf{m}_{19}\Big[10\,\mathrm{d}\ln(l_1) - 3\,\mathrm{d}\ln(l_2) - 4\,\mathrm{d}\ln(l_4) - 4\,\mathrm{d}\ln(l_7) + 2\,\mathrm{d}\ln(l_8) + 2\,\mathrm{d}\ln(l_{11})\Big],\\
\epsilon^{-1}\mathrm{d}\mathbf{m}_{20} &= \mathbf{m}_3\Big[-\mathrm{d}\ln(l_1) + \mathrm{d}\ln(l_2) - \mathrm{d}\ln(l_3) - \frac{1}{2}\mathrm{d}\ln(l_6) + \mathrm{d}\ln(l_7)\Big]\\
&+ \mathbf{m}_4\Big[-4\,\mathrm{d}\ln(l_1) + 4\,\mathrm{d}\ln(l_2) - 4\,\mathrm{d}\ln(l_3) - 2\,\mathrm{d}\ln(l_6) + 4\,\mathrm{d}\ln(l_7)\Big]\\
&+ \mathbf{m}_5\Big[\mathrm{d}\ln(l_1) - \mathrm{d}\ln(l_2) + \mathrm{d}\ln(l_3) + \frac{1}{2}\mathrm{d}\ln(l_6) - \mathrm{d}\ln(l_7)\Big]\\
&+ \mathbf{m}_8\Big[-2\,\mathrm{d}\ln(l_1) + 2\,\mathrm{d}\ln(l_2) - 2\,\mathrm{d}\ln(l_3) - \mathrm{d}\ln(l_6) + 2\,\mathrm{d}\ln(l_7)\Big] + \mathbf{m}_{20}\Big[-4\,\mathrm{d}\ln(l_2)\\
&- 4\,\mathrm{d}\ln(l_7) + 2\,\mathrm{d}\ln(l_9) + 2\,\mathrm{d}\ln(l_{10})\Big] + \mathbf{m}_{21}\Big[-2\,\mathrm{d}\ln(l_1) + \mathrm{d}\ln(l_2)\Big],\\
\epsilon^{-1}\mathrm{d}\mathbf{m}_{21} &= \mathbf{m}_1\Big[-\frac{1}{2}\mathrm{d}\ln(l_2) + \mathrm{d}\ln(l_3) + \frac{1}{2}\mathrm{d}\ln(l_4) + \frac{1}{2}\mathrm{d}\ln(l_6) - \frac{1}{2}\mathrm{d}\ln(l_8) - \frac{1}{2}\mathrm{d}\ln(l_{11})\Big]\\
&+ \mathbf{m}_3\Big[2\,\mathrm{d}\ln(l_1) - \frac{3}{2}\mathrm{d}\ln(l_2) + \mathrm{d}\ln(l_3) - \frac{1}{2}\mathrm{d}\ln(l_4) + \frac{1}{2}\mathrm{d}\ln(l_6) - 2\,\mathrm{d}\ln(l_7) + \frac{1}{2}\mathrm{d}\ln(l_8)\\
&+ \frac{1}{2}\mathrm{d}\ln(l_{11})\Big] + \mathbf{m}_4\Big[6\,\mathrm{d}\ln(l_1) - 6\,\mathrm{d}\ln(l_2) + 6\,\mathrm{d}\ln(l_3) + 3\,\mathrm{d}\ln(l_6) - 6\,\mathrm{d}\ln(l_7)\Big]\\
&+ \mathbf{m}_5\Big[-2\,\mathrm{d}\ln(l_1) + 2\,\mathrm{d}\ln(l_2) - 2\,\mathrm{d}\ln(l_3) - \mathrm{d}\ln(l_6) + 2\,\mathrm{d}\ln(l_7)\Big]\\
&+ \mathbf{m}_8\Big[6\,\mathrm{d}\ln(l_1) - 4\,\mathrm{d}\ln(l_2) + 2\,\mathrm{d}\ln(l_3) - 2\,\mathrm{d}\ln(l_4) + \mathrm{d}\ln(l_6) - 6\,\mathrm{d}\ln(l_7) + 2\,\mathrm{d}\ln(l_8)\\
&+ 2\,\mathrm{d}\ln(l_{11})\Big] + \mathbf{m}_{20}\Big[12\,\mathrm{d}\ln(l_1) - 6\,\mathrm{d}\ln(l_4)\Big]\\
&+ \mathbf{m}_{21}\Big[10\,\mathrm{d}\ln(l_1) - 5\,\mathrm{d}\ln(l_2) - 4\,\mathrm{d}\ln(l_4) - 4\,\mathrm{d}\ln(l_7) + 2\,\mathrm{d}\ln(l_9) + 2\,\mathrm{d}\ln(l_{10})\Big],\\
\epsilon^{-1}\mathrm{d}\mathbf{m}_{22} &= \mathbf{m}_9\Big[-2\,\mathrm{d}\ln(l_2)\Big] + \mathbf{m}_{22}\Big[4\,\mathrm{d}\ln(l_1) - 2\,\mathrm{d}\ln(l_2)\Big],\\
\epsilon^{-1}\mathrm{d}\mathbf{m}_{23} &= \mathbf{m}_3\Big[\mathrm{d}\ln(l_1) - \frac{1}{2}\mathrm{d}\ln(l_2)\Big] + \mathbf{m}_4\Big[4\,\mathrm{d}\ln(l_1) - 2\,\mathrm{d}\ln(l_2)\Big]\\
&+ \mathbf{m}_5\Big[-\mathrm{d}\ln(l_1) + \frac{1}{2}\mathrm{d}\ln(l_2)\Big] + \mathbf{m}_9\Big[2\,\mathrm{d}\ln(l_2)\Big] + \mathbf{m}_{10}\Big[2\,\mathrm{d}\ln(l_2)\Big]\\
&+ \mathbf{m}_{23}\Big[4\,\mathrm{d}\ln(l_1) - 2\,\mathrm{d}\ln(l_2)\Big],\\
\epsilon^{-1}\mathrm{d}\mathbf{m}_{24} &= \mathbf{m}_{10}\Big[-2\,\mathrm{d}\ln(l_2)\Big] + \mathbf{m}_{24}\Big[6\,\mathrm{d}\ln(l_1) - 3\,\mathrm{d}\ln(l_2)\Big],\\
\epsilon^{-1}\mathrm{d}\mathbf{m}_{25} &= \mathbf{m}_3\Big[-\frac{1}{2}\mathrm{d}\ln(l_1) + \frac{1}{4}\mathrm{d}\ln(l_2)\Big] + \mathbf{m}_4\Big[-2\,\mathrm{d}\ln(l_1) + \mathrm{d}\ln(l_2)\Big]\\
&+ \mathbf{m}_5\Big[\frac{1}{2}\mathrm{d}\ln(l_1) - \frac{1}{4}\mathrm{d}\ln(l_2)\Big] + \mathbf{m}_{10}\Big[\mathrm{d}\ln(l_2)\Big] + \mathbf{m}_{11}\Big[\mathrm{d}\ln(l_1) - \frac{1}{2}\mathrm{d}\ln(l_2)\Big]\\
&+ \mathbf{m}_{12}\Big[-\frac{1}{2}\ln(l_2)\Big] + \mathbf{m}_{25}\Big[4\,\mathrm{d}\ln(l_1) - 2\,\mathrm{d}\ln(l_2)\Big],\\
\epsilon^{-1}\mathrm{d}\mathbf{m}_{26} &= \mathbf{m}_8\Big[-2\,\mathrm{d}\ln(l_2) - 2\,\mathrm{d}\ln(l_7) + \mathrm{d}\ln(l_9) + \mathrm{d}\ln(l_{10})\Big]\\
&+ \mathbf{m}_{11}\Big[-\mathrm{d}\ln(l_2) - \mathrm{d}\ln(l_7) + \frac{1}{2}\mathrm{d}\ln(l_9) + \frac{1}{2}\mathrm{d}\ln(l_{10})\Big] + \mathbf{m}_{12}\Big[-\mathrm{d}\ln(l_2)\Big]
\end{aligned}
$$

$$
\begin{aligned}
&+ \mathbf{m}_{26}\Big[8\,\mathrm{d}\ln(l_1) - 4\,\mathrm{d}\ln(l_2) + 2\,\mathrm{d}\ln(l_3) + \mathrm{d}\ln(l_6) - \mathrm{d}\ln(l_7) - \frac{1}{2}\mathrm{d}\ln(l_9) - \frac{1}{2}\mathrm{d}\ln(l_{10})\Big] \\
&+ \mathbf{m}_{27}\Big[-\frac{1}{2}\mathrm{d}\ln(l_9) + \frac{1}{2}\mathrm{d}\ln(l_{10})\Big], \\
\epsilon^{-1}\mathrm{d}\mathbf{m}_{27} &= \mathbf{m}_1\Big[-\mathrm{d}\ln(l_8) + \mathrm{d}\ln(l_{11})\Big] + \mathbf{m}_3\Big[\mathrm{d}\ln(l_8) - \mathrm{d}\ln(l_{11})\Big] + \mathbf{m}_8\Big[4\,\mathrm{d}\ln(l_8) \\
&- 3\,\mathrm{d}\ln(l_9) + 3\,\mathrm{d}\ln(l_{10}) - 4\,\mathrm{d}\ln(l_{11})\Big] + \mathbf{m}_{11}\Big[-\frac{3}{2}\mathrm{d}\ln(l_9) + \frac{3}{2}\mathrm{d}\ln(l_{10})\Big] \\
&+ \mathbf{m}_{12}\Big[-\mathrm{d}\ln(l_6)\Big] + \mathbf{m}_{26}\Big[\frac{3}{2}\mathrm{d}\ln(l_9) - \frac{3}{2}\mathrm{d}\ln(l_{10})\Big] + \mathbf{m}_{27}\Big[4\,\mathrm{d}\ln(l_1) - 4\,\mathrm{d}\ln(l_2) \\
&- 2\,\mathrm{d}\ln(l_3) - 4\,\mathrm{d}\ln(l_5) + \mathrm{d}\ln(l_6) - \mathrm{d}\ln(l_7) + \frac{3}{2}\mathrm{d}\ln(l_9) + \frac{3}{2}\mathrm{d}\ln(l_{10})\Big], \\
\epsilon^{-1}\mathrm{d}\mathbf{m}_{28} &= \mathbf{m}_1\Big[-\frac{1}{2}\mathrm{d}\ln(l_1) - \frac{1}{2}\mathrm{d}\ln(l_3) - \frac{1}{4}\mathrm{d}\ln(l_6) + \frac{1}{4}\mathrm{d}\ln(l_9) + \frac{1}{4}\mathrm{d}\ln(l_{10})\Big] \\
&+ \mathbf{m}_3\Big[\frac{1}{2}\mathrm{d}\ln(l_1) + \frac{1}{2}\mathrm{d}\ln(l_3) + \frac{1}{4}\mathrm{d}\ln(l_6) - \frac{1}{4}\mathrm{d}\ln(l_9) - \frac{1}{4}\mathrm{d}\ln(l_{10})\Big] \\
&+ \mathbf{m}_4\Big[3\,\mathrm{d}\ln(l_1) + 3\,\mathrm{d}\ln(l_3) + \frac{3}{2}\mathrm{d}\ln(l_6) - \frac{3}{2}\mathrm{d}\ln(l_9) - \frac{3}{2}\mathrm{d}\ln(l_{10})\Big] \\
&+ \mathbf{m}_5\Big[-\frac{1}{2}\mathrm{d}\ln(l_1) - \frac{1}{2}\mathrm{d}\ln(l_3) - \frac{1}{4}\mathrm{d}\ln(l_6) + \frac{1}{4}\mathrm{d}\ln(l_9) + \frac{1}{4}\mathrm{d}\ln(l_{10})\Big] \\
&+ \mathbf{m}_8\Big[-4\,\mathrm{d}\ln(l_1) - 4\,\mathrm{d}\ln(l_3) - 2\,\mathrm{d}\ln(l_6) + 2\,\mathrm{d}\ln(l_9) + 2\,\mathrm{d}\ln(l_{10})\Big] \\
&+ \mathbf{m}_{15}\Big[\mathrm{d}\ln(l_1) + \mathrm{d}\ln(l_3) + \frac{1}{2}\mathrm{d}\ln(l_6) - \frac{1}{2}\mathrm{d}\ln(l_9) - \frac{1}{2}\mathrm{d}\ln(l_{10})\Big] \\
&+ \mathbf{m}_{17}\Big[2\,\mathrm{d}\ln(l_1) + 2\,\mathrm{d}\ln(l_3) + \mathrm{d}\ln(l_6) - \mathrm{d}\ln(l_9) - \mathrm{d}\ln(l_{10})\Big] \\
&+ \mathbf{m}_{20}\Big[-6\,\mathrm{d}\ln(l_1) - 6\,\mathrm{d}\ln(l_3) - 3\,\mathrm{d}\ln(l_6) + 3\,\mathrm{d}\ln(l_9) + 3\,\mathrm{d}\ln(l_{10})\Big] \\
&+ \mathbf{m}_{21}\Big[-2\,\mathrm{d}\ln(l_1) - 2\,\mathrm{d}\ln(l_3) - \mathrm{d}\ln(l_6) + \mathrm{d}\ln(l_9) + \mathrm{d}\ln(l_{10})\Big] \\
&+ \mathbf{m}_{28}\Big[2\,\mathrm{d}\ln(l_1) - 2\,\mathrm{d}\ln(l_2) + 2\,\mathrm{d}\ln(l_3) + \mathrm{d}\ln(l_6) - 2\,\mathrm{d}\ln(l_8) + \mathrm{d}\ln(l_9) + \mathrm{d}\ln(l_{10}) \\
&- 2\,\mathrm{d}\ln(l_{11})\Big] + \mathbf{m}_{29}\Big[2\,\mathrm{d}\ln(l_3) + \mathrm{d}\ln(l_6) - \mathrm{d}\ln(l_8) - \mathrm{d}\ln(l_{11})\Big], \\
\epsilon^{-1}\mathrm{d}\mathbf{m}_{29} &= \mathbf{m}_1\Big[\mathrm{d}\ln(l_1) + \frac{3}{4}\mathrm{d}\ln(l_2) + \frac{1}{2}\mathrm{d}\ln(l_3) + \frac{1}{2}\mathrm{d}\ln(l_4) + \frac{1}{4}\mathrm{d}\ln(l_6) + \frac{3}{2}\mathrm{d}\ln(l_7) \\
&- \mathrm{d}\ln(l_9) - \mathrm{d}\ln(l_{10})\Big] + \mathbf{m}_2\Big[-\mathrm{d}\ln(l_2) + 4\,\mathrm{d}\ln(l_3) + \mathrm{d}\ln(l_4) + 2\,\mathrm{d}\ln(l_6) - 2\,\mathrm{d}\ln(l_7) \\
&- \mathrm{d}\ln(l_9) - \mathrm{d}\ln(l_{10})\Big] + \mathbf{m}_3\Big[-\mathrm{d}\ln(l_1) + \frac{1}{12}\mathrm{d}\ln(l_2) - \frac{3}{2}\mathrm{d}\ln(l_3) - \frac{1}{6}\mathrm{d}\ln(l_4) \\
&- \frac{3}{4}\mathrm{d}\ln(l_6) + \frac{1}{6}\mathrm{d}\ln(l_7) + \frac{2}{3}\mathrm{d}\ln(l_9) + \frac{2}{3}\mathrm{d}\ln(l_{10})\Big] + \mathbf{m}_4\Big[-6\,\mathrm{d}\ln(l_1) + \frac{3}{2}\mathrm{d}\ln(l_2) \\
&- 9\,\mathrm{d}\ln(l_3) - \frac{9}{2}\mathrm{d}\ln(l_6) + 3\,\mathrm{d}\ln(l_7) + 3\,\mathrm{d}\ln(l_9) + 3\,\mathrm{d}\ln(l_{10})\Big] + \mathbf{m}_5\Big[\mathrm{d}\ln(l_1) \\
&- \frac{1}{12}\mathrm{d}\ln(l_2) + \frac{3}{2}\mathrm{d}\ln(l_3) + \frac{1}{6}\mathrm{d}\ln(l_4) + \frac{3}{4}\mathrm{d}\ln(l_6) - \frac{1}{6}\mathrm{d}\ln(l_7) - \frac{2}{3}\mathrm{d}\ln(l_9) - \frac{2}{3}\mathrm{d}\ln(l_{10})\Big]
\end{aligned}
$$

$$
\begin{aligned}
&+\mathbf{m}_6\Big[\mathrm{d}\ln(l_2)-6\,\mathrm{d}\ln(l_3)-2\,\mathrm{d}\ln(l_4)-3\,\mathrm{d}\ln(l_6)+2\,\mathrm{d}\ln(l_7)+2\,\mathrm{d}\ln(l_9)\\
&+2\,\mathrm{d}\ln(l_{10})\Big]+\mathbf{m}_8\Big[8\,\mathrm{d}\ln(l_1)+4\,\mathrm{d}\ln(l_3)-2\,\mathrm{d}\ln(l_4)+2\,\mathrm{d}\ln(l_6)-2\,\mathrm{d}\ln(l_9)\\
&-2\,\mathrm{d}\ln(l_{10})\Big]+\mathbf{m}_{13}\Big[\mathrm{d}\ln(l_2)-2\,\mathrm{d}\ln(l_3)-\mathrm{d}\ln(l_6)+2\,\mathrm{d}\ln(l_7)\Big]\\
&+\mathbf{m}_{15}\Big[-2\,\mathrm{d}\ln(l_1)-\frac{1}{2}\mathrm{d}\ln(l_2)-\mathrm{d}\ln(l_3)-\frac{1}{2}\mathrm{d}\ln(l_6)-\mathrm{d}\ln(l_7)+\mathrm{d}\ln(l_9)+\mathrm{d}\ln(l_{10})\Big]\\
&+\mathbf{m}_{16}\Big[\frac{2}{3}\mathrm{d}\ln(l_2)+\frac{2}{3}\mathrm{d}\ln(l_4)+\frac{4}{3}\mathrm{d}\ln(l_7)-\frac{2}{3}\mathrm{d}\ln(l_9)-\frac{2}{3}\mathrm{d}\ln(l_{10})\Big]\\
&+\mathbf{m}_{17}\Big[-4\,\mathrm{d}\ln(l_1)+\frac{1}{3}\mathrm{d}\ln(l_2)-2\,\mathrm{d}\ln(l_3)+\frac{4}{3}\mathrm{d}\ln(l_4)-\mathrm{d}\ln(l_6)+\frac{2}{3}\mathrm{d}\ln(l_7)\\
&+\frac{2}{3}\mathrm{d}\ln(l_9)+\frac{2}{3}\mathrm{d}\ln(l_{10})\Big]+\mathbf{m}_{20}\Big[12\,\mathrm{d}\ln(l_1)-3\,\mathrm{d}\ln(l_2)+6\,\mathrm{d}\ln(l_3)-6\,\mathrm{d}\ln(l_4)\\
&+3\,\mathrm{d}\ln(l_6)-6\,\mathrm{d}\ln(l_7)\Big]+\mathbf{m}_{21}\Big[4\,\mathrm{d}\ln(l_1)-3\,\mathrm{d}\ln(l_2)+2\,\mathrm{d}\ln(l_3)-4\,\mathrm{d}\ln(l_4)\\
&+\mathrm{d}\ln(l_6)-6\,\mathrm{d}\ln(l_7)+2\,\mathrm{d}\ln(l_9)+2\,\mathrm{d}\ln(l_{10})\Big]+\mathbf{m}_{28}\Big[3\,\mathrm{d}\ln(l_2)-2\,\mathrm{d}\ln(l_3)-\mathrm{d}\ln(l_6)\\
&+6\,\mathrm{d}\ln(l_7)-2\,\mathrm{d}\ln(l_8)-2\,\mathrm{d}\ln(l_{11})\Big]+\mathbf{m}_{29}\Big[2\,\mathrm{d}\ln(l_1)-\mathrm{d}\ln(l_2)-2\,\mathrm{d}\ln(l_3)-\mathrm{d}\ln(l_6)\\
&+2\,\mathrm{d}\ln(l_7)-\mathrm{d}\ln(l_8)+\mathrm{d}\ln(l_9)+\mathrm{d}\ln(l_{10})-\mathrm{d}\ln(l_{11})\Big],\\
\epsilon^{-1}\mathrm{d}\mathbf{m}_{30}&=\mathbf{m}_3\Big[\mathrm{d}\ln(l_2)\Big]+\mathbf{m}_4\Big[6\,\mathrm{d}\ln(l_2)\Big]+\mathbf{m}_5\Big[-\mathrm{d}\ln(l_2)\Big]+\mathbf{m}_{16}\Big[2\,\mathrm{d}\ln(l_2)\Big]\\
&+\mathbf{m}_{17}\Big[4\,\mathrm{d}\ln(l_2)\Big]+\mathbf{m}_{22}\Big[-2\,\mathrm{d}\ln(l_2)\Big]+\mathbf{m}_{23}\Big[2\,\mathrm{d}\ln(l_2)\Big]+\mathbf{m}_{24}\Big[-2\,\mathrm{d}\ln(l_2)\Big]\\
&+\mathbf{m}_{30}\Big[6\,\mathrm{d}\ln(l_1)-4\,\mathrm{d}\ln(l_2)+2\,\mathrm{d}\ln(l_3)\Big],\\
\epsilon^{-1}\mathrm{d}\mathbf{m}_{31}&=\mathbf{m}_3\Big[-\frac{1}{2}\mathrm{d}\ln(l_8)+\frac{1}{2}\mathrm{d}\ln(l_{11})\Big]+\mathbf{m}_4\Big[-2\,\mathrm{d}\ln(l_9)+2\,\mathrm{d}\ln(l_{10})\Big]\\
&+\mathbf{m}_5\Big[\frac{1}{2}\mathrm{d}\ln(l_9)-\frac{1}{2}\mathrm{d}\ln(l_{10})\Big]+\mathbf{m}_7\Big[-3\,\mathrm{d}\ln(l_8)+3\,\mathrm{d}\ln(l_9)-3\,\mathrm{d}\ln(l_{10})\\
&+3\,\mathrm{d}\ln(l_{11})\Big]+\mathbf{m}_{10}\Big[2\,\mathrm{d}\ln(l_6)\Big]+\mathbf{m}_{14}\Big[-\mathrm{d}\ln(l_8)+\mathrm{d}\ln(l_9)-\mathrm{d}\ln(l_{10})+\mathrm{d}\ln(l_{11})\Big]\\
&+\mathbf{m}_{18}\Big[3\,\mathrm{d}\ln(l_8)-3\,\mathrm{d}\ln(l_{11})\Big]+\mathbf{m}_{19}\Big[\mathrm{d}\ln(l_8)+\mathrm{d}\ln(l_9)-\mathrm{d}\ln(l_{10})-\mathrm{d}\ln(l_{11})\Big]\\
&+\mathbf{m}_{24}\Big[-2\,\mathrm{d}\ln(l_9)+2\,\mathrm{d}\ln(l_{10})\Big]+\mathbf{m}_{31}\Big[4\,\mathrm{d}\ln(l_1)-3\,\mathrm{d}\ln(l_2)-2\,\mathrm{d}\ln(l_3)-2\,\mathrm{d}\ln(l_5)\\
&+\mathrm{d}\ln(l_9)+\mathrm{d}\ln(l_{10})\Big],\\
\epsilon^{-1}\mathrm{d}\mathbf{m}_{32}&=\mathbf{m}_1\Big[-\frac{1}{4}\mathrm{d}\ln(l_2)+\frac{1}{4}\mathrm{d}\ln(l_9)-\frac{1}{4}\mathrm{d}\ln(l_{10})-\frac{1}{2}\mathrm{d}\ln(l_{13})+\frac{1}{2}\mathrm{d}\ln(l_{14})\Big]\\
&+\mathbf{m}_3\Big[-\frac{1}{4}\mathrm{d}\ln(l_2)-\frac{1}{2}\mathrm{d}\ln(l_6)-\frac{1}{2}\mathrm{d}\ln(l_7)-\frac{1}{2}\mathrm{d}\ln(l_9)+\frac{1}{2}\mathrm{d}\ln(l_{13})-\frac{1}{2}\mathrm{d}\ln(l_{14})\\
&+\frac{1}{2}\mathrm{d}\ln(l_{15})+\frac{1}{2}\mathrm{d}\ln(l_{16})\Big]+\mathbf{m}_4\Big[-\mathrm{d}\ln(l_2)-2\,\mathrm{d}\ln(l_6)-2\,\mathrm{d}\ln(l_7)-2\,\mathrm{d}\ln(l_9)
\end{aligned}
$$

$$
\begin{aligned}
&+ 2\,\mathrm{d}\ln(l_{13}) - 2\,\mathrm{d}\ln(l_{14}) + 2\,\mathrm{d}\ln(l_{15}) + 2\,\mathrm{d}\ln(l_{16})\Big] + \mathbf{m}_5\Big[\frac{1}{4}\mathrm{d}\ln(l_2) + \frac{1}{2}\mathrm{d}\ln(l_6)\\
&+ \frac{1}{2}\mathrm{d}\ln(l_7) + \frac{1}{2}\mathrm{d}\ln(l_9) - \frac{1}{2}\mathrm{d}\ln(l_{13}) + \frac{1}{2}\mathrm{d}\ln(l_{14}) - \frac{1}{2}\mathrm{d}\ln(l_{15}) - \frac{1}{2}\mathrm{d}\ln(l_{16})\Big]\\
&+ \mathbf{m}_8\Big[-2\,\mathrm{d}\ln(l_2) + 2\,\mathrm{d}\ln(l_9) - 2\,\mathrm{d}\ln(l_{10}) - 4\,\mathrm{d}\ln(l_{13}) + 4\,\mathrm{d}\ln(l_{14})\Big]\\
&+ \mathbf{m}_{10}\Big[2\,\mathrm{d}\ln(l_1) + \mathrm{d}\ln(l_2) + 2\,\mathrm{d}\ln(l_7) + 2\,\mathrm{d}\ln(l_9) - 2\,\mathrm{d}\ln(l_{13}) - 2\,\mathrm{d}\ln(l_{14})\\
&+ 2\,\mathrm{d}\ln(l_{15}) - 2\,\mathrm{d}\ln(l_{16})\Big] + \mathbf{m}_{11}\Big[-\frac{1}{2}\mathrm{d}\ln(l_2) + \frac{1}{2}\mathrm{d}\ln(l_9) - \frac{1}{2}\mathrm{d}\ln(l_{10}) - \mathrm{d}\ln(l_{13})\\
&+ \mathrm{d}\ln(l_{14})\Big] + \mathbf{m}_{12}\Big[-\mathrm{d}\ln(l_1) - \frac{1}{2}\mathrm{d}\ln(l_2) - \mathrm{d}\ln(l_7) - \mathrm{d}\ln(l_9) + \mathrm{d}\ln(l_{13})\\
&+ \mathrm{d}\ln(l_{14}) - \mathrm{d}\ln(l_{15}) + \mathrm{d}\ln(l_{16})\Big]\\
&+ \mathbf{m}_{15}\Big[\frac{1}{2}\mathrm{d}\ln(l_2) - \frac{1}{2}\mathrm{d}\ln(l_9) + \frac{1}{2}\mathrm{d}\ln(l_{10}) + \mathrm{d}\ln(l_{13}) - \mathrm{d}\ln(l_{14})\Big]\\
&+ \mathbf{m}_{20}\Big[-3\,\mathrm{d}\ln(l_2) + 3\,\mathrm{d}\ln(l_9) - 3\,\mathrm{d}\ln(l_{10}) - 6\,\mathrm{d}\ln(l_{13}) + 6\,\mathrm{d}\ln(l_{14})\Big]\\
&+ \mathbf{m}_{21}\Big[-3\,\mathrm{d}\ln(l_2) - 2\,\mathrm{d}\ln(l_6) - 2\,\mathrm{d}\ln(l_7) - 2\,\mathrm{d}\ln(l_{10}) - 2\,\mathrm{d}\ln(l_{13}) + 2\,\mathrm{d}\ln(l_{14})\\
&+ 2\,\mathrm{d}\ln(l_{15}) + 2\,\mathrm{d}\ln(l_{16})\Big] + \mathbf{m}_{24}\Big[-2\,\mathrm{d}\ln(l_2) - 2\,\mathrm{d}\ln(l_6) - 2\,\mathrm{d}\ln(l_7) - \mathrm{d}\ln(l_9)\\
&- \mathrm{d}\ln(l_{10}) + 2\,\mathrm{d}\ln(l_{15}) + 2\,\mathrm{d}\ln(l_{16})\Big]\\
&+ \mathbf{m}_{25}\Big[\mathrm{d}\ln(l_2) - \mathrm{d}\ln(l_9) + \mathrm{d}\ln(l_{10}) + 2\,\mathrm{d}\ln(l_{13}) - 2\,\mathrm{d}\ln(l_{14})\Big] + \mathbf{m}_{26}\Big[3\,\mathrm{d}\ln(l_2)\\
&+ 3\,\mathrm{d}\ln(l_6) + 3\,\mathrm{d}\ln(l_7) + \frac{3}{2}\mathrm{d}\ln(l_9) + \frac{3}{2}\mathrm{d}\ln(l_{10}) - 3\,\mathrm{d}\ln(l_{15}) - 3\,\mathrm{d}\ln(l_{16})\Big]\\
&+ \mathbf{m}_{27}\Big[\frac{1}{2}\mathrm{d}\ln(l_9) - \frac{1}{2}\mathrm{d}\ln(l_{10}) + \mathrm{d}\ln(l_{15}) - \mathrm{d}\ln(l_{16})\Big]\\
&+ \mathbf{m}_{32}\Big[4\,\mathrm{d}\ln(l_1) - \mathrm{d}\ln(l_2) - 2\,\mathrm{d}\ln(l_3) + 2\,\mathrm{d}\ln(l_7) + \mathrm{d}\ln(l_9) + \mathrm{d}\ln(l_{10}) - 2\,\mathrm{d}\ln(l_{12})\Big],
\end{aligned}
$$

$$
\begin{aligned}
\epsilon^{-1}\mathrm{d}\mathbf{m}_{33} = {}& \mathbf{m}_1\Big[\frac{3}{4}\mathrm{d}\ln(l_9) - \frac{3}{4}\mathrm{d}\ln(l_{10})\Big] + \mathbf{m}_2\Big[\mathrm{d}\ln(l_9) - \mathrm{d}\ln(l_{10})\Big] + \mathbf{m}_3\Big[-\frac{13}{12}\mathrm{d}\ln(l_9)\\
&+ \frac{13}{12}\mathrm{d}\ln(l_{10})\Big] + \mathbf{m}_4\Big[-\frac{11}{2}\mathrm{d}\ln(l_9) + \frac{11}{2}\mathrm{d}\ln(l_{10})\Big] + \mathbf{m}_5\Big[\frac{13}{12}\mathrm{d}\ln(l_9) - \frac{13}{12}\mathrm{d}\ln(l_{10})\Big]\\
&+ \mathbf{m}_6\Big[-\mathrm{d}\ln(l_9) + \mathrm{d}\ln(l_{10})\Big] + \mathbf{m}_8\Big[6\,\mathrm{d}\ln(l_9) - 6\,\mathrm{d}\ln(l_{10})\Big] + \mathbf{m}_9\Big[-2\,\mathrm{d}\ln(l_6)\Big]\\
&+ \mathbf{m}_{10}\Big[-4\,\mathrm{d}\ln(l_6)\Big] + \mathbf{m}_{11}\Big[2\,\mathrm{d}\ln(l_9) - 2\,\mathrm{d}\ln(l_{10})\Big] + \mathbf{m}_{12}\Big[2\,\mathrm{d}\ln(l_6)\Big]\\
&+ \mathbf{m}_{13}\Big[-\frac{1}{3}\mathrm{d}\ln(l_9) + \frac{1}{3}\mathrm{d}\ln(l_{10})\Big] + \mathbf{m}_{15}\Big[-\frac{3}{2}\mathrm{d}\ln(l_9) + \frac{3}{2}\mathrm{d}\ln(l_{10})\Big]\\
&+ \mathbf{m}_{16}\Big[-\frac{2}{3}\mathrm{d}\ln(l_9) + \frac{2}{3}\mathrm{d}\ln(l_{10})\Big] + \mathbf{m}_{17}\Big[-\frac{7}{3}\mathrm{d}\ln(l_9) + \frac{7}{3}\mathrm{d}\ln(l_{10})\Big]\\
&+ \mathbf{m}_{20}\Big[5\,\mathrm{d}\ln(l_9) - 5\,\mathrm{d}\ln(l_{10})\Big] + \mathbf{m}_{21}\Big[3\,\mathrm{d}\ln(l_9) - 3\,\mathrm{d}\ln(l_{10})\Big]
\end{aligned}
$$

$$
\begin{aligned}
&+ \mathbf{m}_{22}\Big[2\,\mathrm{d}\ln(l_9) - 2\,\mathrm{d}\ln(l_{10})\Big] + \mathbf{m}_{23}\Big[-\mathrm{d}\ln(l_9) + \mathrm{d}\ln(l_{10})\Big] \\
&+ \mathbf{m}_{24}\Big[2\,\mathrm{d}\ln(l_9) - 2\,\mathrm{d}\ln(l_{10})\Big] + \mathbf{m}_{25}\Big[-2\,\mathrm{d}\ln(l_9) + 2\,\mathrm{d}\ln(l_{10})\Big] \\
&+ \mathbf{m}_{26}\Big[-2\,\mathrm{d}\ln(l_9) + 2\,\mathrm{d}\ln(l_{10})\Big] + \mathbf{m}_{28}\Big[4\,\mathrm{d}\ln(l_8) - \mathrm{d}\ln(l_9) + \mathrm{d}\ln(l_{10}) - 4\,\mathrm{d}\ln(l_{11})\Big] \\
&+ \mathbf{m}_{29}\Big[2\,\mathrm{d}\ln(l_8) - \mathrm{d}\ln(l_9) + \mathrm{d}\ln(l_{10}) - 2\,\mathrm{d}\ln(l_{11})\Big] \\
&+ \mathbf{m}_{32}\Big[2\,\mathrm{d}\ln(l_9) - 2\,\mathrm{d}\ln(l_{10}) + 4\,\mathrm{d}\ln(l_{15}) - 4\,\mathrm{d}\ln(l_{16})\Big] \\
&+ \mathbf{m}_{33}\Big[2\,\mathrm{d}\ln(l_1) - 4\,\mathrm{d}\ln(l_2) - 2\,\mathrm{d}\ln(l_3) - 6\,\mathrm{d}\ln(l_5) + 2\,\mathrm{d}\ln(l_6) - 2\,\mathrm{d}\ln(l_7) \\
&+ 2\,\mathrm{d}\ln(l_9) + 2\,\mathrm{d}\ln(l_{10})\Big] + \mathbf{m}_{35}\Big[-2\,\mathrm{d}\ln(l_6)\Big] + \mathbf{m}_{36}\Big[2\,\mathrm{d}\ln(l_9) - 2\,\mathrm{d}\ln(l_{10})\Big],
\end{aligned}
$$

$$
\begin{aligned}
\epsilon^{-1}\mathrm{d}\mathbf{m}_{34} &= \mathbf{m}_1\Big[-\frac{1}{2}\mathrm{d}\ln(l_2) - \frac{1}{2}\mathrm{d}\ln(l_7) + \frac{1}{4}\mathrm{d}\ln(l_9) + \frac{1}{4}\mathrm{d}\ln(l_{10})\Big] \\
&+ \mathbf{m}_2\Big[-2\,\mathrm{d}\ln(l_2) - 2\,\mathrm{d}\ln(l_7) + \mathrm{d}\ln(l_9) + \mathrm{d}\ln(l_{10})\Big] + \mathbf{m}_3\Big[\frac{7}{6}\mathrm{d}\ln(l_2) + \frac{7}{6}\mathrm{d}\ln(l_7) \\
&- \frac{7}{12}\mathrm{d}\ln(l_9) - \frac{7}{12}\mathrm{d}\ln(l_{10})\Big] + \mathbf{m}_4\Big[5\,\mathrm{d}\ln(l_2) + 5\,\mathrm{d}\ln(l_7) - \frac{5}{2}\mathrm{d}\ln(l_9) - \frac{5}{2}\mathrm{d}\ln(l_{10})\Big] \\
&+ \mathbf{m}_5\Big[-\frac{7}{6}\mathrm{d}\ln(l_2) - \frac{7}{6}\mathrm{d}\ln(l_7) + \frac{7}{12}\mathrm{d}\ln(l_9) + \frac{7}{12}\mathrm{d}\ln(l_{10})\Big] \\
&+ \mathbf{m}_6\Big[2\,\mathrm{d}\ln(l_2) + 2\,\mathrm{d}\ln(l_7) - \mathrm{d}\ln(l_9) - \mathrm{d}\ln(l_{10})\Big] + \mathbf{m}_8\Big[-4\,\mathrm{d}\ln(l_2) - 4\,\mathrm{d}\ln(l_7) \\
&+ 2\,\mathrm{d}\ln(l_9) + 2\,\mathrm{d}\ln(l_{10})\Big] + \mathbf{m}_9\Big[2\,\mathrm{d}\ln(l_2)\Big] + \mathbf{m}_{10}\Big[4\,\mathrm{d}\ln(l_2)\Big] \\
&+ \mathbf{m}_{11}\Big[-2\,\mathrm{d}\ln(l_2) - 2\,\mathrm{d}\ln(l_7) + \mathrm{d}\ln(l_9) + \mathrm{d}\ln(l_{10})\Big] + \mathbf{m}_{12}\Big[-2\,\mathrm{d}\ln(l_2)\Big] \\
&+ \mathbf{m}_{13}\Big[\frac{2}{3}\mathrm{d}\ln(l_2) + \frac{2}{3}\mathrm{d}\ln(l_7) - \frac{1}{3}\mathrm{d}\ln(l_9) - \frac{1}{3}\mathrm{d}\ln(l_{10})\Big] + \mathbf{m}_{15}\Big[\mathrm{d}\ln(l_2) + \mathrm{d}\ln(l_7) \\
&- \frac{1}{2}\mathrm{d}\ln(l_9) - \frac{1}{2}\mathrm{d}\ln(l_{10})\Big] + \mathbf{m}_{16}\Big[\frac{4}{3}\mathrm{d}\ln(l_2) + \frac{4}{3}\mathrm{d}\ln(l_7) - \frac{2}{3}\mathrm{d}\ln(l_9) - \frac{2}{3}\mathrm{d}\ln(l_{10})\Big] \\
&+ \mathbf{m}_{17}\Big[\frac{2}{3}\mathrm{d}\ln(l_2) + \frac{2}{3}\mathrm{d}\ln(l_7) - \frac{1}{3}\mathrm{d}\ln(l_9) - \frac{1}{3}\mathrm{d}\ln(l_{10})\Big] + \mathbf{m}_{20}\Big[2\,\mathrm{d}\ln(l_2) + 2\,\mathrm{d}\ln(l_7) \\
&- \mathrm{d}\ln(l_9) - \mathrm{d}\ln(l_{10})\Big] + \mathbf{m}_{21}\Big[-2\,\mathrm{d}\ln(l_2) - 2\,\mathrm{d}\ln(l_7) + \mathrm{d}\ln(l_9) + \mathrm{d}\ln(l_{10})\Big] \\
&+ \mathbf{m}_{22}\Big[-4\,\mathrm{d}\ln(l_1) - 4\,\mathrm{d}\ln(l_3) - 2\,\mathrm{d}\ln(l_6) + 2\,\mathrm{d}\ln(l_9) + 2\,\mathrm{d}\ln(l_{10})\Big] \\
&+ \mathbf{m}_{24}\Big[-4\,\mathrm{d}\ln(l_2) - 4\,\mathrm{d}\ln(l_7) + 2\,\mathrm{d}\ln(l_9) + 2\,\mathrm{d}\ln(l_{10})\Big] + \mathbf{m}_{26}\Big[4\,\mathrm{d}\ln(l_2) + 4\,\mathrm{d}\ln(l_7) \\
&- 2\,\mathrm{d}\ln(l_9) - 2\,\mathrm{d}\ln(l_{10})\Big] + \mathbf{m}_{28}\Big[2\,\mathrm{d}\ln(l_2) + 2\,\mathrm{d}\ln(l_7) - \mathrm{d}\ln(l_9) - \mathrm{d}\ln(l_{10})\Big] \\
&+ \mathbf{m}_{29}\Big[2\,\mathrm{d}\ln(l_2) + 2\,\mathrm{d}\ln(l_7) - \mathrm{d}\ln(l_9) - \mathrm{d}\ln(l_{10})\Big] + \mathbf{m}_{30}\Big[-2\,\mathrm{d}\ln(l_2)\Big] \\
&+ \mathbf{m}_{32}\Big[4\,\mathrm{d}\ln(l_2) + 4\,\mathrm{d}\ln(l_6) + 4\,\mathrm{d}\ln(l_7) + 2\,\mathrm{d}\ln(l_9) + 2\,\mathrm{d}\ln(l_{10})
\end{aligned}
$$

$$
\begin{aligned}
&- 4\,\mathrm{d}\ln(l_{15}) - 4\,\mathrm{d}\ln(l_{16})\Big] + \mathbf{m}_{33}\Big[\mathrm{d}\ln(l_9) - \mathrm{d}\ln(l_{10})\Big] \\
&+ \mathbf{m}_{34}\Big[4\,\mathrm{d}\ln(l_1) - 4\,\mathrm{d}\ln(l_2) - 2\,\mathrm{d}\ln(l_7) + \mathrm{d}\ln(l_9) + \mathrm{d}\ln(l_{10})\Big] + \mathbf{m}_{35}\Big[2\,\mathrm{d}\ln(l_2)\Big] \\
&+ \mathbf{m}_{36}\Big[-4\,\mathrm{d}\ln(l_2) - 4\,\mathrm{d}\ln(l_7) + 2\,\mathrm{d}\ln(l_9) + 2\,\mathrm{d}\ln(l_{10})\Big], \\
\epsilon^{-1}\mathrm{d}\mathbf{m}_{35} &= \mathbf{m}_1\Big[-\frac{3}{4}\mathrm{d}\ln(l_2)\Big] + \mathbf{m}_2\Big[\mathrm{d}\ln(l_2)\Big] + \mathbf{m}_3\Big[\frac{5}{12}\mathrm{d}\ln(l_2)\Big] + \mathbf{m}_4\Big[\frac{7}{2}\mathrm{d}\ln(l_2)\Big] \\
&+ \mathbf{m}_5\Big[-\frac{5}{12}\mathrm{d}\ln(l_2)\Big] + \mathbf{m}_6\Big[-\mathrm{d}\ln(l_2)\Big] + \mathbf{m}_8\Big[-6\,\mathrm{d}\ln(l_2)\Big] + \mathbf{m}_{13}\Big[-\frac{1}{3}\mathrm{d}\ln(l_2)\Big] \\
&+ \mathbf{m}_{15}\Big[\frac{3}{2}\mathrm{d}\ln(l_2)\Big] + \mathbf{m}_{16}\Big[\frac{4}{3}\mathrm{d}\ln(l_2)\Big] + \mathbf{m}_{17}\Big[\frac{11}{3}\mathrm{d}\ln(l_2)\Big] + \mathbf{m}_{20}\Big[-\mathrm{d}\ln(l_2)\Big] \\
&+ \mathbf{m}_{21}\Big[\mathrm{d}\ln(l_2)\Big] + \mathbf{m}_{22}\Big[-2\,\mathrm{d}\ln(l_2)\Big] + \mathbf{m}_{25}\Big[2\,\mathrm{d}\ln(l_2)\Big] + \mathbf{m}_{26}\Big[-2\,\mathrm{d}\ln(l_2)\Big] \\
&+ \mathbf{m}_{27}\Big[2\,\mathrm{d}\ln(l_6)\Big] + \mathbf{m}_{28}\Big[-3\,\mathrm{d}\ln(l_2)\Big] + \mathbf{m}_{29}\Big[-\mathrm{d}\ln(l_2)\Big] \\
&+ \mathbf{m}_{30}\Big[-2\,\mathrm{d}\ln(l_2) - 2\,\mathrm{d}\ln(l_7) + \mathrm{d}\ln(l_9) + \mathrm{d}\ln(l_{10})\Big] + \mathbf{m}_{32}\Big[4\,\mathrm{d}\ln(l_1) + 2\,\mathrm{d}\ln(l_2) \\
&+ 4\,\mathrm{d}\ln(l_7) + 4\,\mathrm{d}\ln(l_9) - 4\,\mathrm{d}\ln(l_{13}) - 4\,\mathrm{d}\ln(l_{14}) + 4\,\mathrm{d}\ln(l_{15}) - 4\,\mathrm{d}\ln(l_{16})\Big] \\
&+ \mathbf{m}_{33}\Big[2\,\mathrm{d}\ln(l_6)\Big] + \mathbf{m}_{35}\Big[2\,\mathrm{d}\ln(l_1) - 2\,\mathrm{d}\ln(l_2) - 2\,\mathrm{d}\ln(l_3) - 2\,\mathrm{d}\ln(l_6) + 2\,\mathrm{d}\ln(l_7) \\
&+ \mathrm{d}\ln(l_9) + \mathrm{d}\ln(l_{10})\Big] + \mathbf{m}_{36}\Big[-4\,\mathrm{d}\ln(l_2)\Big], \\
\epsilon^{-1}\mathrm{d}\mathbf{m}_{36} &= \mathbf{m}_1\Big[\frac{5}{4}\mathrm{d}\ln(l_1) - \frac{3}{8}\mathrm{d}\ln(l_2) + \frac{1}{2}\mathrm{d}\ln(l_3) + \frac{1}{4}\mathrm{d}\ln(l_6) - \frac{1}{4}\mathrm{d}\ln(l_9) - \frac{1}{4}\mathrm{d}\ln(l_{10})\Big] \\
&+ \mathbf{m}_2\Big[\mathrm{d}\ln(l_1) + \frac{1}{2}\mathrm{d}\ln(l_2) + 2\,\mathrm{d}\ln(l_3) + \mathrm{d}\ln(l_6) - \mathrm{d}\ln(l_9) - \mathrm{d}\ln(l_{10})\Big] \\
&+ \mathbf{m}_3\Big[-\frac{17}{12}\mathrm{d}\ln(l_1) - \frac{1}{24}\mathrm{d}\ln(l_2) - \frac{3}{2}\mathrm{d}\ln(l_3) - \frac{3}{4}\mathrm{d}\ln(l_6) + \frac{3}{4}\mathrm{d}\ln(l_9) + \frac{3}{4}\mathrm{d}\ln(l_{10})\Big] \\
&+ \mathbf{m}_4\Big[-\frac{13}{2}\mathrm{d}\ln(l_1) - \frac{1}{4}\mathrm{d}\ln(l_2) - 7\,\mathrm{d}\ln(l_3) - \frac{7}{2}\mathrm{d}\ln(l_6) + \frac{7}{2}\mathrm{d}\ln(l_9) + \frac{7}{2}\mathrm{d}\ln(l_{10})\Big] \\
&+ \mathbf{m}_5\Big[\frac{17}{12}\mathrm{d}\ln(l_1) + \frac{1}{24}\mathrm{d}\ln(l_2) + \frac{3}{2}\mathrm{d}\ln(l_3) + \frac{3}{4}\mathrm{d}\ln(l_6) - \frac{3}{4}\mathrm{d}\ln(l_9) - \frac{3}{4}\mathrm{d}\ln(l_{10})\Big] \\
&+ \mathbf{m}_6\Big[-\mathrm{d}\ln(l_1) - \frac{1}{2}\mathrm{d}\ln(l_2) - 2\,\mathrm{d}\ln(l_3) - \mathrm{d}\ln(l_6) + \mathrm{d}\ln(l_9) + \mathrm{d}\ln(l_{10})\Big] \\
&+ \mathbf{m}_8\Big[6\,\mathrm{d}\ln(l_1) - 3\,\mathrm{d}\ln(l_2)\Big] + \mathbf{m}_9\Big[-\mathrm{d}\ln(l_2)\Big] + \mathbf{m}_{10}\Big[-\mathrm{d}\ln(l_2)\Big] \\
&+ \mathbf{m}_{13}\Big[-\frac{1}{3}\mathrm{d}\ln(l_1) - \frac{1}{6}\mathrm{d}\ln(l_2) - \frac{2}{3}\mathrm{d}\ln(l_3) - \frac{1}{3}\mathrm{d}\ln(l_6) + \frac{1}{3}\mathrm{d}\ln(l_9) + \frac{1}{3}\mathrm{d}\ln(l_{10})\Big] \\
&+ \mathbf{m}_{15}\Big[-\frac{5}{2}\mathrm{d}\ln(l_1) + \frac{3}{4}\mathrm{d}\ln(l_2) - \mathrm{d}\ln(l_3) - \frac{1}{2}\mathrm{d}\ln(l_6) + \frac{1}{2}\mathrm{d}\ln(l_9) + \frac{1}{2}\mathrm{d}\ln(l_{10})\Big] \\
&+ \mathbf{m}_{16}\Big[\frac{2}{3}\mathrm{d}\ln(l_1) - \frac{1}{3}\mathrm{d}\ln(l_2)\Big] + \mathbf{m}_{17}\Big[-\frac{5}{3}\mathrm{d}\ln(l_1) - \frac{1}{6}\mathrm{d}\ln(l_2) - 2\,\mathrm{d}\ln(l_3) - \mathrm{d}\ln(l_6) \\
&+ \mathrm{d}\ln(l_9) + \mathrm{d}\ln(l_{10})\Big] + \mathbf{m}_{20}\Big[7\,\mathrm{d}\ln(l_1) - \frac{1}{2}\mathrm{d}\ln(l_2) + 6\,\mathrm{d}\ln(l_3) + 3\,\mathrm{d}\ln(l_6) - 3\,\mathrm{d}\ln(l_9)
\end{aligned}
$$

$$
\begin{aligned}
&- 3\,\mathrm{d}\ln(l_{10})\Big] + \mathbf{m}_{21}\Big[\mathrm{d}\ln(l_1) + \frac{1}{2}\mathrm{d}\ln(l_2) + 2\,\mathrm{d}\ln(l_3) + \mathrm{d}\ln(l_6) - \mathrm{d}\ln(l_9) - \mathrm{d}\ln(l_{10})\Big] \\
&+ \mathbf{m}_{22}\Big[2\,\mathrm{d}\ln(l_1) + 2\,\mathrm{d}\ln(l_3) + \mathrm{d}\ln(l_6) - \mathrm{d}\ln(l_9) - \mathrm{d}\ln(l_{10})\Big] + \mathbf{m}_{23}\Big[-2\,\mathrm{d}\ln(l_1) \\
&+ \mathrm{d}\ln(l_2) - 2\,\mathrm{d}\ln(l_3) - \mathrm{d}\ln(l_6) + \mathrm{d}\ln(l_7) + \frac{1}{2}\mathrm{d}\ln(l_9) + \frac{1}{2}\mathrm{d}\ln(l_{10})\Big] \\
&+ \mathbf{m}_{24}\Big[-2\,\mathrm{d}\ln(l_1) + \mathrm{d}\ln(l_2)\Big] + \mathbf{m}_{25}\Big[-2\mathrm{d}\ln(l_1) + \mathrm{d}\ln(l_2)\Big] + \mathbf{m}_{26}\Big[4\,\mathrm{d}\ln(l_1) \\
&- \mathrm{d}\ln(l_2) + 2\,\mathrm{d}\ln(l_3) + \mathrm{d}\ln(l_6) - \mathrm{d}\ln(l_9) - \mathrm{d}\ln(l_{10})\Big] + \mathbf{m}_{27}\Big[-\mathrm{d}\ln(l_9) + \mathrm{d}\ln(l_{10})\Big] \\
&+ \mathbf{m}_{28}\Big[\mathrm{d}\ln(l_1) - \frac{3}{2}\mathrm{d}\ln(l_2) - 2\,\mathrm{d}\ln(l_3) - \mathrm{d}\ln(l_6) + \mathrm{d}\ln(l_9) + \mathrm{d}\ln(l_{10})\Big] \\
&+ \mathbf{m}_{29}\Big[-\mathrm{d}\ln(l_1) - \frac{1}{2}\mathrm{d}\ln(l_2) - 2\,\mathrm{d}\ln(l_3) - \mathrm{d}\ln(l_6) + \mathrm{d}\ln(l_9) + \mathrm{d}\ln(l_{10})\Big] \\
&+ \mathbf{m}_{30}\Big[2\,\mathrm{d}\ln(l_2)\Big] + \mathbf{m}_{32}\Big[-3\,\mathrm{d}\ln(l_2) - 2\,\mathrm{d}\ln(l_6) - 2\,\mathrm{d}\ln(l_7) - 2\,\mathrm{d}\ln(l_{10}) - 2\,\mathrm{d}\ln(l_{13}) \\
&+ 2\,\mathrm{d}\ln(l_{14}) + 2\,\mathrm{d}\ln(l_{15}) + 2\,\mathrm{d}\ln(l_{16})\Big] + \mathbf{m}_{33}\Big[-\mathrm{d}\ln(l_9) + \mathrm{d}\ln(l_{10})\Big] \\
&+ \mathbf{m}_{35}\Big[-2\,\mathrm{d}\ln(l_2)\Big] + \mathbf{m}_{36}\Big[4\,\mathrm{d}\ln(l_1) + 2\,\mathrm{d}\ln(l_7) - \mathrm{d}\ln(l_9) - \mathrm{d}\ln(l_{10})\Big].
\end{aligned}
\tag{7.38}
$$

8 Calculation of the amplitude

This chapter is based on Ref. [85], in which we calculated the mixed EW-QCD two-loop corrections to all helicity amplitudes to the Drell-Yan process. As we briefly mentioned in that reference, we performed an independent check of this calculation by calculating the spin-averaged, unpolarized amplitude as a part of this thesis. In the present chapter, we will focus more on the calculation of this unpolarized amplitude, which was performed using a similar setup as described in Chapter 3.

During the calculation of the amplitudes, we had to overcome several technical difficulties. Firstly, the calculation of the master integrals involving two masses was very complicated and required new insights into differential equations involving algebraic letters; we discussed this in the previous chapter. Secondly, one needs a solid understanding of the γ_5 problem in dimensional regularization [186–190]. In Ref. [85], we therefore performed the calculation in two different γ_5-schemes, namely the 't Hooft-Veltman-Breitenlohner-Maison (HVBM) scheme [89, 186–188] and the Kreimer scheme [191–194]. We found that intermediate results actually depend on the choice of the used scheme. Only after taking into account the IR subtraction function, the scheme dependence drops out in the hard scattering function. Since in the present chapter we focus on the calculation of the unpolarized amplitude, which was performed in Kreimer's scheme, we will present only that scheme here. Details on the differences between the HVBM and the Kreimer scheme can be found in Ref. [85].

This chapter is organized as follows. In Section 8.1, we review the problem related to dimensional regularization in the presence of chiral couplings. We introduce Kreimer's γ_5 scheme, which allows us to treat γ_5 consistently in d dimensions. In Section 8.2, we introduce the kinematics and the form factor decomposition that we used in Ref. [85] to calculate the helicity amplitudes. Although, as a part of this thesis, we calculated the unpolarized amplitude only, we need these definitions to make contact with the results obtained in that reference. In Section 8.3, we derive all renormalization constants and counterterms that we need for the calculation. In Sections 8.4 and 8.5, we show the diagrammatic structure as well as the definition of master integrals for the one-loop and two-loop amplitudes. In Section 8.6, we present the calculation of the unpolarized amplitude in Kreimer's scheme which, as mentioned above, was the main contribution of the present thesis to the results of Ref. [85] and served as an independent check on the calculation of the helicity amplitudes in that reference. In Section 8.7, we study the IR structure of two-loop mixed EW-QCD corrections and define the hard scattering function. This function is IR finite and, as we found in Ref. [85] by using two different schemes, also independent of the γ_5 scheme. In Section 8.8, we show some numerical results that we obtained in Ref. [85] for the different helicity amplitudes. We conclude in Section 8.9.

8.1 γ_5 in dimensional regularization and Kreimer's scheme

It has been clear from its inception that the treatment of γ_5 in dimensional regularization is conceptual challenging. It was already emphasized by the inventors of dimensional regularization themselves in Ref. [89], that an anti-commuting γ_5 together

with the usual trace identity is ill-defined. This can be easily seen by considering the following identity, which makes use of the usual anti-commutation relation of γ matrices in d dimensions, as given in Eq. (2.9):

$$\begin{aligned}\operatorname{tr}(\gamma_5\gamma_\alpha\gamma_{\mu_1}\gamma_{\mu_2}\gamma_{\mu_3}\gamma_{\mu_4}\gamma_{\mu_5}) =& 2\left[\operatorname{tr}(\gamma_5\gamma_{\mu_2}\gamma_{\mu_3}\gamma_{\mu_4}\gamma_{\mu_5})g_{\alpha\mu_1} - \operatorname{tr}(\gamma_5\gamma_{\mu_1}\gamma_{\mu_3}\gamma_{\mu_4}\gamma_{\mu_5})g_{\alpha\mu_2}\right.\\ &+ \operatorname{tr}(\gamma_5\gamma_{\mu_1}\gamma_{\mu_2}\gamma_{\mu_4}\gamma_{\mu_5})g_{\alpha\mu_3} - \operatorname{tr}(\gamma_5\gamma_{\mu_1}\gamma_{\mu_2}\gamma_{\mu_3}\gamma_{\mu_5})g_{\alpha\mu_4}\\ &\left.+ \operatorname{tr}(\gamma_5\gamma_{\mu_1}\gamma_{\mu_2}\gamma_{\mu_3}\gamma_{\mu_4})g_{\alpha\mu_5}\right]. \end{aligned} \tag{8.1}$$

Contraction with $g^{\mu_5\alpha}$ and using cyclicity of the trace together with an anti-commuting γ_5,

$$\{\gamma_5, \gamma^\mu\} = 0, \tag{8.2}$$

Eq. (8.1) yields

$$(d-4)\operatorname{tr}(\gamma_5\gamma_{\mu_1}\gamma_{\mu_2}\gamma_{\mu_3}\gamma_{\mu_4}) = 0. \tag{8.3}$$

This clearly shows, that a cyclic trace together with the anti-commutation relation (8.2) give inconsistent results in $d \neq 4$ dimensions. In the literature, different solutions to this problem have been discussed, the first one being proposed already in the original reference on dimensional regularization, Ref. [89]. In their scheme, later referred to as the 't Hooft-Veltman-Breitenlohner-Maison's (HVBM's) scheme, γ_5 is treated as a purely four-dimensional object. As a result, one has to give up the usual anti-commutation relation (8.2) and distinguish between the four-dimensional space and the $d-4$ dimensional subspace, such that one has:

$$\{\gamma_\mu, \gamma_5\} = 0 \qquad \text{for} \quad \mu = 0, 1, 2, \text{ and } 3 \tag{8.4}$$

$$\text{and} \qquad [\gamma_\mu, \gamma_5] = 0 \qquad \text{in the } (-2\epsilon)\text{-dimensional subspace.} \tag{8.5}$$

This, of course, complicates the Dirac algebra in the calculation of Feynman amplitudes since one has to distinguish between the two spaces. Furthermore, it has the additional drawback that the chiral symmetry of the Standard Model is violated in the HVBM scheme. In order to restore that symmetry, one needs to include finite counterterms.

A different scheme, that avoids these problems, was introduced by Kreimer in Ref. [191]. In Kreimer's γ_5 scheme the identity given in Eq. (8.2) is valid in d dimensions. Instead, one gives up the cyclicity of the trace; Kreimer introduces a new linear functional acting on products of Dirac matrices, which we called Tr to distinguish from the usual trace (tr), which only corresponds to the usual trace in four dimensions. This functional projects out the four-dimensional part of a string of γ matrices. Specifically, given a product

$$\Gamma = \gamma_{\mu_1} \cdots \gamma_{\mu_n}, \tag{8.6}$$

one expands in terms of the exterior product in d dimensions:

$$\Gamma = a_0 \mathbf{1}_{4x4} + a_1^\mu \gamma_\mu + a_2^{\mu_1,\mu_2} \gamma_{\mu_1} \wedge \gamma_{\mu_2} + \ldots + a_n^{\mu_1\ldots\mu_n} \gamma_{\mu_1} \wedge \cdots \wedge \gamma_{\mu_n}, \tag{8.7}$$

where the exterior product between Dirac matrices is defined as

$$\gamma_{\mu_1} \wedge \gamma_{\mu_2} \wedge \ldots \wedge \gamma_{\mu_n} = \frac{1}{n!} \sum_{\text{perm}} \text{sign(perm)} \gamma_{\text{perm}(\mu_1)} \cdots \gamma_{\text{perm}(\mu_n)}. \tag{8.8}$$

From Eq. (8.7) we can define the action of Tr on a string of γ matrices as a projection on specific coefficients as follows:

$$\operatorname{Tr}(a_0 \mathbf{1}_{4x4} + a_1^\mu \gamma_\mu + \ldots) = 4a_0, \tag{8.9}$$

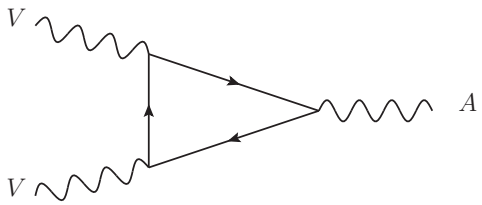

FIGURE 8.1.1: The famous VVA triangle diagram which is the source of the Adler–Bell–Jackiw anomaly. In Ref. [191] it was shown that in Kreimer's scheme the anomaly can correctly be reproduced if one chooses the axial vertex as the starting point of the trace. However, in the Standard Model, the above diagram is zero after summing over all fermions in the loop. Therefore, any vertex can be used as starting point as long as it is consistently used in the full calculation.

$$\mathrm{Tr}\left(\gamma_5(a_0\mathbf{1}_{4x4}+\ldots+a_4^{0123}\frac{-i}{4!}\varepsilon_{\mu_1\mu_2\mu_3\mu_4}\gamma^{\mu_1}\gamma^{\mu_2}\gamma^{\mu_3}\gamma^{\mu_4}+\ldots)\right)=4a_4^{0123}, \tag{8.10}$$

where $\varepsilon_{\mu_1\mu_2\mu_3\mu_4}$ denotes the four-dimensional Levi-Civita symbol. As an example let us consider a product of four Dirac matrices. Expanding in terms of the exterior product, we find [191]

$$\begin{aligned}\gamma_{\mu_1}\gamma_{\mu_2}\gamma_{\mu_3}\gamma_{\mu_4} =&(g_{\mu_1\mu_2}g_{\mu_3\mu_4}-g_{\mu_1\mu_3}g_{\mu_2\mu_4}+g_{\mu_1\mu_4}g_{\mu_2\mu_3})\mathbf{1}_{4x4}+g_{\mu_3\mu_4}\gamma_{\mu_1}\wedge\gamma_{\mu_2}\\ &-g_{\mu_2\mu_4}\gamma_{\mu_1}\wedge\gamma_{\mu_3}+g_{\mu_2\mu_3}\gamma_{\mu_1}\wedge\gamma_{\mu_4}+g_{\mu_1\mu_2}\gamma_{\mu_3}\wedge\gamma_{\mu_4}\\ &-g_{\mu_1\mu_3}\gamma_{\mu_2}\wedge\gamma_{\mu_4}+g_{\mu_1\mu_4}\gamma_{\mu_2}\wedge\gamma_{\mu_3}+\gamma_{\mu_1}\wedge\gamma_{\mu_2}\wedge\gamma_{\mu_3}\wedge\gamma_{\mu_4}.\end{aligned} \tag{8.11}$$

We therefore can easily deduce, that

$$\begin{aligned}\mathrm{Tr}(\gamma_{\mu_1}\gamma_{\mu_2}\gamma_{\mu_3}\gamma_{\mu_4})&=4(g_{\mu_1\mu_2}g_{\mu_3\mu_4}-g_{\mu_1\mu_3}g_{\mu_2\mu_4}+g_{\mu_1\mu_4}g_{\mu_2\mu_3}),\\ \mathrm{Tr}(\gamma^{\mu_1}\gamma^{\mu_2}\gamma^{\mu_3}\gamma^{\mu_4}\gamma_5)&=4i\varepsilon_{\mu_1\mu_2\mu_3\mu_4}.\end{aligned} \tag{8.12}$$

Note, that the identity in Eq. (8.10) can also be expressed in terms of the usual trace:

$$\mathrm{Tr}(\Gamma\gamma_5)=\frac{-i}{4!}\varepsilon^{\mu_1\mu_2\mu_3\mu_4}\,\mathrm{tr}\left(\Gamma\gamma_{\mu_1}\gamma_{\mu_2}\gamma_{\mu_3}\gamma_{\mu_4}\right). \tag{8.13}$$

This shows the practicability of the scheme; one can easily implement Tr in existing computer algebra programs, in which the usual trace is already implemented. One has just to distinguish between traces with even and odd numbers of γ_5. For a trace with an even number of γ_5, the usual trace can be used. A trace with an odd number of γ_5 can always be reduced to Eq. (8.13), using the anti-commutation relation (8.2) and $\gamma_5^2=1$. Then, the usual trace can be used with an additional number of four Dirac matrices as shown in Eq. (8.13). Let us stress again, that the Levi-Civita tensor in Eq. (8.13) is defined in four dimensions, such that contractions with d dimensional objects always are projected onto the four-dimensional subspace. As a consequence, one has to be careful when contracting $\varepsilon^{\mu_1\mu_2\mu_3\mu_4}$ with d dimensional loop momenta. In Ref. [85], we introduced split momenta to perform this contraction, in which the loop momenta k is split into a four-dimensional and a $d-4$ dimensional component. Here, we will use an alternative way and employ a Passarino-Veltman (PV) reduction, such that the Levi-Civita tensors can safely be contracted with external momenta only.

As mentioned above, Tr is not cyclic and thus depends on a reading point prescription, i.e. the choice where the trace is started. In Ref. [191] it was shown that the Adler–Bell–Jackiw anomaly can be reproduced if one starts reading the trace at

the chiral coupling, cf. Fig. 8.1.1. In the case of several chiral couplings in a diagram, Kreimer suggests to average over all possibilities starting at these couplings. However, as mentioned in Ref. [191] this does not matter in the case of an anomaly free model, like the Standard Model. In this case, one can in fact choose any vertex to start reading the trace. The crucial point is, that the same prescription has to be used throughout the whole calculation for all contributions, such that spurious anomalies cancel out in the end. In our case, we use a fixed reading point prescription, in which we start reading the trace always at the same vertex. We will specify this in Section 8.6.

8.2 Kinematic definitions

In this chapter, we study lepton pair production from annihilation of an up quark with an up antiquark,

$$u(p_1) + \bar{u}(p_2) \to \ell^-(p_3) + \ell^+(p_4)\,, \tag{8.14}$$

at one and two loops. In Ref. [85] we obtained complete results for all helicity amplitudes at order $\alpha_{\rm em}\alpha_{\rm s}$, order $\alpha_{\rm em}^2$, and order $\alpha_{\rm em}^2\alpha_{\rm s}$ in the approximation of vanishing light quark and lepton masses, *i.e.* $p_1^2 = p_2^2 = p_3^2 = p_4^2 = 0$. In this thesis, we will focus only on the calculation of the unpolarized amplitude, which served as an independent cross check.

As usual, we use the Mandelstam variables,

$$s = (p_1 + p_2)^2 \quad \text{and} \quad t = (p_1 - p_3)^2; \quad u = (p_2 - p_3)^2 = -s - t, \tag{8.15}$$

in order to describe process (8.14). In total, five independent kinematic scales, s, t, m_w, m_z, and m_h, appear in the calculation. Here, m_w is the mass of the W boson, m_z is the mass of the Z boson, and m_h is the mass of the Higgs boson. As mentioned in the previous chapter, we calculated the most complicated master integrals only for $s > 4m_w^2$ or $s > 4m_z^2$, depending on the diagram. To avoid further technical complications due to analytic continuation of these integrals and also to avoid a complex mass renormalization scheme, we will restrict our calculation to the physical phase-space region where s is above all two-particle thresholds,

$$s > (m_h + m_z)^2 \qquad (-s < t < 0\,). \tag{8.16}$$

In order to be able to perform the check between the calculation of the helicity amplitudes with the calculation of the unpolarized amplitude carried out as a part of this thesis, we will introduce the Lorentz structures that were used in Ref. [85] in the following. Considering massless external fermions, the amplitude in conventional dimensional regularization can be written up to two loops in terms of the following Lorentz structures [195]:

$$\bar{\mathcal{T}}_1 = \bar{v}(p_2)\gamma^\mu u(p_1)\ \bar{u}(p_3)\gamma_\mu v(p_4), \tag{8.17}$$

$$\bar{\mathcal{T}}_2 = \bar{v}(p_2)\not{p}_3 u(p_1)\ \bar{u}(p_3)\not{p}_1 v(p_4), \tag{8.18}$$

$$\bar{\mathcal{T}}_3 = \bar{v}(p_2)\gamma^\mu\gamma^\nu\gamma^\rho u(p_1)\ \bar{u}(p_3)\gamma_\mu\gamma_\nu\gamma_\rho v(p_4), \tag{8.19}$$

$$\bar{\mathcal{T}}_4 = \bar{v}(p_2)\gamma^\mu\not{p}_3\gamma^\nu u(p_1)\ \bar{u}(p_3)\gamma_\mu\not{p}_1\gamma_\nu v(p_4), \tag{8.20}$$

$$\bar{\mathcal{T}}_5 = \bar{v}(p_2)\gamma^\mu\gamma^\nu\gamma^\rho\gamma^\sigma\gamma^\tau u(p_1)\ \bar{u}(p_3)\gamma_\mu\gamma_\nu\gamma_\rho\gamma_\sigma\gamma_\tau v(p_4), \tag{8.21}$$

and $$\bar{\mathcal{T}}_6 = \bar{v}(p_2)\gamma^\mu\gamma^\nu\not{p}_3\gamma^\rho\gamma^\sigma u(p_1)\ \bar{u}(p_3)\gamma_\mu\gamma_\nu\not{p}_1\gamma_\rho\gamma_\sigma v(p_4), \tag{8.22}$$

where we suppressed color and spin indices and ignored insertions of γ_5. In the case of the EW-QCD corrections, structures $\bar{\mathcal{T}}_5$ and $\bar{\mathcal{T}}_6$ can be omitted even in a general R_ξ gauge because the gluon couples only to the initial-state quark line. As mentioned before, in Ref. [85] the calculation of the helicity amplitudes was performed in two different γ_5 schemes. We adopt the notation, and use a bar on top of a Lorentz structure or an amplitude to indicate that the quantity was calculated in Kreimer's scheme. We will use this notation throughout this chapter.

Allowing also for insertions of γ_5 at the end of each Dirac chain, we obtain in total 16 different Lorentz structures. In $d = 4$ dimensions, only four out of these 16 Lorentz structures are independent, as can be seen using Schouten and Fierz identities. In order to facilitate a smooth $d \to 4$ limit, we can define a d-dimensional basis of the four structures derived from $\bar{\mathcal{T}}_1$ by inserting γ_5 matrices:

$$\bar{\mathcal{T}}_{\mathrm{VV}} = \bar{v}(p_2)\gamma^\mu u(p_1)\ \bar{u}(p_3)\gamma_\mu v(p_4), \tag{8.23}$$

$$\bar{\mathcal{T}}_{\mathrm{AA}} = \bar{v}(p_2)\gamma^\mu\gamma_5 u(p_1)\ \bar{u}(p_3)\gamma_\mu\gamma_5 v(p_4), \tag{8.24}$$

$$\bar{\mathcal{T}}_{\mathrm{AV}} = \bar{v}(p_2)\gamma^\mu\gamma_5 u(p_1)\ \bar{u}(p_3)\gamma_\mu v(p_4), \tag{8.25}$$

$$\bar{\mathcal{T}}_{\mathrm{VA}} = \bar{v}(p_2)\gamma^\mu u(p_1)\ \bar{u}(p_3)\gamma_\mu\gamma_5 v(p_4), \tag{8.26}$$

and 12 further structures (derived from $\bar{\mathcal{T}}_2$, $\bar{\mathcal{T}}_3$, and $\bar{\mathcal{T}}_4$ in a similar way), which are strictly "orthogonal" in d dimensions and smoothly vanish for $d \to 4$ (see also Appendix A in Ref. [85]). Of course, these four independent structures in $d = 4$ are directly related to the four independent helicity amplitudes.

8.3 Renormalization

8.3.1 $\overline{\mathrm{MS}}$ renormalization of α_{em} and α_{s}

In our calculation, we use for both coupling constants, α_{em} and α_{s}, the $\overline{\mathrm{MS}}$ subtraction scheme. As we neglect all fermion masses, this choice is particularly convenient for the calculation of the two-loop mixed EW-QCD corrections to the neutral-current Drell-Yan process. Furthermore, we neglect the gauge-invariant subset of Feynman diagrams with closed fermion loops and any contributions involving top quark. This includes in particular the two-loop Standard Model vacuum polarization of order $\alpha_{\mathrm{em}}\alpha_{\mathrm{s}}$, i.e. diagrams with a single quark loop and a gluon exchange inside that quark loop. Note that the electric charge renormalization constant therefore vanishes identically at order $\alpha_{\mathrm{em}}\alpha_{\mathrm{s}}$ in our setup.

Throughout this chapter, we follow the convention of [76] for fixed-order results. Quantities in Standard Model perturbation theory are written in the form

$$\mathbf{Z} = \sum_{m,n=0}^{\infty} \mathbf{Z}^{(m,n)} \left(\frac{\alpha_{\mathrm{em}}}{4\pi}\right)^m \left(\frac{\alpha_{\mathrm{s}}}{4\pi}\right)^n \tag{8.27}$$

to all orders in the coupling constants. In this notation, neglecting contributions with closed fermion loops which are proportional to the number of light leptons (n_l) or light quarks (n_q) or involve the mass of the top quark (m_t), we have

$$\delta Z_e^{(1,1)}\Big|_{n_\ell, n_q \to 0;\, m_t \to \infty} = 0\,, \tag{8.28}$$

for the order $\alpha_{\mathrm{em}}\alpha_{\mathrm{s}}$ corrections to the electric charge renormalization constant.

Since the tree-level Drell-Yan amplitude is of order $\alpha_{\rm em}$, the renormalization of the strong coupling constant is just given by

$$(4\pi)^{\epsilon} e^{-\gamma_E \epsilon} \alpha_{\rm s}^{\rm bare} = \alpha_{\rm s} \tag{8.29}$$

at order $\alpha_{\rm em}^2 \alpha_{\rm s}$. On the other hand, the one-loop electric charge renormalization constant does contribute in our setup. In the $\overline{\rm MS}$ scheme it is given by,

$$\delta Z_e^{(1,0)}\Big|_{n_\ell, n_q \to 0;\, m_t \to \infty} = -\frac{7}{2\epsilon}\,. \tag{8.30}$$

For notational convenience, we will suppress the indicated limits $n_\ell, n_q \to 0$; $m_t \to \infty$ provided on the left-hand sides of Eqs. (8.28) and (8.30) throughout the rest of this chapter.

8.3.2 On-shell electroweak gauge boson wavefunction and mass renormalization

In this section, we review the on-shell renormalization of the electroweak gauge bosons in a generalized 't Hooft-Feynman gauge. We use the Feynman rules provided in Refs. [196–199]. The electroweak gauge boson renormalization constants are defined using the same renormalization on-shell conditions as in these references. However, in contrast to the aforementioned references, we factor the squared electroweak gauge boson mass, m_v^2, out of the mass renormalization constants, $Z_{m_v^2}$, to render them dimensionless.

As usual, a particularly convenient choice for the gauge parameter renormalization constants is

$$Z_{\xi_\gamma} = Z_{\gamma\gamma}, \quad Z_{\xi_z} = Z_{ZZ}, \quad \text{and} \quad Z_{\xi_w} = Z_{W^\pm} \tag{8.31}$$

because it simplifies the all-orders form of the electroweak gauge boson kinetic terms in the renormalized Lagrange density. The 't Hooft-Feynman gauge is then defined by setting all of the renormalized gauge parameters to one at the outset,

$$\xi_\gamma = \xi_z = \xi_w = 1\,. \tag{8.32}$$

This is justified because, due to Eqs. (8.31), the gauge parameters in this scheme receive no radiative corrections.

We decompose all electroweak gauge-boson self energies as:

$$-i\,\Sigma^{\mu\nu}_{\gamma\gamma}(q) = -i\left(g^{\mu\nu} - \frac{q^\mu q^\nu}{q^2}\right)\Sigma^T_{\gamma\gamma}\left(q^2\right) - i\frac{q^\mu q^\nu}{q^2}\Sigma^L_{\gamma\gamma}\left(q^2\right)\,, \tag{8.33}$$

$$-i\,\Sigma^{\mu\nu}_{\gamma Z}(q) = -i\left(g^{\mu\nu} - \frac{q^\mu q^\nu}{q^2}\right)\Sigma^T_{\gamma Z}\left(q^2\right) - i\frac{q^\mu q^\nu}{q^2}\Sigma^L_{\gamma Z}\left(q^2\right)\,, \tag{8.34}$$

$$-i\,\Sigma^{\mu\nu}_{ZZ}(q) = -i\left(g^{\mu\nu} - \frac{q^\mu q^\nu}{q^2}\right)\Sigma^T_{ZZ}\left(q^2\right) - i\frac{q^\mu q^\nu}{q^2}\Sigma^L_{ZZ}\left(q^2\right)\,, \tag{8.35}$$

$$\text{and} \quad -i\,\Sigma^{\mu\nu}_{W^+W^-}(q) = -i\left(g^{\mu\nu} - \frac{q^\mu q^\nu}{q^2}\right)\Sigma^T_{W^+W^-}\left(q^2\right) - i\frac{q^\mu q^\nu}{q^2}\Sigma^L_{W^+W^-}\left(q^2\right)\,, \tag{8.36}$$

where the longitudinal components $\Sigma^L_{VV'}$ are unphysical and need not be calculated explicitly and the transverse components $\Sigma^T_{VV'}$ are gauge invariant and are needed to calculate the renormalization constants.

In order to project out the transverse component of the self energies only, we define the following projector in d dimensions:

$$\left(\mathbb{P}^T_{VV'}\right)_{\mu\nu} = \frac{i}{3-2\epsilon}\left(g_{\mu\nu} - \frac{q_\mu q_\nu}{q^2}\right). \tag{8.37}$$

For the Lorentz projection operators considered in this section, a sum over the available open Lorentz and spin indices is always implied for their action on Feynman diagrams. Following Ref. [197], we define the on-shell renormalization constants as:

$$\begin{aligned}
\delta Z_{\gamma\gamma} &= -\left.\frac{\mathrm{d}\Sigma^T_{\gamma\gamma}(q^2)}{\mathrm{d}q^2}\right|_{q^2=0}, & \delta Z_{Z\gamma} &= \left.\frac{2\Sigma^T_{\gamma Z}(q^2)}{m_z^2}\right|_{q^2=0}, \\
\delta Z_{\gamma Z} &= -\left.\frac{2\Sigma^T_{\gamma Z}(q^2)}{m_z^2}\right|_{q^2=m_z^2}, & \delta Z_{ZZ} &= -\left.\frac{\mathrm{d}\Sigma^T_{ZZ}(q^2)}{\mathrm{d}q^2}\right|_{q^2=m_z^2}, \\
\delta Z_{m_z^2} &= \left.\frac{\Sigma^T_{ZZ}(q^2)}{m_z^2}\right|_{q^2=m_z^2}, & \delta Z_{m_w^2} &= \left.\frac{\Sigma^T_{W^+W^-}(q^2)}{m_w^2}\right|_{q^2=m_w^2}.
\end{aligned} \tag{8.38}$$

Apart from light fermion and top quark contributions which, as mentioned above, we consistently neglect throughout this work, explicit expressions for the self-energies and counterterms at order α_{em} relevant to the higher-order corrections of interest to us can be found in the ancillary files in our `arXiv` submission of Ref. [85] to all orders in ϵ. Note that we do not provide an explicit expression for $\delta Z^{(1,0)}_{W^\pm}$ because it plays no role in the renormalization of any of the Feynman diagrams we calculate.

8.3.3 On-shell renormalization for massless fermion fields

In this section, we review the systematics of on-shell renormalization of the wavefunctions for massless fermion fields in the Standard Model. The on-shell scheme for massless fermions is widely used in QCD because, due to the scalelessness of the contributing gluon-exchange diagram, the one-loop quark wavefunction counterterm vanishes identically in dimensional regularization. The Lorentz decomposition of the fermion self energy in the Standard Model is given by

$$i\left(\bar{\Sigma}_f(q)\right)_{\alpha\beta} = i\,\bar{\Sigma}_{\mathrm{V},f}\left(q^2\right)\left(\not{q}\right)_{\alpha\beta} + i\,\bar{\Sigma}_{\mathrm{A},f}\left(q^2\right)\left(\not{q}\gamma_5\right)_{\alpha\beta} \tag{8.39}$$

where q^2 is taken to be different from zero.[1] In writing Eq. (8.39), we have implicitly assumed Kreimer's γ_5 scheme (indicated by the bar, i.e. we write $\bar{\Sigma}_f(q)$ instead of $\Sigma_f(q)$); analogous calculations in HVBM's γ_5 scheme can be found in Ref. [85].

We employ the notation of [196] for the interactions of the electroweak gauge bosons with matter. The Z interaction is parametrized by flavor-dependent axial vector and vector coupling coefficients,

$$a_f = \frac{m_z^2\, I_f^3}{2m_w\sqrt{m_z^2-m_w^2}} \quad \text{and} \quad v_f = \frac{m_z^2}{2m_w\sqrt{m_z^2-m_w^2}}\left(I_f^3 - 2\frac{m_z^2-m_w^2}{m_z^2}Q_f\right). \tag{8.40}$$

[1] Throughout this section, we suppress the color indices of the quarks to streamline our discussion and allow for a unified description of propagator corrections at one loop. The two-loop mixed EW-QCD scattering amplitudes of primary interest to us in this work always come with a color factor of C_F, due to the fact that all contributing Feynman diagrams feature exactly one gluon exchange between quark lines.

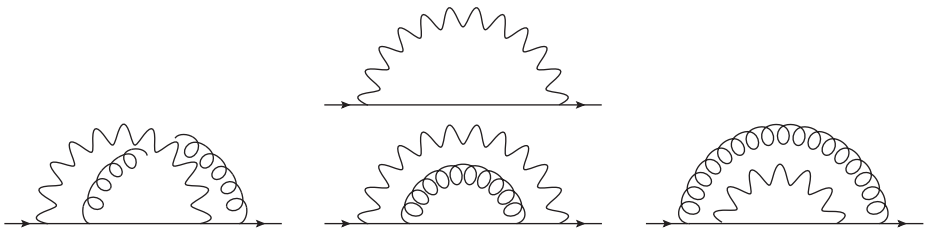

FIGURE 8.3.1: Independent Z exchange diagrams at one and two loops. Due to the absence of fermion masses, diagrams which feature only gluon and/or photon exchanges vanish identically.

The W interaction, on the other hand, is parametrized by a universal coupling coefficient

$$a_w = v_w = \frac{m_z}{2\sqrt{2}\sqrt{m_z^2 - m_w^2}}\,. \tag{8.41}$$

We will make extensive use of these aliases throughout the rest of this chapter.

At first sight, it might seem counterproductive not to employ Eq. (8.41) to eliminate a_w and v_w, as they are equal and have no dependence on the fermion flavor. However, as will become clear later on in this section, it is useful to retain the dependence on a_w and v_w at intermediate stages of fermion self-energy and vertex calculations because it generically allows for a determination of axial-vector components from vector components through chiral symmetry. The fermion self-energies considered in this section are particularly simple and have no independent W-exchange Feynman diagrams; all W-exchange diagrams can be obtained from the Z-exchange diagrams by making the replacements $a_f \to a_w$ and $v_f \to v_w$ (see Figure 8.3.1).

Thus, for the relatively low perturbative orders of interest to us, it suffices to consider the calculation of the Z-exchange contributions to the vector component of the fermion self-energy.

We now proceed by calculating the Z-exchange diagram to the vector component of the fermion self-energy. It is given by:

$$\left(\bar{\Sigma}^{(1,0)}_{\mathrm{V},f}(q^2)\Big|_{Z\text{ exchange}}\right)\left(\not{q}\right) = -\,c_1\left(\epsilon,\mu^2\right)\left(a_f^2+v_f^2\right)\int \mathrm{d}^d k_1 \frac{\gamma^\nu(\not{q}+\not{k}_1)\gamma_\nu}{(q+k_1)^2(k_1^2-m_z^2)}\,, \tag{8.42}$$

where

$$c_1\left(\epsilon,\mu^2\right) = \frac{e^{\gamma_E \epsilon}\left(\mu^2\right)^\epsilon}{i\pi^{2-\epsilon}}\,. \tag{8.43}$$

As Eq. (8.42) does not depend on γ_5, it can be trivially simplified using the contraction identity of the γ matrices in d dimensions. After carrying out the numerator algebra, we obtain:

$$\left(\bar{\Sigma}^{(1,0)}_{\mathrm{V},f}(q^2)\Big|_{Z\text{ exchange}}\right)\left(\not{q}\right) = 2\,c_1\left(\epsilon,\mu^2\right)\left(a_f^2+v_f^2\right)(1-\epsilon)\int \mathrm{d}^d k_1 \frac{\not{q}+\not{k}_1}{(q+k_1)^2(k_1^2-m_z^2)}. \tag{8.44}$$

To extract $\bar{\Sigma}^{(1,0)}_{\mathrm{V},f}(q^2)\Big|_{Z\text{ exchange}}$, we need to identify the coefficient in front of $\not{q}$ on the rhs of the above equation. This can be done using a PV reduction, which yields:

$$\bar{\Sigma}^{(1,0)}_{\mathrm{V},f}(q^2)\Big|_{Z\text{ exchange}} = \frac{c_1\left(\epsilon,\mu^2\right)\left(a_f^2+v_f^2\right)(1-\epsilon)}{q^2}\left(\left(q^2-m_z^2\right)\int \frac{\mathrm{d}^d k_1}{(q+k_1)^2(k_1^2-m_z^2)}\right.$$

$$+\int \frac{\mathrm{d}^d k_1}{k_1^2 - m_z^2}\Bigg), \tag{8.45}$$

where, using Feynman/Schwinger parameters,

$$\int \frac{\mathrm{d}^d k_1}{k_1^2 - m_z^2} = -\frac{e^{\gamma_E \epsilon}}{c_1\left(\epsilon, \mu^2\right)} \left(\frac{\mu^2}{m_z^2}\right)^\epsilon m_z^2\, \Gamma(-1+\epsilon) \quad \text{and} \tag{8.46}$$

$$\int \frac{\mathrm{d}^d k_1}{(q+k_1)^2(k_1^2 - m_z^2)} = 2\frac{e^{\gamma_E \epsilon}}{c_1\left(\epsilon, \mu^2\right)} \left(\frac{\mu^2}{m_z^2}\right)^\epsilon \frac{\Gamma(\epsilon)\Gamma(2-2\epsilon)}{\Gamma(3-2\epsilon)}\, {}_2F_1\left(1, \epsilon; 2-\epsilon; \frac{q^2}{m_z^2}\right). \tag{8.47}$$

In writing Eq. (8.47), q^2 was assumed to be less than m_z^2. From Eqs. (8.46) and (8.47) we now have to take the limit $q^2 \to 0$ of Eq. (8.45). Using l'Hôpital's rule, we find:

$$\lim_{q^2 \to 0} \left(\bar{\Sigma}^{(1,0)}_{\mathrm{V},f}(q^2)\Big|_{Z \text{ exchange}} \right) = \frac{2\left(a_f^2 + v_f^2\right)(1-\epsilon)\Gamma(\epsilon) e^{\gamma_E \epsilon}}{2-\epsilon} \left(\frac{\mu^2}{m_z^2}\right)^\epsilon. \tag{8.48}$$

Note that taking the limit $q^2 \to 0$ before expanding in ϵ, becomes technical challenging at higher orders in perturbation theory. In Ref. [85] we used a different approach and obtained all counterterms by defining projectors that project out the self-energy directly at $q^2 = 0$. This facilitates the calculation from the beginning.

In order to derive the axial component of the lepton one-loop self energy, we note that in the Standard Model right- and left-handed components of the Z-exchange contributions are exchanged under $\gamma_5 \to -\gamma_5$. Thus, the axial vector component of the Z-exchange contribution to the fermion self-energy can be obtained by a replacement of the form $v_f^2 + a_f^2 \to \pm 2\, a_f v_f$ in Eq. (8.48). In order to fix the overall sign, recall that the coupling of the W to matter is exactly left-handed, that the W-exchange contribution is obtained by making the replacements $a_f \to a_w$ and $v_f \to v_w$, and that $a_w = v_w$. Taken together, these considerations allow us to conclude that

$$\bar{\Sigma}^{(1,0)}_{\mathrm{A},f}(0)\Big|_{Z \text{ exchange}} = -\frac{4\, a_f v_f (1-\epsilon)\Gamma(\epsilon) e^{\gamma_E \epsilon}}{2-\epsilon} \left(\frac{\mu^2}{m_z^2}\right)^\epsilon \tag{8.49}$$

with no additional calculation.

In the on-shell scheme, massless fermion wavefunction counterterms are defined to exactly cancel the perturbative corrections to the corresponding fermion self-energies order-by-order. Therefore, we find

$$\begin{aligned}
\delta Z^{(1,0)}_{\mathrm{V},f} &= -\bar{\Sigma}^{(1,0)}_{\mathrm{V},f}(0) \\
&= -\frac{2\left(a_f^2 + v_f^2\right)(1-\epsilon)\Gamma(\epsilon) e^{\gamma_E \epsilon}}{2-\epsilon} \left(\frac{\mu^2}{m_z^2}\right)^\epsilon - \frac{2\left(a_w^2 + v_w^2\right)(1-\epsilon)\Gamma(\epsilon) e^{\gamma_E \epsilon}}{2-\epsilon} \left(\frac{\mu^2}{m_w^2}\right)^\epsilon
\end{aligned} \tag{8.50}$$

$$\begin{aligned}
\delta Z^{(1,0)}_{\mathrm{A},f} &= -\bar{\Sigma}^{(1,0)}_{\mathrm{A},f}(0) \\
&= \frac{4\, a_f v_f (1-\epsilon)\Gamma(\epsilon) e^{\gamma_E \epsilon}}{2-\epsilon} \left(\frac{\mu^2}{m_z^2}\right)^\epsilon + \frac{4\, a_w v_w (1-\epsilon)\Gamma(\epsilon) e^{\gamma_E \epsilon}}{2-\epsilon} \left(\frac{\mu^2}{m_w^2}\right)^\epsilon
\end{aligned} \tag{8.51}$$

for the vector and axial vector components of the one-loop fermion wavefunction counterterm.

We now turn to the vector and axial vector components of the two-loop quark self-energy of order $\alpha_{\mathrm{em}}\alpha_{\mathrm{s}}$. In contrast to our calculation presented in Ref. [85] where

we used projectors to access the self energies at $q^2 = 0$ directly, here we will showcase a different derivation of the counterterms starting from the off-shell self energies. These were obtained using a PV reduction. For the vector component of the quark self energy $\bar{\Sigma}_q$ we find

$$\bar{\Sigma}^{(1,1)}_{\mathrm{V},q}(q^2) = (a_q^2 + v_q^2) f(q^2, m_z^2) + (a_w^2 + v_w^2) f(q^2, m_w^2), \tag{8.52}$$

where

$$\begin{aligned}
f(q^2,m^2) = &-\frac{m^2\left(2\epsilon^3m^2 - 5\epsilon^2m^2 + 2\epsilon m^2 + 3m^2 + q^2\epsilon^2 - 2q^2\epsilon\right)}{q^4(\epsilon-2)\epsilon^2(2\epsilon-1)^2} m_{17} \\
&+ \frac{4(\epsilon-1)\left(q^2-m^2\right)\left(-\epsilon m^2 + m^2 + q^2\epsilon^2\right)}{q^4\epsilon^3(2\epsilon-1)^2} m_{24} \\
&+ \frac{2(\epsilon-1)\left(q^2-m^2\right)\left(-2\epsilon^2m^2 + \epsilon m^2 - 2m^2 + q^2\epsilon\right)}{q^4\epsilon^3(2\epsilon-1)^2} m_{25} \\
&+ \frac{m_{19}}{q^4(\epsilon-2)\epsilon^3(2\epsilon-1)(3\epsilon-2)(3\epsilon-1)} \Big(28q^2\epsilon^5m^2 - 90q^2\epsilon^4m^2 \\
&\quad + 124q^2\epsilon^3m^2 - 90q^2\epsilon^2m^2 + 40q^2\epsilon m^2 - 8q^2m^2 + 9\epsilon^4m^4 - 36\epsilon^3m^4 \\
&\quad + 65\epsilon^2m^4 - 42\epsilon m^4 + 8m^4 + 16q^4\epsilon^5 - 18q^4\epsilon^4 - 30q^4\epsilon^3 + 24q^4\epsilon^2\Big) \\
&+ \frac{-(\epsilon-1)m_{13}}{q^4\epsilon^3(2\epsilon-1)^2(3\epsilon-2)(3\epsilon-1)} \Big(-30q^2\epsilon^4m^2 + 32q^2\epsilon^3m^2 - 38q^2\epsilon^2m^2 \\
&\quad + 26q^2\epsilon m^2 - 4q^2m^2 + 18\epsilon^4m^4 - 27\epsilon^3m^4 + 31\epsilon^2m^4 - 20\epsilon m^4 + 4m^4 \\
&\quad + 8q^4\epsilon^4 + 7q^4\epsilon^3 - 3q^4\epsilon^2 - 2q^4\epsilon\Big) \\
&+ \frac{-2m_{18}}{q^4(\epsilon-2)\epsilon^3(2\epsilon-1)(3\epsilon-2)(3\epsilon-1)} \Big(59q^2\epsilon^5m^2 - 176q^2\epsilon^4m^2 + 229q^2\epsilon^3m^2 \\
&\quad - 188q^2\epsilon^2m^2 + 92q^2\epsilon m^2 - 16q^2m^2 + 4\epsilon^5m^4 - 58\epsilon^3m^4 + 135\epsilon^2m^4 \\
&\quad + 5\epsilon^4m^4 - 90\epsilon m^4 + 16m^4 + 25q^4\epsilon^5 - 27q^4\epsilon^4 - 55q^4\epsilon^3 + 51q^4\epsilon^2 - 6q^4\epsilon\Big) \\
&+ \frac{2\left(-2\epsilon^2m^2 + 6\epsilon m^2 - 4m^2 + 5q^2\epsilon^2 - 10q^2\epsilon + 3q^2\right)}{q^2(\epsilon-2)\epsilon^2(2\epsilon-1)^2} m_{15},
\end{aligned} \tag{8.53}$$

and where the master integrals $\{m_{13}, m_{15}, m_{17}, m_{18}, m_{19}, m_{24}, m_{25}\}$ are all provided in Ref. [107]. As stated above, the axial component of the self energy can be obtained from Eq. (8.52) by the replacement $v_f^2 + a_f^2 \to -2\, a_f v_f$.

In order to derive the counterterms, we have to take first the limit $q^2 \to 0$ and then expand in ϵ. For all integrals despite m_{15} the limits $q^2 \to 0$ and $\epsilon \to 0$ commute, such that we can use the ϵ-expanded off-shell expressions, and then take $q^2 \to 0$. For m_{15} we find that taking the limit $q^2 \to 0$ for the ϵ-expanded expression is ill-defined. Note, that m_{15} is the product of a one-loop tadpole and a massless one-loop self-energy integral. Thus, since the massless self-energy becomes scaleless for $q^2 = 0$, we have to set m_{15} to zero from the outset before expanding in ϵ. For all other integrals, the limit $q^2 \to 0$ is well defined and we can safely expand first in ϵ and later take the limit. For our two-loop calculation, we need the counterterms only up to zeroth order in ϵ. We find:

$$\begin{aligned}
\delta Z^{(1,1)}_{\mathrm{V},q} = -\bar{\Sigma}^{(1,1)}_{\mathrm{V},q}(0) = &(a_q^2 + v_q^2) C_F \left[\frac{3}{2\epsilon} + \left(-\frac{7}{4} + 3\ln\left(\frac{\mu^2}{m_z^2}\right)\right)\right] \\
&+ (a_w^2 + v_w^2) C_F \left[\frac{3}{2\epsilon} + \left(-\frac{7}{4} + 3\ln\left(\frac{\mu^2}{m_w^2}\right)\right)\right] + \mathcal{O}(\epsilon),
\end{aligned} \tag{8.54}$$

$$\delta Z_{\mathrm{A},q}^{(1,1)} = -\bar{\Sigma}_{\mathrm{A},q}^{(1,1)}(0) = -2a_q v_q C_F \left[\frac{3}{2\epsilon} + \left(-\frac{7}{4} + 3\ln\left(\frac{\mu^2}{m_z^2}\right)\right)\right] - 2a_w v_w C_F \left[\frac{3}{2\epsilon} + \left(-\frac{7}{4} + 3\ln\left(\frac{\mu^2}{m_w^2}\right)\right)\right] + \mathcal{O}(\epsilon). \tag{8.55}$$

Note, that these expressions agree with the ones we derived in Ref. [85] using projectors up to the given order in ϵ, thus providing a strong check on our previous, projector-based calculation.

8.4 One-loop scattering amplitudes

8.4.1 Diagrammatic structure

In this section, we present the diagrammatic structure of the one-loop perturbative corrections to the neutral-current Drell-Yan process. Due to their familiarity, the renormalized self-energy corrections to the photon and Z propagators,

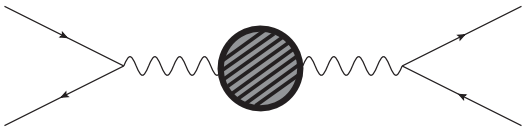

will not be visualized in explicit detail. In what follows, we will also use a generic wavy line for both the photon and the Z, keeping in mind that some contributions involving *e.g.* a coupling to neutrinos can occur only for the Z. As is well-known, just a single class of diagram contributes to the one-loop corrections of relative order α_{s},

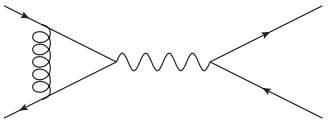

The remaining one-loop corrections of relative order α_{em} fall into three categories: initial state vertex diagrams, final state vertex diagrams, and box diagrams. Both the initial state vertex diagrams

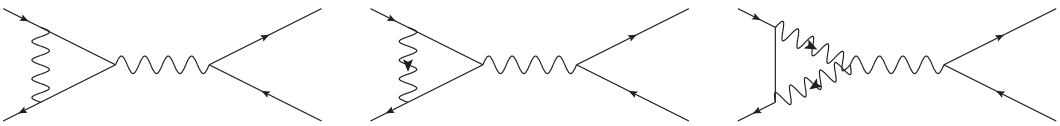

and the final state vertex diagrams

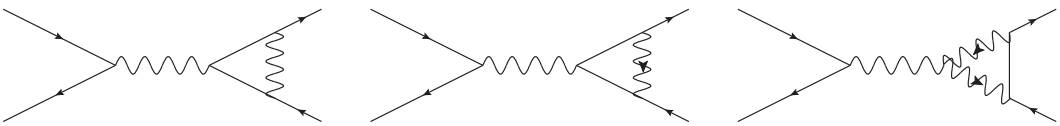

require renormalization,

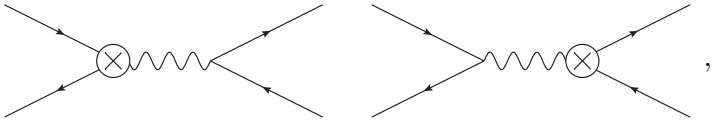

due to the presence of ultraviolet divergences. The box diagrams

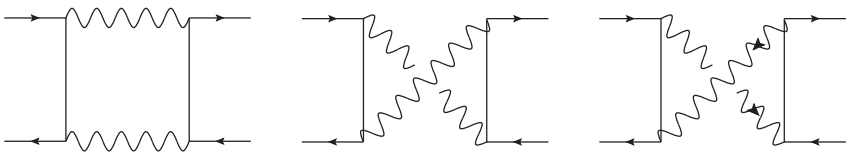

have IR divergences only.

8.4.2 One-loop integral definitions

All of the one-loop integrals defined below are functions of uniform transcendental weight taken in the standard $\overline{\text{MS}}$ normalization. Therefore, all one-loop Feynman integrals are understood to have a multiplicative factor of

$$c_1\left(\epsilon, \mu^2\right) = \frac{e^{\gamma_E \epsilon} \left(\mu^2\right)^\epsilon}{i\pi^{2-\epsilon}} \tag{8.56}$$

in the integration measure. In what follows, thin solid lines denote massless propagators or massless external momenta, thick, dotted lines denote propagators of mass m_w, thick, dashed lines denote propagators of mass m_z, and thick solid lines denote propagators of mass m_h. In total, 31 linearly-independent one-loop integrals appear in the one-loop calculation:

$$I_1 = \epsilon$$ 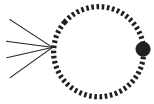 $$\left(m_w^2\right) \tag{8.57}$$

$$I_2 = \sqrt{s(s-4\,m_w^2)}\;\epsilon$$  $$\left(s, m_w^2\right) \tag{8.58}$$

$$I_3 = \sqrt{m_z^2(4\,m_w^2 - m_z^2)}\;\epsilon$$  $$\left(m_w^2, m_z^2\right) \tag{8.59}$$

$$I_4 = \epsilon$$ 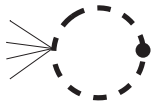 $$\left(m_z^2\right) \tag{8.60}$$

$$I_5 = \epsilon$$ 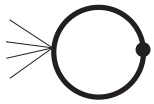 $$\left(m_h^2\right) \tag{8.61}$$

$$I_6 = \sqrt{\lambda\left(s, m_z^2, m_h^2\right)}\;\epsilon$$  $$\left(s, m_z^2, m_h^2\right) \tag{8.62}$$

$$I_7 = \sqrt{m_h^2(4\,m_z^2 - m_h^2)}\;\epsilon$$  $$\left(m_z^2, m_h^2\right) \tag{8.63}$$

$$I_8 = s\,\epsilon$$ 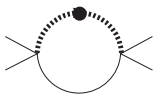 $$\left(s, m_w^2\right) \tag{8.64}$$

$$I_9 = \sqrt{\lambda\left(s, m_w^2, m_z^2\right)}\;\epsilon$$ 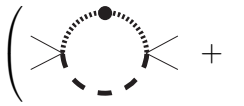 $$\left(s, m_w^2, m_z^2\right) \tag{8.65}$$

$$I_{10} = \sqrt{\lambda\left(s, m_w^2, m_h^2\right)}\,\epsilon \left(\right) \left(s, m_w^2, m_h^2\right) \tag{8.66}$$

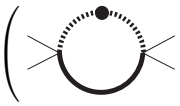

$$I_{11} = \sqrt{m_z^2(4\,m_w^2 - m_z^2)}\,\epsilon \left(\right) \left(m_w^2, m_z^2\right) \tag{8.67}$$

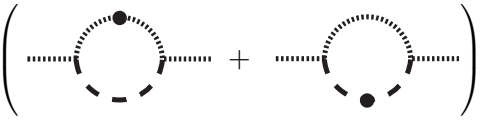

$$I_{12} = \sqrt{m_h^2(4\,m_w^2 - m_h^2)}\,\epsilon \left(\right) \left(m_w^2, m_h^2\right) \tag{8.68}$$

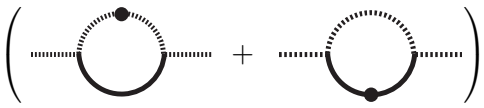

$$I_{13} = s\,\epsilon \quad (s) \tag{8.69}$$

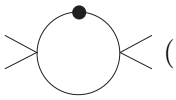

$$I_{14} = s\,\epsilon^2 \quad \left(s, m_z^2\right) \tag{8.70}$$

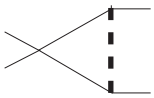

$$I_{15} = s\,\epsilon^2 \quad \left(s, m_w^2\right) \tag{8.71}$$

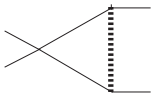

$$I_{16} = s\,\epsilon^2 \quad \left(s, m_w^2\right) \tag{8.72}$$

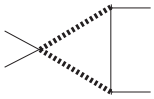

$$I_{17} = t\,\epsilon \quad (t) \tag{8.73}$$

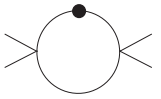

$$I_{18} = u\,\epsilon \quad (u) \tag{8.74}$$

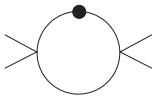

$$I_{19} = s\,t\,\epsilon^2 \quad (s, t) \tag{8.75}$$

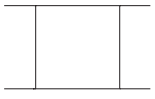

$$I_{20} = s\,u\,\epsilon^2 \quad (s, u) \tag{8.76}$$

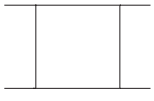

$$I_{21} = s\,\epsilon \quad \left(s, m_z^2\right) \tag{8.77}$$

$$I_{22} = t\,\epsilon^2 \quad \left(t, m_z^2\right) \tag{8.78}$$

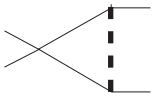

$$I_{23} = u\,\epsilon^2 \quad \left(u, m_z^2\right) \tag{8.79}$$

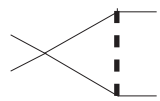

$$I_{24} = t\,\left(s - m_z^2\right)\,\epsilon^2 \quad \left(s, t, m_z^2\right) \tag{8.80}$$

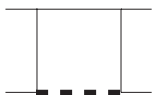

$$I_{25} = u\,\left(s - m_z^2\right)\,\epsilon^2 \quad \left(s, u, m_z^2\right) \tag{8.81}$$

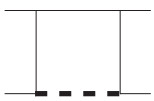

$$I_{26} = \sqrt{s(s - 4\,m_z^2)}\,\epsilon \quad \left(s, m_z^2\right) \tag{8.82}$$

$$I_{27} = s\,\epsilon^2 \quad \left(s, m_z^2\right) \tag{8.83}$$

$$I_{28} = \sqrt{s\,t\,(s\,t - 4m_z^2\,(t + m_z^2))}\;\epsilon^2 \quad \left(s, t, m_z^2\right) \tag{8.84}$$

$$I_{29} = \sqrt{s\,u\,(s\,u - 4m_z^2\,(u + m_z^2))}\;\epsilon^2 \quad \left(s, u, m_z^2\right) \tag{8.85}$$

$$I_{30} = u\,\epsilon^2 \quad \left(u, m_w^2\right) \tag{8.86}$$

$$I_{31} = \sqrt{s\,u\,(s\,u - 4m_w^2\,(u + m_w^2))}\;\epsilon^2 \quad \left(s, u, m_w^2\right)\,, \tag{8.87}$$

where $\lambda(x, y, z)$ is the Källén function,

$$\lambda(x, y, z) = x^2 + y^2 + z^2 - 2xy - 2xz - 2yz. \tag{8.88}$$

For clarity and later convenience, we have made all dependence on the kinematic variables s, t, $u = -s-t$, m_w^2, m_z^2, and m_h^2 completely explicit on the right-hand side. Moreover, we have included integrals for all relevant permutations of the kinematic variables separately. In order to actually calculate the master integrals, it is enough to find explicit expressions for I_1, I_2, I_3, I_6, I_7, I_8, I_{13}, I_{14}, I_{16}, I_{17}, I_{19}, I_{22}, I_{24}, and I_{28}, as all other integrals may be obtained by making simple replacements. For example, I_{31} is obtained from I_{28} by replacing m_z^2 with m_w^2 and t with u. Due to the fact that we consider the physical region $s > (m_z + m_h)^2$ (see (8.16)), the same form of the analytic result can be used in a straightforward way.

Our calculation requires knowledge of the most complicated one-loop box-type master integrals (*i.e.* I_{24} and I_{28}) expanded through to the fourth-order in ϵ. We could not find suitable analytic solutions for all integrals in the literature. Several of the explicit results we could locate in the `Loopedia` database [200] were either not expanded to sufficiently high order in ϵ for our purposes or not provided in a form convenient for numerical evaluations in the physical region of interest to us.

We therefore computed all of the integrals from scratch, either by direct integration for generic ϵ followed by an expansion[2] in ϵ or by using the method of differential equations [202–208]. The integral definitions given above lead to a ϵ-decoupled form for the differential equations [96, 209], which we integrate in terms of multiple polylogarithms. To proceed, we construct real-valued multiple polylogarithms in the region of phase space of interest to us, employing the functional basis presented in [84, 107], together with a few additional logarithms and polylogarithms required to integrate *e.g.* I_6 to sufficiently high order in ϵ. We provided our results in the ancillary file `oneloopmasters.m` attached to the `arXiv` submission of Ref. [85].

8.5 Two-loop scattering amplitudes

8.5.1 Diagrammatic structure

In this section, we present the diagrammatic structure of the two-loop perturbative corrections to the neutral-current Drell-Yan process of relative order $\alpha_{\rm em}\alpha_{\rm s}$. As at

[2]For some of the more complicated expansions, we used the `Mathematica` package `HypExp` [201].

one loop, we do not explicitly identify the photon and Z. Due to their familiarity, diagrams with one-loop renormalized self-energy insertions of the form

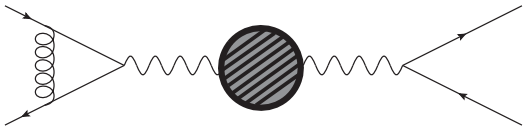

will not be visualized in explicit detail. Several other two-loop diagrams are also trivial, in that they essentially consist of simple products of one-loop contributions:

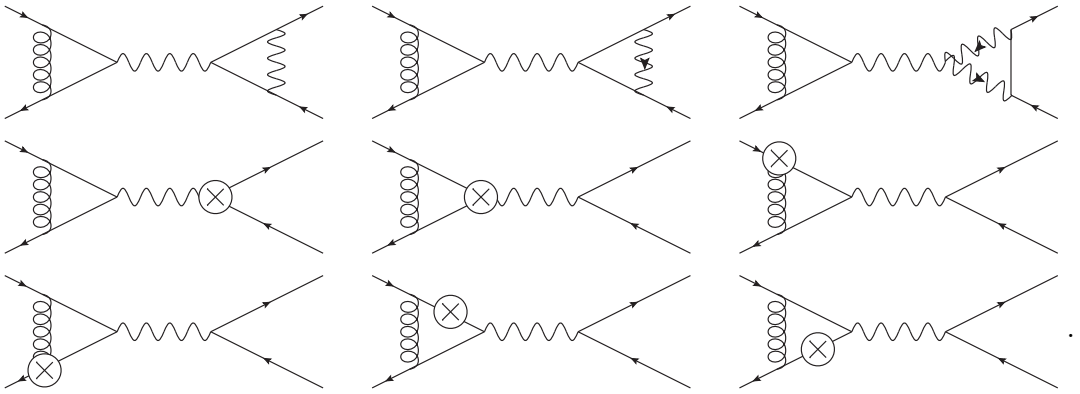

Note that, in the above, the sum of the final four diagrams vanishes identically.

For the sake of brevity, we draw only one half of the two-loop vertex diagrams with a single massive vector boson stretched across the quark line:

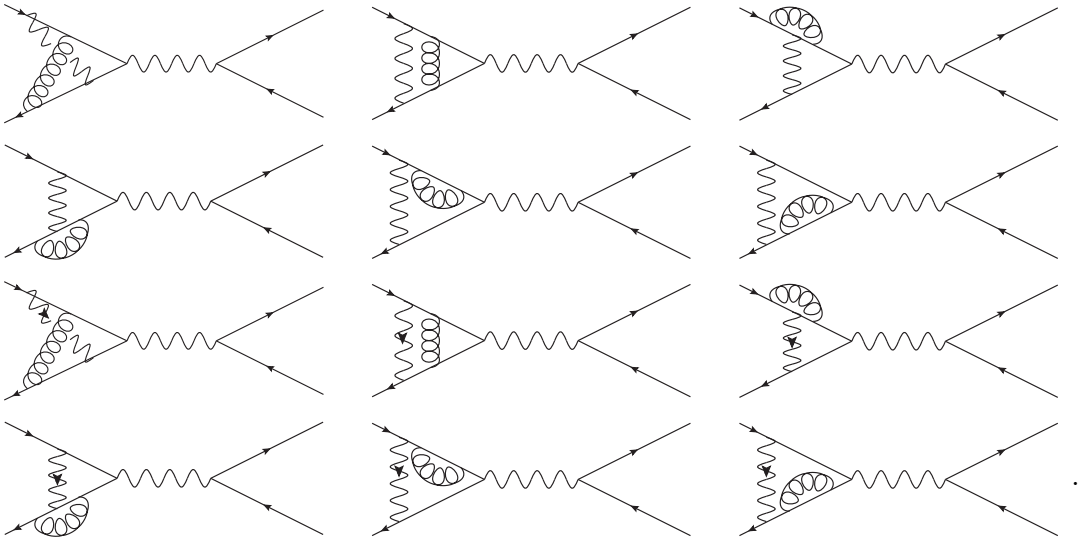

The remaining diagrams of this type may be trivially recovered from the above by exchanging the gluon and the electroweak gauge boson attached to the quark line.

Of course, there are also diagrams with γW^+W^- and ZW^+W^- interactions:

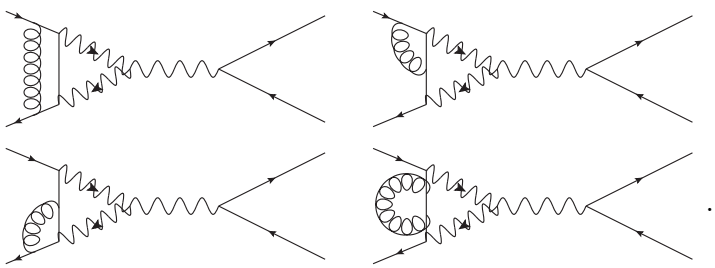

Finally, the order $\alpha_{\text{em}}\alpha_{\text{s}}$ vertex receives a correction from a two-loop vertex counterterm insertion,

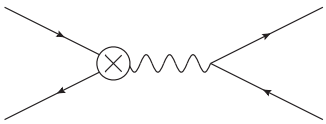

The most complicated two-loop diagrams are those of box type:

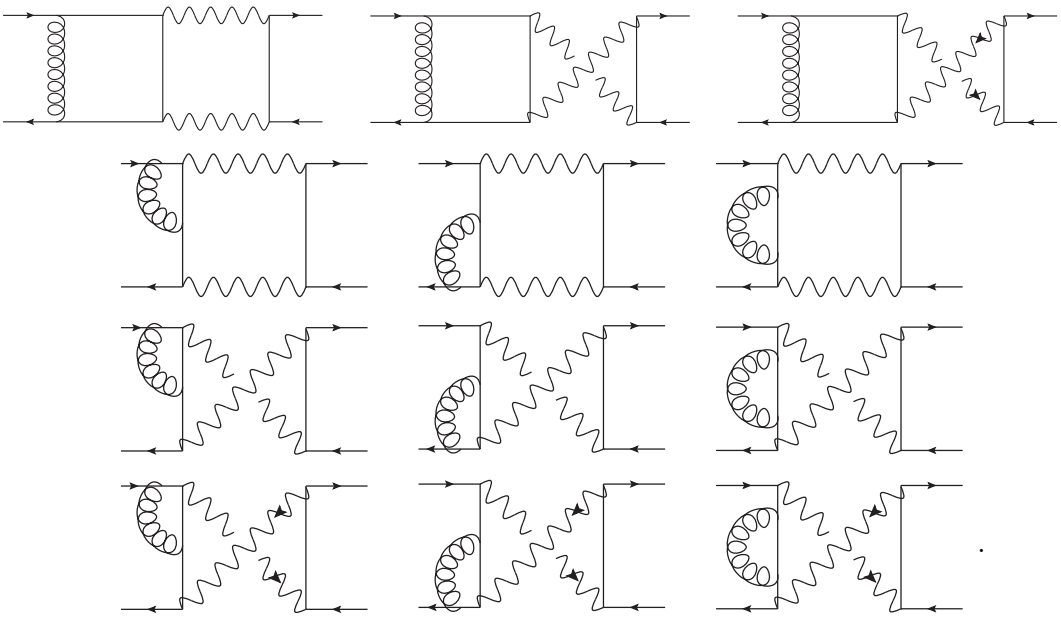

Our evaluation of these box-type diagrams is one of the most important new results of this work. In our calculation in Ref. [85], in the HVBM's γ_5 scheme further diagrams with finite counterterms,

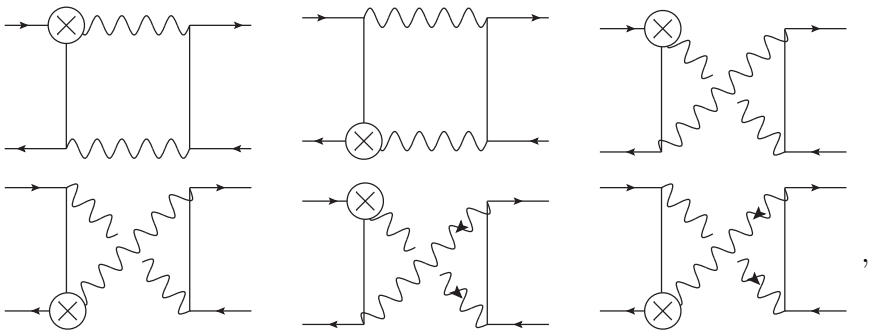

need to be included to ensure that the order $\alpha_{\text{em}}^2\alpha_{\text{s}}$ hard scattering function in HVBM's γ_5 scheme respects the chiral symmetry of the Standard Model. In Kreimer's scheme, which was used for the calculation in this thesis, those diagrams do not exist.

8.5.2 Two-loop integral definitions

All of the two-loop integrals defined below are functions of uniform transcendental weight, converted from the idiosyncratic notation of Refs. [84, 107], where they were originally evaluated in the physical region above all two-particle thresholds, to standard $\overline{\text{MS}}$ normalization. To be explicit, the m_i integrals from [107] and the $\mathbf{m}_i$ integrals from [84] (i.e. the two-mass integrals which were also presented in the previous

chapter) must be multiplied by

$$c_2\left(\epsilon,\mu^2,s\right)=\frac{e^{2\gamma_E\epsilon}}{\Gamma^2(1-\epsilon)}\left(\frac{\mu^2}{s}\right)^{2\epsilon}. \tag{8.89}$$

That is to say, the integral measure of our two-loop integrals is exactly:

$$\left(\frac{e^{\gamma_E\epsilon}\left(\mu^2\right)^{\epsilon}}{i\pi^{2-\epsilon}}\right)^2\int \mathrm{d}^dk_1\int \mathrm{d}^dk_2\,. \tag{8.90}$$

For brevity, we suppress the factors of $c_2\left(\epsilon,\mu^2,s\right)$ which belong in the definitions of all of the non-factorizable two-loop integrals given below. In total, 133 linearly-independent two-loop integrals appear in the full calculation:

$$\begin{aligned}
&J_1=m_{17}\left(m_z^2\right) && J_2=m_{17}\left(m_w^2\right) && J_3=m_1\left(s\right)\\
&J_4=\left(I_{13}\right)^2 && J_5=m_5\left(s\right) && J_6=m_{12}\left(s\right)\\
&J_7=I_4I_{13} && J_8=m_{18}\left(s,m_z^2\right) && J_9=m_{19}\left(s,m_z^2\right)\\
&J_{10}=m_{28}\left(s,m_z^2\right) && J_{11}=m_{31}\left(s,m_z^2\right) && J_{12}=m_{32}\left(s,m_z^2\right)\\
&J_{13}=I_{13}I_{14} && J_{14}=m_{37}\left(s,m_z^2\right) && J_{15}=m_{39}\left(s,m_z^2\right)\\
&J_{16}=m_{42}\left(s,m_z^2\right) && J_{17}=m_{43}\left(s,m_z^2\right) && J_{18}=m_{44}\left(s,m_z^2\right)\\
&J_{19}=m_{56}\left(s,m_z^2\right) && J_{20}=m_{57}\left(s,m_z^2\right) && J_{21}=m_{58}\left(s,m_z^2\right)\\
&J_{22}=m_{15}\left(s,m_w^2\right) && J_{23}=m_{18}\left(s,m_w^2\right) && J_{24}=m_{19}\left(s,m_w^2\right)\\
&J_{25}=m_{28}\left(s,m_w^2\right) && J_{26}=m_{31}\left(s,m_w^2\right) && J_{27}=m_{32}\left(s,m_w^2\right)\\
&J_{28}=I_{13}I_{15} && J_{29}=m_{37}\left(s,m_w^2\right) && J_{30}=m_{39}\left(s,m_w^2\right)\\
&J_{31}=m_{42}\left(s,m_w^2\right) && J_{32}=m_{43}\left(s,m_w^2\right) && J_{33}=m_{44}\left(s,m_w^2\right)\\
&J_{34}=m_{56}\left(s,m_w^2\right) && J_{35}=m_{57}\left(s,m_w^2\right) && J_{36}=m_{58}\left(s,m_w^2\right)\\
&J_{37}=I_2I_{13} && J_{38}=\mathbf{m}_{10}\left(s,m_w^2\right) && J_{39}=\mathbf{m}_{11}\left(s,m_w^2\right)\\
&J_{40}=\mathbf{m}_{12}\left(s,m_w^2\right) && J_{41}=\mathbf{m}_{23}\left(s,m_w^2\right) && J_{42}=\mathbf{m}_{24}\left(s,m_w^2\right)\\
&J_{43}=\mathbf{m}_{25}\left(s,m_w^2\right) && J_{44}=m_2\left(t\right) && J_{45}=m_2\left(u\right)\\
&J_{46}=m_6\left(t\right) && J_{47}=m_6\left(u\right) && J_{48}=m_7\left(s,t\right)\\
&J_{49}=m_7\left(s,u\right) && J_{50}=m_8\left(s,t\right) && J_{51}=m_8\left(s,u\right)\\
&J_{52}=m_9\left(s,t\right) && J_{53}=m_9\left(s,u\right) && J_{54}=m_{10}\left(s,t\right)\\
&J_{55}=m_{10}\left(s,u\right) && J_{56}=m_{11}\left(s,t\right) && J_{57}=m_{11}\left(s,u\right)\\
&J_{58}=I_{13}I_{21} && J_{59}=m_{25}\left(s,m_z^2\right) && J_{60}=m_{26}\left(s,m_z^2\right)\\
&J_{61}=m_{27}\left(t,m_z^2\right) && J_{62}=m_{37}\left(t,m_z^2\right) && J_{63}=m_{38}\left(t,m_z^2\right)\\
&J_{64}=m_{40}\left(s,m_z^2\right) && J_{65}=m_{45}\left(s,t,m_z^2\right) && J_{66}=m_{46}\left(s,t,m_z^2\right)\\
&J_{67}=m_{47}\left(s,t,m_z^2\right) && J_{68}=m_{48}\left(s,t,m_z^2\right) && J_{69}=m_{49}\left(s,t,m_z^2\right)\\
&J_{70}=m_{50}\left(s,t,m_z^2\right) && J_{71}=m_{51}\left(s,t,m_z^2\right) && J_{72}=m_{52}\left(s,t,m_z^2\right)
\end{aligned}$$

$$
\begin{aligned}
J_{73} &= m_{53}\left(s,t,m_z^2\right) & J_{74} &= m_{54}\left(s,t,m_z^2\right) & J_{75} &= m_{55}\left(s,t,m_z^2\right)\\
J_{76} &= m_{27}\left(u,m_z^2\right) & J_{77} &= m_{37}\left(u,m_z^2\right) & J_{78} &= m_{38}\left(u,m_z^2\right)\\
J_{79} &= m_{45}\left(s,u,m_z^2\right) & J_{80} &= m_{46}\left(s,u,m_z^2\right) & J_{81} &= m_{47}\left(s,u,m_z^2\right)\\
J_{82} &= m_{48}\left(s,u,m_z^2\right) & J_{83} &= m_{49}\left(s,u,m_z^2\right) & J_{84} &= m_{50}\left(s,u,m_z^2\right)\\
J_{85} &= m_{51}\left(s,u,m_z^2\right) & J_{86} &= m_{52}\left(s,u,m_z^2\right) & J_{87} &= m_{53}\left(s,u,m_z^2\right)\\
J_{88} &= m_{54}\left(s,u,m_z^2\right) & J_{89} &= m_{55}\left(s,u,m_z^2\right) & J_{90} &= I_{13}I_{26}\\
J_{91} &= \mathbf{m}_{10}\left(s,m_z^2\right) & J_{92} &= \mathbf{m}_{11}\left(s,m_z^2\right) & J_{93} &= \mathbf{m}_{12}\left(s,m_z^2\right)\\
J_{94} &= \mathbf{m}_{23}\left(s,m_z^2\right) & J_{95} &= \mathbf{m}_{24}\left(s,m_z^2\right) & J_{96} &= \mathbf{m}_{25}\left(s,m_z^2\right)\\
J_{97} &= I_{13}I_{27} & J_{98} &= \mathbf{m}_{26}\left(s,t,m_z^2\right) & J_{99} &= \mathbf{m}_{27}\left(s,t,m_z^2\right)\\
J_{100} &= \mathbf{m}_{30}\left(s,m_z^2\right) & J_{101} &= \mathbf{m}_{31}\left(s,t,m_z^2\right) & J_{102} &= \mathbf{m}_{32}\left(s,t,m_z^2\right)\\
J_{103} &= \mathbf{m}_{33}\left(s,t,m_z^2\right) & J_{104} &= \mathbf{m}_{34}\left(s,t,m_z^2\right) & J_{105} &= \mathbf{m}_{35}\left(s,t,m_z^2\right)\\
J_{106} &= \mathbf{m}_{36}\left(s,t,m_z^2\right) & J_{107} &= \mathbf{m}_{26}\left(s,u,m_z^2\right) & J_{108} &= \mathbf{m}_{27}\left(s,u,m_z^2\right)\\
J_{109} &= \mathbf{m}_{31}\left(s,u,m_z^2\right) & J_{110} &= \mathbf{m}_{32}\left(s,u,m_z^2\right) & J_{111} &= \mathbf{m}_{33}\left(s,u,m_z^2\right)\\
J_{112} &= \mathbf{m}_{34}\left(s,u,m_z^2\right) & J_{113} &= \mathbf{m}_{35}\left(s,u,m_z^2\right) & J_{114} &= \mathbf{m}_{36}\left(s,u,m_z^2\right)\\
J_{115} &= m_{27}\left(u,m_w^2\right) & J_{116} &= m_{37}\left(u,m_w^2\right) & J_{117} &= m_{38}\left(u,m_w^2\right)\\
J_{118} &= m_{46}\left(s,u,m_w^2\right) & J_{119} &= m_{47}\left(s,u,m_w^2\right) & J_{120} &= m_{48}\left(s,u,m_w^2\right)\\
J_{121} &= m_{49}\left(s,u,m_w^2\right) & J_{122} &= m_{52}\left(s,u,m_w^2\right) & J_{123} &= m_{53}\left(s,u,m_w^2\right)\\
J_{124} &= I_{13}I_{16} & J_{125} &= \mathbf{m}_{26}\left(s,u,m_w^2\right) & J_{126} &= \mathbf{m}_{27}\left(s,u,m_w^2\right)\\
J_{127} &= \mathbf{m}_{30}\left(s,m_w^2\right) & J_{128} &= \mathbf{m}_{31}\left(s,u,m_w^2\right) & J_{129} &= \mathbf{m}_{32}\left(s,u,m_w^2\right)\\
J_{130} &= \mathbf{m}_{33}\left(s,u,m_w^2\right) & J_{131} &= \mathbf{m}_{34}\left(s,u,m_w^2\right) & J_{132} &= \mathbf{m}_{35}\left(s,u,m_w^2\right)\\
J_{133} &= \mathbf{m}_{36}\left(s,u,m_w^2\right). & & & & \qquad (8.91)
\end{aligned}
$$

In writing the above definitions, we have made all dependence on the kinematic variables s, t, $u = -s - t$, m_w^2, m_z^2, and m_h^2 explicit on the right-hand side for all functions not expressed as a simple product of the one-loop integrals from Section 8.4.2. Note that, out of 124 non-factorizable integrals, only 57 need to be evaluated since the rest may subsequently be accessed by considering simple permutations of the kinematic invariants.

8.6 Calculation of the unpolarized amplitude in Kreimer's γ_5 scheme

In this section, we present details on the calculation of the unpolarized amplitude. To be more specific, we calculate the unpolarized interference between one- and two-loop diagrams with the tree-level. This calculation served as an independent cross-check for the calculation of all helicity amplitudes carried out in Ref. [85], in which we decomposed the Drell-Yan scattering amplitude in terms of the Lorentz tensors introduced in Section 8.2. For the comparison, we use the decomposition in Kreimer's

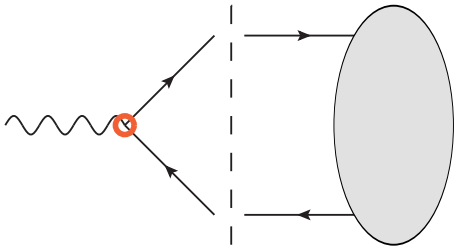

FIGURE 8.6.1: Reading point prescription used in the calculation of the unpolarized amplitude. For all contributions we start reading the trace at the tree level vertex, denoted by the red circle in the figure.

γ_5 scheme. Thus, the amplitude is decomposed as

$$i\bar{\mathcal{A}}_{\rm DY} = i\left(\bar{\mathbf{C}}_{\rm VV}\bar{\mathcal{T}}_{\rm VV} + \bar{\mathbf{C}}_{\rm AA}\bar{\mathcal{T}}_{\rm AA} + \bar{\mathbf{C}}_{\rm VA}\bar{\mathcal{T}}_{\rm VA} + \bar{\mathbf{C}}_{\rm AV}\bar{\mathcal{T}}_{\rm AV} + \ldots\right), \tag{8.92}$$

where the dots denote the additional Lorentz structures, which can be ignored after taking the interference with the tree level, and the Lorentz structures of relevance are defined in (8.23)-(8.26). In order to compare these results with the independent calculation of the unpolarized amplitude, we have to sum over all initial and final state spins. Note that the tree level decomposition is given by just four structures (this is also true in d dimensions):

$$\bar{\mathcal{A}}^{(0,0)}_{\rm DY} = 4\pi\alpha_{\rm em}\left\{\left(\frac{Q_q Q_\ell}{s} + \frac{v_q v_\ell}{s-m_z^2}\right)\bar{\mathcal{T}}_{\rm VV} - \frac{a_\ell v_q}{s-m_z^2}\bar{\mathcal{T}}_{\rm VA} - \frac{a_q v_\ell}{s-m_z^2}\bar{\mathcal{T}}_{\rm AV} + \frac{a_q a_\ell}{s-m_z^2}\bar{\mathcal{T}}_{\rm AA}\right\}. \tag{8.93}$$

Thus, the unpolarized amplitude in terms of the Lorentz structures from Ref. [85] in Kreimer's scheme, is given by

$$\begin{aligned}
&\sum_{\rm spin,color} \bar{\mathcal{A}}^{(0,0)}_{\rm DY}\bar{\mathcal{A}}_{\rm DY} \\
&= \alpha_{\rm em}\pi\left\{\left(-\frac{2}{3s} + \frac{v_q v_l}{s-m_z^2}\right)\left[8\left(s^2(1-\epsilon) + 2t(s+t)\right)\bar{\mathbf{C}}_{\rm VV} + 8s(s+2t)\bar{\mathbf{C}}_{\rm AA}\right]\right. \\
&\quad + \frac{v_q a_l}{s-m_z^2}\left[8\left(s^2(1-\epsilon) + 2t(s+t)\right)\bar{\mathbf{C}}_{\rm VA} + 8s(s+2t)\bar{\mathbf{C}}_{\rm AV}\right] \\
&\quad + \frac{a_q v_l}{s-m_z^2}\left[8s(s+2t)\bar{\mathbf{C}}_{\rm VA} + 8\left(s^2(1-\epsilon) + 2t(s+t)\right)\bar{\mathbf{C}}_{\rm AV}\right] \\
&\quad \left. + \frac{a_q a_l}{s-m_z^2}\left[8s(s+2t)\bar{\mathbf{C}}_{\rm VV} + 8\left(s^2(1-\epsilon) + 2t(s+t)\right)\bar{\mathbf{C}}_{\rm AA}\right]\right\}.
\end{aligned} \tag{8.94}$$

For the independent calculation of the unpolarized amplitude, we used the setup described in Chapter 3. For the two-loop corrections, we generate in total 751 diagrams in `QGRAF` and use `Form` to take traces (in d dimensions) over the lepton and quark lines for the interference terms.

Since we use Kreimer's scheme to treat γ_5, we have to define a reading point prescription. In our setup, we choose a fixed reading point prescription, in which we always start reading traces at the tree-level vertex, as depicted in Fig. 8.6.1, in which the reading point is marked with a red circle. To get consistent results, one has to make sure that for all contributions (denoted by the blob in Fig. 8.6.1) all traces are treated in the same way. Using this fixed reading point corresponds to the same prescription we used in Ref. [85], in which we begin reading the trace always at

the projector insertion. This makes a comparison with that calculation easy. Other choices, like a symmetric reading point prescription in which one reads the trace starting from all γ_5 insertions and averages over all possibilities, are also possible.

Since in Kreimer's scheme traces over γ_5 evaluate to four-dimensional Levi-Civita tensors, which are then contracted with d-dimensional loop momenta, we employ a PV tensor decomposition, such that the contraction can be performed with the external momenta. Although we performed the calculation in Feynman gauge, we implement the PV reduction for two-loop integrals up to rank 10, which would be needed for a calculation in general R_ξ gauge. The calculation of these reduction identities was very cumbersome and relied heavily on finite field methods [93, 94] for the involved linear algebra.

We compared our final result of the unpolarized amplitude to the one, that was obtained using the helicity amplitudes as given in Eq. (8.94). We compared all coefficients of all master integrals in the bare amplitude and find full agreement analytically in d dimensions. Restricting to the mixed two-loop QED-QCD corrections, we were also able to reproduce the results from Ref. [76] in which the unpolarized amplitude for this subset of corrections has been considered.

Although we only considered the unpolarized amplitude in this setup, let us stress that using a PV reduction one could easily also extract helicity amplitudes. It is worth noting that in this setup complications of traces with γ_5 can be avoided: using a PV reduction one never needs to take traces over Dirac matrices. Instead, one extracts all Lorentz structures as defined in Eqs. (8.17)-(8.22) in d dimensions by using only anti-commutator relations between γ matrices and the Dirac equation only. In that way, one can in principle also calculate helicity amplitudes using, for instance, just an anti-commuting γ_5 (called naive γ_5 scheme in the literature). Since the PV reduction only depends on the external kinematics, our setup might also be useful for future calculations of other massless two-to-two processes.

8.7 Infrared dipole singularity structure and subtraction functions

Having obtained the renormalized, UV finite amplitude, we now proceed to define the finite hard scattering function by subtracting all IR divergences. Those can be predicted for a general scattering amplitude in two-loop QCD in a process independent way [210–215]. The dipole formula [216–222] provides a particularly concise and straightforward recipe for the generation of IR subtraction terms at two loops.[3] While, historically, the singularity structures of scattering amplitudes in particularly simple models such as massless QED, massless QCD, and $\mathcal{N} = 4$ super Yang-Mills theory were discussed most frequently in the literature, broader applications to theories with massive particles or mixed gauge groups are certainly possible and have long been known, see *e.g.* [76, 233]. In particular, it was shown in [76] that with straightforward modifications, the dipole formula can be extended to describe the singularity structure of two-loop mixed QED-QCD Drell-Yan scattering amplitudes. This setup covers also the case of the mixed EW-QCD corrections discussed here.

We begin by introducing the building blocks required to describe the IR singularities of the order $\alpha_{\text{em}}\alpha_{\text{s}}$, order α_{em}^2, and order $\alpha_{\text{em}}^2\alpha_{\text{s}}$ neutral-current Drell-Yan scattering amplitudes. As has long been clear, the leading IR singularities of gauge theory scattering amplitudes are governed by cusp anomalous dimensions [234]. For

[3] At three loops and beyond, an extension of the formalism is necessary [223–232].

the one-loop quark cusp anomalous dimension in QCD, one has

$$\Gamma_q^{(0,1)} = 4\,C_F\,, \tag{8.95}$$

whereas in QED the result can be obtained from Eq. (8.95) by replacing the quadratic Casimir invariant C_F with the squared charge of the fermion flavor,

$$\Gamma_f^{(1,0)} = 4\,Q_f^2\,. \tag{8.96}$$

However, as pointed out in [76], the mixed quark cusp anomalous dimension vanishes:

$$\Gamma_q^{(1,1)} = 0\,. \tag{8.97}$$

The next-to-leading IR singularities are more complicated and receive contributions from both soft anomalous dimensions and resummation functions derived from the ϵ^{-1} poles of massless vertex form factors with an appropriate number of gluon and/or photon exchanges. The one-loop Drell-Yan soft anomalous dimensions are well-known and have been calculated in many places in the literature, see *e.g.* [217, 218] for a thorough discussion. Note that, for general QCD scattering processes, the soft anomalous dimension becomes a mixing matrix in color space. For processes with just two partons in the initial state such as the Drell-Yan process, the color space structure trivializes and all matrices in the dipole formula may be replaced with functions. Rewriting the results to make all imaginary parts explicit in the physical kinematic region of interest, we find

$$S_{\rm DY}^{(0,1)} = \left(-4\ln\left(\frac{\mu^2}{s}\right) - 4i\pi\right) C_F \tag{8.98}$$

and

$$S_{\rm DY}^{(1,0)} = \left(-4\ln\left(\frac{\mu^2}{s}\right) - 4i\pi\right)\left(Q_\ell^2 + Q_q^2\right) + 8Q_\ell Q_q \ln\left(\frac{t}{u}\right). \tag{8.99}$$

Once again, as shown in [76], the two-loop mixed EW-QCD Drell-Yan soft anomalous dimension vanishes identically:

$$S_{\rm DY}^{(1,1)} = 0\,. \tag{8.100}$$

We define our massless QCD resummation functions in the framework of [235]. In practice, following [76], all results may be derived from the one- and two-loop quark resummation functions of massless QCD by making simple replacements. In what follows, $f[k]$ denotes the coefficient of ϵ^k in the Taylor series expansion of $f(\epsilon)$,

$$f(\epsilon) = \sum_{k=0}^{\infty} f[k]\epsilon^k\,. \tag{8.101}$$

To the relevant ϵ orders, we have

$$G_q^{(0,1)}[0] = 6\,C_F\,, \tag{8.102}$$

$$G_q^{(0,1)}[1] = \left(16 - 2\zeta_2\right) C_F\,, \tag{8.103}$$

$$G_q^{(0,1)}[2] = \left(32 - 3\zeta_2 - \frac{28}{3}\zeta_3\right) C_F\,, \tag{8.104}$$

$$G_q^{(0,1)}[3] = \left(64 - 8\zeta_2 - 14\zeta_3 - \frac{47}{10}\zeta_2^2\right) C_F\,, \tag{8.105}$$

$$G_q^{(0,2)}[0] = \left(3 - 24\zeta_2 + 48\zeta_3\right) C_F^2 + \left(\frac{2545}{27} + \frac{44}{3}\zeta_2 - 52\zeta_3\right) C_A C_F \,, \tag{8.106}$$

and

$$G_q^{(0,2)}[1] = \left(\frac{1}{2} - 116\zeta_2 + 120\zeta_3 + \frac{176}{5}\zeta_2^2\right) C_F^2 + \left(\frac{70165}{162} + \frac{575}{9}\zeta_2 - \frac{520}{3}\zeta_3 - \frac{176}{5}\zeta_2^2\right) C_A C_F \tag{8.107}$$

from Eqs. (3.10) and (3.11) of [235] after discarding all contributions proportional to the number of light quarks.

As with the cusp anomalous dimensions, the one-loop QED results may be obtained by making the replacement $C_F \to Q_f^2$ in Eqs. (8.102)-(8.105). Explicitly, we have

$$G_f^{(1,0)}[0] = 6\, Q_f^2 \,, \tag{8.108}$$

$$G_f^{(1,0)}[1] = \left(16 - 2\zeta_2\right) Q_f^2 \,, \tag{8.109}$$

$$G_f^{(1,0)}[2] = \left(32 - 3\zeta_2 - \frac{28}{3}\zeta_3\right) Q_f^2 \,, \tag{8.110}$$

and

$$G_f^{(1,0)}[3] = \left(64 - 8\zeta_2 - 14\zeta_3 - \frac{47}{10}\zeta_2^2\right) Q_f^2 \,. \tag{8.111}$$

Finally, the two-loop mixed EW-QCD quark resummation functions are obtained from Eqs. (8.106) and (8.107) by setting C_A to zero and replacing C_F^2 with $Q_q^2 C_F$:

$$G_q^{(1,1)}[0] = \left(3 - 24\zeta_2 + 48\zeta_3\right) Q_q^2 C_F \tag{8.112}$$

and

$$G_q^{(1,1)}[1] = \left(\frac{1}{2} - 116\zeta_2 + 120\zeta_3 + \frac{176}{5}\zeta_2^2\right) Q_q^2 C_F \,. \tag{8.113}$$

Given the ingredients discussed above, we are now in a position to present the predictions of the generalized dipole formula for the ultraviolet-renormalized, infrared-divergent scattering amplitudes. We adopt the notation of our previous work, Ref. [85], in which we had to distinguish between the amplitudes calculated using Kreimer's γ_5 scheme and the HVBM scheme. Like before, we denote the amplitude in Kreimer's scheme with a bar in the following, $\bar{\mathcal{A}}_{\rm DY}$, while the amplitude in the HVBM scheme is denoted by $\mathcal{A}_{\rm DY}$. At tree level we have

$$\overset{\frown}{\mathcal{A}}_{\rm DY} = 4\pi\alpha_{\rm em}\overset{\frown}{\mathcal{H}}{}_{\rm DY}^{(0,0)}[0] + \cdots \,, \tag{8.114}$$

where the dots stand for terms of higher order in the coupling constants. As the notation suggests, the tree-level hard functions, $\mathcal{H}_{\rm DY}^{(0,0)}[0]$ and $\bar{\mathcal{H}}_{\rm DY}^{(0,0)}[0]$, are defined to be independent of the coupling constants. We have

$$\overset{\frown}{\mathcal{H}}{}_{\rm DY}^{(0,0)}[0] = \left(\frac{Q_q Q_\ell}{s} + \frac{v_q v_\ell}{s - m_z^2}\right)\overset{\frown}{\mathcal{T}}_{\rm VV} - \frac{a_\ell v_q}{s - m_z^2}\overset{\frown}{\mathcal{T}}_{\rm VA} - \frac{a_q v_\ell}{s - m_z^2}\overset{\frown}{\mathcal{T}}_{\rm AV} + \frac{a_q a_\ell}{s - m_z^2}\overset{\frown}{\mathcal{T}}_{\rm AA}. \tag{8.115}$$

As is clear from the form of Eqs. (8.115), the tree-level amplitudes in the two γ_5 schemes, trivially coincide in the four-dimensional limit, because all of the differences between the schemes disappear in four spacetime dimensions:

$$\lim_{\epsilon\to 0}\left\{\mathcal{H}_{\rm DY}^{(0,0)}[0]\right\} = \lim_{\epsilon\to 0}\left\{\bar{\mathcal{H}}_{\rm DY}^{(0,0)}[0]\right\} . \tag{8.116}$$

In the following, it will be convenient to view the hard scattering functions in the two schemes as vectors of coefficients with respect to $\overset{(\sim)}{\mathcal{T}}_{\rm VV}$, $\overset{(\sim)}{\mathcal{T}}_{\rm VA}$, $\overset{(\sim)}{\mathcal{T}}_{\rm AV}$, and $\overset{(\sim)}{\mathcal{T}}_{\rm AA}$. This minor abuse of notation will allow us to rewrite *e.g.* Eq. (8.116) as

$$\mathcal{H}^{(0,0)}_{\rm DY}[0] = \bar{\mathcal{H}}^{(0,0)}_{\rm DY}[0]\,. \tag{8.117}$$

At higher perturbative orders, we have

$$\overset{(\sim)}{\mathcal{A}}_{\rm DY} = 4\pi\alpha_{\rm em}\left(\overset{(\sim)}{\mathcal{A}}^{(0,0)}_{\rm DY} + \overset{(\sim)}{\mathcal{A}}^{(0,1)}_{\rm DY}\left(\frac{\alpha_{\rm s}}{4\pi}\right) + \overset{(\sim)}{\mathcal{A}}^{(1,0)}_{\rm DY}\left(\frac{\alpha_{\rm em}}{4\pi}\right) + \overset{(\sim)}{\mathcal{A}}^{(1,1)}_{\rm DY}\left(\frac{\alpha_{\rm em}}{4\pi}\right)\left(\frac{\alpha_{\rm s}}{4\pi}\right) + \cdots\right), \tag{8.118}$$

where

$$\overset{(\sim)}{\mathcal{A}}^{(0,0)}_{\rm DY} = \overset{(\sim)}{\mathcal{H}}^{(0,0)}_{\rm DY}\,, \tag{8.119}$$

$$\begin{aligned}\overset{(\sim)}{\mathcal{A}}^{(0,1)}_{\rm DY} = {}& \frac{1}{\epsilon^2}\left(-\frac{1}{2}\Gamma^{(0,1)}_q\overset{(\sim)}{\mathcal{H}}^{(0,0)}_{\rm DY}[0]\right) + \frac{1}{\epsilon}\left(\frac{1}{2}\left[S^{(0,1)}_{\rm DY} - G^{(0,1)}_q[0]\right]\overset{(\sim)}{\mathcal{H}}^{(0,0)}_{\rm DY}[0]\right)\\ & - \frac{1}{2}G^{(0,1)}_q[1]\overset{(\sim)}{\mathcal{H}}^{(0,0)}_{\rm DY}[0] + \overset{(\sim)}{\mathcal{H}}^{(0,1)}_{\rm DY}[0] + \epsilon\left(-\frac{1}{2}G^{(0,1)}_q[2]\overset{(\sim)}{\mathcal{H}}^{(0,0)}_{\rm DY}[0] + \overset{(\sim)}{\mathcal{H}}^{(0,1)}_{\rm DY}[1]\right)\\ & + \epsilon^2\left(-\frac{1}{2}G^{(0,1)}_q[3]\overset{(\sim)}{\mathcal{H}}^{(0,0)}_{\rm DY}[0] + \overset{(\sim)}{\mathcal{H}}^{(0,1)}_{\rm DY}[2]\right) + \cdots\,,\end{aligned} \tag{8.120}$$

$$\begin{aligned}\overset{(\sim)}{\mathcal{A}}^{(1,0)}_{\rm DY} = {}& \frac{1}{\epsilon^2}\left(-\frac{1}{2}\left[\Gamma^{(1,0)}_\ell + \Gamma^{(1,0)}_q\right]\overset{(\sim)}{\mathcal{H}}^{(0,0)}_{\rm DY}[0]\right) + \frac{1}{\epsilon}\left(\frac{1}{2}\left[S^{(1,0)}_{\rm DY} - G^{(1,0)}_\ell[0] - G^{(1,0)}_q[0]\right]\overset{(\sim)}{\mathcal{H}}^{(0,0)}_{\rm DY}[0]\right)\\ & - \frac{1}{2}\left[G^{(1,0)}_\ell[1] + G^{(1,0)}_q[1]\right]\overset{(\sim)}{\mathcal{H}}^{(0,0)}_{\rm DY}[0] + \overset{(\sim)}{\mathcal{H}}^{(1,0)}_{\rm DY}[0] + \epsilon\left(-\frac{1}{2}\left[G^{(1,0)}_\ell[2] + G^{(1,0)}_q[2]\right]\overset{(\sim)}{\mathcal{H}}^{(0,0)}_{\rm DY}[0]\right.\\ & \left. + \overset{(\sim)}{\mathcal{H}}^{(1,0)}_{\rm DY}[1]\right) + \epsilon^2\left(-\frac{1}{2}\left[G^{(1,0)}_\ell[3] + G^{(1,0)}_q[3]\right]\overset{(\sim)}{\mathcal{H}}^{(0,0)}_{\rm DY}[0] + \overset{(\sim)}{\mathcal{H}}^{(1,0)}_{\rm DY}[2]\right) + \cdots\,,\end{aligned} \tag{8.121}$$

and

$$\begin{aligned}\overset{(\sim)}{\mathcal{A}}^{(1,1)}_{\rm DY} = {}& \frac{1}{\epsilon^4}\left(\frac{1}{4}\Gamma^{(0,1)}_q\left[\Gamma^{(1,0)}_\ell + \Gamma^{(1,0)}_q\right]\overset{(\sim)}{\mathcal{H}}^{(0,0)}_{\rm DY}[0]\right) + \frac{1}{\epsilon^3}\left(-\frac{1}{4}\left(\Gamma^{(0,1)}_q\left[S^{(1,0)}_{\rm DY} - G^{(1,0)}_\ell[0]\right.\right.\right.\\ & \left.\left.\left. - G^{(1,0)}_q[0]\right] + \left[\Gamma^{(1,0)}_\ell + \Gamma^{(1,0)}_q\right]\left[S^{(0,1)}_{\rm DY} - G^{(0,1)}_q[0]\right]\right)\overset{(\sim)}{\mathcal{H}}^{(0,0)}_{\rm DY}[0]\right) + \frac{1}{\epsilon^2}\left(\frac{1}{4}\left(\Gamma^{(0,1)}_q\left[G^{(1,0)}_\ell[1]\right.\right.\right.\\ & \left.\left.\left. + G^{(1,0)}_q[1]\right] + \left[\Gamma^{(1,0)}_\ell + \Gamma^{(1,0)}_q\right]G^{(0,1)}_q[1] + \left[S^{(0,1)}_{\rm DY} - G^{(0,1)}_q[0]\right]\left[S^{(1,0)}_{\rm DY} - G^{(1,0)}_\ell[0]\right.\right.\right.\\ & \left.\left.\left. - G^{(1,0)}_q[0]\right]\right)\overset{(\sim)}{\mathcal{H}}^{(0,0)}_{\rm DY}[0] - \frac{1}{2}\Gamma^{(0,1)}_q\overset{(\sim)}{\mathcal{H}}^{(1,0)}_{\rm DY}[0] - \frac{1}{2}\left[\Gamma^{(1,0)}_\ell + \Gamma^{(1,0)}_q\right]\overset{(\sim)}{\mathcal{H}}^{(0,1)}_{\rm DY}[0]\right)\\ & + \frac{1}{\epsilon}\left(\frac{1}{4}\left(\Gamma^{(0,1)}_q\left[G^{(1,0)}_\ell[2] + G^{(1,0)}_q[2]\right] + \left[\Gamma^{(1,0)}_\ell + \Gamma^{(1,0)}_q\right]G^{(0,1)}_q[2]\right.\right.\\ & \left.\left. - G^{(0,1)}_q[1]\left[S^{(1,0)}_{\rm DY} - G^{(1,0)}_\ell[0] - G^{(1,0)}_q[0]\right] - \left[G^{(1,0)}_\ell[1] + G^{(1,0)}_q[1]\right]\left[S^{(0,1)}_{\rm DY} - G^{(0,1)}_q[0]\right]\right.\right.\\ & \left.\left. - 2G^{(1,1)}_q[0]\right)\overset{(\sim)}{\mathcal{H}}^{(0,0)}_{\rm DY}[0] - \frac{1}{2}\Gamma^{(0,1)}_q\overset{(\sim)}{\mathcal{H}}^{(1,0)}_{\rm DY}[1] - \frac{1}{2}\left[\Gamma^{(1,0)}_\ell + \Gamma^{(1,0)}_q\right]\overset{(\sim)}{\mathcal{H}}^{(0,1)}_{\rm DY}[1]\right.\\ & \left. + \frac{1}{2}\left[S^{(1,0)}_{\rm DY} - G^{(1,0)}_\ell[0] - G^{(1,0)}_q[0]\right]\overset{(\sim)}{\mathcal{H}}^{(0,1)}_{\rm DY}[0] + \frac{1}{2}\left[S^{(0,1)}_{\rm DY} - G^{(0,1)}_q[0]\right]\overset{(\sim)}{\mathcal{H}}^{(1,0)}_{\rm DY}[0]\right)\end{aligned}$$

$$
\begin{aligned}
&+\frac{1}{4}\Bigg(\Gamma_q^{(0,1)}\left[G_\ell^{(1,0)}[3]+G_q^{(1,0)}[3]\right]+\left[\Gamma_\ell^{(1,0)}+\Gamma_q^{(1,0)}\right]G_q^{(0,1)}[3]\\
&-G_q^{(0,1)}[2]\left[S_{\rm DY}^{(1,0)}-G_\ell^{(1,0)}[0]-G_q^{(1,0)}[0]\right]-\left[G_\ell^{(1,0)}[2]+G_q^{(1,0)}[2]\right]\left[S_{\rm DY}^{(0,1)}-G_q^{(0,1)}[0]\right]\\
&+G_q^{(0,1)}[1]\left[G_\ell^{(1,0)}[1]+G_q^{(1,0)}[1]\right]-2G_q^{(1,0)}[1]\Bigg)\overset{\frown}{\mathcal{H}}{}_{\rm DY}^{(0,0)}[0]-\frac{1}{2}G_q^{(0,1)}[1]\overset{\frown}{\mathcal{H}}{}_{\rm DY}^{(1,0)}[0]\\
&-\frac{1}{2}\left[G_\ell^{(1,0)}[1]+G_q^{(1,0)}[1]\right]\overset{\frown}{\mathcal{H}}{}_{\rm DY}^{(0,1)}[0]+\frac{1}{2}\left[S_{\rm DY}^{(0,1)}-G_q^{(0,1)}[0]\right]\overset{\frown}{\mathcal{H}}{}_{\rm DY}^{(1,0)}[1]\\
&+\frac{1}{2}\left[S_{\rm DY}^{(1,0)}-G_\ell^{(1,0)}[0]-G_q^{(1,0)}[0]\right]\overset{\frown}{\mathcal{H}}{}_{\rm DY}^{(0,1)}[1]-\frac{1}{2}\Gamma_q^{(0,1)}\overset{\frown}{\mathcal{H}}{}_{\rm DY}^{(1,0)}[2]\\
&-\frac{1}{2}\left[\Gamma_\ell^{(1,0)}+\Gamma_q^{(1,0)}\right]\overset{\frown}{\mathcal{H}}{}_{\rm DY}^{(0,1)}[2]+\overset{\frown}{\mathcal{H}}{}_{\rm DY}^{(1,1)}[0]+\cdots\,. \qquad (8.122)
\end{aligned}
$$

The one- and two-loop hard scattering functions which appear above are determined by demanding equality between Eqs. (8.118) and the corresponding explicit calculations at one and two loops.

All other things being equal, it is generally believed that HVBM's γ_5 scheme and Kreimer's γ_5 scheme produce identical results through to one loop and $\mathcal{O}\left(\epsilon^0\right)$ [199]. At order $\alpha_{\rm em}^2$, our explicit one-loop calculations do indeed show that

$$\mathcal{H}_{\rm DY}^{(1,0)}[0]=\bar{\mathcal{H}}_{\rm DY}^{(1,0)}[0]\,. \qquad (8.123)$$

However, in Ref. [85] we also find that

$$\mathcal{H}_{\rm DY}^{(1,0)}[k]\neq\bar{\mathcal{H}}_{\rm DY}^{(1,0)}[k] \qquad \text{for } k>0\,. \qquad (8.124)$$

Thus, in light of the fact that the higher-order-in-ϵ one-loop hard functions first enter Eqs. (8.118) at the level of the ϵ^{-1} poles of the relative order $\alpha_{\rm em}\alpha_{\rm s}$ expressions, it is not obvious that an analog of Eq. (8.123) continues to hold at higher orders in perturbation theory:

$$\mathcal{H}_{\rm DY}^{(1,1)}[0]\overset{?}{=}\bar{\mathcal{H}}_{\rm DY}^{(1,1)}[0]\,. \qquad (8.125)$$

While it is generally expected that all terms of virtual and real radiative corrections sensitive to ambiguities in the treatment of γ_5 eventually cancel out of combinations, that furnish complete fixed-order perturbative corrections to physical observables, hard partonic scattering functions by themselves are not physical observables. However, as a result from our explicit calculation in Ref. [85] in both γ_5 schemes, we found that (8.125) actually *is* an equality.

8.8 Numerical results

8.8.1 Helicity amplitudes

In this section, we show some numerical results for the helicity amplitudes that we obtained in Ref. [85]. To calculate helicity amplitudes we first derive the four-dimensional spinor in the chiral representation. Due to the form of the massless fermion propagator and how the electroweak gauge bosons couple to matter, the helicity quantum number is conserved along the initial and final fermion lines (see *e.g.* [236] for a review). This implies that there are just four non-vanishing helicity amplitudes, those where both the quark and the antiquark have opposite helicity and the lepton and antilepton have opposite helicity. We parametrize the center-of-momentum frame according to

$$p_1=\frac{\sqrt{s}}{2}(1,0,0,1), \qquad p_3=\frac{\sqrt{s}}{2}(1,\sin\theta,0,\cos\theta),$$

$$p_2 = \frac{\sqrt{s}}{2}(1,0,0,-1), \qquad p_4 = \frac{\sqrt{s}}{2}(1,-\sin\theta,0,-\cos\theta), \tag{8.126}$$

with

$$-\frac{t}{s} = \frac{1-\cos\theta}{2}, \tag{8.127}$$

and use an explicit basis of spinor states in the chiral representation [237]

$$\begin{aligned}
u_+(p_1) &= s^{1/4}(0,0,1,0), & u_+(p_3) &= s^{-1/4}(0,0,\sqrt{-u},\sqrt{-t}),\\
u_-(p_1) &= s^{1/4}(0,1,0,0), & u_-(p_3) &= s^{-1/4}(-\sqrt{-t},\sqrt{-u},0,0),\\
v_+(p_2) &= s^{1/4}(-1,0,0,0), & v_+(p_4) &= s^{-1/4}(-\sqrt{-u},-\sqrt{-t},0,0),\\
v_-(p_2) &= s^{1/4}(0,0,0,1), \quad \text{and} & v_-(p_4) &= s^{-1/4}(0,0,-\sqrt{-t},\sqrt{-u}).
\end{aligned} \tag{8.128}$$

Plugging these representations[4] into our Lorentz structures directly gives us results for the helicity amplitudes. Decomposing the hard functions (or finite remainders) according to

$$\overset{(\frown)}{\mathcal{H}}{}^{(m,n)}_{\rm DY}[0] = \overset{(\frown)}{\mathbf{C}}{}^{(m,n),\,\rm fin}_{\rm VV}\,\overset{(\frown)}{\mathcal{T}}_{\rm VV} + \overset{(\frown)}{\mathbf{C}}{}^{(m,n),\,\rm fin}_{\rm AA}\,\overset{(\frown)}{\mathcal{T}}_{\rm AA} + \overset{(\frown)}{\mathbf{C}}{}^{(m,n),\,\rm fin}_{\rm VA}\,\overset{(\frown)}{\mathcal{T}}_{\rm VA} + \overset{(\frown)}{\mathbf{C}}{}^{(m,n),\,\rm fin}_{\rm AV}\,\overset{(\frown)}{\mathcal{T}}_{\rm AV}\,, \tag{8.129}$$

we obtain for the polarized hard scattering functions $\mathcal{H}^{(m,n)}_{\lambda_1\lambda_2\lambda_3\lambda_4}$:

$$\mathcal{H}^{(m,n)}_{+-+-} = -2(s+t)\left(\mathbf{C}^{(m,n),\,\rm fin}_{\rm VV} + \mathbf{C}^{(m,n),\,\rm fin}_{\rm AA} + \mathbf{C}^{(m,n),\,\rm fin}_{\rm VA} + \mathbf{C}^{(m,n),\,\rm fin}_{\rm AV}\right), \tag{8.130}$$

$$\mathcal{H}^{(m,n)}_{-+-+} = -2(s+t)\left(\mathbf{C}^{(m,n),\,\rm fin}_{\rm VV} + \mathbf{C}^{(m,n),\,\rm fin}_{\rm AA} - \mathbf{C}^{(m,n),\,\rm fin}_{\rm VA} - \mathbf{C}^{(m,n),\,\rm fin}_{\rm AV}\right), \tag{8.131}$$

$$\mathcal{H}^{(m,n)}_{+--+} = -2t\left(\mathbf{C}^{(m,n),\,\rm fin}_{\rm VV} - \mathbf{C}^{(m,n),\,\rm fin}_{\rm AA} - \mathbf{C}^{(m,n),\,\rm fin}_{\rm VA} + \mathbf{C}^{(m,n),\,\rm fin}_{\rm AV}\right), \tag{8.132}$$

and

$$\mathcal{H}^{(m,n)}_{-++-} = -2t\left(\mathbf{C}^{(m,n),\,\rm fin}_{\rm VV} - \mathbf{C}^{(m,n),\,\rm fin}_{\rm AA} + \mathbf{C}^{(m,n),\,\rm fin}_{\rm VA} - \mathbf{C}^{(m,n),\,\rm fin}_{\rm AV}\right). \tag{8.133}$$

for coupling orders m and n. In Eqs. (8.130) - (8.133), due to the observed γ_5 scheme-independence of the hard scattering functions at zeroth order in the ϵ expansion (see Section 8.7), we drop the dual notation employed in Eq. (8.129).

8.8.2 Final results from Ref. [85]

In this section we present visualizations of the polarized hard scattering functions $\mathcal{H}^{(0,0)}_{\lambda_1\lambda_2\lambda_3\lambda_4}$, $\mathcal{H}^{(0,1)}_{\lambda_1\lambda_2\lambda_3\lambda_4}$, $\mathcal{H}^{(1,0)}_{\lambda_1\lambda_2\lambda_3\lambda_4}$, and $\mathcal{H}^{(1,1)}_{\lambda_1\lambda_2\lambda_3\lambda_4}$ defined in Section 8.8.1 for all four non-trivial helicity configurations which we obtained in Ref. [85]. In the numerical analysis, we set the gauge boson and Higgs masses to their on-shell values as listed in [168],

$$m_w = 80.379\ \text{GeV}, \qquad m_z = 91.1876\ \text{GeV}, \qquad m_h = 125.10\ \text{GeV}, \tag{8.134}$$

and the renormalization scale $\mu_R = \sqrt{s}$. Since we keep powers of $\alpha_{\rm em}$ and $\alpha_{\rm s}$ factored out of the expressions we plot, we do not need to specify their values here. For illustrative purposes, we found it sufficient to consider up-type quarks in the initial state. Our figures do look rather different for down-type quarks, but our impression

[4] The phase conventions of (8.128) above are in line with the spinor helicity formalism, as in [238] where $u_\pm(p_i) = v_\mp(p_i)$ for all i. Let us stress, however, that we do *not* adopt the all-outgoing convention for the external four-momenta. We made use of Eqs. (8.126) and (8.127) to derive Eqs. (8.128).

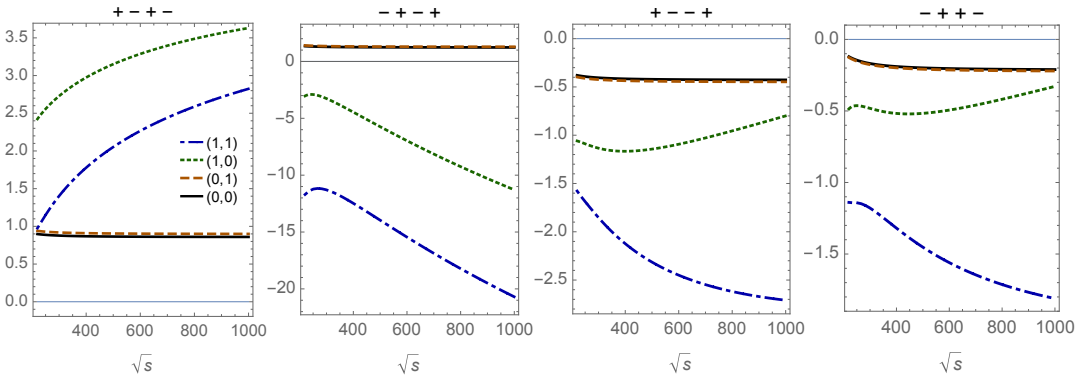

FIGURE 8.8.1: Helicity amplitudes for $u\bar{u} \to \ell^+\ell^-$ in dependence on the center-of-momentum energy for central scattering, $\cos\theta = 0$, and $\mu_R = \sqrt{s}$. The figure shows the real parts of the polarized hard scattering functions (finite remainders) $\mathrm{Re}\,\mathcal{H}^{(m,n)}_{\lambda_1\lambda_2\lambda_3\lambda_4}/(4\pi)^{m+n}$, see Eqs. (8.130)-(8.133), where the relative orders in the electroweak and strong couplings are denoted by (m, n).

is that, on the whole, they do not introduce completely new features which would be of paramount importance to discuss here. We elected to plot only the real parts of our final results, as the real parts of $\mathcal{H}^{(1,1)}_{\lambda_1\lambda_2\lambda_3\lambda_4}$ contain the most complicated weight four multiple polylogarithms appearing in our calculations.

In our numerical analysis, we focus on larger values of $\sqrt{s}$ where the previously unknown non-factorizable two-loop box-type Feynman diagrams of Section 8.5.1 are expected to be important. In order to compare the different orders in α_{em} and α_s, we find it convenient to include in our plots the 4π suppression factors taken out of each higher-order term in Eq. (8.118); that is, we consider $\mathcal{H}^{(m,n)}_{\lambda_1\lambda_2\lambda_3\lambda_4}/(4\pi)^{m+n}$, where the relative orders in the electroweak and strong couplings are given by (m, n) (see also Eq. (8.27)).

In all plots, we include the tree-level and relative order α_s results for reference, they show a rather simple behavior. The one-loop QCD corrections lie almost on top of the tree level results. Indeed, they fully factorize from the tree results; we have

$$\mathcal{H}^{(0,1)}_{\lambda_1\lambda_2\lambda_3\lambda_4}/(4\pi) = \left(\frac{\pi}{3} - i\right)\mathcal{H}^{(0,0)}_{\lambda_1\lambda_2\lambda_3\lambda_4} \tag{8.135}$$

for all helicity configurations and both up- and down-type quarks in the initial state. For the real part we see that $\pi/3 \approx 1.05$, thus explaining the observed similarity.

Figure 8.8.1 shows the dependence of the hard functions on the center-of-mass energy $\sqrt{s}$ for fixed central scattering angle. We observe that the absolute values of all plotted real parts of relative order $\alpha_{\mathrm{em}}\alpha_s$ increase as a function of $\sqrt{s}$, justifying the expectation that the calculation of the mixed two-loop EW-QCD corrections for the leptonic final state is well-motivated in the kinematic regime depicted in the figure. We note that the real parts of the one-loop EW and the two-loop EW-QCD corrections are not aligned for all helicity configurations.

Figure 8.8.2 shows the dependence of the hard functions on the cosine of the scattering angle for fixed center-of-mass energy $\sqrt{s}$. The electroweak corrections show a rather complex angular dependence. While the one-loop EW and the two-loop EW-QCD corrections show a similarity in their angular dependence, they differ in the details.

We also compared the curves of Figure 8.8.2 to analogous ones for the pure QED-QCD model studied in [76]. While maybe not instructive from the phenomenological

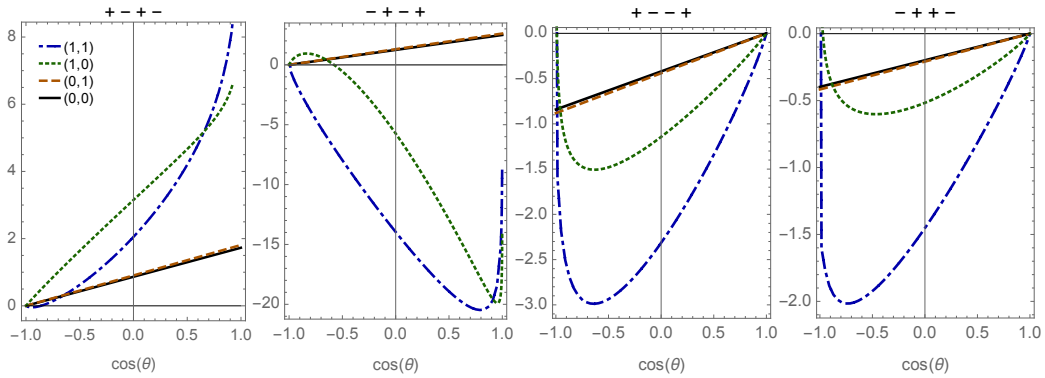

FIGURE 8.8.2: Helicity amplitudes for $u\bar{u} \to \ell^+\ell^-$ in dependence on the cosine of the scattering angle for $\sqrt{s} = 500$ GeV and $\mu_R = \sqrt{s}$. The figure shows the real parts of the polarized hard scattering functions (finite remainders) $\mathrm{Re}\,\mathcal{H}^{(m,n)}_{\lambda_1\lambda_2\lambda_3\lambda_4}/(4\pi)^{m+n}$, see Eqs. (8.130)-(8.133), where the relative orders in the electroweak and strong couplings are denoted by (m, n).

point of view, it was interesting to see a somewhat similar qualitative angular dependence emerge when comparing the two-loop polarized hard scattering functions for QED-QCD and EW-QCD normalized by their respective tree-level contributions.

8.9 Summary and outlook

In this chapter, we discussed the calculation of the relative order $\alpha_{\mathrm{em}}\alpha_s$ unpolarized mixed EW-QCD corrections to Drell-Yan lepton pair production, $q\bar{q} \to \ell^+\ell^-$. This calculation served as an independent check to the results obtained in Ref. [85], where the helicity amplitudes have been considered. For the unpolarized amplitude, we find full agreement with the results obtained there.

In Ref. [85] we performed the calculation in two γ_5 schemes, the 't Hooft-Veltman-Breitenlohner-Maison and the Kreimer scheme. While the two-loop scattering amplitudes were found to be scheme dependent starting at $\mathcal{O}(\epsilon^{-1})$, unique polarized hard scattering functions in $d = 4$ were obtained after IR subtraction.

Our calculation provides a major building block for the calculation of the relative order $\alpha_{\mathrm{em}}\alpha_s$ corrections to off-shell Drell-Yan production in the high energy region, which is particularly relevant to new physics searches and the establishment of constraints on possible extensions of the Standard Model.

9 Acknowledgements

First, I would like my two advisors, Marc Vanderhaeghen and Andreas von Manteuffel, for the opportunity to conduct my PhD thesis under their supervision as well as for their collaboration and advice. I also want to thank Robert Schabinger and [redacted] for many enlightening discussions and the nice collaboration. Furthermore, I am grateful to my family and friends for their support during the last five years.

This work was supported in part by the German Research Foundation (DFG), through the Collaborative Research Center, Project ID 204404729, SFB 1044, and the Cluster of Excellence PRISMA$^+$, Project ID 39083149, EXC 2118/1. Furthermore, I acknowledge support from the graduate school "Symmetry Breaking" (DFG/GRK 1581).

Bibliography

[1] B. Abi and others (Muon g-2 Coll.) "Measurement of the Positive Muon Anomalous Magnetic Moment to 0.46 ppm". In: *Phys. Rev. Lett.* 126.14 (2021), p. 141801. DOI: 10.1103/PhysRevLett.126.141801. arXiv: 2104.03281 [hep-ex].

[2] T. Aoyama et al. "Complete Tenth-Order QED Contribution to the Muon g-2". In: *Phys. Rev. Lett.* 109 (2012), p. 111808. DOI: 10.1103/PhysRevLett.109.111808. arXiv: 1205.5370 [hep-ph].

[3] R. Tarrach. "Invariant Amplitudes for Virtual Compton Scattering Off Polarized Nucleons Free from Kinematical Singularities, Zeros and Constraints". In: *Nuovo Cim. A* 28 (1975), p. 409. DOI: 10.1007/BF02894857.

[4] C. L. Oxley and V. L. Telegdi. "Scattering of 30- to 95-Mev Photons by Protons". In: *Phys. Rev.* 100 (1955), pp. 435–436. DOI: 10.1103/PhysRev.100.435.

[5] P. A. M. Guichon et al. "The Role of nucleon structure in finite nuclei". In: *Nucl. Phys. A* 601 (1996), pp. 349–379. DOI: 10.1016/0375-9474(96)00033-4. arXiv: nucl-th/9509034.

[6] M. Gorchtein et al. "Light-front interpretation of Proton Generalized Polarizabilities". In: *Phys. Rev. Lett.* 104 (2010), p. 112001. DOI: 10.1103/PhysRevLett.104.112001. arXiv: 0911.2882 [hep-ph].

[7] H. Fonvieille, B. Pasquini, and N. Sparveris. "Virtual Compton Scattering and Nucleon Generalized Polarizabilities". In: *Prog. Part. Nucl. Phys.* 113 (2020), p. 103754. DOI: 10.1016/j.ppnp.2020.103754. arXiv: 1910.11071 [nucl-ex].

[8] K. Pachucki. "Theory of the Lamb shift in muonic hydrogen". In: *Phys. Rev. A* 53 (1996), pp. 2092–2100. DOI: 10.1103/PhysRevA.53.2092.

[9] C. E. Carlson and M. Vanderhaeghen. "Higher order proton structure corrections to the Lamb shift in muonic hydrogen". In: *Phys. Rev. A* 84 (2011), p. 020102. DOI: 10.1103/PhysRevA.84.020102.

[10] M. C. Birse and J. A. McGovern. "Proton polarisability contribution to the Lamb shift in muonic hydrogen at fourth order in chiral perturbation theory". In: *Eur. Phys. J. A* 48 (2012), p. 120. DOI: 10.1140/epja/i2012-12120-8.

[11] A. Antognini et al. "Theory of the 2S-2P Lamb shift and 2S hyperfine splitting in muonic hydrogen". In: *Annals Phys.* 331 (2013), pp. 127–145. DOI: 10.1016/j.aop.2012.12.003.

[12] V. Lensky et al. "Sum rules across the unpolarized Compton processes involving generalized polarizabilities and moments of nucleon structure functions". In: *Phys. Rev. D* 97.7 (2018), p. 074012. DOI: 10.1103/PhysRevD.97.074012.

[13] J. M. Alarcon, V. Lensky, and V. Pascalutsa. "Chiral perturbation theory of muonic hydrogen Lamb shift: polarizability contribution". In: *Eur. Phys. J. C* 74.4 (2014), p. 2852. DOI: 10.1140/epjc/s10052-014-2852-0.

[14] O. Tomalak and M. Vanderhaeghen. "Two-photon exchange correction to muon–proton elastic scattering at low momentum transfer". In: *Eur. Phys. J. C* 76.3 (2016), p. 125. DOI: 10.1140/epjc/s10052-016-3966-3.

[15] V. Pauk, C. E. Carlson, and M. Vanderhaeghen. "Low-energy doubly virtual Compton scattering from dilepton electroproduction on a nucleon". In: *Phys. Rev. C* 102.3 (2020), p. 035201. DOI: 10.1103/PhysRevC.102.035201. arXiv: 2001.10626 [hep-ph].

[16] M. Heller, N. Keil, and M. Vanderhaeghen. "Soft-photon radiative corrections to the $e^- p \to e^- p l^- l^+$ process". In: *Phys. Rev. D* 104.7 (2021), p. 073007. DOI: 10.1103/PhysRevD.104.073007. arXiv: 2108.02088 [hep-ph].

[17] E. D. Bloom et al. "High-Energy Inelastic e p Scattering at 6-Degrees and 10-Degrees". In: *Phys. Rev. Lett.* 23 (1969), pp. 930–934. DOI: 10.1103/PhysRevLett.23.930.

[18] X.-D. Ji. "Gauge-Invariant Decomposition of Nucleon Spin". In: *Phys. Rev. Lett.* 78 (1997), pp. 610–613. DOI: 10.1103/PhysRevLett.78.610. arXiv: hep-ph/9603249.

[19] D. Müller et al. "Wave functions, evolution equations and evolution kernels from light ray operators of QCD". In: *Fortsch. Phys.* 42 (1994), pp. 101–141. DOI: 10.1002/prop.2190420202. arXiv: hep-ph/9812448.

[20] A. Radyushkin. "Scaling limit of deeply virtual Compton scattering". In: *Phys. Lett. B* 380 (1996), pp. 417–425. DOI: 10.1016/0370-2693(96)00528-X. arXiv: hep-ph/9604317.

[21] X.-D. Ji. "Deeply virtual Compton scattering". In: *Phys. Rev. D* 55 (1997), pp. 7114–7125. DOI: 10.1103/PhysRevD.55.7114. arXiv: hep-ph/9609381.

[22] A. Airapetian and others (HERMES Coll.) "Measurement of the beam spin azimuthal asymmetry associated with deeply virtual Compton scattering". In: *Phys. Rev. Lett.* 87 (2001), p. 182001. DOI: 10.1103/PhysRevLett.87.182001. arXiv: hep-ex/0106068.

[23] C. Adloff and others (H1 Coll.) "Measurement of deeply virtual Compton scattering at HERA". In: *Phys. Lett. B* 517 (2001), pp. 47–58. DOI: 10.1016/S0370-2693(01)00939-X. arXiv: hep-ex/0107005.

[24] S. Stepanyan and others (CLAS Coll.) "Observation of exclusive deeply virtual Compton scattering in polarized electron beam asymmetry measurements". In: *Phys. Rev. Lett.* 87 (2001), p. 182002. DOI: 10.1103/PhysRevLett.87.182002. arXiv: hep-ex/0107043.

[25] F. X. Girod and others (CLAS Coll.) "Measurement of Deeply virtual Compton scattering beam-spin asymmetries". In: *Phys. Rev. Lett.* 100 (2008), p. 162002. DOI: 10.1103/PhysRevLett.100.162002. arXiv: 0711.4805 [hep-ex].

[26] P. Chatagnon and others (CLAS Coll.) "First-time measurement of Timelike Compton Scattering". In: (Aug. 2021). arXiv: 2108.11746 [hep-ex].

[27] M. Heller, N. Keil, and M. Vanderhaeghen. "Leading-order QED radiative corrections to timelike Compton scattering on the proton". In: *Phys. Rev. D* 103.3 (2021), p. 036009. DOI: 10.1103/PhysRevD.103.036009. arXiv: 2012.09565 [hep-ph].

[28] M. Guidal and M. Vanderhaeghen. "Double deeply virtual Compton scattering off the nucleon". In: *Phys. Rev. Lett.* 90 (2003), p. 012001. DOI: 10.1103/PhysRevLett.90.012001. arXiv: hep-ph/0208275.

[29] A. V. Belitsky and D. Mueller. "Exclusive electroproduction of lepton pairs as a probe of nucleon structure". In: *Phys. Rev. Lett.* 90 (2003), p. 022001. DOI: 10.1103/PhysRevLett.90.022001. arXiv: hep-ph/0210313.

[30] A. Accardi et al. "e$^+$@JLab White Paper: An Experimental Program with Positron Beams at Jefferson Lab". In: (July 2020). arXiv: 2007.15081 [nucl-ex].

[31] J. Bernauer and others (A1 Coll.) "High-precision determination of the electric and magnetic form factors of the proton". In: *Phys. Rev. Lett.* 105 (2010), p. 242001. DOI: 10.1103/PhysRevLett.105.242001. arXiv: 1007.5076 [nucl-ex].

[32] J. Bernauer and others (A1 Coll.) "Electric and magnetic form factors of the proton". In: *Phys. Rev. C* 90.1 (2014), p. 015206. DOI: 10.1103/PhysRevC.90.015206. arXiv: 1307.6227 [nucl-ex].

[33] R. Pohl et al. "The size of the proton". In: *Nature* 466 (2010), pp. 213–216. DOI: 10.1038/nature09250.

[34] A. Antognini et al. "Proton Structure from the Measurement of $2S-2P$ Transition Frequencies of Muonic Hydrogen". In: *Science* 339 (2013), pp. 417–420. DOI: 10.1126/science.1230016.

[35] A. Beyer et al. "The Rydberg constant and proton size from atomic hydrogen". In: *Science* 358.6359 (2017), pp. 79–85. DOI: 10.1126/science.aah6677.

[36] N. Bezginov et al. "A measurement of the atomic hydrogen Lamb shift and the proton charge radius". In: *Science* 365.6457 (2019), pp. 1007–1012. DOI: 10.1126/science.aau7807.

[37] W. Xiong et al. "A small proton charge radius from an electron–proton scattering experiment". In: *Nature* 575.7781 (2019), pp. 147–150. DOI: 10.1038/s41586-019-1721-2.

[38] R. Gilman. "Studying the proton 'radius' puzzle with μp elastic scattering". In: *AIP Conf. Proc.* 1563.1 (2013). Ed. by R. Milner, R. Carlini, and F. Maas, pp. 167–170. DOI: 10.1063/1.4829401.

[39] R. Gilman and others (MUSE Coll.) "Technical Design Report for the Paul Scherrer Institute Experiment R-12-01.1: Studying the Proton "Radius" Puzzle with μp Elastic Scattering". In: (Sept. 2017). arXiv: 1709.09753 [physics.ins-det].

[40] B. Adams et al. "Letter of Intent: A New QCD facility at the M2 beam line of the CERN SPS (COMPASS++/AMBER)". In: (Aug. 2018). arXiv: 1808.00848 [hep-ex].

[41] D. Tucker-Smith and I. Yavin. "Muonic hydrogen and MeV forces". In: *Phys. Rev. D* 83 (2011), p. 101702. DOI: 10.1103/PhysRevD.83.101702. arXiv: 1011.4922 [hep-ph].

[42] V. Barger et al. "Proton size anomaly". In: *Phys. Rev. Lett.* 106 (2011), p. 153001. DOI: 10.1103/PhysRevLett.106.153001. arXiv: 1011.3519 [hep-ph].

[43] V. Barger et al. "Constraint on parity-violating muonic forces". In: *Phys. Rev. Lett.* 108 (2012), p. 081802. DOI: 10.1103/PhysRevLett.108.081802. arXiv: 1109.6652 [hep-ph].

[44] B. Batell, D. McKeen, and M. Pospelov. "New Parity-Violating Muonic Forces and the Proton Charge Radius". In: *Phys. Rev. Lett.* 107 (2011), p. 011803. DOI: 10.1103/PhysRevLett.107.011803. arXiv: 1103.0721 [hep-ph].

[45] P. Brax and C. Burrage. "Atomic Precision Tests and Light Scalar Couplings". In: *Phys. Rev. D* 83 (2011), p. 035020. DOI: 10.1103/PhysRevD.83.035020. arXiv: 1010.5108 [hep-ph].

[46] U. D. Jentschura. "Lamb Shift in Muonic Hydrogen. II. Analysis of the Discrepancy of Theory and Experiment". In: *Annals Phys.* 326 (2011), pp. 516–533. DOI: 10.1016/j.aop.2010.11.011. arXiv: 1011.5453 [hep-ph].

[47] C. E. Carlson and B. C. Rislow. "New Physics and the Proton Radius Problem". In: *Phys. Rev. D* 86 (2012), p. 035013. DOI: 10.1103/PhysRevD.86.035013. arXiv: 1206.3587 [hep-ph].

[48] L.-B. Wang and W.-T. Ni. "Proton radius puzzle and large extra dimensions". In: *Mod. Phys. Lett. A* 28 (2013), p. 1350094. DOI: 10.1142/S0217732313500946. arXiv: 1303.4885 [hep-ph].

[49] R. Onofrio. "Proton radius puzzle and quantum gravity at the Fermi scale". In: *EPL* 104.2 (2013), p. 20002. DOI: 10.1209/0295-5075/104/20002. arXiv: 1312.3469 [hep-ph].

[50] S. G. Karshenboim, D. McKeen, and M. Pospelov. "Constraints on muon-specific dark forces". In: *Phys. Rev. D* 90.7 (2014). [Addendum: Phys.Rev.D 90, 079905 (2014)], p. 073004. DOI: 10.1103/PhysRevD.90.073004. arXiv: 1401.6154 [hep-ph].

[51] V. Pauk and M. Vanderhaeghen. "Lepton universality test in the photoproduction of e^-e^+ versus $\mu^-\mu^+$ pairs on a proton target". In: *Phys. Rev. Lett.* 115.22 (2015), p. 221804. DOI: 10.1103/PhysRevLett.115.221804. arXiv: 1503.01362 [hep-ph].

[52] M. Heller, O. Tomalak, and M. Vanderhaeghen. "Soft-photon corrections to the Bethe-Heitler process in the $\gamma p \to l^+l^-p$ reaction". In: *Phys. Rev. D* 97.7 (2018), p. 076012. DOI: 10.1103/PhysRevD.97.076012. arXiv: 1802.07174 [hep-ph].

[53] M. Heller et al. "Leading Order Corrections to the Bethe-Heitler Process in the $\gamma p \to l^+l^-p$ Reaction". In: *Phys. Rev. D* 100.7 (2019), p. 076013. DOI: 10.1103/PhysRevD.100.076013. arXiv: 1906.02706 [hep-ph].

[54] S. Drell and T.-M. Yan. "Massive Lepton Pair Production in Hadron-Hadron Collisions at High-Energies". In: *Phys. Rev. Lett.* 25 (1970). [Erratum: Phys. Rev. Lett. **25**, 902 (1970)], pp. 316–320. DOI: 10.1103/PhysRevLett.25.316.

[55] G. Arnison and others (UA1 Coll.) "Experimental Observation of Isolated Large Transverse Energy Electrons with Associated Missing Energy at $\sqrt{s} =$ 540 GeV". In: *Phys. Lett. B* 122 (1983), pp. 103–116. DOI: 10.1016/0370-2693(83)91177-2.

[56] M. Banner and others (UA2 Coll.) "Observation of Single Isolated Electrons of High Transverse Momentum in Events with Missing Transverse Energy at the CERN anti-p p Collider". In: *Phys. Lett. B* 122 (1983), pp. 476–485. DOI: 10.1016/0370-2693(83)91605-2.

[57] J.-C. Peng and J.-W. Qiu. "The Drell-Yan Process". In: *The Universe* 4.3 (2016), pp. 34–44.

[58] G. Altarelli, R. K. Ellis, and G. Martinelli. "Large Perturbative Corrections to the Drell-Yan Process in QCD". In: *Nucl. Phys. B* 157 (1979), pp. 461–497. DOI: 10.1016/0550-3213(79)90116-0.

[59] R. Hamberg, W. van Neerven, and T. Matsuura. "A Complete calculation of the order α_s^2 correction to the Drell-Yan K factor". In: *Nucl. Phys.* B359 (1991), pp. 343–405. DOI: 10.1016/0550-3213(91)90064-5.

[60] R. V. Harlander and W. B. Kilgore. "Next-to-next-to-leading order Higgs production at hadron colliders". In: *Phys. Rev. Lett.* 88 (2002), p. 201801. DOI: 10.1103/PhysRevLett.88.201801. arXiv: hep-ph/0201206 [hep-ph].

[61] C. Anastasiou et al. "High precision QCD at hadron colliders: Electroweak gauge boson rapidity distributions at NNLO". In: *Phys. Rev.* D69 (2004), p. 094008. DOI: 10.1103/PhysRevD.69.094008. arXiv: hep-ph/0312266 [hep-ph].

[62] K. Melnikov and F. Petriello. "The W boson production cross section at the LHC through $\mathcal{O}(\alpha_s^2)$". In: *Phys. Rev. Lett.* 96 (2006), p. 231803. DOI: 10.1103/PhysRevLett.96.231803. arXiv: hep-ph/0603182 [hep-ph].

[63] C. Duhr, F. Dulat, and B. Mistlberger. "The Drell-Yan cross section to third order in the strong coupling constant". In: *Phys. Rev. Lett.* 125 (2020), p. 172001. DOI: 10.1103/PhysRevLett.125.172001. arXiv: 2001.07717 [hep-ph].

[64] C. Duhr, F. Dulat, and B. Mistlberger. "Charged current Drell-Yan production at N^3LO". In: *JHEP* 11 (2020), p. 143. DOI: 10.1007/JHEP11(2020)143. arXiv: 2007.13313 [hep-ph].

[65] F. A. Berends, W. L. van Neerven, and G. J. H. Burgers. "Higher Order Radiative Corrections at LEP Energies". In: *Nucl. Phys.* B297 (1988). [Erratum: Nucl. Phys. **B304**, 921 (1988)], p. 429. DOI: 10.1016/0550-3213(88)90313-6,10.1016/0550-3213(88)90662-1.

[66] J. Blümlein et al. "The $\mathcal{O}(\alpha^2)$ Initial State QED Corrections to e^+e^- Annihilation to a Neutral Vector Boson Revisited". In: *Phys. Lett.* B791 (2019), pp. 206–209. DOI: 10.1016/j.physletb.2019.02.038. arXiv: 1901.08018 [hep-ph].

[67] U. Baur, S. Keller, and D. Wackeroth. "Electroweak radiative corrections to W boson production in hadronic collisions". In: *Phys. Rev. D* 59 (1999), p. 013002. DOI: 10.1103/PhysRevD.59.013002. arXiv: hep-ph/9807417.

[68] U. Baur et al. "Electroweak radiative corrections to neutral current Drell-Yan processes at hadron colliders". In: *Phys. Rev.* D65 (2002), p. 033007. DOI: 10.1103/PhysRevD.65.033007. arXiv: hep-ph/0108274 [hep-ph].

[69] S. Dittmaier and M. Krämer. "Electroweak radiative corrections to W boson production at hadron colliders". In: *Phys. Rev.* D65 (2002), p. 073007. DOI: 10.1103/PhysRevD.65.073007. arXiv: hep-ph/0109062 [hep-ph].

[70] U. Baur and D. Wackeroth. "Electroweak radiative corrections to $p\bar{p} \to W^\pm \to \ell^\pm\nu$ beyond the pole approximation". In: *Phys. Rev.* D70 (2004), p. 073015. DOI: 10.1103/PhysRevD.70.073015. arXiv: hep-ph/0405191 [hep-ph].

[71] A. Arbuzov et al. "One-loop corrections to the Drell-Yan process in SANC. I. The Charged current case". In: *Eur. Phys. J. C* 46 (2006). [Erratum: Eur.Phys.J.C 50, 505 (2007)], pp. 407–412. DOI: 10.1140/epjc/s2006-02505-y. arXiv: hep-ph/0506110.

[72] C. M. Carloni Calame et al. "Precision electroweak calculation of the charged current Drell-Yan process". In: *JHEP* 12 (2006), p. 016. DOI: 10.1088/1126-6708/2006/12/016. arXiv: hep-ph/0609170.

[73] A. B. Arbuzov and R. R. Sadykov. "Inverse bremsstrahlung contributions to Drell-Yan like processes". In: *J. Exp. Theor. Phys.* 106 (2008), pp. 488–494. DOI: 10.1134/S1063776108030096. arXiv: 0707.0423 [hep-ph].

[74] C. M. Carloni Calame et al. "Precision electroweak calculation of the production of a high transverse-momentum lepton pair at hadron colliders". In: *JHEP* 10 (2007), p. 109. DOI: 10.1088/1126-6708/2007/10/109. arXiv: 0710.1722 [hep-ph].

[75] S. Dittmaier and M. Huber. "Radiative corrections to the neutral-current Drell-Yan process in the Standard Model and its minimal supersymmetric extension". In: *JHEP* 01 (2010), p. 060. DOI: 10.1007/JHEP01(2010)060. arXiv: 0911.2329 [hep-ph].

[76] W. B. Kilgore and C. Sturm. "Two-Loop Virtual Corrections to Drell-Yan Production at order $\alpha_s\alpha^3$". In: *Phys. Rev.* D85 (2012), p. 033005. DOI: 10.1103/PhysRevD.85.033005. arXiv: 1107.4798 [hep-ph].

[77] S. Dittmaier, A. Huss, and C. Schwinn. "Mixed QCD-electroweak $\mathcal{O}(\alpha_s\alpha)$ corrections to Drell-Yan processes in the resonance region: pole approximation and non-factorizable corrections". In: *Nucl. Phys.* B885 (2014), pp. 318–372. DOI: 10.1016/j.nuclphysb.2014.05.027. arXiv: 1403.3216 [hep-ph].

[78] S. Dittmaier, A. Huss, and C. Schwinn. "Dominant mixed QCD-electroweak $\mathcal{O}(\alpha_s\alpha)$ corrections to Drell-Yan processes in the resonance region". In: *Nucl. Phys.* B904 (2016), pp. 216–252. DOI: 10.1016/j.nuclphysb.2016.01.006. arXiv: 1511.08016 [hep-ph].

[79] M. Delto et al. "Mixed QCD⊗QED corrections to on-shell Z boson production at the LHC". In: *JHEP* 01 (2020), p. 043. DOI: 10.1007/JHEP01(2020)043. arXiv: 1909.08428 [hep-ph].

[80] F. Buccioni et al. "Mixed QCD-electroweak corrections to on-shell Z production at the LHC". In: *Phys. Lett. B* 811 (2020), p. 135969. DOI: 10.1016/j.physletb.2020.135969. arXiv: 2005.10221 [hep-ph].

[81] R. Bonciani et al. "NNLO QCD×EW corrections to on-shell Z production". In: *Phys. Rev. Lett.* 125.23 (2020), p. 232004. DOI: 10.1103/PhysRevLett.125.232004. arXiv: 2007.06518 [hep-ph].

[82] S. Dittmaier, T. Schmidt, and J. Schwarz. "Mixed NNLO QCD × electroweak corrections of $\mathcal{O}(N_f\alpha_s\alpha)$ to single-W/Z production at the LHC". In: *JHEP* 12 (2020), p. 201. DOI: 10.1007/JHEP12(2020)201. arXiv: 2009.02229 [hep-ph].

[83] A. Behring et al. "Mixed QCD-electroweak corrections to W-boson production in hadron collisions". In: (Sept. 2020). arXiv: 2009.10386 [hep-ph].

[84] M. Heller, A. von Manteuffel, and R. M. Schabinger. "Multiple polylogarithms with algebraic arguments and the two-loop EW-QCD Drell-Yan master integrals". In: *Phys. Rev. D* 102.1 (2020), p. 016025. DOI: 10.1103/PhysRevD.102.016025. arXiv: 1907.00491 [hep-th].

[85] M. Heller et al. "Mixed EW-QCD two-loop amplitudes for $q\bar{q} \to \ell^+\ell^-$ and γ_5 scheme independence of multi-loop corrections". In: *JHEP* 05 (2021), p. 213. DOI: 10.1007/JHEP05(2021)213. arXiv: 2012.05918 [hep-ph].

[86] R. Bonciani et al. "Mixed strong−electroweak corrections to the Drell−Yan process". In: (June 2021). arXiv: 2106.11953 [hep-ph].

[87] M. Heller. "Planar two-loop integrals for $\mu\mathbf{e}$ scattering in QED with finite lepton masses". In: *unpublished* (). arXiv: 2105.08046 [hep-ph].

[88] M. Heller and A. von Manteuffel. "MultivariateApart: Generalized partial fractions". In: *Comput. Phys. Commun.* 271 (2022), p. 108174. DOI: 10.1016/j.cpc.2021.108174. arXiv: 2101.08283 [cs.SC].

[89] G. 't Hooft and M. J. G. Veltman. "Regularization and Renormalization of Gauge Fields". In: *Nucl. Phys. B* 44 (1972), pp. 189–213. DOI: 10.1016/0550-3213(72)90279-9.

[90] J. C. Collins. *Renormalization: An Introduction to Renormalization, The Renormalization Group, and the Operator Product Expansion*. Vol. 26. Cambridge Monographs on Mathematical Physics. Cambridge: Cambridge University Press, 1986. ISBN: 978-0-521-31177-9, 978-0-511-86739-2. DOI: 10.1017/CBO9780511622656.

[91] Z. Bern and D. A. Kosower. "The Computation of loop amplitudes in gauge theories". In: *Nucl. Phys. B* 379 (1992), pp. 451–561. DOI: 10.1016/0550-3213(92)90134-W.

[92] S. Laporta. "High precision calculation of multiloop Feynman integrals by difference equations". In: *Int. J. Mod. Phys. A* 15 (2000), pp. 5087–5159. DOI: 10.1142/S0217751X00002159. arXiv: hep-ph/0102033.

[93] M. Kauers. "Fast solvers for dense linear systems". In: *Nucl. Phys. B Proc. Suppl.* 183 (2008). Ed. by J. Blumlein, S. Moch, and T. Riemann, pp. 245–250. DOI: 10.1016/j.nuclphysbps.2008.09.111.

[94] A. von Manteuffel and R. M. Schabinger. "A novel approach to integration by parts reduction". In: *Phys. Lett.* B744 (2015), pp. 101–104. DOI: 10.1016/j.physletb.2015.03.029. arXiv: 1406.4513 [hep-ph].

[95] C. Bogner and S. Weinzierl. "Feynman graph polynomials". In: *Int.J.Mod.Phys.* A25 (2010), pp. 2585–2618. DOI: 10.1142/S0217751X10049438. arXiv: 1002.3458 [hep-ph].

[96] J. M. Henn. "Multi-loop integrals in dimensional regularization made simple". In: *Phys. Rev. Lett.* 110 (2013), p. 251601. DOI: 10.1103/PhysRevLett.110.251601. arXiv: 1304.1806 [hep-th].

[97] T. Gehrmann et al. "The two-loop master integrals for $q\bar{q} \to VV$". In: *JHEP* 1406 (2014), p. 032. DOI: 10.1007/JHEP06(2014)032. arXiv: 1404.4853 [hep-ph].

[98] R. N. Lee. "Reducing differential equations for multiloop master integrals". In: *JHEP* 04 (2015), p. 108. DOI: 10.1007/JHEP04(2015)108. arXiv: 1411.0911 [hep-ph].

[99] C. Meyer. "Algorithmic transformation of multi-loop master integrals to a canonical basis with CANONICA". In: *Comput. Phys. Commun.* 222 (2018), pp. 295–312. DOI: 10.1016/j.cpc.2017.09.014. arXiv: 1705.06252 [hep-ph].

[100] M. Besier, D. van Straten, and S. Weinzierl. "Rationalizing roots: an algorithmic approach". In: *Commun. Num. Theor. Phys.* 13 (2019), pp. 253–297. DOI: 10.4310/CNTP.2019.v13.n2.a1. arXiv: 1809.10983 [hep-th].

[101] C. Duhr, H. Gangl, and J. R. Rhodes. "From polygons and symbols to polylogarithmic functions". In: *JHEP* 10 (2012), p. 075. DOI: 10.1007/JHEP10(2012)075. arXiv: 1110.0458 [math-ph].

[102] S. Arno, D. H. Bailey, and H. R. P. Ferguson. "Analysis of PSLQ, an integer relation finding algorithm". In: *Math. Comp.* vol. 68, no. 225 (1999), p. 351.

[103] A. von Manteuffel and C. Studerus. "Massive planar and non-planar double box integrals for light N_f contributions to $gg \to t\bar{t}$". In: *JHEP* 1310 (2013), p. 037. DOI: 10.1007/JHEP10(2013)037. arXiv: 1306.3504 [hep-ph].

[104] T. Gehrmann, L. Tancredi, and E. Weihs. "Two-loop master integrals for $q\bar{q} \to VV$: the planar topologies". In: *JHEP* 1308 (2013), p. 070. DOI: 10.1007/JHEP08(2013)070. arXiv: 1306.6344.

[105] T. Gehrmann, A. von Manteuffel, and L. Tancredi. "The two-loop helicity amplitudes for $q\bar{q}' \to V_1V_2 \to 4$ leptons". In: *JHEP* 09 (2015), p. 128. DOI: 10.1007/JHEP09(2015)128. arXiv: 1503.04812 [hep-ph].

[106] M. Becchetti et al. "Master Integrals for the two-loop, non-planar QCD corrections to top-quark pair production in the quark-annihilation channel". In: *JHEP* 08 (2019), p. 071. DOI: 10.1007/JHEP08(2019)071. arXiv: 1904.10834 [hep-ph].

[107] A. von Manteuffel and R. M. Schabinger. "Numerical Multi-Loop Calculations via Finite Integrals and One-Mass EW-QCD Drell-Yan Master Integrals". In: *JHEP* 04 (2017), p. 129. DOI: 10.1007/JHEP04(2017)129. arXiv: 1701.06583 [hep-ph].

[108] A. von Manteuffel and L. Tancredi. "A non-planar two-loop three-point function beyond multiple polylogarithms". In: *JHEP* 06 (2017), p. 127. DOI: 10.1007/JHEP06(2017)127. arXiv: 1701.05905.

[109] M. Besier et al. "Arithmetic and geometry of a K3 surface emerging from virtual corrections to Drell–Yan scattering". In: (2019). arXiv: 1908.01079 [math.AG].

[110] F. Brown and C. Duhr. "A double integral of dlog forms which is not polylogarithmic". In: June 2020. arXiv: 2006.09413 [hep-th].

[111] P. Nogueira. "Automatic Feynman graph generation". In: *J.Comput.Phys.* 105 (1993), pp. 279–289. DOI: 10.1006/jcph.1993.1074.

[112] J. A. M. Vermaseren. "New features of FORM". In: (2000). arXiv: math-ph/0010025 [math-ph].

[113] A. von Manteuffel and C. Studerus. "`Reduze 2` - Distributed Feynman Integral Reduction". In: (2012). arXiv: 1201.4330 [hep-ph].

[114] C. W. Bauer, A. Frink, and R. Kreckel. "Introduction to the `GiNaC` framework for symbolic computation within the `C++` programming language". In: *J. Symb. Comput.* 33 (2002), p. 1. arXiv: cs/0004015 [cs-sc].

[115] J. Vollinga and S. Weinzierl. "Numerical evaluation of multiple polylogarithms". In: *Comput. Phys. Commun.* 167 (2005), p. 177. DOI: 10.1016/j.cpc.2004.12.009. arXiv: hep-ph/0410259 [hep-ph].

[116] B. Agarwal et al. "Two-loop helicity amplitudes for diphoton plus jet production in full color". In: (May 2021). arXiv: 2105.04585 [hep-ph].

[117] S. Badger et al. "Virtual QCD corrections to gluon-initiated diphoton plus jet production at hadron colliders". In: (June 2021). arXiv: 2106.08664 [hep-ph].

[118] F. Caola et al. "Three-loop helicity amplitudes for four-quark scattering in massless QCD". In: (July 2021). arXiv: 2108.00055 [hep-ph].

[119] S. Badger et al. "Two-loop leading-colour QCD helicity amplitudes for Higgs boson production in association with a bottom-quark pair at the LHC". In: (July 2021). arXiv: 2107.14733 [hep-ph].

[120] H. Strubbe. "Manual for Schoonschip: A CDC 6000 / 7000 program for symbolic evaluation of algebraic expressions (program made by M. Veltman)". In: *Comput. Phys. Commun.* 8 (1974), pp. 1–30. DOI: 10.1016/0010-4655(74)90081-2.

[121] E. Remiddi. *Computer algebra, past, present and future*. Talk given at Tini 80 Fest, 2011, https://www.nikhef.nl/~t45/Tini80Fest/Remiddi.pdf.

[122] B. Ruijl, T. Ueda, and J. Vermaseren. "FORM version 4.2". In: (July 2017). arXiv: 1707.06453 [hep-ph].

[123] F. Feng. "`Apart`: A Generalized Mathematica Apart Function". In: *Comput. Phys. Commun.* 183 (2012), pp. 2158–2164. DOI: 10.1016/j.cpc.2012.03.025. arXiv: 1204.2314 [hep-ph].

[124] E. K. Leinartas. "Factorization of rational functions of several variables into partial fractions". In: *Soviet Math. (Iz. VUZ)* 22.10 (1978), pp. 35–38.

[125] A. Raichev. "Leinartas' partial fraction decomposition". In: (2012). arXiv: 1206.4740 [math.AC].

[126] C. Meyer. "Transforming differential equations of multi-loop Feynman integrals into canonical form". In: *JHEP* 04 (2017), p. 006. DOI: 10.1007/JHEP04(2017)006. arXiv: 1611.01087 [hep-ph].

[127] A. Pak. "The Toolbox of modern multi-loop calculations: novel analytic and semi-analytic techniques". In: *J. Phys. Conf. Ser.* 368 (2012). Ed. by L. Teodorescu et al., p. 012049. DOI: 10.1088/1742-6596/368/1/012049. arXiv: 1111.0868 [hep-ph].

[128] S. Abreu et al. "Analytic Form of the Planar Two-Loop Five-Parton Scattering Amplitudes in QCD". In: *JHEP* 05 (2019), p. 084. DOI: 10.1007/JHEP05(2019)084. arXiv: 1904.00945 [hep-ph].

[129] D. A. Cox, J. Little, and D. O'Shea. *Ideals, Varieties, and Algorithms*. Springer, Cham, 2015. DOI: 10.1007/978-3-319-16721-3.

[130] M. Kreuzer and L. Robbiano. *Computational commutative algebra. 1*. Springer, Berlin, Heidelberg, 2000, pp. x+321. ISBN: 3-540-67733-X. DOI: 10.1007/978-3-540-70628-1.

[131] J. Boehm et al. "IBP reduction coefficients made simple". In: *JHEP* 12 (2020), p. 054. DOI: 10.1007/JHEP12(2020)054. arXiv: 2008.13194 [hep-ph].

[132] A. von Manteuffel and R. M. Schabinger. "Quark and gluon form factors to four-loop order in QCD: the N_f^3 contributions". In: *Phys. Rev. D* 95.3 (2017), p. 034030. DOI: 10.1103/PhysRevD.95.034030. arXiv: 1611.00795 [hep-ph].

[133] T. Peraro. "Scattering amplitudes over finite fields and multivariate functional reconstruction". In: *JHEP* 12 (2016), p. 030. DOI: 10.1007/JHEP12(2016)030. arXiv: 1608.01902 [hep-ph].

[134] T. Peraro. "FiniteFlow: multivariate functional reconstruction using finite fields and dataflow graphs". In: *JHEP* 07 (2019), p. 031. DOI: 10.1007/JHEP07(2019)031. arXiv: 1905.08019 [hep-ph].

[135] J. Klappert and F. Lange. "Reconstructing rational functions with FireFly". In: *Comput. Phys. Commun.* 247 (2020), p. 106951. DOI: 10.1016/j.cpc.2019.106951. arXiv: 1904.00009 [cs.SC].

[136] A. V. Smirnov and F. S. Chuharev. "FIRE6: Feynman Integral REduction with Modular Arithmetic". In: *Comput. Phys. Commun.* 247 (2020), p. 106877. DOI: 10.1016/j.cpc.2019.106877. arXiv: 1901.07808 [hep-ph].

[137] A. Smirnov and V. Smirnov. "How to choose master integrals". In: *Nucl. Phys. B* 960 (2020), p. 115213. DOI: 10.1016/j.nuclphysb.2020.115213. arXiv: 2002.08042 [hep-ph].

[138] J. Usovitsch. "Factorization of denominators in integration-by-parts reductions". In: (Feb. 2020). arXiv: 2002.08173 [hep-ph].

[139] S. Abreu et al. "Analytic Form of Planar Two-Loop Five-Gluon Scattering Amplitudes in QCD". In: *Phys. Rev. Lett.* 122.8 (2019), p. 082002. DOI: 10.1103/PhysRevLett.122.082002. arXiv: 1812.04586 [hep-ph].

[140] F. Brown. "The Massless higher-loop two-point function". In: *Commun. Math. Phys.* 287 (2009), pp. 925–958. DOI: 10.1007/s00220-009-0740-5. arXiv: 0804.1660 [math.AG].

[141] E. Panzer. "Algorithms for the symbolic integration of hyperlogarithms with applications to Feynman integrals". In: *Comput. Phys. Commun.* 188 (2015), pp. 148–166. DOI: 10.1016/j.cpc.2014.10.019. arXiv: 1403.3385 [hep-th].

[142] S. Catani et al. "From loops to trees by-passing Feynman's theorem". In: *JHEP* 09 (2008), p. 065. DOI: 10.1088/1126-6708/2008/09/065. arXiv: 0804.3170 [hep-ph].

[143] W. J. Torres Bobadilla. "Loop-tree duality from vertices and edges". In: *JHEP* 04 (2021), p. 183. DOI: 10.1007/JHEP04(2021)183. arXiv: 2102.05048 [hep-ph].

[144] P. Mastrolia and S. Mizera. "Feynman Integrals and Intersection Theory". In: *JHEP* 02 (2019), p. 139. DOI: 10.1007/JHEP02(2019)139. arXiv: 1810.03818 [hep-th].

[145] D. Drechsel et al. "Structure analysis of the virtual Compton scattering amplitude at low-energies". In: *Phys. Rev. C* 57 (1998), pp. 941–952. DOI: 10.1103/PhysRevC.57.941. arXiv: nucl-th/9704064.

[146] E. L. Lomon and S. Pacetti. "Time-like and space-like electromagnetic form factors of nucleons, a unified description". In: *Phys. Rev. D* 85 (2012). [Erratum: Phys.Rev.D 86, 039901 (2012)], p. 113004. DOI: 10.1103/PhysRevD.86.039901. arXiv: 1201.6126 [hep-ph].

[147] V. Pascalutsa, M. Vanderhaeghen, and S. N. Yang. "Electromagnetic excitation of the Delta(1232)-resonance". In: *Phys. Rept.* 437 (2007), pp. 125–232. DOI: 10.1016/j.physrep.2006.09.006. arXiv: hep-ph/0609004.

[148] D. Drechsel, S. Kamalov, and L. Tiator. "Unitary Isobar Model - MAID2007". In: *Eur. Phys. J. A* 34 (2007), pp. 69–97. DOI: 10.1140/epja/i2007-10490-6. arXiv: 0710.0306 [nucl-th].

[149] L. Tiator et al. "Electromagnetic Excitation of Nucleon Resonances". In: *Eur. Phys. J. ST* 198 (2011), pp. 141–170. DOI: 10.1140/epjst/e2011-01488-9. arXiv: 1109.6745 [nucl-th].

[150] M. Vanderhaeghen, P. A. Guichon, and M. Guidal. "Hard electroproduction of photons and mesons on the nucleon". In: *Phys. Rev. Lett.* 80 (1998), pp. 5064–5067. DOI: 10.1103/PhysRevLett.80.5064.

[151] M. Vanderhaeghen, P. A. Guichon, and M. Guidal. "Deeply virtual electroproduction of photons and mesons on the nucleon: Leading order amplitudes and power corrections". In: *Phys. Rev. D* 60 (1999), p. 094017. DOI: 10.1103/PhysRevD.60.094017. arXiv: hep-ph/9905372.

[152] K. Goeke, M. V. Polyakov, and M. Vanderhaeghen. "Hard exclusive reactions and the structure of hadrons". In: *Prog. Part. Nucl. Phys.* 47 (2001), pp. 401–515. DOI: 10.1016/S0146-6410(01)00158-2. arXiv: hep-ph/0106012.

[153] M. Guidal et al. "Nucleon form-factors from generalized parton distributions". In: *Phys. Rev. D* 72 (2005), p. 054013. DOI: 10.1103/PhysRevD.72.054013. arXiv: hep-ph/0410251.

[154] M. Guidal, H. Moutarde, and M. Vanderhaeghen. "Generalized Parton Distributions in the valence region from Deeply Virtual Compton Scattering". In: *Rept. Prog. Phys.* 76 (2013), p. 066202. DOI: 10.1088/0034-4885/76/6/066202. arXiv: 1303.6600 [hep-ph].

[155] R. Dupre, M. Guidal, and M. Vanderhaeghen. "Tomographic image of the proton". In: *Phys. Rev. D* 95.1 (2017), p. 011501. DOI: 10.1103/PhysRevD.95.011501. arXiv: 1606.07821 [hep-ph].

[156] R. Dupré et al. "Analysis of Deeply Virtual Compton Scattering Data at Jefferson Lab and Proton Tomography". In: *Eur. Phys. J. A* 53.8 (2017), p. 171. DOI: 10.1140/epja/i2017-12356-8. arXiv: 1704.07330 [hep-ph].

[157] B. Pasquini, M. Polyakov, and M. Vanderhaeghen. "Dispersive evaluation of the D-term form factor in deeply virtual Compton scattering". In: *Phys. Lett. B* 739 (2014), pp. 133–138. DOI: 10.1016/j.physletb.2014.10.047. arXiv: 1407.5960 [hep-ph].

[158] M. Vanderhaeghen et al. "QED radiative corrections to virtual Compton scattering". In: *Phys. Rev. C* 62 (2000), p. 025501. DOI: 10.1103/PhysRevC.62.025501. arXiv: hep-ph/0001100.

[159] G. 't Hooft and M. Veltman. "Scalar One Loop Integrals". In: *Nucl. Phys. B* 153 (1979), pp. 365–401. DOI: 10.1016/0550-3213(79)90605-9.

[160] O. Gryniuk, F. Hagelstein, and V. Pascalutsa. "Evaluation of the forward Compton scattering off protons: Spin-independent amplitude". In: *Phys. Rev. D* 92 (2015), p. 074031. DOI: 10.1103/PhysRevD.92.074031. arXiv: 1508.07952 [nucl-th].

[161] H. Alvensleben et al. "Experimental verification of the Kramers-Kronig relation at high energy". In: *Phys. Rev. Lett.* 30 (1973), pp. 328–332. DOI: 10.1103/PhysRevLett.30.328.

[162] P. Nadel-Turonski et al. "Timelike Compton Scattering and J/psi photoproduction on the proton in e+e- pair production with CLAS12 at 11 GeV". In: *spokespersons JLab experiment E12-12-001* (). https://www.jlab.org/exp_prog/proposals/12/PR12-12-001.pdf.

[163] P. (C. Chatagnon. "Timelike Compton Scattering with CLAS12 at Jefferson Lab". In: *PoS* LC2019 (2020), p. 033. DOI: 10.22323/1.374.0033.

[164] P. Chatagnon. "Nucleon structure studies with CLAS12 at Jefferson Lab: Timelike Compton scattering and the central neutron detector". PhD thesis. IJCLab, Orsay, 2020.

[165] D. R. Yennie, S. C. Frautschi, and H. Suura. "The infrared divergence phenomena and high-energy processes". In: *Annals Phys.* 13 (1961), pp. 379–452. DOI: 10.1016/0003-4916(61)90151-8.

[166] L. G. Cabral-Rosetti and M. A. Sanchis-Lozano. "Appell functions and the scalar one loop three point integrals in Feynman diagrams". In: *J. Phys. Conf. Ser.* 37 (2006), pp. 82–89. DOI: 10.1088/1742-6596/37/1/015. arXiv: hep-ph/0206081.

[167] B. Pasquini and M. Vanderhaeghen. "Dispersion Theory in Electromagnetic Interactions". In: *Ann. Rev. Nucl. Part. Sci.* 68 (2018), pp. 75–103. DOI: 10.1146/annurev-nucl-101917-020843.

[168] P. Zyla and others (Particle Data Group). "Review of Particle Physics". In: *PTEP* 2020.8 (2020), p. 083C01. DOI: 10.1093/ptep/ptaa104.

[169] B. R. Holstein et al. "Higher order polarizabilities of the proton". In: *Phys. Rev. C* 61 (2000), p. 034316. DOI: 10.1103/PhysRevC.61.034316.

[170] D. van Straten. private communication, received August 6, 2014.

[171] M. Prausa. "`epsilon`: A tool to find a canonical basis of master integrals". In: *Comput. Phys. Commun.* 219 (2017), pp. 361–376. DOI: 10.1016/j.cpc.2017.05.026. arXiv: 1701.00725.

[172] O. Gituliar and V. Magerya. "`Fuchsia`: a tool for reducing differential equations for Feynman master integrals to epsilon form". In: *Comput. Phys. Commun.* 219 (2017), pp. 329–338. DOI: 10.1016/j.cpc.2017.05.004. arXiv: 1701.04269.

[173] R. Bonciani et al. "Two-Loop Master Integrals for the mixed EW-QCD virtual corrections to Drell-Yan scattering". In: *JHEP* 09 (2016), p. 091. DOI: 10.1007/JHEP09(2016)091. arXiv: 1604.08581 [hep-ph].

[174] C. Studerus. "`Reduze`-Feynman Integral Reduction in `C++`". In: *Comput. Phys. Commun.* 181 (2010), pp. 1293–1300. DOI: 10.1016/j.cpc.2010.03.012. arXiv: 0912.2546 [physics.comp-ph].

[175] R. H. Lewis. *Computer Algebra System* `Fermat`. http://home.bway.net/lewis/.

[176] J. Tausk. "Non-planar massless two-loop Feynman diagrams with four on-shell legs". In: *Phys. Lett.* B469 (1999), pp. 225–234. DOI: 10.1016/S0370-2693(99)01277-0. arXiv: hep-ph/9909506 [hep-ph].

[177] A. B. Goncharov. "Multiple polylogarithms and mixed Tate motives". In: (2001). arXiv: math/0103059 [math.AG].

[178] C. Duhr. "Hopf algebras, coproducts and symbols: an application to Higgs boson amplitudes". In: *JHEP* 08 (2012), p. 043. DOI: 10.1007/JHEP08(2012)043. arXiv: 1203.0454 [hep-ph].

[179] R. N. Lee, A. V. Smirnov, and V. A. Smirnov. "Solving differential equations for Feynman integrals by expansions near singular points". In: *JHEP* 03 (2018), p. 008. DOI: 10.1007/JHEP03(2018)008. arXiv: 1709.07525 [hep-ph].

[180] D. Gaiotto et al. "Pulling the straps of polygons". In: *JHEP* 12 (2011), p. 011. DOI: 10.1007/JHEP12(2011)011. arXiv: 1102.0062 [hep-th].

[181] L. J. Dixon, J. M. Drummond, and J. M. Henn. "The one-loop six-dimensional hexagon integral and its relation to MHV amplitudes in $\mathcal{N} = 4$ SYM". In: *JHEP* 06 (2011), p. 100. DOI: 10.1007/JHEP06(2011)100. arXiv: 1104.2787 [hep-th].

[182] S. Caron-Huot. "Superconformal symmetry and two-loop amplitudes in planar $\mathcal{N} = 4$ super Yang-Mills". In: *JHEP* 12 (2011), p. 066. DOI: 10.1007/JHEP12(2011)066. arXiv: 1105.5606 [hep-th].

[183] A. von Manteuffel, E. Panzer, and R. M. Schabinger. "A quasi-finite basis for multi-loop Feynman integrals". In: *JHEP* 02 (2015), p. 120. DOI: 10.1007/JHEP02(2015)120. arXiv: 1411.7392 [hep-ph].

[184] A. von Manteuffel, E. Panzer, and R. M. Schabinger. "On the Computation of Form Factors in Massless QCD with Finite Master Integrals". In: *Phys. Rev.* D93.12 (2016), p. 125014. DOI: 10.1103/PhysRevD.93.125014. arXiv: 1510.06758 [hep-ph].

[185] S. Borowka et al. "SecDec-3.0: numerical evaluation of multi-scale integrals beyond one loop". In: *Comput. Phys. Commun.* 196 (2015), pp. 470–491. DOI: 10.1016/j.cpc.2015.05.022. arXiv: 1502.06595 [hep-ph].

[186] P. Breitenlohner and D. Maison. "Dimensional Renormalization and the Action Principle". In: *Commun. Math. Phys.* 52 (1977), p. 11. DOI: 10.1007/BF01609069.

[187] P. Breitenlohner and D. Maison. "Dimensionally Renormalized Green's Functions for Theories with Massless Particles. 1." In: *Commun. Math. Phys.* 52 (1977), p. 39. DOI: 10.1007/BF01609070.

[188] P. Breitenlohner and D. Maison. "Dimensionally Renormalized Green's Functions for Theories with Massless Particles. 2." In: *Commun. Math. Phys.* 52 (1977), p. 55. DOI: 10.1007/BF01609071.

[189] M. S. Chanowitz, M. Furman, and I. Hinchliffe. "The Axial Current in Dimensional Regularization". In: *Nucl. Phys. B* 159 (1979), pp. 225–243. DOI: 10.1016/0550-3213(79)90333-X.

[190] J. G. Körner et al. "γ_5 and Infrared Dimensional Regularization". In: *Phys. Lett. B* 164 (1985), pp. 136–140. DOI: 10.1016/0370-2693(85)90047-4.

[191] D. Kreimer. "The γ_5 Problem and Anomalies: A Clifford Algebra Approach". In: *Phys. Lett. B* 237 (1990), pp. 59–62. DOI: 10.1016/0370-2693(90)90461-E.

[192] J. G. Körner, D. Kreimer, and K. Schilcher. "A practicable γ_5 scheme in dimensional regularization". In: *Z. Phys. C* 54 (1992), pp. 503–512. DOI: 10.1007/BF01559471.

[193] D. Kreimer. "Dimensionale Regularisierung im Standard Modell". PhD thesis. Johannes Gutenberg University, Faculty of Physics, 1992.

[194] D. Kreimer. "The role of γ_5 in dimensional regularization". In: (Dec. 1993). arXiv: hep-ph/9401354.

[195] E. W. N. Glover. "Two loop QCD helicity amplitudes for massless quark quark scattering". In: *JHEP* 04 (2004), p. 021. DOI: 10.1088/1126-6708/2004/04/021. arXiv: hep-ph/0401119.

[196] M. Böhm, H. Spiesberger, and W. Hollik. "On the One Loop Renormalization of the Electroweak Standard Model and Its Application to Leptonic Processes". In: *Fortsch. Phys.* 34 (1986), pp. 687–751. DOI: 10.1002/prop.19860341102.

[197] A. Denner. "Techniques for calculation of electroweak radiative corrections at the one loop level and results for W physics at LEP-200". In: *Fortsch. Phys.* 41 (1993), pp. 307–420. DOI: 10.1002/prop.2190410402. arXiv: 0709.1075 [hep-ph].

[198] M. Böhm, A. Denner, and H. Joos. *Gauge theories of the strong and electroweak interaction*. Stuttgart/Leipzig/Wiesbaden, Germany: B. G. Teubner, 2001. ISBN: 978-3-519-23045-8, 978-3-322-80162-3, 978-3-322-80160-9.

[199] A. Denner and S. Dittmaier. "Electroweak Radiative Corrections for Collider Physics". In: *Phys. Rept.* 864 (2020), pp. 1–163. DOI: 10.1016/j.physrep.2020.04.001. arXiv: 1912.06823 [hep-ph].

[200] C. Bogner et al. "`Loopedia`, a Database for Loop Integrals". In: *Comput. Phys. Commun.* 225 (2018), pp. 1–9. DOI: 10.1016/j.cpc.2017.12.017. arXiv: 1709.01266 [hep-ph].

[201] T. Huber and D. Maître. "`HypExp`: A `Mathematica` package for expanding hypergeometric functions around integer-valued parameters". In: *Comput. Phys. Commun.* 175 (2006), pp. 122–144. DOI: 10.1016/j.cpc.2006.01.007. arXiv: hep-ph/0507094.

[202] A. Kotikov. "Differential equations method: New technique for massive Feynman diagrams calculation". In: *Phys. Lett.* B254 (1991), pp. 158–164. DOI: 10.1016/0370-2693(91)90413-K.

[203] A. Kotikov. "Differential equations method: The Calculation of vertex type Feynman diagrams". In: *Phys. Lett.* B259 (1991), pp. 314–322. DOI: 10.1016/0370-2693(91)90834-D.

[204] A. Kotikov. "Differential equation method: The Calculation of N point Feynman diagrams". In: *Phys. Lett.* B267 (1991), pp. 123–127. DOI: 10.1016/0370-2693(91)90536-Y.

[205] Z. Bern, L. J. Dixon, and D. A. Kosower. "Dimensionally regulated one-loop integrals". In: *Phys. Lett.* B302 (1993), pp. 299–308. DOI: 10.1016/0370-2693(93)90400-C. arXiv: hep-ph/9212308 [hep-ph].

[206] Z. Bern, L. J. Dixon, and D. A. Kosower. "Dimensionally regulated pentagon integrals". In: *Nucl. Phys.* B412 (1994), pp. 751–816. DOI: 10.1016/0550-3213(94)90398-0. arXiv: hep-ph/9306240 [hep-ph].

[207] E. Remiddi. "Differential equations for Feynman graph amplitudes". In: *Nuovo Cim.* A110 (1997), pp. 1435–1452. arXiv: hep-th/9711188 [hep-th].

[208] T. Gehrmann and E. Remiddi. "Differential equations for two-loop four-point functions". In: *Nucl. Phys.* B580 (2000), pp. 485–518. DOI: 10.1016/S0550-3213(00)00223-6. arXiv: hep-ph/9912329 [hep-ph].

[209] A. V. Kotikov. "The Property of maximal transcendentality in the $\mathcal{N} = 4$ Supersymmetric Yang-Mills". In: *in: Subtleties in Quantum Field Theory: Lev Lipatov Festschrift (D. Diakonov, ed.), Petersburg Nucl. Phys. Inst., Gatchina.* 2010, pp. 150–174. arXiv: 1005.5029 [hep-th]. URL: http://inspirehep.net/record/856436/files/arXiv:1005.5029.pdf.

[210] S. Catani. "The Singular behavior of QCD amplitudes at two loop order". In: *Phys. Lett. B* 427 (1998), pp. 161–171. DOI: 10.1016/S0370-2693(98)00332-3. arXiv: hep-ph/9802439.

[211] C. Anastasiou et al. "Two-loop QCD corrections to the scattering of massless distinct quarks". In: *Nucl. Phys. B* 601 (2001), pp. 318–340. DOI: 10.1016/S0550-3213(01)00079-7. arXiv: hep-ph/0010212.

[212] C. Anastasiou et al. "Two loop QCD corrections to massless identical quark scattering". In: *Nucl. Phys. B* 601 (2001), pp. 341–360. DOI: 10.1016/S0550-3213(01)00080-3. arXiv: hep-ph/0011094.

[213] Z. Bern, A. De Freitas, and L. J. Dixon. "Two loop helicity amplitudes for gluon-gluon scattering in QCD and supersymmetric Yang-Mills theory". In: *JHEP* 03 (2002), p. 018. DOI: 10.1088/1126-6708/2002/03/018. arXiv: hep-ph/0201161.

[214] C. Anastasiou, E. W. N. Glover, and M. E. Tejeda-Yeomans. "Two loop QED and QCD corrections to massless fermion boson scattering". In: *Nucl. Phys. B* 629 (2002), pp. 255–289. DOI: 10.1016/S0550-3213(02)00140-2. arXiv: hep-ph/0201274.

[215] Z. Bern, L. J. Dixon, and D. A. Kosower. "Two-loop g —> gg splitting amplitudes in QCD". In: *JHEP* 08 (2004), p. 012. DOI: 10.1088/1126-6708/2004/08/012. arXiv: hep-ph/0404293.

[216] G. F. Sterman and M. E. Tejeda-Yeomans. "Multiloop amplitudes and resummation". In: *Phys. Lett. B* 552 (2003), pp. 48–56. DOI: 10.1016/S0370-2693(02)03100-3. arXiv: hep-ph/0210130.

[217] S. Mert Aybat, L. J. Dixon, and G. F. Sterman. "The Two-loop anomalous dimension matrix for soft gluon exchange". In: *Phys. Rev. Lett.* 97 (2006), p. 072001. DOI: 10.1103/PhysRevLett.97.072001. arXiv: hep-ph/0606254.

[218] S. Mert Aybat, L. J. Dixon, and G. F. Sterman. "The Two-loop soft anomalous dimension matrix and resummation at next-to-next-to leading pole". In: *Phys. Rev. D* 74 (2006), p. 074004. DOI: 10.1103/PhysRevD.74.074004. arXiv: hep-ph/0607309.

[219] T. Becher and M. Neubert. "Infrared singularities of scattering amplitudes in perturbative QCD". In: *Phys. Rev. Lett.* 102 (2009). [Erratum: *Phys. Rev. Lett.* **111**, 199905 (2013)], p. 162001. DOI: 10.1103/PhysRevLett.102.162001, 10.1103/PhysRevLett.111.199905. arXiv: 0901.0722.

[220] E. Gardi and L. Magnea. "Factorization constraints for soft anomalous dimensions in QCD scattering amplitudes". In: *JHEP* 03 (2009), p. 079. DOI: 10.1088/1126-6708/2009/03/079. arXiv: 0901.1091.

[221] T. Becher and M. Neubert. "On the Structure of Infrared Singularities of Gauge-Theory Amplitudes". In: *JHEP* 06 (2009). [Erratum: *JHEP* **11** (2013) 024], p. 081. DOI: 10.1088/1126-6708/2009/06/081,10.1007/JHEP11(2013)024. arXiv: 0903.1126.

[222] L. J. Dixon. "Matter Dependence of the Three-Loop Soft Anomalous Dimension Matrix". In: *Phys. Rev. D* 79 (2009), p. 091501. DOI: 10.1103/PhysRevD.79.091501. arXiv: 0901.3414 [hep-ph].

[223] S. Caron-Huot. "When does the gluon reggeize?" In: *JHEP* 05 (2015), p. 093. DOI: 10.1007/JHEP05(2015)093. arXiv: 1309.6521 [hep-th].

[224] Ø. Almelid, C. Duhr, and E. Gardi. "Three-loop corrections to the soft anomalous dimension in multileg scattering". In: *Phys. Rev. Lett.* 117 (2016), p. 172002. DOI: 10.1103/PhysRevLett.117.172002. arXiv: 1507.00047 [hep-ph].

[225] J. M. Henn and B. Mistlberger. "Four-Gluon Scattering at Three Loops, Infrared Structure, and the Regge Limit". In: *Phys. Rev. Lett.* 117.17 (2016), p. 171601. DOI: 10.1103/PhysRevLett.117.171601. arXiv: 1608.00850 [hep-th].

[226] S. Moch et al. "Four-Loop Non-Singlet Splitting Functions in the Planar Limit and Beyond". In: *JHEP* 10 (2017), p. 041. DOI: 10.1007/JHEP10(2017)041. arXiv: 1707.08315 [hep-ph].

[227] S. Moch et al. "On quartic colour factors in splitting functions and the gluon cusp anomalous dimension". In: *Phys. Lett. B* 782 (2018), pp. 627–632. DOI: 10.1016/j.physletb.2018.06.017. arXiv: 1805.09638 [hep-ph].

[228] S. Catani, D. De Florian, and M. Grazzini. "Soft-gluon effective coupling and cusp anomalous dimension". In: *Eur. Phys. J.* C79.8 (2019), p. 685. DOI: 10.1140/epjc/s10052-019-7174-9. arXiv: 1904.10365 [hep-ph].

[229] T. Becher and M. Neubert. "Infrared Singularities of Scattering Amplitudes and N^3LL Resummation for n-Jet Processes". In: *JHEP* 2020.1 (Jan. 2020), p. 025. DOI: 10.1007/JHEP01(2020)025. arXiv: 1908.11379 [hep-ph].

[230] J. M. Henn, G. P. Korchemsky, and B. Mistlberger. "The full four-loop cusp anomalous dimension in $\mathcal{N} = 4$ super Yang-Mills and QCD". In: *JHEP* 04 (2020), p. 018. DOI: 10.1007/JHEP04(2020)018. arXiv: 1911.10174 [hep-th].

[231] T. Huber et al. "The four-loop cusp anomalous dimension from the $N = 4$ Sudakov form factor". In: *Phys. Lett. B* 807 (2020), p. 135543. DOI: 10.1016/j.physletb.2020.135543. arXiv: 1912.13459 [hep-th].

[232] A. von Manteuffel, E. Panzer, and R. M. Schabinger. "Cusp and collinear anomalous dimensions in four-loop QCD from form factors". In: *Phys. Rev. Lett.* 124.16 (2020), p. 162001. DOI: 10.1103/PhysRevLett.124.162001. arXiv: 2002.04617 [hep-ph].

[233] T. Becher and M. Neubert. "Infrared singularities of QCD amplitudes with massive partons". In: *Phys. Rev. D* 79 (2009). [Erratum: *Phys. Rev. D* **80** (2009) 109901], p. 125004. DOI: 10.1103/PhysRevD.79.125004, 10.1103/PhysRevD.80.109901. arXiv: 0904.1021.

[234] G. P. Korchemsky and A. V. Radyushkin. "Loop Space Formalism and Renormalization Group for the Infrared Asymptotics of QCD". In: *Phys. Lett. B* 171 (1986), pp. 459–467. DOI: 10.1016/0370-2693(86)91439-5.

[235] S. Moch, J. A. M. Vermaseren, and A. Vogt. "The Quark form-factor at higher orders". In: *JHEP* 08 (2005), p. 049. DOI: 10.1088/1126-6708/2005/08/049. arXiv: hep-ph/0507039.

[236] L. J. Dixon. "A brief introduction to modern amplitude methods". In: *Theoretical Advanced Study Institute in Elementary Particle Physics: The Higgs Boson and Beyond*. 2014, pp. 31–67. DOI: 10.5170/CERN-2014-008.31. arXiv: 1310.5353 [hep-ph].

[237] M. E. Peskin and D. V. Schroeder. *An introduction to quantum field theory*. Reading, USA: Addison-Wesley, 1995. ISBN: 978-0-201-50397-5.

[238] L. J. Dixon. "Calculating scattering amplitudes efficiently". In: *Theoretical Advanced Study Institute in Elementary Particle Physics: QCD and Beyond*. Jan. 1996, pp. 539–584. arXiv: hep-ph/9601359.

10 List of acronyms

QFT	Quantum field theory
QED	Quantum electrodynamics
EW	Electroweak
QCD	Quantum chromodynamics
LHC	Large-Hadron-Collider
JLab	Jefferson Lab
RCS	real Compton scattering
VCS	virtual Compton scattering
TCS	timelike Compton scattering
DVCS	deeply-virtual Compton scattering
VVCS	forward double-virtual Compton scattering
dVCS	double virtual Compton scattering
DDVCS	double deeply virtual Compton scattering
BH	Bethe-Heitler
SL	spacelike
TL	timelike
FF	form factor
DIS	deep inelastic scattering
PD	Parton Distribution
GPD	Generalized Parton Distribution
ERBL	Efremov-Radyushkin-Brodsky-Lepage
DY	Drell-Yan
PV	Passarino-Veltman
UV	ultraviolet
IR	infrared
IBP	Integration-By-Part
HVBM	t Hooft-Veltman-Breitenlohner-Maison